

BASIC DATA: COMPOSITION, THERMODYNAMIC PROPERTIES AND TRANSPORT COEFFICIENTS APPLIED TO FUSES.

P. André⁽¹⁾, J. Aubreton⁽²⁾, W. Bussière⁽¹⁾, M.F. Elchinger⁽²⁾, S. Memiaghe⁽¹⁾,
D. Rochette⁽¹⁾

LAEPT⁽¹⁾, 24 av des Landais, 63177 Aubière Cedex, France, E-mail: pascal.andre@univ-bpclermont.fr
SPCTS⁽²⁾, 47 av Albert Thomas, 87065 Limoges Cedex, E-mail: marie-francoise.elchinger@unilim.fr

Abstract: Two main areas of research can be determined for the basic data that are composition, thermodynamic properties and transport coefficients: the polyphasic area and the gas phase and plasma phase area. In the case of mixture of (Ag, SiO₂) that can be found in fuses field, we depict the main results available at the present time.

Keywords: e.g. fuse, composition, transport coefficients, polyphasic, thermal plasma.

1. Introduction

Two main areas of research can be determined for the basic data: the polyphasic area and the gas phase and plasma phase area. In the case of mixture as Ag-SiO₂, few studies are given [1-4]. The fuse operation can be described by successive steps [5, 6]: firstly the electric current produces the heating of the silver strip around constrictions; secondly, the fusion and the vaporization of the constriction opens a gap in which an electrical arc is initiated; thirdly, the arc interacts with the surrounding silica sand and the silver fuse element continues to melt and to vaporize (burn-back) [7, 8] until the circuit voltage is not high enough to maintain the arc.

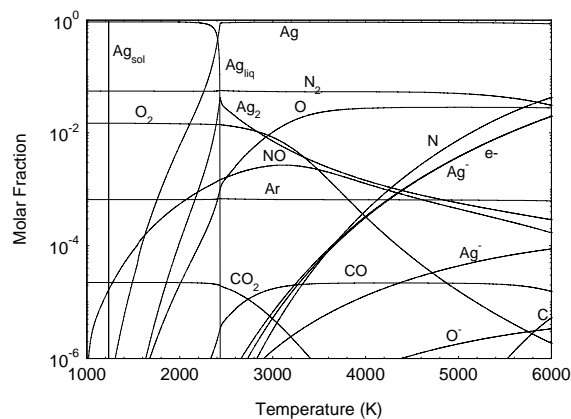
In this paper we give some results for the polyphasic area: composition, enthalpy and pressure dependence on temperature and for the gas and plasma phase we give the composition, the enthalpy, the viscosity, the electrical and thermal conductivities.

2. Polyphasic area

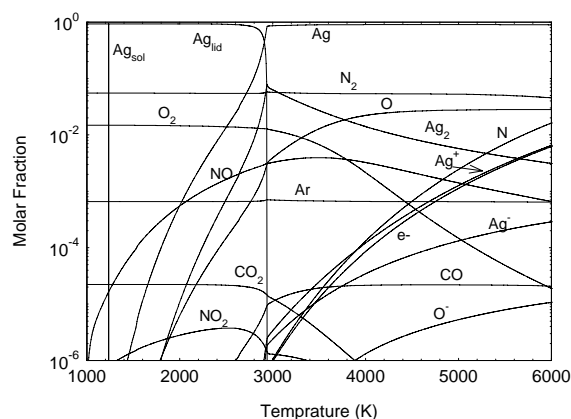
By using a Gibbs Free Energy minimization method [3, 9], one can obtain the molar fraction versus temperature. Firstly since the silver ribbon melt and vaporized, one can assume that the mixture is mainly composed of silver and air. Furthermore the temperature increases due to Joule heating the pressure increases. That is why the calculation has been made with air and silver for two pressures: 1 bar and 10 bars. For these calculation we take into account : 16 monatomic species Ar, Ar⁺, Ag⁻, Ag, Ag⁺, C, C⁻, C⁺, O, O⁻, O⁺, N, N⁺, Si, Si⁺, Si⁻ and

electrons, 23 diatomic species Ag₂, C₂, C₂⁻, C₂⁺, CN, CN⁻, CN⁺, CO, CO⁻, CO⁺, CSi, N₂, N₂⁻, N₂⁺, NO, NO⁻, NO⁺, NSi, O₂, O₂⁻, O₂⁺, Si₂, SiO and 15 polyatomic species CNO, CNN, CO₂, CO₂⁻, NO₂, NO₃, N₂O, NCN, NO₂⁻, NSi₂, N₂O⁺, N₃, O₃, SiO₂, Si₃.

The results of the molar fractions are shown in figures 1 and 2.

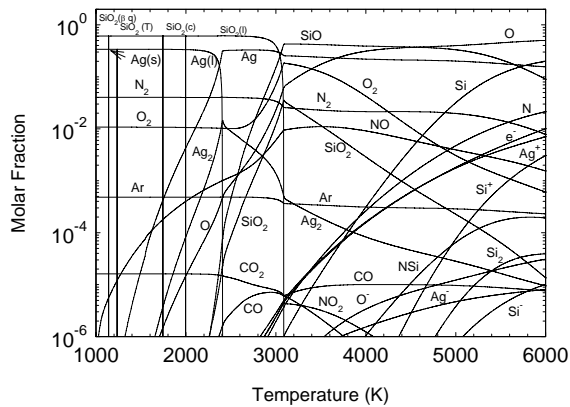


a) P=1 bar

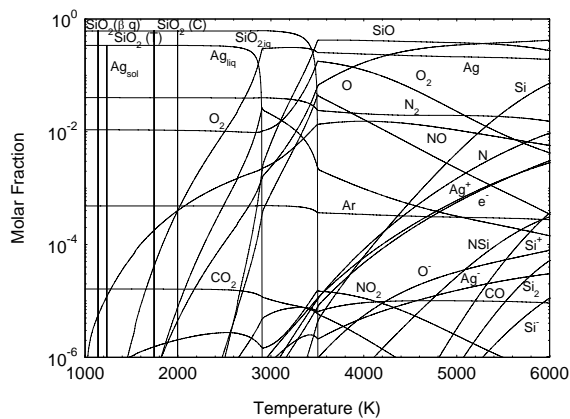


b) P=10 bars

Fig. 1: Molar fractions of chemical species versus temperature calculated at 1 bar and 10 bars. The weight percentage of air is fixed at 2% and for the silver at 98%.



a) P=1 bar



b) P=10 bars

Fig. 2: Molar fractions of chemical species versus temperature calculated at 1 bar and 10 bars. The weight percentage of air is fixed at 2% and for the silver at 49% and for SiO₂ at 49%.

Figure 1 shows the molar fraction for silver and air: 98% Ag and 2% of Air in weight percentage for two pressures 1 and 10 bars. Figure 2 shows the molar fraction for mixture of silver, silica and air: 49% SiO₂, 49% Ag and 2% of Air in weight percentage for two pressures 1 and 10 bars.

At low temperature (<1,500 K) the gaseous species are only due to air namely N₂, O₂, Ar and CO₂. The liquid silver vaporizes in gaseous silver Ag for both cases (Fig. 1 and 2). The liquid silica vaporizes in SiO and O₂ (Fig. 2). An increase of NO molar fraction when the liquid silica vaporizes can be observed. So, a part of N₂ reacts with O₂ to produce NO during this vaporization. A break in CO₂ molar fraction can be observed when the liquid silica vaporized. So, the liquid silica vaporization influences the dissociation of CO₂. The monatomic species Si is mainly due to the dissociation of SiO at high temperature (>5,000 K) and the dissociation of SiO₂ and SiO for lower temperature. The electrical neutrality between charged particles is mainly made between Ag⁺ and electrons.

The vaporization of silver and SiO₂ appears for higher temperature when the pressure is higher (Fig. 1 and 2). At low temperature, the gaseous species are those of air. The liquid silver vaporizes at 2,400 K for 1 bar and 2,915 K for 10 bars in the case of considered mixture of SiO₂, Ag and Air. The liquid silica vaporizes in SiO and O₂ for temperatures around 3,090 K at 1 bar and 3,500 K for 10 bars. Then O₂ dissociates in O, SiO dissociates to give Si and O. These latter become the main chemical species. The polyatomic species are still observed present at higher temperatures for higher pressures, for example, CO₂. Molar fraction of NO₂ has a higher value for 10 bars than for 1 bar. Since the ionization appears at higher temperature, the electronic concentration is lower for higher pressures. The electrical neutrality is made mainly between Ag⁺ and e⁻ for lower considered pressures and between Ag⁺, e⁻, O⁻ and Ag⁻ for higher pressures.

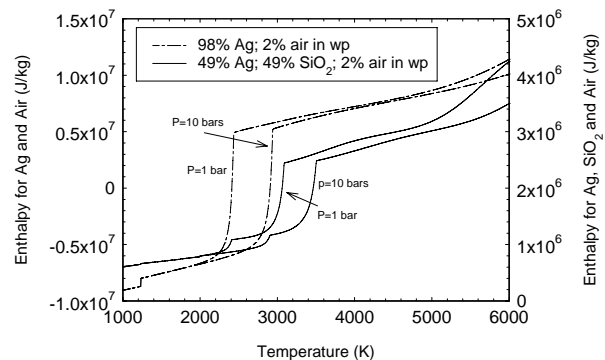


Fig. 3: Enthalpy versus temperature calculated at 1 and 10 bars for mixtures of air with silver and air with silica and silver.

Figure 3 shows the calculated total enthalpy versus the temperature for silver with air and silica and silver with air at 1 bar and 10 bars. Concerning the silver with air, two breaks in the enthalpy curves can be observed. The first break corresponds to the melting of solid silver at a temperature of 1,234 K and the second break to the vaporization of liquid silver at a temperature around 2,400 K for a pressure of 1 bar and 2,900 K for a pressure of 10 bars. Concerning the silica and silver with air, a break around a temperature of 3,050 K for 1 bar and 3,450 K for 10 bars that corresponds to the silica vaporization can be observed. The two breaks associate to silver vaporization can also be noted. The phase changes of silica, namely, β -quartz to tridymite, tridymite to cristobalite and cristobalite to liquid silica and the phase change of silver liquid to solid can be hardly seen due to the enthalpy scale. As a matter of fact, the involved energies in this phase transformations are low [9].

The vapor pressure of Ag can be deduced from the partial pressure of gaseous Ag. By using an

equation as $\text{Log}(p_{\text{vap}}) = A + B/T + C \text{Log}(T)$ with p_{vap} in mm of Hg and T in K, the vapor pressure of Ag is well approximated with $A=11.3$, $B=-14,300$ and $C=-0.738$. Concerning the vapor pressure of SiO_2 , since liquid SiO_2 vaporizes mainly in SiO and O_2 . These two molecules reacting with the air, the vapor pressure can not be directly deduced from the partial pressures. Nevertheless, with a calculation pressure dependence on temperature in SiO_2 , the coefficients can be determined. So the vapor pressure of SiO_2 is well approximated with $A=26$, $B=-31,600$ and $C=-3.76$. So we have to calculate the temperature dependence on pressure for each mixture of silica, silver and air.

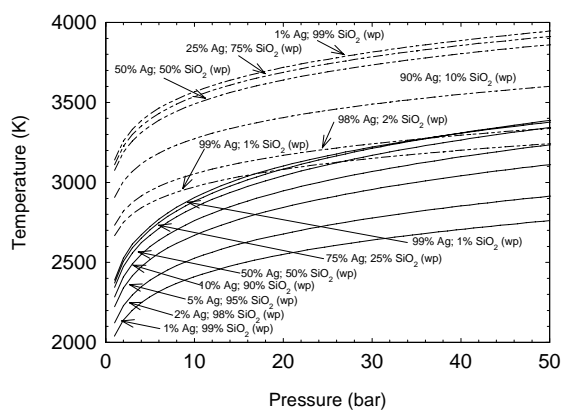


Fig. 4: Vaporization temperature of liquid silver and liquid silica calculated for various pressures. The weight percentage of air is fixed at 2% and the silver and silica proportion is given in weight percentage.

In figure 4, the vaporization temperatures of liquid silver and liquid silica calculated for various pressures are given. A large variation of vaporization temperature around a factor 1.3 between silver percentages of 1% to 75 % for a given pressure can be observed; for higher silver percentage the variation in vaporization temperature is lower. For vaporization temperature of liquid silica, a large variation around a factor 1.2 between silica weight percentages of 1% to 50 % for a given pressure can be observed; for higher silica percentage the variation in vaporization temperature is lower.

3. Gas and plasma phase

The transport coefficients and the thermodynamic properties, in the field of high temperatures ($> 4,000$ K) and high pressures (1 to 30 atm.), are essential data in the modelling of plasma processes during the fuse operation [11]. To determine the transport coefficients, we use the well-known solution of the Boltzmann equation due to Chapman and Enskog

[12, 13]. This assumes two-body interactions between chemical species. This interaction can be described by a potential interaction between two particles. By successive integrations of these potentials, we obtain collision integrals which are the basic data of the transport coefficients. The potentials depend on the type of molecules that interact [14]:

- Neutral-neutral molecules
- Charged-neutral molecules
- Charged-charged molecules
- Electron-neutral molecules

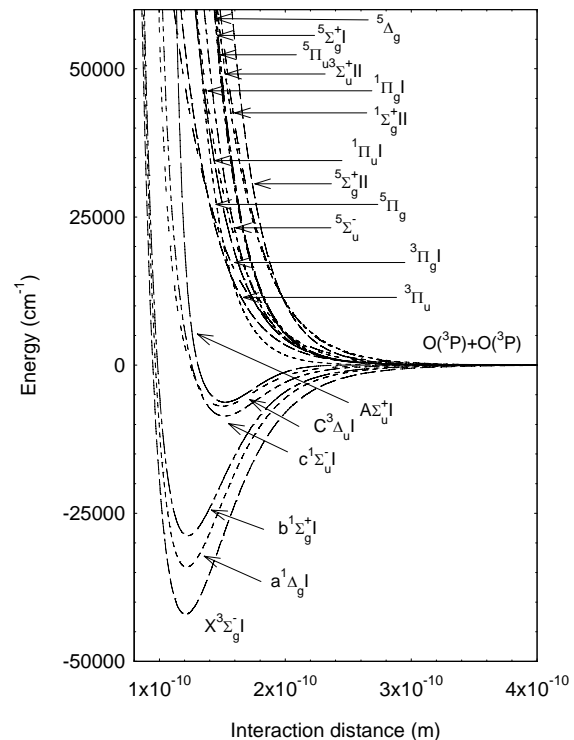
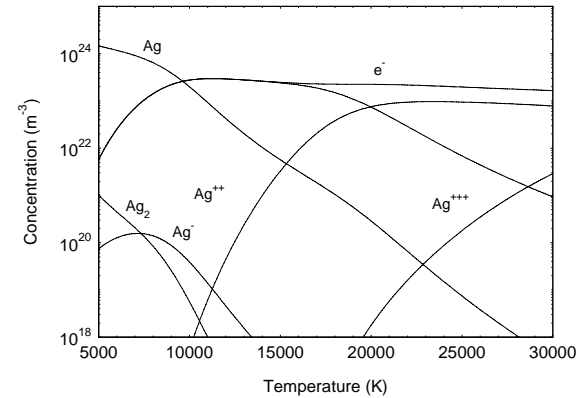


Fig. 5: Hulbert-Hirschfelder and repulsive potentials taken into account for the interaction between oxygen atoms versus the interaction distance.

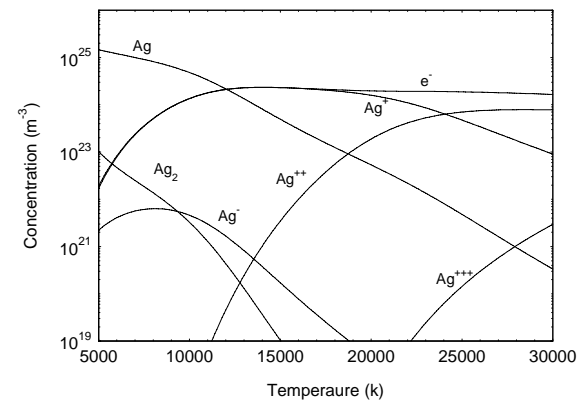
In figure 5, the potential curves are represented in the case of (O, O) in ^3P state. For the two other collisions (Ag, Ag) and (Si, Si) the results are given in [4]. From these three collisions one can obtain a Lennard Jones potential [12] that allows to obtain all the potential for the collisions between neutral molecules with the help of combination rules.

For the collisions between neutral and charged molecules a non elastic process namely charged transfer has to be taken into account. For the elastic processes we consider a dipole potential. For the collision between the charged molecules we consider a Coulomb potential shielded by a Debye length. For collisions between electron and neutral species, the collision Integrals are obtained from the literature or from the polarisability of neutral species.

Thus the data base to obtain all the collisions integral from the potential are determined. We have to calculate the composition for high temperature. From a Gibbs energy method [1, 3], we obtain the composition versus temperature. We have chosen to study two plasmas: silica plasma and silver plasma.

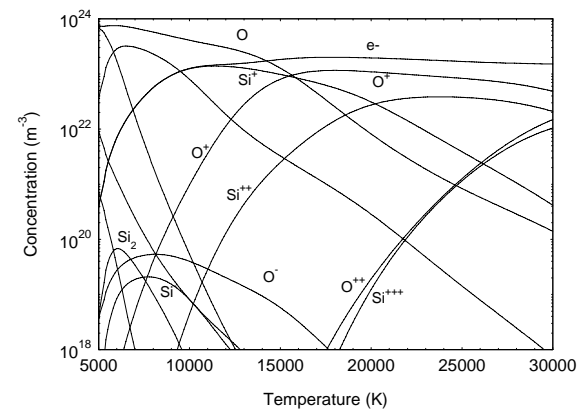


a) P=1 atm

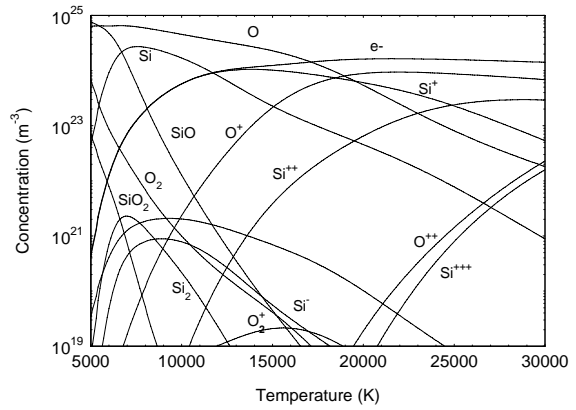


b) P=10 atm

Fig. 6: Composition calculation of silver plasma versus temperature for two pressures



a) P=1 atm



b) P=10 atm

Fig. 7: Composition calculation of silica plasma versus temperature for two pressures.

We give the concentration versus the temperature for silver plasma in figure 6. The main species in temperature range from 5,000K to 9,550K at 1 atm and in temperatures range from 5,000K to 12,000K is monatomic silver. For high temperature the main chemical species is electrons. The electrical neutrality is made between electrons and ionized silver before 19,900 K for 1 atm and 24,000 K for 10 atm and then with silver ionized two times for higher temperature.

For silica plasma the concentration is given in figure 7. The main species is monatomic oxygen between 5,000 K and 14,000 K for 1 atm and between 5,000 K and 17,000 K for 10 atm. For higher temperature the main chemical species is electrons.

By comparison the graphs devoted to 1 atm and those devoted to 10 atm, we remark that the ionisation of neutral species appears at higher temperature for higher pressure.

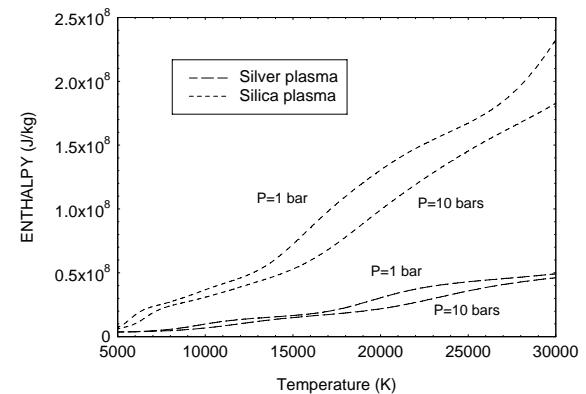


Fig. 8: Massic enthalpy versus temperature for silica plasma and silver plasma for two pressures.

Once the concentration calculation is made we can determine the enthalpy versus temperature. We present the results in figure 8. As we remark previously higher pressure higher temperature for which the chemical reaction appears. So for a given enthalpy the temperature is higher for a higher

pressure. Some changes in the slope of the curve can be associated to chemical reactions. In the case of silica plasma around 5,200 K the dissociation of SiO appears and around 14,000 K for 1 atm and 17,000K for 10 atm appear the ionisation of oxygen. In the case of silver plasma, the change of the slope around 9,550K at 1 atm and 12,000K at 10 atm can be associated to the ionisation of monatomic silver.

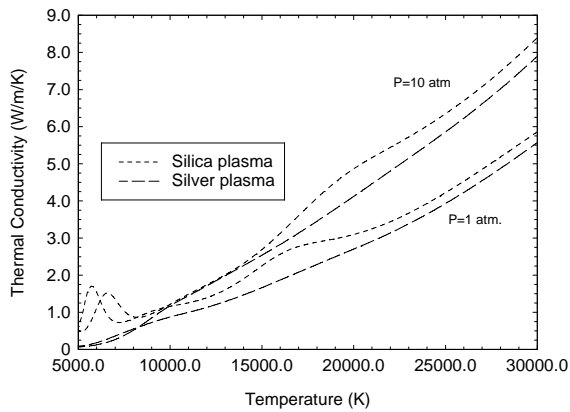


Fig. 9: Thermal conductivity versus temperature for silica plasma and silver plasma for two pressures.

In figure 9, we plot the thermal conductivity for the two considered pressures and for the two considered plasmas. The total thermal conductivity λ_{tot} can be separated into four terms with a good accuracy [15, 16]:

$$\lambda_{tot} = \lambda_{tr}^e + \lambda_{tr}^h + \lambda_{int} + \lambda_{react}$$

where λ_{tr}^e is the translational thermal conductivity due to the electrons, λ_{tr}^h the translational thermal conductivity due to the heavy species particles, λ_{int} the internal thermal conductivity and λ_{react} the chemical reaction thermal conductivity. The peak appearing in the thermal conductivity can be associated to the chemical reactions. Since the chemical reaction is made at higher temperature for higher pressure, the peak associated to SiO dissociation appears at higher temperature: 5,700K at 1 atm., 6,600 K at 10 atm. When the electrons become the main species the thermal conductivity due to the electron become the main contribution to the total thermal conductivity. Since the electronical thermal conductivity follows the electrons density and that electrons density follows the Dalton law, we observe higher thermal conductivity for higher pressure.

In figure 10, we plot the viscosity versus temperature for the two considered pressures and for the two considered plasmas. For silver plasma the results show an increase followed by a decrease versus temperature. Since the degree of ionization depends on the pressure, the temperature at which the peak occurs depends on the pressure. We obtain 6,300 K

for 1 atm., 7,750 K for 10 atm for silver plasma. In the case of silica plasma, we obtain two peaks at 7,500 K and 11,750 K for 1 atm, 8,800K and 13,600K for 10 atm. The first change in the slope is mainly due to the dissociation of SiO; the second peak is due to the ionisation of O.

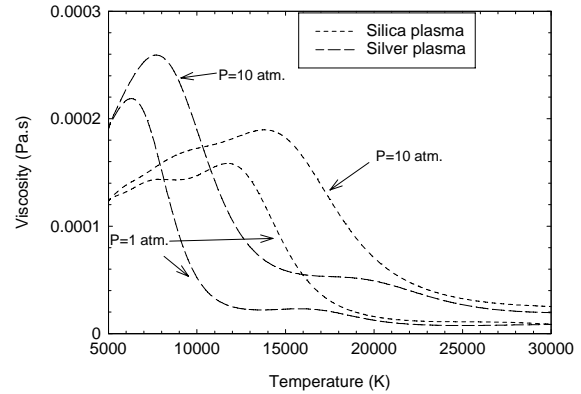


Fig. 10: Viscosity versus temperature for silica plasma and silver plasma for two pressures.

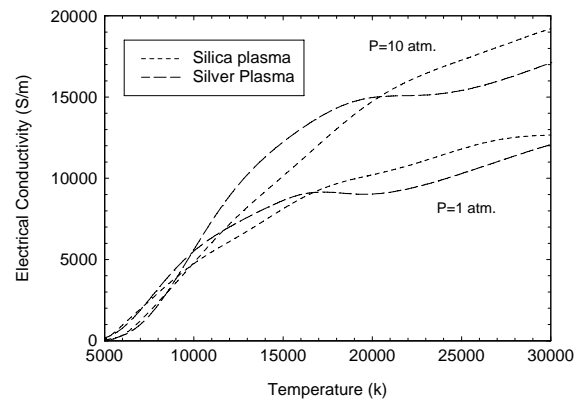


Fig. 11: Electrical conductivity versus temperature for silica plasma and silver plasma for two pressures.

In figure 11, we present the influence of pressure on the electrical conductivity for the two considered plasmas. For the same pressure, the electrical conductivities differ for the two plasmas. The reason is that the electrical neutrality is not made between the same species, that is to say between e^- , Ag^+ and Ag^{++} for silver plasma and between e^- , Si^+ , O^+ and Si^{++} . When pressure is higher, the ionization appears at higher temperatures. So, the electron density is lower at low temperatures. Consequently, the electrical conductivity is lower. When the pressure is higher and when the plasma is fully ionized, the electrons density follows the Dalton law and its value is higher. So, we observe higher electrical conductivity.

4. Conclusion

From the calculation of the composition in the polyphasic area we have shown the great role played by the chemical species. Notably with the liquid silica that are transformed in monoxide silica and oxygene. This temperature of vaporization depends on the proportion of silver with silica. The electrical neutrality is mainly made between ionized gaseous silver and electrons even with a low amount of silver. So, at low temperature the electrical conductivity depends on silver. When the pressure and the amount of silver are high, there is an increase in molar fraction of electronegative chemical species as Ag⁻ and O⁻.

In the gas and plasma phase, we have compared and explained the results of transport coefficients for two plasmas: silica plasma and silver plasma at 1 atm and 10 atm. The remarkable results are concerning the viscosity. The silver plasma has a lower viscosity between 10,000 K and 20,000 K at atmospheric pressure 15,000 K and 25,000 K for 10 atm. and between 17,000 K and 27,000 K for 30 atm. than the silica plasma This result explains the fact that we observe silver at a large distance from the fuse element and also can explain the variation of the composition in the fulgurite after the working of the fuse. Furthermore we have presented all the data needed to model the fuse working: electrical and thermal conductivity, enthalpy, viscosity.

The development of such calculation will be made with the kinetics chemical reactions to involve time scale lower than 1 ms and by the addition of compounds as CaF₂.

Acknowledgments

We thank for their financial support MM. T. Rambaud and JL. Gelet from Ferraz Shawmut, M. F. Gentils from Schneider Electric, and M. JC. Perez-Quesada from Mesa.

References

- [1] W. Bussière, P. André, "Evaluation of the composition, the pressure, the thermodynamic properties and the monatomic spectral lines at fixed volume for a SiO₂-Ag plasma in the temperature range 5 000 - 25 000 K", *Journal of Physics D: applied physics* **34**, 1657-1664, 2001.
- [2] W. Bussière, D. Rochette, P. André, "Study of the SiO₂ plasma physical parameters: temperature, electron density, pressure, radiation", *Proceedings of the 7th Icefa (Gdansk Univ. of Techn., Gdansk, Poland), 8-10 Sept.*, pp 119-125, 2003.
- [3] D. Rochette, W. Bussière, P. André, « Composition, Enthalpy, and Vaporization Temperature Calculation of Ag-SiO₂ Plasmas with Air in the Temperature Range from 1000 to 6000 K and for Pressure Included between 1 and 50 bars" *Plasma Chemistry and Plasma Processing* **24**, No 3, 475-492, 2004.
- [4] P. André, W. Bussière, D. Rochette, « Transport coefficients of Ag-SiO₂ plasmas », PCPP, to be published, Vol 27, N°4, 2007.

- [5] A. Wright and P.G. Newberry, « Electric Fuses», 2nd Edition, IEE Power Series, 1997.
- [6] S. Gnanalingam and R. Wilkins, *IEE Proc. Vol 127, n°6*, p 434-440, 1980.
- [7] H.W. Turner and C. Turner, *Proc. of the 3rd Int. Symp. on Switching Arc Phenomena (Lodz, Poland)*, pp 334-337, 1977.
- [8] Bussière W., « Estimation of the burn-back rate in high breaking capacity fuses using fast imagery », *J.Phys. D : Appl. Phys.*, **34**, pp. 1007-1016, 2001.
- [9] Gordon and McBride, « Computer Program for Calculation of Complex Chemical Equilibrium Compositions, Rocket Performance, Incident and Reflected Shocks, and Chapman-Jouguet Detonations », NASA SP-273, 1976.
- [10] CRC Handbook of Chemistry and Physics 2001 81th Ed.
- [11] D.Rochette, S. Clain, "Mathematical model and simulation of gas flow through a porous medium in high breaking capacity fuses", *International Journal of Heat and Fluid Flow* **25**, Issue 1, 115-126, 2004.
- [12] J.O. Hirschfelder, C.F. Curtiss, R. Byron Bird, "Molecular theory of gases and liquids", New York: Wiley, 1964.
- [13] S. Chapman and T.G., *The mathematical Theory of Non-Uniform Gases*, 3rd edn, Wiley, New York, 1964.
- [14] J Aubreton, P Fauchais "Influence des potentiels d'interaction sur les propriétés de transport des plasmas thermiques : exemple d'application le plasma argon hydrogène à la pression atmosphérique », *Revue Phys. Appl*, **18**, 51-66, 1983.
- [15] R.S. Devoto, "Simplified Expressions for the Transport Properties of Ionized Monatomic Gases", *The Physics of Fluids*, **10**, N°10, 2105-2112, 1967.
- [16] J.T. Vanderslice, Stanley Weismann, EA Mason, RJ Fallon, "High Temperature Transport Properties of Dissociating Hydrogen", *The Physics of Fluids*, **5**, N°2, 155-164, 1962.

THE BACKGROUND AND AIMS OF PROFUSE

John Bassford C.Eng
President of Profuse International

Synopsis: the aim of this paper is to show the contribution that Profuse has made to the promotion and communication of the use of fuse and fused technology in Europe and the rest of the world, the origins and background of the organisation and how it aims to assist both the educational and user worlds in their appreciation of the vital need to use this seemingly simple but technically complex product.

Within the electrical protective industry there had been over the last 2 decades an accelerated move to use circuit breakers as a protective device but now the technical and educational world is recognising that the fuse, which had been decried as dated and a dinosaur, actually gives economic, environmental and technical advantages.

With this scenario a group of European fuse link and fused equipment manufacturers came together on June 5, 1998 to discuss how they could “Convey Knowledge on the use of Protective Devices” to the world at large and the educational areas of both the user and student world.

The founder members were Katko from Finland, MEM from the UK, Holec from Holland who are now both part of the Eaton Organisation, Ferraz Shawmutt from France who now have a worldwide connection, M. Schneider from Austria Weber from Germany and Socomec from France and by September of 1998 the articles of Association had been registered.

Since then the numbers of members have changed upwards but due to current market trends of mergers and takeovers we now have 11 members but if this was broken down into companies who were individual members the actual base is 16 of whom 5 are on the Administrative Board. The members come from a wide range of disciplines but are all manufacturers of fuses or fused equipment, sometimes both and vary in size for example from a multinational company such as ABB or a company with a national base but an international market such as say OEZ. Though the members are fuse based many of them manufacture within their own

company circuit breakers recognising the parallel benefits of both products.

Each year a General Meeting is held to discuss matters of current interest and to attempt to ensure that any market trends are noted and to take advantage of the individual strengths of the members to spread technical benefits to the wider world.

So what simplistically are the benefits of fuse technology, which I am sure most of you are aware, how do we communicate them and where do we see Profuse contributing in the future.

Let us for completeness state some simple benefits which in this ultra conservative world must be considered

- HRC Fuses are safe at all fault levels when used correctly
- As new operation after all faults
- Availability and interchange ability worldwide
- Simple safe consistent operation
- Proven technology in a modern environment
- Energy limitation so smaller cables needed
- Lower energy use than most protective devices
- All products tested to more onerous conditions than would be encountered in any application

So having recognised there are benefits how do Profuse communicate this information to a sceptical world or to a user who is unaware of any possibility of using any product apart from a circuit breaker. Here it must be stated that Profuse is not anti breaker but strongly in favour of the fuse benefits. In fact in an ideal world the two together is probably the best solution from a technical stand point. If we turn back to the early days then the mode of communication was simplistic in that hand outs were provided stating both the advantages and varying applications of fuses but not looking further in the real education of how to use a fuse and its varying component parts.

Hence the move was to a website which over the years has developed into a technical tool both for the members of Profuse, the fuse and fused equipment user and the student. The address is www.profuseinternational.com and here are found technical papers and application notes written by the members and specialists to augment the members inherent knowledge plus a selection of papers, thanks to "The Fuse Club" from the last ICEFA Conference. This information contains everything from the FAQ's to details on individual components. So in this way we communicate knowledge, though an approach to an individual member will always provide the needed assistance. Within the website considerable technical documentation exists from both application guides on both low and medium voltage applications, interpretation and advice on standards plus sections on frequently asked questions in respect of design and use of fuses and the associated equipment.

Another area of particular interest is the environment, where, in addition to the ecological benefits in fuse use, product recycling is important, outside of the current requirements of the WEEE directive. This started in Germany and now through company contact is spreading initially Europe wide but we trust will continue to spread further. The initial costs encountered in any product using say copper are high but for a fuse, recycling used fuses yields copper at a lower cost than initially mining the material. More details on this topic can be found either on the Profuse web site or the papers from the last ICEFA Conference.

And as final typical area where we are trying to aid the market in knowledge we must consider safety be it in the field of application notes or the use of materials, topics such as "Arc Flash" which is a major problem in certain parts of the world are considered and advice given where appropriate.

So what of the future where energy costs continue to rise and product size to diminish with safety being the watchword in a more demanding environment, a greater need for communication of safe solutions is needed and here due to the constant technical updating of information via the Profuse network we trust the evidence for the fuse solution will be available from Profuse and its members.

These are some thoughts on Profuse, an organisation in mainly Europe, crossing country borders with support from Trade Organisation in the various countries but basically a professional organisation of companies supporting fuses and fuse technology and trying to communicate

information on safe and economical protective systems.

INCORRECT USE OF FUSE CHARACTERISTICS IN IEC 62271-105 RESTRICTS H.V. FUSE APPLICATION IN RING MAIN UNITS

Dr.-Ing. Herbert Bessei

fuseXpert, Geibstraße 27, D-55545 Bad Kreuznach, hbessei@fuseXpert.de

Abstract: IEC 62271-105 “Alternating current switch-fuse combinations” goes back to IEC 420:1973, when relatively slow acting switches in air and under oil were used in ring main units. SF₆ insulated switchgear did not exist in m.v. secondary distribution systems by then. This may explain why no one cared about the limitations in the use of fuse time-current characteristics in a time range below 100 ms.

The paper highlights the conflicting claims of IEC 62271-105 to IEC 60282-1 “High voltage fuses” and IEC TR 60787 “Application guide for the selection of high voltage current-limiting fuse-links for transformer circuits” and explains the consequences with respect to h.v. fuse application in combinations with SF₆ switches. Indeed, important and well established fuse applications will virtually be ruled out by IEC 62271-105.

Alternative proposals are presented to resolve the conflicting situation in the International Standards.

Keywords: h.v. fuse, fuse-switch combination, IEC 62271-105, transfer current.

1 Introduction

Distribution type transformers are commonly protected by means of current limiting back-up fuses on the h.v. side. Switch-fuse combinations, according to IEC 62271-105, with trip-free switches operated by the fuse striker, have gained importance with the introduction of metal encapsulated SF₆ insulated switchgear. Major objectives of this combinations are three-pole disconnection in case of fuse operation and thermal protection of the fuse compartment in case of partially damaged fuse-elements.

IEC 62271-105 is by definition a switchgear standard that describes a full-range protective device. It interferes however heavily with transformer protection rules and is at least partly conflicting with fuse standards and transformer back-up protection practice. Conflicts result mainly from one single postulation laid down in sub clause 8.101.2 of IEC 62271-105:

The transfer current of the combination shall be less than the primary fault current caused by a solid short-circuit on the transformer secondary terminals.

$$I_{\text{transfer}} \leq I_{\text{SC}} \quad (1)$$

The solid l.v. terminal short-circuit current on the primary side can be calculated from the Transformer rated current I_T and the relative short-circuit voltage u_K as follows:

$$I_{\text{SC}} = I_T / u_K \% \quad (2)$$

A primary fault current, caused by a solid short-circuit on the transformer secondary terminals, corresponds to very high TRV values which a switch may not be able to cope with. The fuses shall therefore be selected to interrupt such fault currents without transferring any breaking duty to the switch currents without transferring any breaking duty to the switch, i.e. before the switch opens

This postulation sounds reasonable and may be applied to switch-fuse combinations having a fuse initiated opening time of 100 ms and above. The application to fast acting switches, that open within 20 to 30 ms is just unrealistic, as real time-current characteristics of fuses do not exist in this time range.

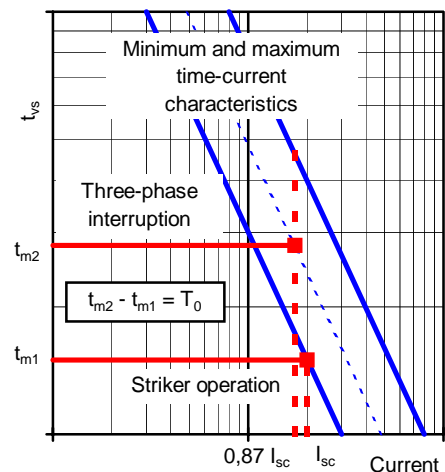


Fig. 1: Determination of transfer current

2 Determination of transfer currents

The transfer current I_{transfer} represents the value of the three-phase symmetrical current at which the fuse and the switch exchange breaking duties. It applies to striker initiated switch operation and depends on the

tolerances of fuse time-current characteristics and the fuse-initiated opening time of the switch. Above this value a three-phase current short-circuit is interrupted by the fuses only. Overcurrents below this value are interrupted by a fuse in one phase and by the switch in the other phases.

Fig. 1 illustrates the practical determination of the transfer current:

- The symmetrical three-phase fault current I_{SC} melts the first fuse-link at the melting time t_{m1} and initiates striker operation.
- The three-phase fault current turns into a two-phase current of $0,87 I_{SC}$ intensity.
- The second fuse-link operates at the time t_{m2} and interrupts the fault current.
- The switch opens after the fuse-initiated opening time T_0 .

The transfer current $I_{transfer}$ represents the current value at which T_0 equals the time difference $t_{m2} - t_{m1}$.

$$T_0 = t_{m2} - t_{m1} \quad (3)$$

Fault currents above this value are cleared by the fuses only. Below this value the breaking duty is transferred from the fuses to the switch.

In a simplified method explained in IEC 62271-105 Annex B, assuming a statistic tolerance for the fuse time-current characteristics of $\pm 6,5 \%$ and gradient of 4, the transfer current can be determined from the minimum time-current characteristic of the fuse using equation (4):

$$I_{transfer} = I_{(0,9 T_0)} \quad (4)$$

As fuse manufacturers usually publish mean time-current characteristics rather than minimum values, the author suggests a further, more user oriented, approximation given in equation (5):

$$I_{transfer} = I_{(T_0)} \quad (5)$$

The transfer current is approximately the current that corresponds to the time T_0 on the mean time-current characteristic.

3 Fuse selection acc. to IEC TR 60787

Distribution type transformers are preferably protected against the effects of internal faults by means of h.v. current-limiting fuses on the primary side. Overloads and faults on the l.v. side are disconnected by a main fuse or a c.b. in the feeder line (fig. 2). (Transformers with overload protection by means of non-current-limiting fuses on the h.v. side are not considered here.)

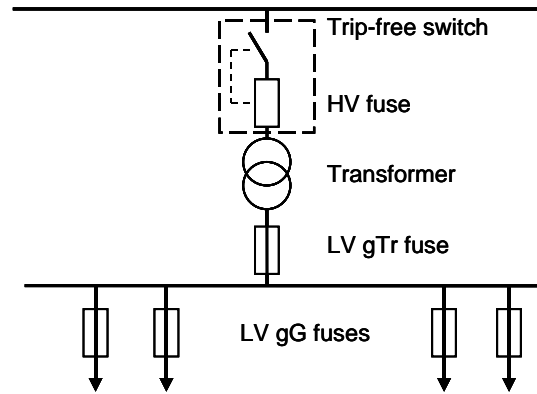


Fig. 2: Circuit diagram of ring main unit

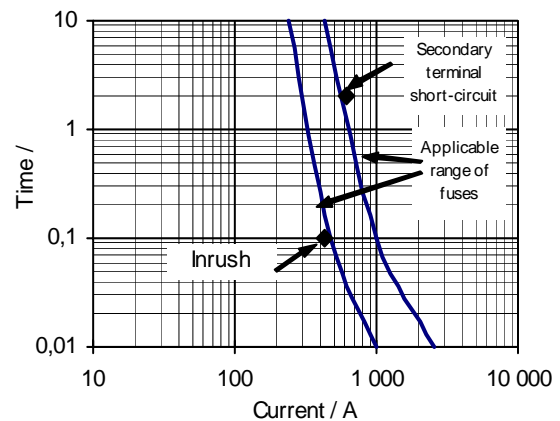


Fig. 3: Fuse selection for transformer circuits

Fuse-links for transformer circuits have to meet two basic requirements that limit the range of applicable fuses:

- The fuses shall interrupt a solid short-circuit current (I_{sc}) on the l.v. terminals within the specified short-circuit withstand duration of the transformer in order to prevent disruptive transformer failure. According to IEC 60076-5, the short-circuit withstand duration of transformer shall be at least 2 s unless otherwise stated by the manufacturer.
- The fuses shall withstand transformer inrush without deterioration in order to avoid nuisance operation and potential malfunction. Transformer inrush may be assumed equivalent 10 times to 12 times transformer rated current for a duration of 100 ms.

It is obvious that the time-current characteristics of appropriate fuse-links have to pass through the gate formed by these two corner points to meet the requirements (fig 3). In practice, the user may select from 4 to 5 consecutive fuse rated currents that fit the applicable range. Additional criteria, e.g. coordination with upstream and downstream protective devices may apply to make up the final choice.

4 Fuse selection acc. to IEC 62271-105

As mentioned above, fuse selection for switch-fuse combinations in transformer circuits is governed by the solid short-circuit current (I_{sc}) on the l.v. terminals and the transfer current $I_{transfer}$ of the combination, i.e. by the fuse initiated opening time T_0 of the switch. Whereby T_0 represents the time interval from arc initiation in the fuse to the instant when the arcing contacts of the switch have separated in all three poles.

T_0 depends on the duration of travel of the striker as well as on the mechanical opening time of the switch. As strikers commonly act very fast, i.e. within some milliseconds, T_0 is dominated by the mechanical behaviour of the switch. (The 50 ms maximum duration of strikers travel as defined in IEC 60282-1 cannot be considered representative. It is required for the arcing withstand and shall allow for the switch to open before the fuse body breaks at currents below the minimum breaking current.)

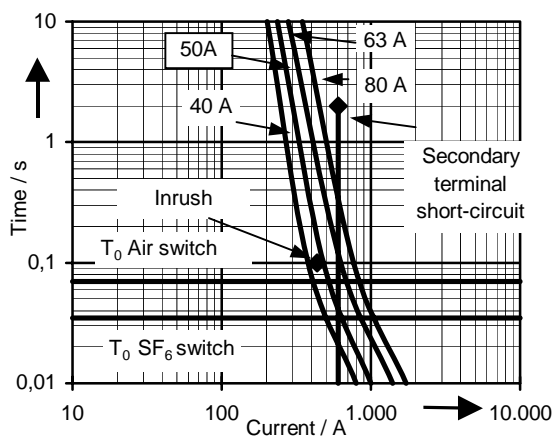


Fig. 4: Fuse selection acc. to IEC 62271-105

While IEC TR 60787 requires that the fuses interrupt the secondary terminal fault current I_{sc} within 2 s in order to prevent disruptive transformer failures, IEC 62271-105 claims that fuses shall interrupt this current within the fuse initiated opening time T_0 of the switch. Since the opening time of the switch is generally much below 2 s, selection according to IEC 62271-105 will result in smaller fuse rated currents and in different fuse rated currents depending on the type of switch, e.g. air switch and SF₆ switch.

Because of superior dielectric strength and arc quenching performance of the gas, SF₆ switches exhibit more compact dimensions. The mass as well as the travel distances of moving parts are significantly less than the ones of air switches. Consequently, SF₆ switches open much faster than air switches.

A simple procedure to select appropriate fuses for switch-fuse combinations by means of a time-current chart, is to draw a horizontal line corresponding to the fuse initiated opening time of the switch T_0 and a vertical line at the secondary terminal short-circuit current I_{sc} (fig. 4). The point of intersection of these two lines discriminates acceptable and unacceptable fuses: Only fuse characteristics that pass below the point of intersection meet the requirements of IEC 62271-105.

Fig. 4 shows the example of a 10 kV, 630 kVA transformer, that would usually be protected by means of a 80 A fuse. In combination with an air switch having an opening time of 70 ms, a 50 A fuse will have to be chosen. The same transformer in combination with an SF₆ switch would require a 40 A fuse. The latter that does however not exhibit enough tolerance to the transformer inrush. Strictly speaking, would fuses be eliminated from this application and a circuit-breaker would have to be used instead.

As can be seen from fig. 4, fuse selection according to IEC 62271-105 leads to significantly (2 to 3 steps) smaller current ratings than selection according to IEC 60787 with the following consequences:

- Greater power dissipation,
- higher risk of inrush damage,
- loss of selectivity to l.v. fuses,
- limitation in fuse applications.

The severity of these consequences increases with the operating speed of the switch and the size and short-circuit impedance of distribution transformers (see table 1). SF₆ switches have opening times down to 20 ms. Combinations with fast acting SF₆ switches can therefore not meet the inrush requirements of larger size transformers having a common short-circuit impedance, e.g. $S_N \geq 630$ kVA, $u_K = 6\%$.

Table 1: Fuse selection for transformer circuits

Transformer	Fuse rated currents acc. to IEC 60787	IEC 62271-105	
		Air switch $T_0=70$ ms	SF ₆ switch $T_0 = 35$ ms
400	50A	50A	40A
500	63A	63A	50A
630	80A	80A	63A
630	80A	50A	40A
800	100A	63A	50A
1000	125A	80A	63A

*) acc. to CENELEC HD 428.1 S1

As a matter-of-fact, IEC 62271-105 is discriminating fuses by claiming unreasonably low current ratings and thus actually limiting fuse application to relatively small size transformers.

Table 1 gives a comparison of actual fuse selection acc. to IEC 60787, representative for German public utility 10 kV distribution transformers, and fuse selection for air and SF₆ switches in combinations acc. to IEC 62271-105.

IEC 62271-105 does not only make fuse selection very complicated, may be too complicated for users, but is in some respect conflicting with IEC 60787, IEC 60282-1 and well established transformer protection practice:

- IEC 62271-105 requires smaller fuse rated currents for SF₆ insulated switchgear while IEC 60787 claims greater current ratings for fuses in enclosures.
- IEC 60787 recommends a relatively high operating current in the 0,1 s (inrush) region, while IEC 62271-105 requires fuse characteristics much closer to the inrush point.
- IEC 62271-105 defines the performance of the combination in a range below I_{SC}, while many applications with back-up fuses are selected for a protection range starting with I_{SC} to greater fault currents.

The latter may imply that there is no rational in the application of IEC 62271-105 rules for transformer protection by means of h.v. back-up fuses as there is no overlap in the application range. For applications without overcurrent release and where the fuses provide short-circuit protection only, IEC 62271-105 does not contain any applicable performance tests. What's left is solely the requirement of equation (1) concerning transfer currents. It seems that this requirement is causing more problems than it solves.

Indeed, the German National Committee made clear that in case of conflicting results of fuse selection for transformer protection, existing rules for transformer protection shall have priority over IEC 62271-105. This decision was justified by the excellent long-term experience with national practice and some uncertainty about solid short-circuit current (I_{sc}) on the l.v. terminals the determination of transfer currents for SF₆ switches.

5 Incorrect use of fuse characteristics

The limitations in fuse application has caused irritation among customers, switchgear and fuse manufacturers alike. This is even more annoying as there is no real physical background for transfer current determination in the respective time range of SF₆ switch operation. IEC 62271-105 suggests that the switch of a combination would not be involved in fault current interruption below the transfer current. This suggestion is misleading when transfer currents are determined according to Annex B of said standard in a time range significantly below 100 ms, for the following reasons:

- IEC 60282-1 says clearly that for the purpose of coordination between fuses and other protective devices, time-current characteristics may not be employed in a time range below 100 ms.
- IEC 62271-105 assumes a symmetric short-circuit current without aperiodic d.c. component.
- IEC 62271-105 assumes same instantaneous current values in all three phases.
- IEC 62271-105 assumes time-current characteristics without discontinuities, having a tolerance of ± 6,5 % on the current.

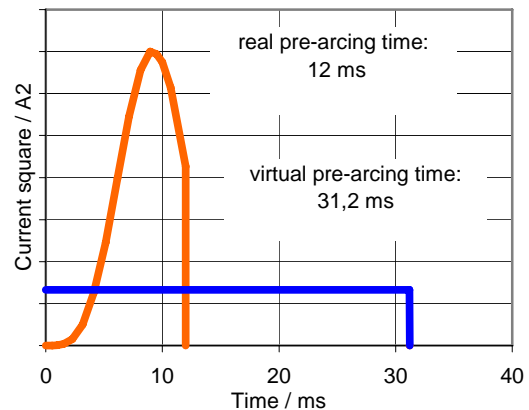


Fig. 5: Real and virtual pre-arcing time

- IEC 62271-105 assumes fuse characteristics representing real operating time to compare with opening time of the switch.

Unfortunately, it is not mentioned in IEC 62271-105 that none of these assumptions apply in the time range well below 100 ms and transfer currents can therefore not be determined by means of time-current characteristics as demonstrated in Annex B.

Fuse time-current characteristics represent virtual time values calculated from I²t values and cannot be compared with real time values, e.g. opening times of a switch. Real pre-arcing time values may be

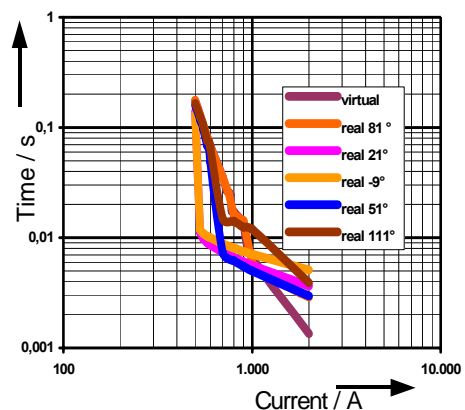


Fig. 6: "Chaotic" pre-arcing time range

significantly different to the calculated values (Fig. 5). Depending on the power factor and making angle of a solid short-circuit, the currents passing through the fuses of a three-phase system are significantly different and their pre-arcing times may vary much more than the manufacturing tolerances assumed in Annex B of IEC 62271-105.

Figure 6 shows calculated pre-arcing time-current curves for different making angles of a short-circuit current. The graph illustrates why the respective time range is called “chaotic”. Due to the fact that fuses do not melt near current zero, the curves show periodic steps in the direction of time according to the frequency of the current. The pre-arcing time variation and consequent tolerances on the current caused by the nature of the three-phase a.c. power supply system are not considered for the determination of transfer currents in Annex B and would have to be added to the manufacturing tolerances of the fuses.

Two conclusions may be drawn from these facts:

- The determination of transfer currents according to Annex B of IEC 62271-105 cannot be applied to switches having opening times in the range of 20 ms to 40 ms as is typical for SF₆ switches. Because of greater tolerances between real time-current characteristics, breaking duty may still be transferred to the switch.
- Annex B and probably the entire Standard IEC 62271-105 was likely not meant for this application originally. Annex B mentions an opening time range of 50ms to 300 ms for the simplified method for determination of transfer current which sounds more realistic.

That’s why revision or amending of IEC 62271-105 in co-operation with fuse committees seems to be advisable.

6 Proposals to eliminate contradictory requirements

SF₆ switch-fuse combinations non-complying with IEC 62271-105 have been installed in many countries over decades with excellent results. As shown above, there are good reasons for to believe that formal compliance with the standard does not mean more safety in reality. The good results in the field may just be based on the fact that fast acting switches exhibit better breaking capacity than tested and certified or on the fact that bolted l.v. terminal short-circuits don’t happen very often.

There is some doubt on whether the advantages of meeting the requirements of IEC 62271-105 outweigh the greater risk of inrush damage and greater power dissipation. Nevertheless users and manufacturers share the desire to comply with applicable standards.

6.1 De-activation of strikers

To eliminate interaction between fuses and switch has been a solution chosen by some utilities. This way to comply with the standard means to give up several important features of the combination, e.g. automatic three-phase disconnection and thermal protection of fuse canisters.

6.2 Delayed switch operation

This solution is costly and may require special fuses with extended arcing withstand time to meet the requirements of IEC 62271-105.

6.3 Fused circuit switcher

A new standard, IEC 62271-107, has been developed describing functional assemblies of a circuit switcher and a current-limiting fuse with the switching device being able to interrupt small short-circuit currents as may occur on distribution type transformers. Commercial availability is still somewhat open.

6.4 Closer definition of the standard’s scope

The scope of IEC 62271-105 could be closer defined. The application of annex B should be limited to a time range of 100 ms and above.

6.5 Elimination of subjects concerning transformer protection

IEC 62271-105 is a switchgear standard by definition. Requirements for transformer protection are covered in IEC 60787 and should consequently be taken off. At least IEC 62271-105 should not be applicable to transformer back-up protection covering solely the fault current range from I_{SC} and above.

6.6 Reducing u_k

As shown above, low short-circuit impedance makes it easier to select fuses that meet the requirements of both standards and application guide respectively. This may be a viable solution for some applications

7 Summary

Fuses appear to be simple products to those not familiar with fuse technology. In reality, fuse operation is not easy to understand and not many engineers are familiar with fuse application. More information on fuse application and involvement in education and fuse related standardisation work seems to be necessary to control the results and prevent negative effects on the use of fuses. Lack of information and applications mistakes are detrimental to fuses an their application.

TIME CORRELATED TECHNIQUES TO INVESTIGATE ARCING DYNAMICS ABOUT THE PEAK VOLTAGE INSTANT DURING CURRENT INTERRUPTION IN SAND FILLED FUSES USING AN OPTICAL SPECTRUM ANALYSER

Robert E. Brown

Director, Sensdata Limited,
Unit B1, Sheffield Technology Parks, 60 Shirland Lane, Sheffield,
South Yorkshire, United Kingdom, S9 3SP

Tel: 0044 (0) 1709 739228, Email: robert.brown@sensdata.com, Web: www.sensdata.com

Abstract: This paper will present attributes of apparatus and results from a study of disintegration and arcing in quasi short notched HBC sand filled fuses. Discussion will be centred around the aspects of time correlation of data captured from several data sources yet focusing on data acquired from a scanning optical spectrum analyser. Techniques for synchronising the scanning cycle of the spectrum analyser to the disruption period of the fuse element yet more accurately to the sub time domains of element disintegration will be discussed. Importantly, results indicating the possible nature of arcing phenomena about the peak fuse voltage instance will be presented.

Keywords: Fuse, Disintegration, Arcing, Spectrograph, Instrumentation.

1. Introduction

Many studies have been carried out to evaluate the magnitude and nature of parameters of fuse operation using a spectrographic type instrument to capture data related to light spectra emitted during the arcing phase of the interruption of high fault current by the fuse. Moreover, in these investigations many different forms of spectrograph have been used as the focus of data capture, however only a small amount of time correlated spectral data exists which relates to the transient nature of the arc relative to the phenomena of element disintegration. The possible cause of this is proposed to be accountable to the very short time period of operation of the fuse relative to the data capture time period of the spectrograph and the difficulty in correlating the data to fuse voltage and current waveforms. With the advancement of data logging equipment and optical image capturing devices the investigation of the transient nature of light spectra inherent in the fuse arc during the sub time domains of the arcing period are now possible. Consequently, the phenomena of fuse element disintegration during the passage of fault current can be hypothesised.

Many researchers have studied attributes of the voltage developed across a fuse during the prearcing and arcing phases of the fuse operation. Moreover, much attention has been given to the nature of the voltage measured across the fuse terminals during the arcing phase in an effort to understand the physical phenomena of element disintegration in anticipation of developing a model to replicate fuse operation and subsequently to aid future fuse component manufacture.

Great attention has been given to the way the voltage quickly rises [1] which is generally believed to be at the onset of arcing and the subsequent multiple fragmentation [2] of the fuse element provoking multiple arcing [3].

Moreover, consideration has been given to the magnitude of the voltage peak [4] and its correlation with current density, filler compaction and filler material type.

Finally, much interest and postulation has been focused on the causation of the decreasing voltage trend following the voltage peak and the causation and association with multiple arcing [5].

Gomez and McEwan [6] referred to the phases of arcing relative to the peak of the voltage transient wave as, pre-peak arc and post peak arcing time periods and as such developed a hypothesis as to the nature of the course of the voltage transient wave relative to fuse element disintegration.

It was during the course of studying the disintegration and arcing in electrical fuses [7] by the author that the spectral observations of the fuse arc were undertaken.

2. Evaluation of Spectroscopic Studies of Fuse Arcing

A brief evaluation of the portfolio of fuse/spectrograph investigative work is worthy at this point yet focusing on the attributes of the data capturing apparatus.

Numerous experimental set ups have been used to monitor the characteristics of the fuse arc. The range of fuse designs which allow the light, emitted from the arc to be monitored are numerous and include,

- Standard HBC fuse designs with optical fibers inserted through the walls of the fuse to penetrate the arc column [8].
- Fuse patterns with 'glass windows' with the fuse element pressed against the window so that light from the arc can be detected directly by a spectrograph or conveyed again via an optical fiber [9]
- In studies of the attributes of an ablation arc, fuses have been constructed of very thin wires and subjected to very high current densities to provoke arcing whilst surrounded by a tube of ice, which provided access to directly monitor and observe the arc [10].
The type of spectrograph used in investigations can be categorised thus.
- Monochromatic Spectrograph: A system where narrow band interference filters and light sensitive devices i.e. photo diodes, are used to monitor pre-selected spectra from the arc spectrum [11].
- Polychromatic: A system where data representative of all spectra between a predetermined light wavelength bandwidth are captured. Polychromatic systems where originally analogue devices where the spectrum was captured by an 'arc array' of photo multiplier tubes or photographic film. These systems have now been superseded by digital systems where collections of charge coupled devices (CCD's) in array or matrix formation have been used [9].
- Time Integrated: These systems can be either analogue or digital, mono or polychromatic, yet the spectrum is captured over a finite time period which, fundamentally is the time period of the light collecting device i.e. CCD or film. The time period can be very short (μ Secs) so numerous spectra can be captured during the arcing phase of the fuse [10].
- Scanning: These systems can also be analogue or digital yet here the spectroscope uses a light sensitive device to scan the light output of a diffraction grating. The angular scanning velocity of the device is in the order of 12Hz, hence only a single spectrum can be captured at a specific time instance during the arcing phase of the clearance of short circuit fault current by the fuse [8].

Generally spectroscopic studies of fuse arcing have been carried out to determine arc temperature [11] [12], electron density [13] and arc pressure [13] and most often the studies have paid attention to the vapour medium in which arcing is occurring and at the time instant from the application of fault current that data representative of the arc spectrum is captured and analysed, i.e. from the injection of fault current, the beginning of the pre-arcing time period. Only a small amount of spectral data exists which correlates the intensity and element type of spectra relative to the separate time domains of the voltage waveform during the arcing period in

an attempt to propose the evolution and dynamic nature of arcing relative to the phenomena of fuse element disintegration.

Experimental Arrangement for Spectral Data Capture from Arcs in Short notched Element Quasi HBC Sand Filled Fuses

This paper reports a spectroscopic investigation, which was part of a much larger fundamental investigation, undertaken to capture insight into the phenomena of fuse element disintegration and arcing. A scanning type spectrometer was used, and therefore only a single spectrum could be captured for each fuse operation.

Time correlation of the fuse voltage and current is straight forward using dual channel oscilloscopes yet synchronizing these parameters with the exact time instant of data representative of arc spectra is most difficult because of the amount of data, the short data capture time period and because several items of test equipment have to be triggered at the same time instance.

To obtain data that could be cross correlated between fuse samples strict procedures in the manufacturing of fuse samples were adopted so that a near homogenous batch of fuses could be used. To accomplish this a 'jig' was used in the construction of the fuses, so that the fuse elements were consistently aligned with the horizontal and vertical axis of the spectrograph. Furthermore, bespoke equipment was manufactured so that the repeatability of the fuse test duty used was very high (>98%). Consequently, the integrity of any hypothesis regarding the phenomena of element disintegration could be upheld for these circumstances.

3. Experimental Arrangement for Spectral Data Capture from Arcs in Short notched Element Quasi HBC Sand Filled Fuses

3.1 Sample Fuses

Special robust experimental enclosures were devised to monitor arcing in fuse elements, compacted in silica filler to ensure good acuity of arc light emission and the protection of the spectrograph from expelled arc products as shown in Figure 1. The short-notched fuse element samples were mounted in close proximity to glass slides, and were pressed against the glass by the pressure of the filler, consequential of compaction by vigorous mechanical vibration. Hence the glass slides acted as a data capture window to the arcing phenomena and an arc shield for the spectrograph.

In support of the investigation reported here a short study was carried out to determine the influence of the glass slide on fuse operation. In a

series of tests the short notched fuse element was gradually moved, in 0.5mm increments, away from the glass slide. The fuse voltage, current and spectrographic results for each of the tests indicated no significant deviations enabling the conclusion to be drawn that the influence of the glass on fuse operation and data capture was minimal.

3.2 Fuse Test Circuit

The experimental energy source was derived from a three-phase ac generator with the generated test circuit ac voltage being obtained from the single phase and neutral of the stator of the three phase star connected generator.

Current flow through the test fuse was accomplished by controlled switching of a thyristor, of type NO60RHX. Switching was initiated relative to the zero crossing point of the supply voltage which was determined using a bespoke 'point on wave' monitoring circuit with additional adjustable time delay circuitry to facilitate fuse operation in accordance with different fuse test duties.

3.3 Data Capturing Equipment

3.3.1 Spectrograph

Spectroscopic analysis of arcing phenomena was carried using a 6800 Series Optical Spectrum Analyser (OSA), manufactured by Rees Instruments Limited. A block diagram of the OSA configuration interfaced to the fuse test facility is shown in Figure

2 and a photograph of the experimental arrangements is shown in Figure 3

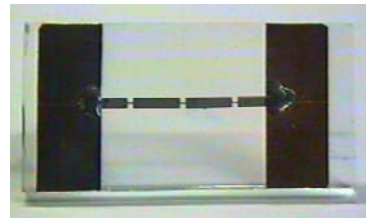


Fig 1i Examples of a short-notched fuse element window/substrate test samples used in experimental investigations.

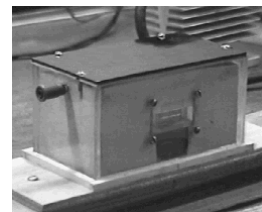


Fig 1ii Fuse test samples and test enclosure showing glass substrate-mounted fuse element

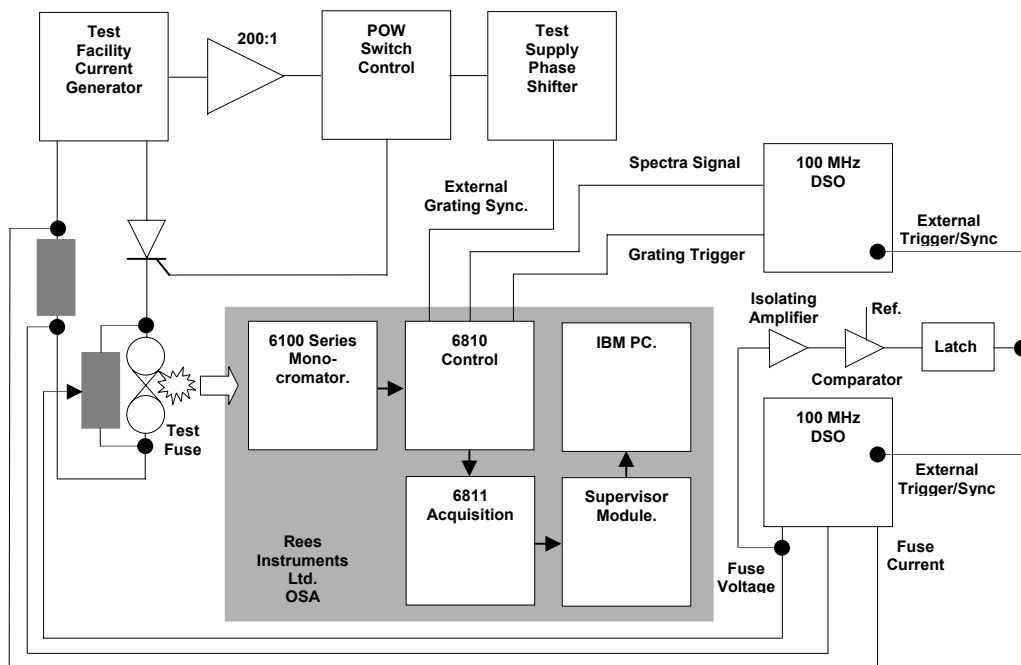


Figure 2 Diagram of optical spectrum analyser interfaced to the fuse test facility

The 6100 monochromator comprised a rotating grating and Si (6111) photo detector with a bandwidth of 200nm~900nm. The 6810 control module of the system, controlled the scanning speed of the monochromator, signal gain of the photo

detector and the data acquisition sampling interval. For the investigation the spectrograph utilised a 1200g/mm grating, which provided a sampling wavelength interval of 0.25nm.



Figure 3 Experimental arrangement used in the spectroscopic analysis of HBC conductive film substrate fuse arcing phenomena.

3.3.2 Oscilloscopes

Two separate 100 MHz digital storage oscilloscopes of type DSO 400, distributed by Gould Instrument Systems Limited, were used to capture fuse voltage and current data, a grating trigger signal and light spectra data.

3.4 Time Correlation/Triggering Mechanisms

For this investigation the monochromator was controlled externally to enable synchronisation between the disintegration of the fuse and the sampling window of the OSA.

This was accomplished by first monitoring the test facility 'ac' generated voltage waveform, and then phase shifting the monitored signal to supply the monochromator and control the speed, which basically controls the angular position of the OSA grating. Consequently, due to the homogeneity of the sample fuses the phase difference could be set so that the spectroscope monitored light emitted during the pre peak or the post peak arc voltage time period.

Both oscilloscopes were triggered relative to the onset of fuse element disintegration, to enable specific light spectra to be correlated to a time instant in the disintegration period. This was accomplished using a fast, accurate comparator and latch circuit.

3.5 Overall Experimental Arrangement

The sample fuses were embodied in an opaque box with a small aperture located exactly in the forefront of the fuse element. The aperture was then accurately positioned so that the horizontal and

vertical axis of the fuse element and the OSA grating were in precise alignment (Figure 4).

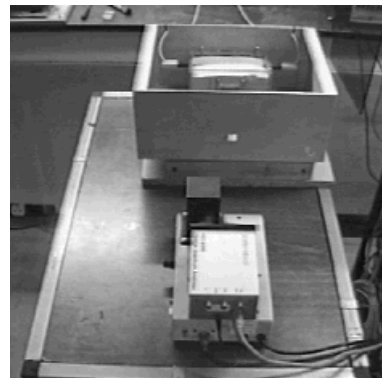


Figure 4 Experimental arrangement of OSA and fuse enclosure (Shown without top cover and opaque shroud)

A nominal distance between the fuse and the OSA was experimentally established to eliminate saturation of the photo detector output by the high intensity arc light and to allow analysis of the relative intensity of spectra. The apparatus containing the fuse and the OSA were finally enclosed in an opaque shroud to prevent ingress of light from ambient sources.

4. Investigation Objective

The spectroscopic analysis of arcing in short notched element quasi HBC sand filled fuses was carried out from separate investigations of the arc

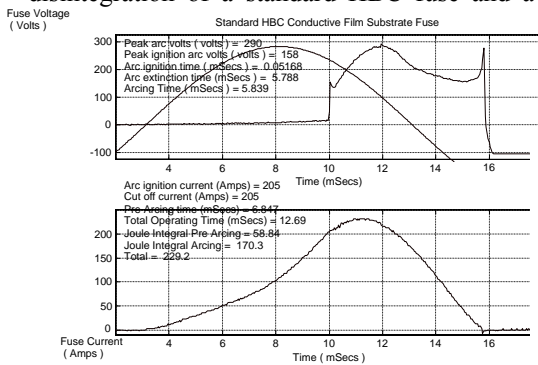
light components captured in the pre-peak and post peak arc voltage time periods. The fundamental aim of this investigation was to establish:

- In the pre-peak arc voltage time period whether the arc light spectrum comprised mainly of spectra of fuse element material wavelengths.
- In the post-peak arc voltage time period whether the arc light spectrum comprised mainly of spectra of fuse filler material wavelengths.

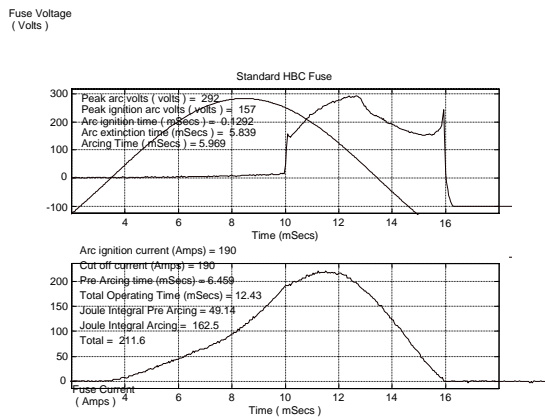
5. Results

Figures 5i and 5ii present time correlated supply voltage, fuse voltage and current data captured during separate instances of the disintegration of a standard HBC fuse and a quasi

HBC fuse as used in the spectrographic investigation reported. Figures 6 and 7 present light spectrum data captured during the pre peak and post peak arc voltage time periods of fuse disintegration. The time reference points of the oscilloscope trigger signal and spectrum capture points for wavelengths of 300nm and 500nm are indicated. To clarify the latter, the two wavelengths superimposed on the fuse voltage record indicate the time instances during fuse operation that the spectrograph was sampling light at the specified wavelength. Consequently, some degree of judgement can be gained of the span of the full light spectrum over the course of fuse operation.



(i) Quasi HBC sand filled fuse



(ii) Standard HBC fuse

Figure 5 Supply voltage, fuse voltage and current oscillograms

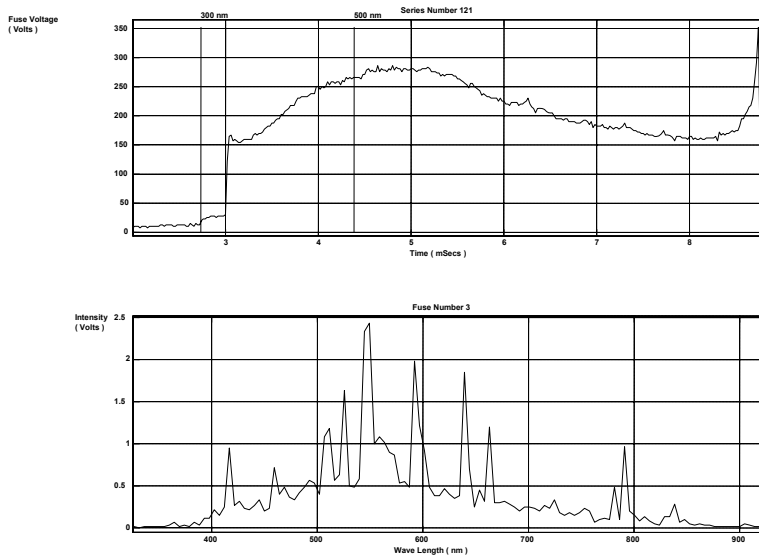


Figure 6 Typical arc light spectrum and correlated fuse voltage oscillogram captured during the pre-peak arc voltage time period of disintegration in a short notch silver element fuse

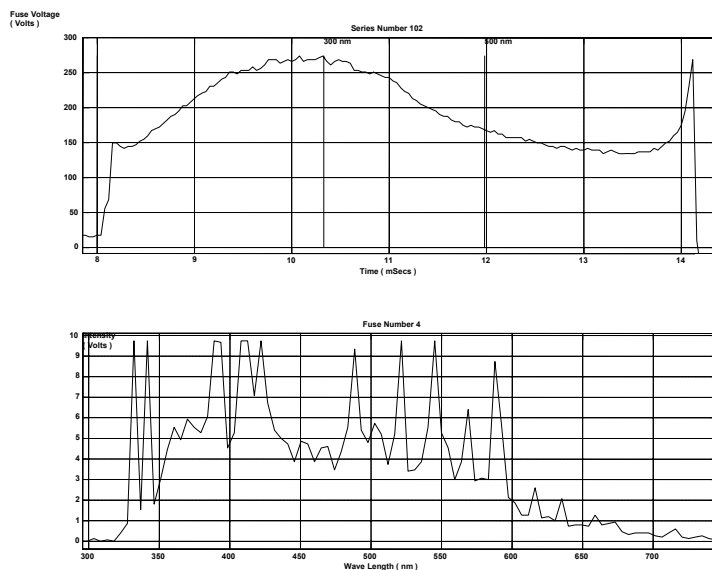


Figure 7 Typical arc light spectrum and correlated fuse voltage oscillogram captured during the post-peak arc voltage time period of disintegration in a short notch silver element fuse

6. Discussions

A large number of fuses were tested to capture data in both arcing time domains of fuse operation (~30/Domain) and generally, the spectrum for each domain was most similar to those presented in Figures 6 and 7.

Relationships between spectral lines and possible fundamental elements of fuse materials have not been identified here since these associations are beyond the scope of this report. However, the spectrums for each arcing time domain in the circumstances of this investigation are suggested to be quite different and hence postulations for element disintegration phenomenon can be somewhat securely presented. For example, it could be considered that during the pre-peak arc voltage time period if element spectra were dominant then notions of arc elongation due to element burn back and the arc being supported between element electrodes could be plausible. Alternatively, if the spectrum in the post peak arc voltage period were dominated by filler spectra then notions of fulgurite commutation of the fault current could be credible.

7. Conclusions

The procedures for the manufacture of fuse samples in this investigation were strict with tight tolerance limits in order to produce homogenous batches of fuses. This provided high repeatability of the onset of fuse element disintegration with respect to a time instant on the

supply voltage waveform. Subsequently, this allowed the spectrographic instrument to monitor light emitted from the fuse during separate time periods of the arcing phase.

In this investigation four separate parameters relative to fuse element disintegration were captured simultaneously. Subsequently, the separate data sets could be cross correlated with respect to time due to use of a single time datum signal source, i.e. triggering of the comparator/latch circuit.

The overall data capture time period of the spectrographic instrument used in this investigation was relatively slow compared with current technology however it was considered, at the time of the investigation to be marginally capable of capturing data for subsequent analysis and differentiation of spectra from the sub time domains of the fuse arcing phase and hence able provide evidence for possible disintegration phenomena hypothesis.

With currently available fast spectrographic instruments and using the techniques reported, the results of this investigation have shown that it is most possible to cross correlate several data sets with respect to a single instance in time so that a better understanding of the phenomenon of fuse element disintegration and arcing could be forth coming.

References

- [1] Wolny A.: "Effect of Fuse Element Confinement on the Rate of Rise of Fuse Arc Ignition Voltage". *Conference Proceedings of the 6th ICEFA, Turin (Italy) Sept. 1999, pp135-139.*

- [2] Nasilowski, J.: "Unduloids and Striated Disintegration of Wires" *Exploding Wires Vol. 3, Planum Press, New York U.S.A., 1964, p 295-313*
- [3] Hibner, J.: "The Number of Arcs Initiated during Striated Disintegration of the Uniform Strip H.B.C. Fuse Elements at AC Short Circuit Current Interruption" *International Conference on Electric Fuses and Their Applications, Trondheim Norway, 13-15 June 1984, p 60 - 69.*
- [4] Hibner, J.: "Calculation of the Over Voltage Peak Values when breaking Short Circuits by means of Multi Strip Fuses", *Conference Proceedings, 2nd International Symposium on Switching Arc Phenomena, Lodz, Poland, September 1973, pp269-274.*
- [5] Rex, H.: "A Simple Method to Calculate the Maximum Voltage that Arises When a Fuse Link Breaks a DC Short Circuit Current" *Conference Proceedings, 6th International Symposium on Switching Arc Phenomena, Lodz, Poland. 1989.*
- [6] Gomez, J.C., McEwan, P.M.: "Experimental Investigation of Wall Stabilised Arc Mechanisms of Wires in Fuse Filler", *International Conference on Electrical Fuses and their Applications, Ilmenau, Germany, September 1995 pp243-250*
- [7] Brown, R.E., "Investigation of Disintegration and Arcing in Electric Fuses", Ph.D. Thesis, Sheffield Hallam University, UK, January 2000.
- [8] Barrow, D.R., Howe, A.F.: "The use of Optical Spectroscopy in the Analysis of Electrical Fuse Arcing." *Conference Proceedings, 4th International Conference on Electrical Fuses and their Applications, Nottingham, U.K., September 1991, pp221-225.*
- [9] Bussiere W., Besborodko P., Pellet R.: "Spectroscopic Study of a Cutting Electric Arc in H.B.C. Fuse", *Sixth International Conference on Electrical Fuses and Their Applications, Turin, Italy, Sept. 1999, pp113-117*
- [10] Cao, L.J., Stokes, A.D.: "Spectrum Analysis of an Ablation Stabilised Arc in Ice" *Conference Proceedings, 4th International Conference on Electrical Fuses and their Applications, Nottingham, U.K., September 1991, p27-32.*
- [11] Cheim, L.A.V., Howe, A.F.: "Spectroscopic Observations of High Breaking Capacity Fuse Arcs.", *IEE Proc.-Sci. Meas. Technol., Vol. 141, No. 2, March 1994, pp 123-128.*
- [12] Chikata, T., Ueda, Y., Murai, Y., Miyamota, T.: "Spectroscopic Observations of Arcs in Current Limiting Fuse through Sand", *Conference Proceedings, International Conference on Electrical Fuses and their Applications, Liverpool, U.K., 1976, pp114-121.*
- [13] Bussiere W., Rochette D., Andre P.: "Study of the SiO₂ Plasma Physical Parameters: Temperature, Electron Density, Pressure Radiation" *Seventh International Conference on Electrical Fuses and Their Applications, Gdansk, Poland Sept. 2003 p119-125*

ARC ROOTS FEM MODELLING AND SIMULATION AT PLANE ELECTRODES

J.M. Bueno Barrachina⁽¹⁾, S. Catalán Izquierdo⁽²⁾, C.S. Cañas Peñuelas⁽³⁾, F. Cavallé Sesé⁽⁴⁾

Instituto de Tecnología Eléctrica⁽¹⁾,
Avda. Juan de la Cierva, 24 - Parque Tecnológico de Valencia - 46980 Paterna (Valencia) - España,
jmanuel.bueno@ite.es

Instituto de Tecnología Eléctrica^(2,3,4),
Avda. Juan de la Cierva, 24 - Parque Tecnológico de Valencia - 46980 Paterna (Valencia) - España,
saturnino.catalan@ite.es⁽²⁾, cesar.canas@ite.es⁽³⁾, fcavalle@ite.upv.es⁽⁴⁾

Abstract: The aim of this work is to model and to simulate the arc root generation processes in plane electrodes using a three-dimensional solid model based on the finite elements method (FEM). For this purpose, a loop integrating an electrical model in transient state and a solid model constituted by two plane electrodes has been used. The model includes: current, voltage, circuit impedance, plasma parameters, current density and temperature.

The simulation results show that local heating is non-significant at the electrode surface, hence uniform flows of current are obtained and a plasma column is generated without the appearance of intense metal-melting arc roots. These are steps into a more comprehensive fluid-thermo-electrical model of the arc using 3D FEM aimed at the development of more precise design and analysis engineering tools of arc based protection elements.

Keywords: current limitation, arcs in air, arcing phenomena, electric arc.

1. Introduction

The electrical arc can be defined as an independent discharge able by itself to generate the amount of ions and electrons necessary for the circulation of current. In these conditions some electrons have sufficient energy to cause the dielectric and thermal rupture of the insulating material that there is between the contacts (air in most of the current breakers).

The homogeneous and isotropic characteristics considered as well as the non-existence of macroscopic imperfections at the surface and inside the electrical contact (plane electrodes) causes that, even when distance between contacts is very small, the separation is uniformly constant along the surface

hence, current concentration can not occur nor hot spots and arc roots.

The models developed in this paper study some of the thermal-electrical processes that take place in the electrical contacts and in the air when opening an electrical circuit.

2. Simulation

The model is formed by two contacts of cylindrical form Fig 1 and the air between them.

The process is started with the circuit in normal steady state operation. Next a short-circuit is introduced and the separation of the electrodes is started.

The implemented system allow to obtain [1] the initial current and voltage conditions, and, inside the 3D model, the transient arc voltage, current density and temperature distribution. The physical properties of high temperature air is taken from [2].

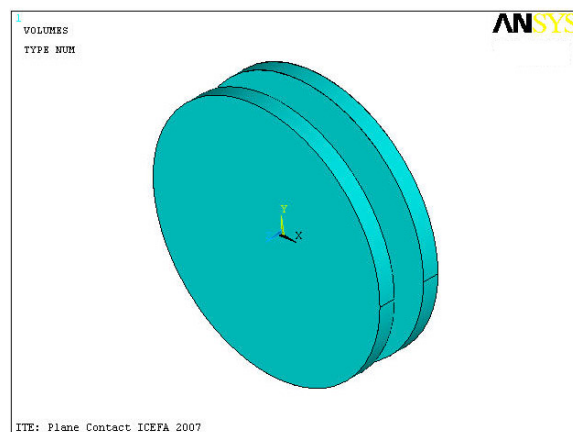


Fig. 1: Plane copper electrodes of a circuit breaker.

2.1. Heat Balance

The power balance equation for each volume element dV in the integral formulation is shown in equation 1. This equation is the balance between the

heat stored by temporal change of temperature, the power removed from the element by thermal conduction and the heating power from the current flow [3]. In this model is not yet considered fluid mass transport.

$$\frac{j^2}{\sigma} = \rho \cdot C_p \cdot \frac{\partial T}{\partial t} - \text{div}(\lambda \cdot \nabla T) \quad (1)$$

Where:

$$\frac{j^2}{\sigma} = \text{Joule heating}$$

$$\rho \cdot C_p \cdot \frac{\partial T}{\partial t} = \text{Heat storage}$$

$$\text{div}(\lambda \cdot \nabla T) = \text{Thermal conduction}$$

$$j = \text{Current density}$$

$$\sigma = \text{Electrical conductivity}$$

$$\rho = \text{Mass density}$$

$$C_p = \text{Specific heat at constant pressure}$$

$$T = \text{Absolute temperature}$$

$$t = \text{Time}$$

$$\lambda = \text{Thermal conductivity}$$

$$\nabla T = \text{Thermal gradient}$$

2.2. Current density and Electric potential

The current density j necessary in equation 1 follows from

$$j_x = \sigma \frac{\partial U}{\partial x} \quad j_y = \sigma \frac{\partial U}{\partial y} \quad j_z = \sigma \frac{\partial U}{\partial z} \quad (2)$$

$$j = \sqrt{j_x^2 + j_y^2 + j_z^2}$$

Where U is the electric potential, that follows the Laplace equation:

$$\text{div}(\nabla U) = 0 \quad (3)$$

The current density J and the electric potential U must also satisfy the external circuit equation:

$$e(t) = L \frac{di}{dt} + Ri + U \quad (4)$$

Where $e(t)$, L and R are the external circuit characteristics, and U is the anode potential minus the cathode potential.

3. Materials and Methods

The simulation is started with the electrical model in sine stationary regime as in Fig 2.

This electrical model is constituted by a sine voltage generator (50 Hz) (1), the line impedance upwards from the arcing element (2), the two

contacts equivalent resistors (3) and the line and load equivalent impedance downwards from it (4).

The voltage of the sine generator is 230Vrms, the line impedances have been calculated to obtain a current of 630 Arms with a very resistive power factor.

In time = 0.02 seconds a short circuit is introduced just downwards from the protective element. Fig. 3 shows the electrical circuit used to model this new condition.

The current of the circuit increases until the tripping level of the protective element, almost 880 amperes.

The electrical model to use in this condition is shown in Fig. 4.

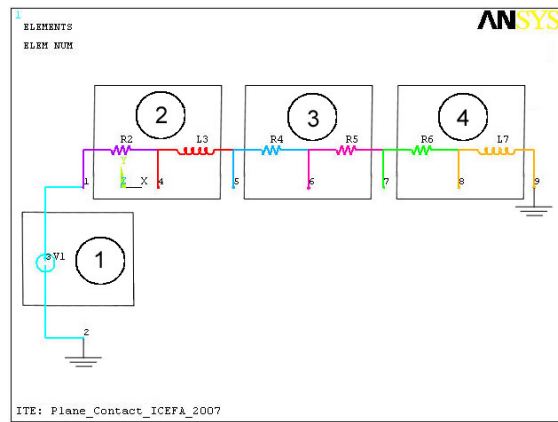


Fig. 2: Initial, steady state, electrical model.

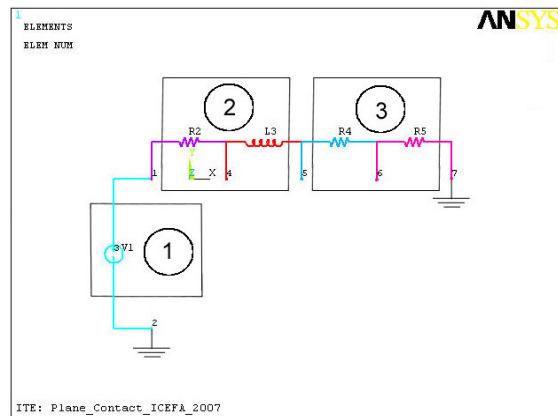


Fig. 3: Electrical model in short circuit.

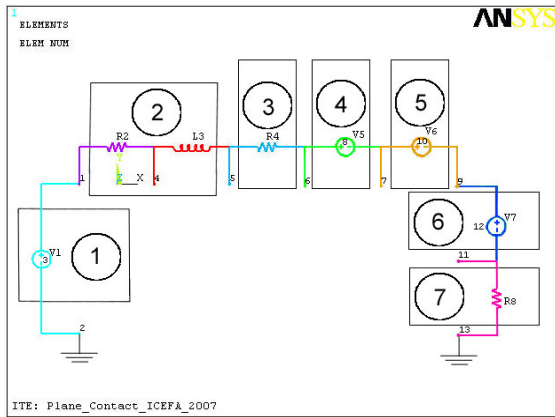


Fig. 4: Electrical model while contacts are opening.

The new electrical model is formed by a sine voltage generator (1), the line impedance upwards the element (2), the anode equivalent resistor (3), the voltage of the anode sheath (4), the plasma column voltage (5), the voltage of the cathode sheath (6), and the cathode equivalent resistor of the element (7).

As a first approximation, constant voltage anode and cathode sheath have been considered.

The air between electrodes is, at first, relatively cold and therefore its resistivity is very high. This causes that voltage drop between electrodes increases. This affects the electric field increasing it.

At the same time, following equation 1, the temperature of the air between contacts increases. This causes that the resistivity of the air diminishes, and therefore the voltage drop between electrodes also diminishes, which causes that the electric field diminishes.

The combined effect of voltage drop, current and temperature cause the voltage drop to reach a balance at plasma air temperature.

In addition, it is also necessary to consider the increasing separation between electrodes that increases voltage drop forcing current to finally extinguish.

The plasma column and the electrodes have been modelled as pure resistive [4], this 3D model, based on the use of the method of the finite elements (FEM), has been generated with ANSYS® [5]. The FEM model in each iteration receives the electrical current and temperature at each node from the previous iteration and calculates the drop potential between the electrodes and the new distribution of temperature. At the same time the model separates the electrodes at a prefixed speed. The new electrical current for the next iteration is calculated by the electrical model circuit.

Provided that electrode surface is considered ideal and that no fluid analysis has been yet included, no radial motion is obtained. It has been chosen, as a first approximation, to situate the arc in the middle of the electrode surface.

Fig. 5 shows the 3D model used. This model is constituted by three volumes, first is the metallic electrode of the cathode (1), second is the sheath and the arc cathodic root (2) and third is the electrical arc (3).

In this analysis electric copper contacts have been modelled.

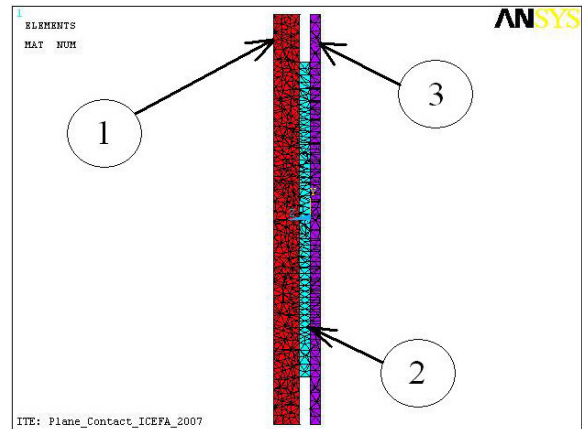


Fig. 5: Model at time = 20.527 ms.

4. Results

The simulation results show that local heating is non-significant at the electrode surface, hence uniform flows of current are obtained and the plasma column is generated without the appearance of intense metal-melting arc roots.

Fig. 6, 7, 8 show temperature, voltage and current density obtained in ANSYS® for the 3D model at several steps of the simulation.

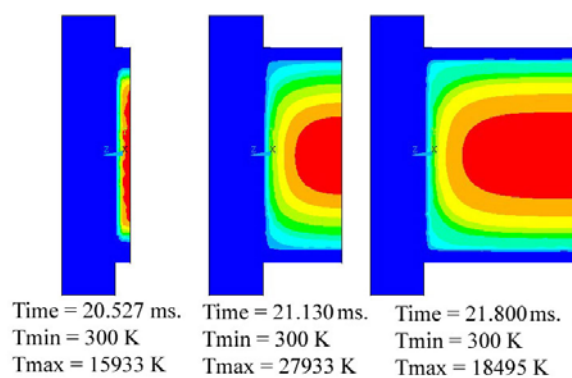


Fig. 6: Temperature distribution for the model at several steps of the simulation.

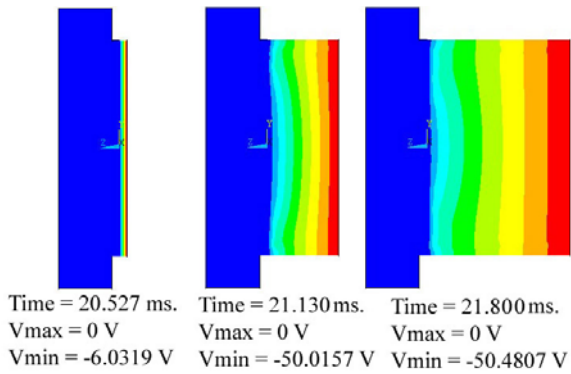


Fig. 7: Voltage distribution for the model at several steps of the simulation.

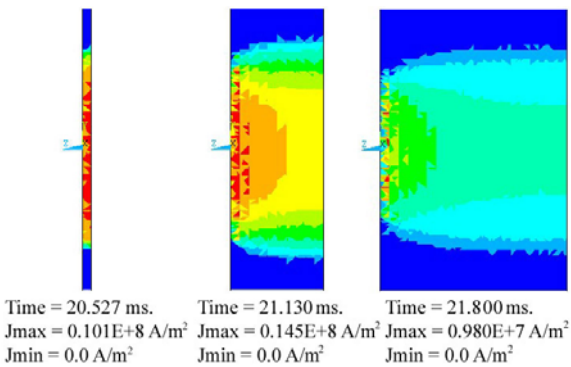


Fig. 8: Current density distribution for the model at several steps of the simulation.

Fig. 9 shows the simulation diagram used for this FEM model.

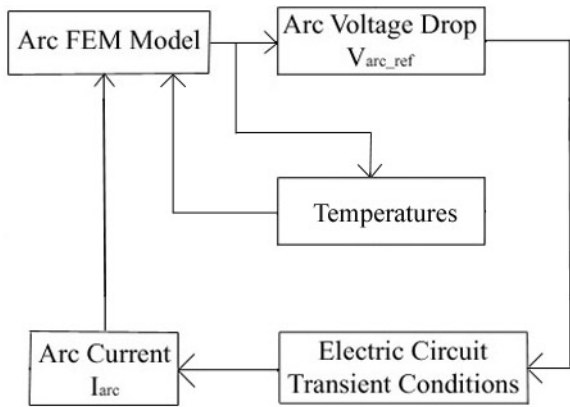


Fig. 9: Process diagram used in the simulation.

At the first step of the simulation the electric current obtained from the electric circuit shown in figure 3 is applied to the 3D arc FEM model. Using this 3D model the voltage drop between electrodes is obtained by a transient analysis. This voltage drop is applied into the electric circuit shown in figure 4 and the transient analysis solution obtained from this circuit is the new input current to the arc FEM model.

A summary of the results obtained for arc voltage and current from the simulation is shown in Fig. 10. In this figure is presented part of the transient electric analysis (from 20.30 ms to 20.46 ms) just before the beginning of the aperture of the contacts. At 20.46 ms the electric arc process is started.

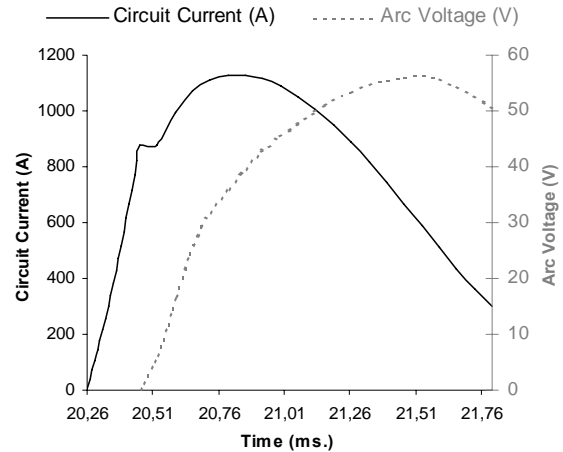


Fig. 10: Current and arc voltage waveforms.

Greater voltages do not appear at the first moments [1,4] because, as a first approximation, the initial plasma condition of the air is obtained by heating a small area of air between the contacts only in the first separation step.

Fig. 11 shows the temperature distribution as a function of the radius. The plasma column consists mainly of two zones: a low temperature area (LTA) between [300, 5000] K, and a high temperature area (HTA) in the range [10000, 20000] K. Most of the current is obtained from the HTA. It can be observed that there is a relatively small area between LTA and HTA in which the temperature changes abruptly.

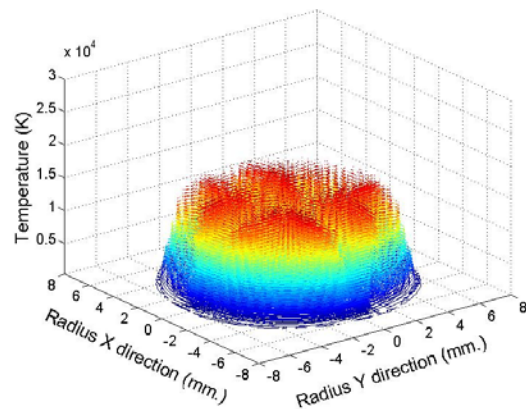


Fig. 11: Calculated temperature distribution along the radius at the centre of the arc in the first step of the simulation (time = 20.527 ms).

Fig. 12 and 13 show the temperature distribution from the centre of the plasma column at several simulation steps.

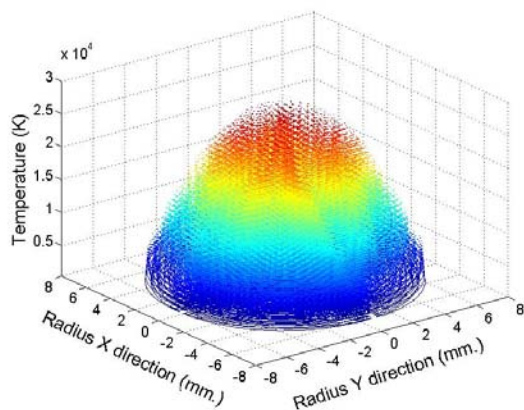


Fig. 12: Calculated temperature distribution along the radius at the centre of the plasma column (time = 21.13 ms).

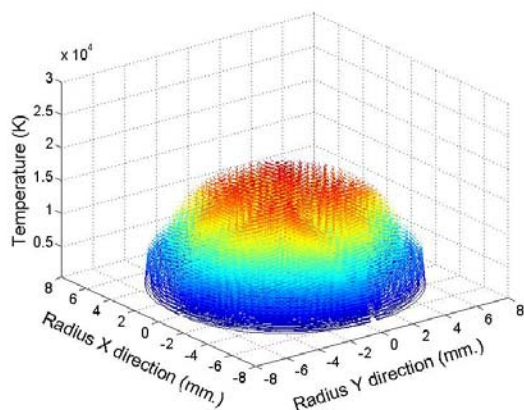


Fig. 13: Calculated temperature distribution along the radius at the centre of the plasma column in the last step of the simulation (time = 21.8 ms).

The obtained distribution agrees quite well with other published results [4].

5. Conclusions

The simulation results show that local heating is non-significant at the electrode surface, hence uniform flows of current are obtained and the plasma column is generated without the appearance of intense metal-melting arc roots.

The obtained arc consists mainly of two zones: a low temperature area (LTA) between [300, 5000] K, and a high temperature area (HTA) in the range [10000, 20000] K separated by a thin layer where temperature changes abruptly. Most of the current flows through the HTA.

These are steps into a more comprehensive fluid-thermo-electrical model of the arc using 3D FEM aimed at the development of more precise design and analysis engineering tools of arc based protection elements.

References

- [1] M. Lindmayer, "The process of arc splitting between metalplates in low voltage arc chutes", *IEEE Trans. Comp., Packag., Manufact. Technol. A*, vol. 29, no. 2, pp. 310-317, June 2006.
- [2] M. Capitelli, G. Colonna, C. Gorse and A. D'Angola, "Transport properties of high temperature air in local thermodynamic equilibrium", *Eur. Phys. J. D*, vol. 11, pp. 279-289, 2000.
- [3] M. Lindmayer, "3D simulation of fusing characteristics including the "M-EFFECT"", *Proc. of the 6th ICEFA, Torino (Italy)*, Sept. 1999, pp. 13-20.
- [4] C. Lüders, T. Suwanasri and R. Dommerque, "Investigation of an SF₆ – selfblast circuit breaker", *J. Phys. D: Appl. Phys.*, vol. 39, pp. 666-672, 2006.
- [5] ANSYS® 9.0, User Documentation.

STUDY OF THE SiO₂ PLASMA RADIATION. APPLICATION TO THE FUSE ARC PLASMA

William Bussière¹, David Rochette², Pascal André¹, Gérard Velleaud² and Steeve Memiaghe¹

¹ LAEPT CNRS UMR 6069, Phys. Bât. 5, Université Blaise Pascal, 24 Avenue des Landais, F63177 AUBIERE Cedex, France, Phone: +33 4 73 40 77 04, Fax: +33 4 73 40 76 50, william.bussiere@univ-bpclermont.fr, steeve.memiaghe@univ-bpclermont.fr, pascal.andre@univ-bpclermont.fr

² LAEPT CNRS UMR 6069, Université Blaise Pascal, IUT de Montluçon, Avenue Aristide Briand, BP 2235, F03101 Montluçon Cedex, France, Phone: +33 4 70 02 20 16, Fax: +33 4 70 02 20 78, rochette@moniu.univ-bpclermont.fr, gerard.velleaud@moniu.univ-bpclermont.fr

Abstract: During the HBC fuse working, the fault current implies the initiation of an electric arc which is composed of metallic species vapours mainly, generally silver. This defines the end of the pre-arcing time. This electric arc interacts quickly with the surrounding silica sand grains or quartz sand. Thus a silver plasma is formed around the reduced sections of the fuse element. This silver plasma interacts with the silica sand grains and this interaction gives rise to the ignition of a plasma composed of vapours resulting from the dissociation of the SiO₂ molecules. The radiation escaped from the SiO₂ plasma can be used to assess experimentally the temperature (T) and the electron density (n_e), two fundamental parameters for modelling purposes. T and n_e are difficult to interpret because of the strong gradients in pressure, temperature, and material densities from the centre to the surroundings where the measurement is done. We propose a first formulation to calculate this radiation in order to increase the understanding of the radiation measurements.

Keywords: SiO₂ plasma, fuse arc plasma, radiation, continuum, discrete radiation.

1. Introduction

This paper is especially concerned by HBC fuse that basically comprises: two electrodes, the fuse element (generally in silver), the filling cavity, and the arc quenching material that is to say the silica sand (or quartz sand). The aim of the study is to give a first assessment by calculation to the radiative properties of the fuse arc plasma initiated during the fuse working. In fact many attempts have been done in the past to evaluate the temperature [1-4] and the electron density [5-8] by means of the study of the discrete radiation emitted either by the metallic species or the silicon lines observed in the neutral state, or ionised once or

twice. From the set of papers published until now several disparities are observed in the temperature and electron density results.

This work is especially focussed on the understanding of the spectral line shapes of the silicon lines ionised once. In many studies the temperature is obtained from the classical method by calculating the ratio of the intensities of these Si II lines. This method implies to consider a Boltzmann law for the energy level distribution, and to assume that the Local Thermodynamic Equilibrium (LTE) is valid. These hypotheses are discussed in Section 4. The Si II lines are also used to assess to the electron density [1, 5, 6, 9]. In this case the Stark broadening is assumed to be the greatest broadening for the considered spectral lines.

Many studies have depicted the burn-back – erosion of the fuse element – and the evolution of the fulgurite volume during the fuse working [10-12]. It is well known that the SiO₂ plasma is defined by a strong temperature – about 20,000 K at the most [5, 6, 9] – a high electron density – about 10¹⁸ cm⁻³ to 10¹⁹ cm⁻³ at the most [1,9] – and a strong pressure – about 10 to 50 bars [13, 14]. This plasma is surrounded by a concentric layer made of fused silica with partly eroded sand gains inside. And this layer is itself surrounded by solid silica sand grains. So there exist very strong gradients in temperature, density and pressure from the centre to the point of observation, which are responsible for more or less absorption of the radiation escaped from the core of the SiO₂ plasma. At our knowledge there is no published study concerning the calculation of the radiation for Ag-SiO₂ plasma, except in [15]. But in this latter study the intensity of the monoatomic spectral lines is calculated without taking into account the influence of the broadening mechanisms on the resulting spectral line shape and thus on the intensity of the radiations. To obtain such results it is necessary to calculate the volumetric emission coefficient, and thus to depict the broadening mechanisms.

In Section 2 we depict briefly the observation of the radiation with our experimental fuse and the assessment of the temperature. In Section 3 we give the formulation used to calculate the radiation emitted by a SiO₂ plasma by distinguishing the continuum and the discrete line emission. The calculated results are given for the SiO₂ plasma by considering various configurations for the gradients.

2. Light emission during the fuse working

2.1. Industrial fuse and experimental fuse

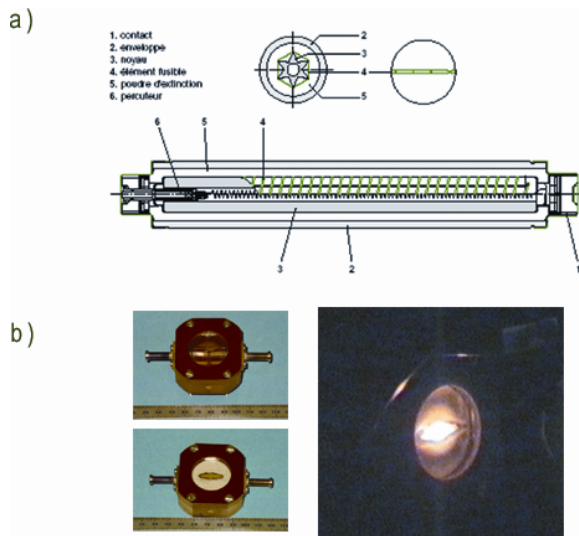


Fig. 1: a) Schematic view of a typical industrial fuse [16]. b) Experimental fuse designed to spectroscopic observations (before the test, during the test with a strong radiation, and after the test with the fulgurite) [9].

The observation of the light escaped from the fuse arc plasma is impossible in the case of an industrial fuse because of the closed filling cavity (Fig.1.a). In the case of an experimental fuse (Fig.1.b) a quartz window can be fitted on the fuse cartridge to collect directly the radiation [9] ; or instead of a quartz window, an optical fibre can be inserted directly through the silica sand, the light being collected by the optical fibre end close to the plasma volume [4, 5, 6]. In this latter case the optical fibre end can be damaged due to the plasma proximity because of the very high temperature. So the properties – optical and geometrical – of the collecting end change during the measurement. And the interpretation of the measurement is difficult.

In the case of the quartz window the hot plasma interacts with the window during the fuse working. This implies the shift of the plasma volume on the quartz area. This shift can be limited if the section of the fuse element is directly put on

the quartz window, rather than putting the fuse ribbon over the plane defined by the window. The escaped radiation is focussed by means of a lens to the entrance end of an optical fibre connected to the entrance slit of a Chromex spectroscope equipped with a 1,242×1,152 CCD matrix [8]. The use of this CCD matrix in kinetic mode allows the assessment of the evolution of the temperature on the whole duration of the fuse working.

Therefore the light escaped from the centre of the radiating plasma volume is integrated over a depth that is not known with an outer limit defined by the quartz window. This depth can be estimated around the initial width of the fuse strip. Over this depth the collected radiation crosses many layers with different values for the temperature, the pressure and the density.

2.2. Measurement of the temperature

The evolution of the temperature on the fuse working duration is obtained by studying the Si II (1) and (3) triplets radiation [9] and taking into account the calculated intensity ratios according to LS coupling for the energy levels within a multiplet [17]. Considering the Boltzmann law for the energy levels at a given temperature, the total intensity of a spectral line $I_{SiII,ul}$ of frequency ν_{ul} is given by:

$$I_{SiII,ul} = \frac{1}{4\pi} \cdot \frac{h\nu_{ul}}{c} \cdot L \cdot g_u \cdot A_{ul} \cdot \frac{N(T)}{U(T)} \cdot e^{-\frac{E_u - E_l}{kT}} \quad (1)$$

where: g_u is the statistical weight of the upper emitting level u , A_{ul} is the transition probability from the upper level u to the lower level l , L is the optical thickness of the radiating volume, $N(T)$ is the total density of the radiating species Si II, $U(T)$ is the Si II internal partition function, E_u and E_l are respectively the upper and lower energy levels of the studied radiation, and T is the temperature identified to the excitation temperature. If we consider two lines from Si II (1) and Si II (3), the temperature T can be obtained without the calculation of $N(T)$ and $Z(T)$.

From Eq.(1) we notice that the temperature assessment is sensitive to four main factors.

The uncertainty for the A_{kj} values

For the two stronger lines of Si II (1), 385.602 nm and 386.260 nm, the estimated accuracy is inferior to 18%, and for the two stronger lines of Si II (3), 412.807 nm and 413.089 nm, the estimated accuracy is inferior to 10% [18].

The optical thickness L

It depends in part of the wavelengths of the studied spectral lines. In our case the triplets Si II

(1) and (3) are separated by about 27 nm, which can be considered as weak in regards to the other factors influencing the measurement of the temperature.

The calibration in intensity of the CCD matrix

An absolute calibration in intensity is necessary if the temperature is deduced from the absolute intensity of the spectral lines. In this case one temperature is deduced from each studied line. The use of this method is difficult in our case because of the various possible errors linked to the optical device and the fluctuations of the radiating volume. But a calibration is necessary to calibrate the response of the optical line and of the spectroscopy plus CCD matrix. This is done by using a calibrated tungsten ribbon lamp [8]. Thus the experimental acquisition is corrected for the given spectral interval comprising the four Si II lines.

The experimental assessment of the intensity $I_{SiII,jk}$ of the studied line

Usually a direct assessment of the total area of the spectral lines is good enough. In the case of the fuse arc plasma, and because of the strong values for the electron density and the pressure, it is necessary to fit the experimental spectral line profile by using a profile taking into consideration the physical effects responsible for the broadening of the observed lines. In our case the experimental profiles are fitted by means of a Voigt profile [8]. This profile results from the combination of a Gaussian profile: apparatus function, Doppler broadening, and of a Lorentz profile: natural, Van der Waals, resonance and quadratic Stark broadenings.

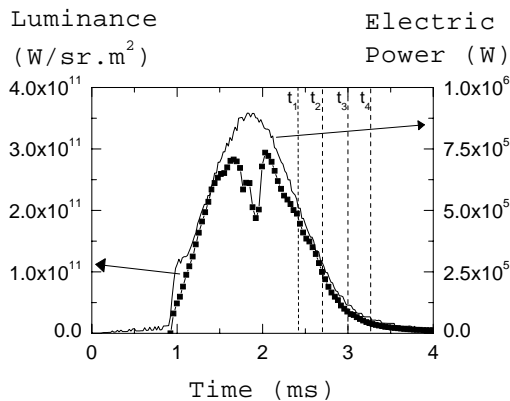


Fig. 2: Evolution versus time of the total intensity or luminance observed in the range 360 nm-800 nm and of the electric power [8]. Fuse test performed with a capacitor bank discharge (stored voltage: 460 V, presumed current: 3.2 kA, pre-arcing time: 0.9 ms). The times t_1 , t_2 , t_3 and t_4 correspond to the calculation of the radiation (Section 3.2)

2.3. Light emission during the fuse working

The intensity of the total radiation escaped from the fuse arc plasma is directly linked to the instantaneous electric power. The evolution versus time of the luminance and of the electric power is given in Fig. 2. The radiation is integrated for the spectral interval [360-800] nm. At the beginning of the arcing time the luminance increases as the electric power (from 0.9 ms to ~1.5 ms). Due to the energy brought by the fault current the energy of the plasma increases. The losses of energy linked to the cooling of the plasma increases, especially the radiation. The opposite trend is observed at the decrease of the current (from ~2.1 ms to 4 ms). There exists a particular decrease in luminance for the time scale corresponding to the higher values of the electric power. Moreover the higher values in pressure are also observed for this time scale.

From the Figure 2 the influence of the radiation absorption appears clearly. As the temperature and the electron density are deduced from the study of the radiation properties, it is necessary to understand what could be the influence of the density, the pressure on the escaped radiation. In fact these latter parameters are directly linked to the density and the temperature of the radiating species, to the absorption of the escaped radiation when it crosses various layers in the plasma volume from the hot centre to the colder surroundings.

3. Calculation of the radiation

The radiation intensity is expressed in terms of the spectral emission coefficient (ϵ_λ) which is the result of [19-23]:

3.1. Spectral line

Spectral emissivity for one isolated line

For each radiating species one defines the spectral emissivity by [19]:

$$\epsilon_{i,ul,\lambda}(\lambda, T) = \frac{hc}{4\pi} \times A_{i,ul} \times n_{i,u}(T) \times P_{i,ul}(\lambda, T) \quad (2)$$

where $A_{i,ul}$ is the transition probability from the upper energy level u to the lower energy level l , $n_{i,u}(T)$ is the population density for the energy level E_u corresponding to the i^{th} radiating species at temperature T , $P_{i,ul}(\lambda, T)$ is the normalized spectral profile at temperature T . For the spectral lines studied in this work the transition probabilities are obtained from [18]. The population density $n_{i,u}(T)$ for the i^{th} species is deduced from:

$$n_{i,u}(T) = \frac{n_i(T)g_u}{Z(T)} \times e^{-\frac{E_u}{kT}} \times \omega_u \quad (3)$$

where $n_i(T)$ is the total density of the i^{th} species at temperature T , g_u is the statistical weight for the upper energy level E_u , $Z(t)$ is the total partition function [15,37-38], and ω_u is the population probability of the corresponding energy level [18]. In the case of the fuse arc plasma the use of an approximate profile $P_{i,ul}(\lambda, T)$ is enough especially as the use of a precise Voigt profile is computationally expensive. The normalized spectral profile $P_{i,ul}(\lambda, T)$ is evaluated by using the approximate formula [19]:

$$P_{i,ul}(\lambda, T) = \frac{\varepsilon_{i,L_{ul},\lambda_{ul}}}{\varepsilon_{i,L_{ul},int}} \times f_{i,w_L,w_V,\lambda_{ul}}(\lambda) \quad (4)$$

where $f_{i,w_L,w_V,\lambda_{ul}}(\lambda)$ is a numerical expression defined for the studied line of wavelength λ_{ul} , w_L is the Lorentz half-width, w_V is the Voigt half-width. The two terms $\varepsilon_{i,L_{ul},\lambda_{ul}}$ and $\varepsilon_{i,L_{ul},int}$ are respectively the centreline magnitude and the integrated intensity for the studied line [19]. The following items consist in a depiction of the physical broadening mechanisms responsible for the Lorentz and Gaussian half-widths [22].

Broadening mechanisms resulting in a Gaussian profile

- The Doppler broadening is described by a Gaussian profile and is of negligible contribution in the total half-width.
- The apparatus function is not generated by a physical mechanism. It is the response of the monochromator plus CCD matrix device to an isolated and thin line. It has to be taken into account especially at the end of the arcing period because the spectral lines are weakly broadened.

Broadening mechanisms resulting in a Lorentz profile

- The resonance broadening is due to an atom or ion in a resonance state interacting with another like atom or ion in a ground state. It is not the case for the once ionised silicon lines studied.
- The natural broadening is due to the finite lifetimes of an atom or ion. It is calculated using the formulation given in [22] but it is of negligible contribution for the studied lines.
- The Van der Waals broadening is of great contribution in the case of neutral emitters. In the case of the once ionised silicon lines, this broadening exists but it is negligible. An approximated calculation can be made with the hydrogenic assumption [19].

- The Stark broadening is the greatest contribution in the case of the studied plasma. In fact the fast energy release linked to the power supply produces silica vapours from the early beginning of the arcing period. These vapours are enclosed in a surrounding fused silica layer which maintains an overpressure on the plasma volume. Because of the energy of the fault current the temperature of the plasma increases, and so does the amount of vapours. Thus the pressure of the plasma increases strongly [13-14]. Therefore the number and the strength of the collisions between charged particles increase which imply the splitting of the emitting energy levels of the radiating atom or ion. In the case of a plasma the quadratic Stark broadening is dominant in comparison to the linear Stark broadening, and it can be evaluated using the results given by Griem [24-25].

Resulting Voigt profile

The resulting profile is known as the Voigt profile, with the half-width defined by [19]:

$$w_V = \frac{w_L}{2} + \sqrt{\frac{w_L^2}{2} + w_G^2} \quad (5)$$

where w_G and w_L are respectively the Gaussian half-width and the Lorentzian half-width taking into account each of the broadening mechanisms defined.

3.2. Continuous radiation

There exist many works dedicated to the calculation of the continuous radiation [26] in the case of the most common elements such as H₂, He, N₂, O₂ [27], Ar [28], SF₆ [29], rare gases [30] [31] [32] and highly ionised elements. Some information can also be found about the calculation of the volumetric emission coefficient dedicated to typical applications such high current breakers [33-34].

For the calculation of the continuum, two contributions are calculated, namely the free-bound continuum and the free-free continuum. Considering that the aim of the study is a first step in the understanding of the radiated properties in electric fuses on one side, and that the fuse plasma is characterized by strong values of the temperature, electron density and pressure on the other side, the molecular contribution is neglected. This latter assumption supposes that the chemical species in the plasma are completely dissociated.

Free-bound continuum

The free-bound continuum or recombination radiation is due to the capture of a free electron by an ion. The contribution of the continuum due to negative ions (attachment of an electron to an atom or a molecule) is neglected is so far as the concentration of these negative ions is very low

compared to the other contributing species [15]. The free-bound continuum is defined from the ξ_{fb} factor or Biberman factor [19] by:

$$\varepsilon_{fb,\lambda,i,z \geq 2} = 2.177 \times \frac{e^6}{c^2 m_e^{1.5}} \sqrt{\frac{\pi}{k}} \frac{g_{i,z,1}}{U_{i,z}} \times \frac{n_e n_{i,z} (z-1)^2}{\lambda^2 \sqrt{T}} \times \left(1 - e^{-\frac{hc}{\lambda k T}} \right) \times \xi_{fb,i,z}(T, \lambda) \quad (6)$$

where e is the elementary charge, c is the speed of light, m_e is the electron mass, $g_{i,z,1}$ is the statistical weight of the ground state for the particle i in the ionisation stage z ($z=1$ for atom, $z=2$ for the first ion, etc.), $U_{i,z}$ is the partition function, n_e is the electron density, $n_{i,z}$ is the density of particle i in the ionisation stage z , λ is the wavelength, T is the temperature, h is the Planck constant, k is the Boltzmann constant, $\xi_{fb,i,z}$ is the Biberman factor whose values are tabulated in [35]. In this study the equation is given in absorption coefficient form.

Free-free continuum

The free-free radiation corresponds to the emission of a photon when an electron is subjected to the electric field of an ion (case 1), or an atom subjected to a transition from a free state to another free state with lower kinetic energy (case 2). In the case 1 the free-free continuum is given by:

$$\varepsilon_{ff,\lambda,i,z \geq 2} = 2.177 \times \frac{e^6}{c^2 m_e^{1.5}} \sqrt{\frac{\pi}{k}} \times \frac{n_e n_{i,z} (z-1)^2}{\lambda^2 \sqrt{T}} \times e^{-\frac{hc}{\lambda k T}} \times g_{ff,z \geq 2}(T, \lambda) \quad (7)$$

where the free-free Gaunt factor is used to correct the non-classical behaviour:

$$g_{ff,z \geq 2}(T, \lambda) = 1 + 0.1728 \times \left(\frac{hc}{\lambda E_H (z-1)^2} \right)^{1/3} \times \left(1 + \frac{2kT\lambda}{hc} \right) \quad (8)$$

where E_H is the ionization energy of hydrogen. The expression (8) is defined from the hydrogenic approximation [36]. In the case 2 the following equation is used to calculate the free-free continuum:

$$\varepsilon_{ff,\lambda,i,z=1} = 3.771 \times \frac{e^2}{c^2} \times \left(\frac{k}{\pi m_e} \right)^{1.5} \times \frac{n_e n_{j,z}}{\lambda^2} \sqrt{T} \times Q(T) \times \left[\left(1 + \frac{hc}{\lambda k T} \right)^2 + 1 \right] \times e^{-\frac{hc}{\lambda k T}} \quad (9)$$

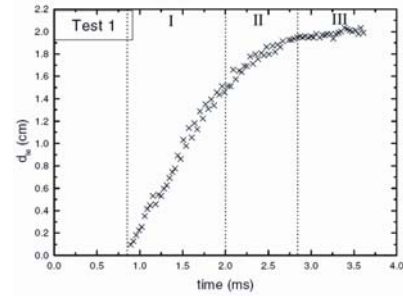
where $Q(T)$ is the electron-neutral collision cross-section. This term can be neglected in the case of

the fuse arc plasma in so far as it is important at low temperatures.

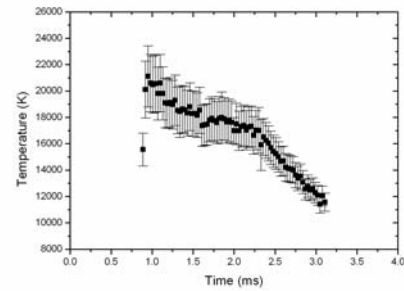
Resulting continuum for the fuse arc plasma

The total continuum is the sum of the free-bound and free-free continuum calculated for all the chemical species observed in the fuse arc. These chemical species can be deduced from the calculation of the plasma composition published in [15, 37-38] where the chemical species concentration is given versus the temperature. For the current paper the chemical species considered are: Si, Si⁺, Si⁺⁺, Si⁺⁺⁺, Si⁺⁺⁺⁺, Si⁻, O, O⁺, O⁺⁺, O⁺⁺⁺, O⁺⁺⁺⁺, O⁻ and electrons. These chemical species are chosen because:

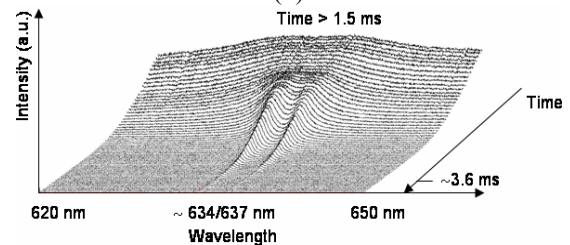
- the calculation is made in the case of spectral observations obtained for high level of the electric power;
- from measurements we know that the temperature is high;



(a)



(b)



(c)

Fig. 3: Evolution versus time of: (a) length between electrodes (d_{ie}) [12], temperature [9], spectral radiation observed in the domain focussed around the Si II (2) multiplet.

- for the time of observation, the gap between the two eroded parts of the fuse element is around 15 mm to 20 mm ; thus the silver element is supposed to be emitted in the surroundings of the plasma volume, near the two erosion fronts ; and the spectral observations are done close to the centre of the initial reduced section.

The evolution of the temperature, the inter-electrodes length, and the observed radiation in the spectral domain focussed around 634 nm is given in Fig. 3.

The radiation escaped from the fuse arc plasma is difficult to study in a spectroscopic way. This is due to the strong gradients in temperature, pressure and density from the centre to the colder surroundings. It can be easily seen in Fig. 3 (c). The quoted spectral domain comprises the Si II lines used to assess the electron density assuming that the Stark broadening is the major broadening effect [9]. The beginning of the emission starts around 0.9 ms and is not shown. We give the radiation after around 1.5 ms for which the maximum value of the electric power is observed.

The current calculation is made to understand the profile line shape observed for the Si II (2) multiplet during the decrease of the electric power, that is to say to understand the physical conditions responsible for the emission of radiation.

Resulting radiation for the fuse arc plasma

The first step is to calculate the total spectral emissivity defined by:

$$\varepsilon_{\lambda}(\lambda, T) = \varepsilon_{i,ul,\lambda}(\lambda, T) + \varepsilon_{fb,\lambda,i}(\lambda, T) + \varepsilon_{ff,\lambda,i}(\lambda, T) \quad (10)$$

which is expressed in $W/sr.m^4$.

To compare the experimental spectral observation with the calculated one, one had to calculate the spectral intensity in $W/sr.m^3$ defined by:

$$I_{\lambda}(R) = \int_0^R \varepsilon_{\lambda}(x, T) \cdot \exp\left(-\int_x^R k_{\lambda}(x', T) dx'\right) dx \quad (11)$$

where R indicates the edge of the integration domain (Fig. 4), k_{λ} is the spectral absorption coefficient in m^{-1} defined by:

$$k_{\lambda} = \frac{\lambda_{ul}^4}{8\pi c} A_{ul} g_u \frac{n_Z}{U_Z} \times \left(e^{-\frac{E_l}{kT}} - e^{-\frac{E_u}{kT}} \right) P_{\lambda} \quad (12)$$

The expression (12) can be used to evaluate the optical thickness $\tau_{\lambda}(x, T)$.

3.3. Spectral radiation for the fuse arc plasma

The calculation is done for the Si II lines of the multiplet (2) whose spectroscopic constants are given in Table 1. These lines are chosen because

they are used for the electron density evaluation on one side, and they are isolated from other lines observed in the whole spectrum on the other side. Thus the pseudo-continuum due to the merging of the wings of strongly broadened lines can be neglected for the calculation.

Table 1. Spectroscopic constants for the two Si II lines of the multiplet (2) [18].

λ nm	Transition	A_{ul} $10^8 s^{-1}$	g_u g_l	E_u / eV E_l / eV
634.711	$4s \ ^2S_{\frac{1}{2}} - 4p \ ^2P_{\frac{3}{2}}^0$	$7.0 \cdot 10^{-1}$	4 2	10.073961 8.121089
637.137	$4s \ ^2S_{\frac{1}{2}} - 4p \ ^2P_{\frac{1}{2}}^0$	$6.9 \cdot 10^{-1}$	2 2	10.066524 8.121089

The calculation is made for two times of observation during the fuse working. In this case the prospective current is provided by a capacitor bank discharge with $\hat{I}_p \sim 3.2$ kA, $V_{sup ply} \sim 460$ V [8]. The pre-arcing time is around 0.87 ms and the arcing time is around 3 ms. The fuse element put in the tests is equipped with two reduced sections, 5 mm in width, 0.105 mm in thickness.

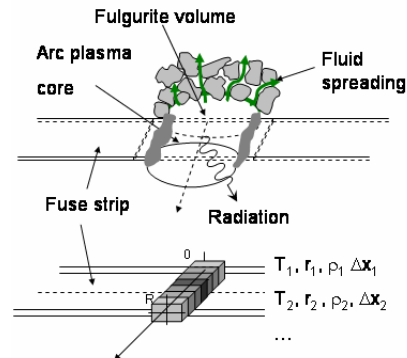


Fig. 4: Schematic explanation of the geometry chosen for the calculation ; $x = 0$ corresponds to the edge of the fuse strip in the sand, $x = R$ corresponds to the edge in contact with the quartz window from which the light is integrated.

Figure 4 illustrates the fulgurite and the plasma volume in the case of the experimental fuse. The back edge of the fulgurite is delimited by the silica sand grains, and the front edge of the plasma volume is in contact with the quartz window from which the light is collected. The calculation is performed for the domain $x \in [0, R]$ and it is assumed that the radiation is emitted in the R -direction only, in so far as in the 0-direction the radiation is unable to escape.

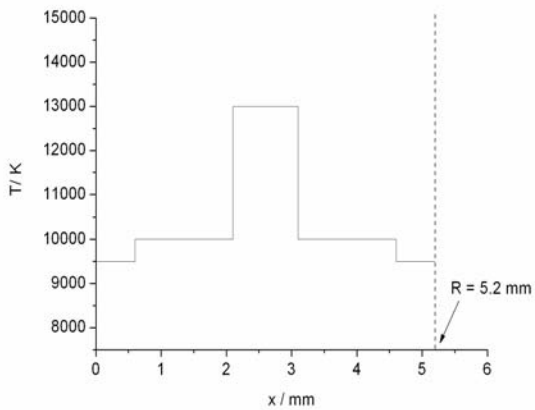
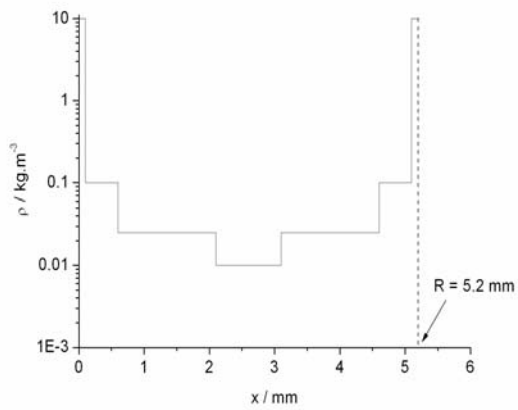
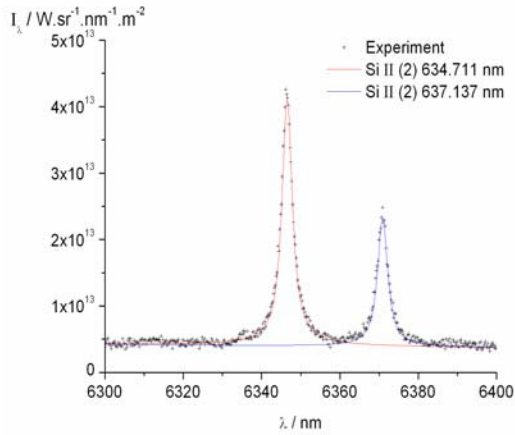


Fig. 5: Comparison at $t_4 = 3.24$ ms between experiment and calculation for the Si II (2) multiplet: spectral profile, plasma density, and temperature. $T_{EXP} = 11,988$ K.

In the lower part of Fig. 4 we show the configuration chosen for the calculation. We consider that the experimental observation corresponds to one line of sight which is divided in a fixed number of volume elements of length Δx_k from $x = 0$ to $x = R$ ($k = 1, 2, \dots$).

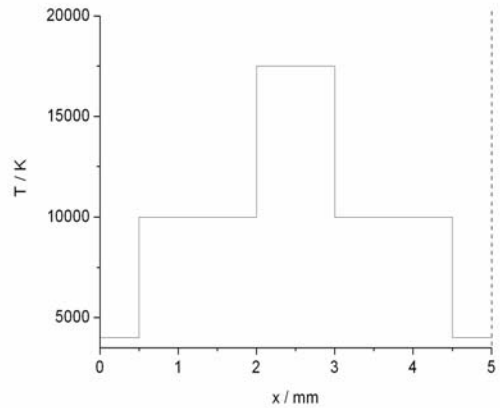
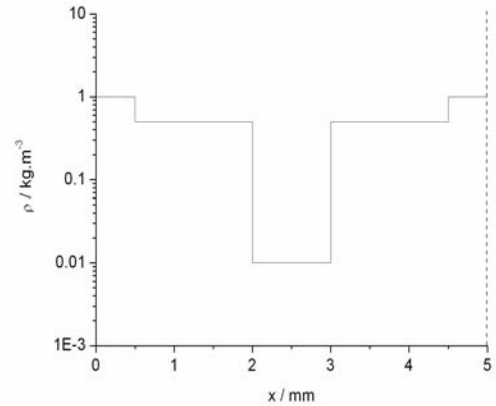
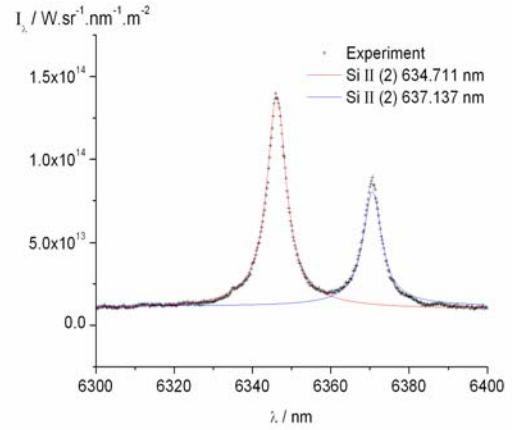


Fig. 6: Comparison at $t_3 = 2.97$ ms between experiment and calculation for the Si II (2) multiplet: spectral profile, plasma density, and temperature. $T_{EXP} = 12,914$ K.

For each Δx_k : the temperature value is fixed according to the mean temperature obtained for the same observation time by spectroscopic diagnostic, and the plasma density value is set according to the experimental electron density. The variations of the temperature and the plasma density are chosen symmetrical to the axis of symmetry of the fuse

strip. The calculation is done for $t_1 = 2.43$ ms, $t_2 = 2.70$ ms, $t_3 = 2.97$ ms, $t_4 = 3.24$ ms (Fig. 2). The first result is given in Fig. 5 for $t_4 = 3.24$ ms, that is to say during the decrease of the electric power near the end of the arcing time.

The characteristics of the domain are given for the temperature and the plasma density. For these values we see that the calculated profiles fit well with the experimental profile. The plasma density decreases strongly from 10 kg.m^{-3} at $x = 0$ down to 0.01 kg.m^{-3} in the centre.

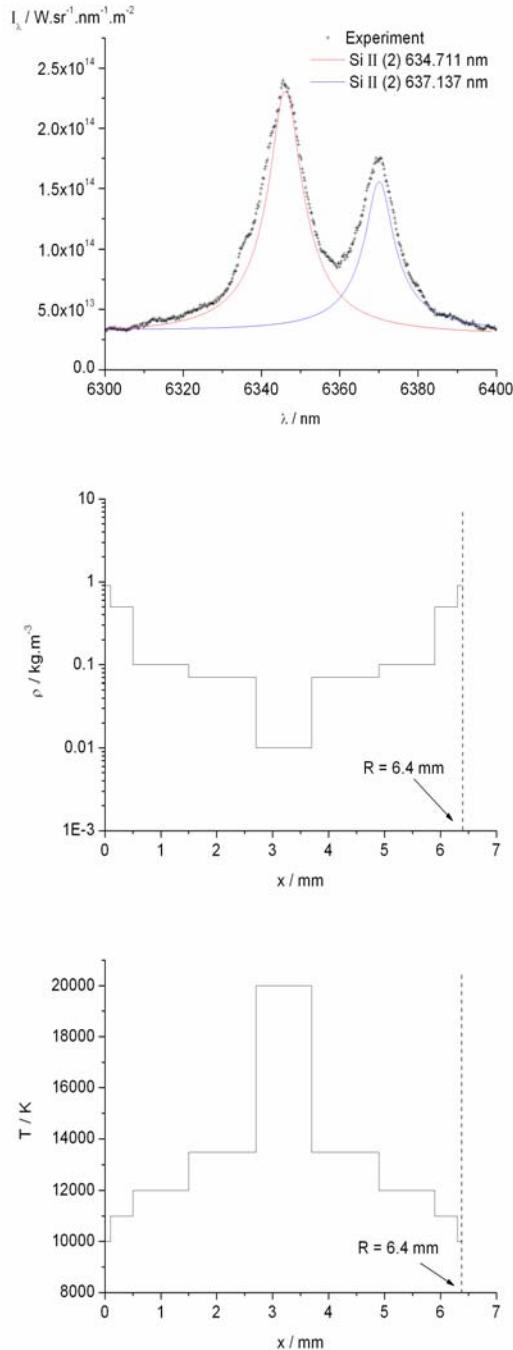


Fig. 7: Comparison at $t_2 = 2.70$ ms between experiment and calculation for the Si II (2) multiplet: spectral profile, plasma density, and temperature. $T_{EXP} = 13,839$ K.

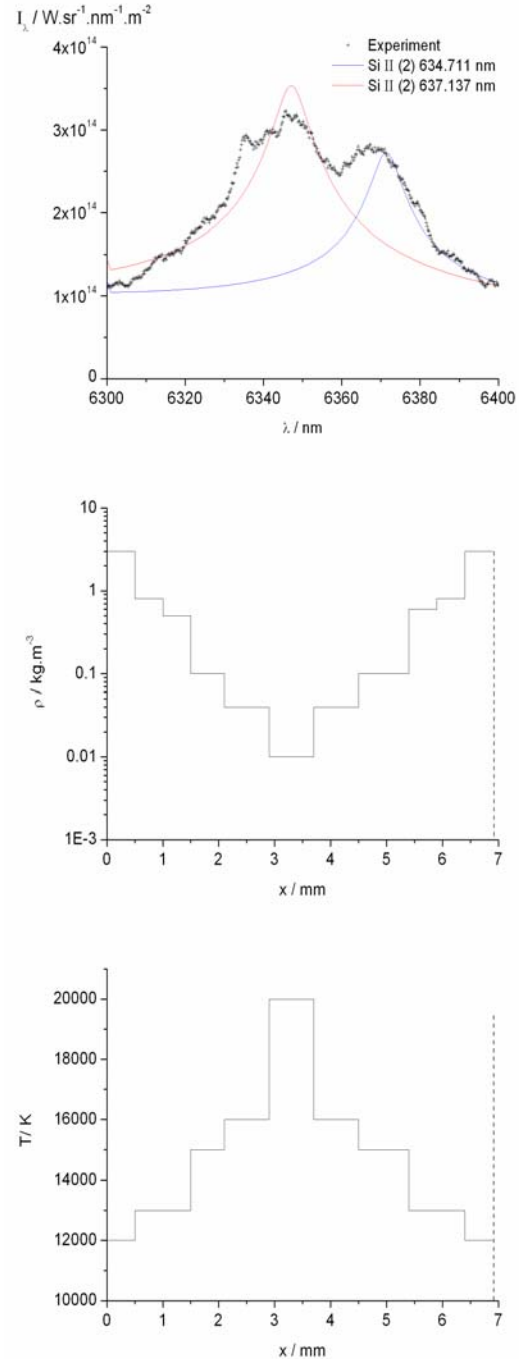


Fig. 8: Comparison at $t_1 = 2.43$ ms between experiment and calculation for the Si II (2) multiplet: spectral profile, plasma density, and temperature. $T_{EXP} = 14,765$ K.

The plasma temperature increase from 9500 K at $x=0$ to 13000K in the centre. The calculated trend for the temperature clearly shows that the experimental temperature can not be considered as uniform on the whole plasma thickness.

On the contrary the experimental temperature has to be considered as a mean value of the temperature which is the result of the contribution of different volumes with a given temperature.

Similar results are obtained for t_3 and t_2 . We can notice that there is an increase of the domain $[0, R]$ with higher values of R . This is consistent with the fact that for this time interval the pressure increases – linked to the increase of the temperature, and the vaporization – and implies a higher width of the plasma volume. For the spectral observations given on Fig. 5 to Fig. 8, the width of the two reduced sections fuse element is 5 mm in the initial state. The corresponding widths put in the calculation are 5.2 mm, 5 mm, 6.4 mm and 6.9 mm respectively for t_4, t_3, t_2 and t_1 . This parameter is difficult to determine in so far as the fuse arc plasma radiation is collected through a quartz window directly in contact with the plasma. Thus the plasma interacts with the quartz window and can imply strong fluctuations at the surroundings. Moreover the experimental temperature increases regularly from t_4 to t_1 . This trend is consistent with the increase of the calculated maximum temperature observed close to $x = R/2$. For t_4, t_3, t_2 and t_1 we obtain respectively 13,000 K, 17,500 K, and 20,000 K for t_2 and t_1 . These values can not be considered as the true values but the rise seems to be in good agreement with the rise in pressure and electron density.

The case $t_1 = 2.43$ ms is more problematic because it corresponds to a high level of electric power: the continuous radiation is strong and the spectral lines are strongly broadened. From Fig. 2 and Fig. 3c we see that this time is close to the time for which it is difficult to distinguish the discret radiation from the continuous radiation. The calculation has been tested to evaluate if it is able to give a realistic result concerning the influence of the plasma density and temperature, especially to estimate the conditions implying a strong broadening with a dissymmetrical spectral line shape like in experiments. The result of the calculation is given in Fig. 8 for $t_1 = 2.43$ ms. The experimental profiles are strongly disturbed and the calculated profiles do not fit well with the experimental ones.

This case illustrates clearly the limit of the calculation. From our opinion the time domain corresponding to the time observation with $t < t_1$ is

characterized by very strong and quick variations of the gradients in temperature, pressure, plasma density, plasma composition and also in the dependant properties such as the optical thickness of the plasma. Such observations have been made in the case of the interaction between a metallic plasma and a polymer wall [39]. In this latter case the rise in pressure is highly brisk and the pressure value is high. It implies the spreading of the pressure wave with transmitted and reflected components. The interference between these two components is directly linked to the strong broadening of the spectral lines, to the increase of the continuous radiation intensity, and to the strong increase of the plasma optical thickness that implies absorption of the emitted radiation. In this case also the spectral line shape can not be used for a spectroscopic diagnostic and other experimental methods have to be used.

4. Synthesis and conclusion

For modelling purposes [40] one has to calculate the radiative term of the fuse arc plasma. This calculation consists in the evaluation of the evolution of the net emission coefficient versus the temperature for a given plasma composition. But the hypotheses linked to the calculation have to be checked. The way described in this study is to compare the experimental spectrum observed during the fuse operation with the result of the calculation including the continuous and spectral components.

The first attempt given in this paper clearly shows that some hypotheses have to be used with great care, especially:

- the calculation of the radiation is usually a complex task, and especially in the case of the fuse working as far as the plasma volume is not a cylindrical volume well appropriate to use classical methods such as the Abel inversion necessary to obtain the local emissivities ;
- due to the short duration of the arcing time – typically around 5 ms – there exist strong gradients which evolve on the whole duration of the fuse working ; these gradients concern the temperature, the plasma composition, the optical thickness, the values of the transport coefficients, namely the electrical conductivity, the thermal conductivity, and the viscosity ;
- therefore the following assumptions have to be discussed:
 - *the plasma is supposed in Local Thermodynamic Equilibrium (LTE)*: this can be easily justified for the areas close to the centre of the fuse arc plasma because the pressure is high ; but for the areas close to the surroundings, near the fused silica layer surrounding the plasma core, and near

the quartz window, the gradients are very high and the LTE hypothesis is not valid ; these areas correspond to the colder surroundings ;

- *the influence of the spectroscopic constants* : in the case of the radiation measurements by means of spectroscopy, and the calculation of the discrete and continuous radiations, one uses the transition strengths A_{ul} quoted in various databases ; if possible, the experimental values are preferred but usually these experimental values correspond to measurements performed in different plasma sources ; and most of these plasma sources are uniform in temperature, density and the influence of the gradients in physical properties is negligible ; in the case of the fuse arc plasma, the pressure is very high and can affect the transition strengths;
- *the variations of the plasma composition* : the composition of the plasma at a given time of observation is one of the key parameters to obtain a consistent assessment of the radiation ; as it has been shown in [37] an addition of metallic species implies very strong changes in the resulting plasma composition for a given temperature ; thus the radiated intensity is modified and it depends directly on the concentration of these metallic species ; furthermore the radiated properties of the metallic spectral lines is hard to calculate as soon as the pressure moves far away the atmospheric pressure: the low energy level of two typical silver lines, namely Ag I 520,907 nm and Ag I 546.550 nm, is close to the ground level of the silver atom ; therefore these lines are highly subjected to self-absorption when they are observed during the fuse working ; such lines are unusable for a spectroscopic diagnostic, and the calculation of the emissivity should imply a specific knowledge of the physical characteristics of the fuse arc plasma.
- *the influence of the calibration of the experimental observation* : due to the geometry of the experimental fuse, it is rather complex to perform a valuable calibration in intensity ; many mistakes can be made and they make more difficult the choice of the initial values in the calculation.

The comparison of the experimental and theoretical intensities given in this paper clearly shows a good agreement at the end of the arcing time. The calculation of the discrete and the continuous radiations fits well with the measurement. The calculated broadening and

shifting of the Si II (2) lines by Stark effect are also in good agreement. But for the time corresponding to high levels of electric power and pressure, the calculation of the continuum in particular becomes more complicated as far as it depends strongly on the concentration of the various chemical species in the fuse arc plasma.

The next step of this work is thus to improve the depiction of the $x \in [0, R]$ domain. Physical arguments have to be defined in order to build an iterative calculation for the determination of Δx_k . A solution could be to calculate the radiation for the final microseconds of radiation emission for the lowest levels of the electric power. By means of the high sensitivity CCD matrix the radiation emission can be observed even if the level of radiation is very low. In this case the broadening of the spectral is minimum and the contribution of the Stark broadening is very weak in the total broadening. The main broadening is due to the apparatus function.

In the future these calculations could be very helpful to define the true net emission coefficients used in the modelling of the fuse working.

Acknowledgements

First, we thank both for their financial support and their help through many discussions, Mr. J.L. Gelet and Mr. T. Rambaud from Ferraz Shawmut, Mr. J.C. Perez Quesada from Mesa, and Mr. F. Gentils from Schneider Electric.

Second, we thank Dr. D. Hofsaess for having provided the ξ_{bf} and ξ_{ff} factors to calculate the continuum.

References

- [1] T Chikata, Y Ueda, Y Murai, T Miyamoto, Spectroscopic observations of arcs in current limiting fuse through sand, Proceedings of the Icefa (Liverpool, England), April, pp 114-121, 1976
- [2] P. Bezborodko, J. Fauconneau, R. Pellet, Experimental set-up for spectroscopic measurements of plasma arcs in fuses, Proceedings of the 5th Icefa (TU Ilmenau, Germany), 25-27 Sept., pp 259-264, 1995
- [3] W. Bussière, P. Bezborodko, R. Pellet, Spectroscopic study of a cutting electrical arc in HBC fuse, Proceedings of the 6th Icefa (IEN Galileo Ferraris, Torino, Italy), 20-22 Sept., pp 113-118, 1999
- [4] M.A. Saqib, A.D. Stokes, B.W. James, I.S. Falconner, Arc temperature measurement in a high voltage fuse, Proceedings of the 6th Icefa (IEN Galileo Ferraris, Torino, Italy), 20-22 Sept., pp 107-112, 1999
- [5] L. Cheim, A. Howe, Spectroscopic measurement of fuse arc temperature, Proceedings of the 5th Icefa (TU Ilmenau, Germany), 25-27 Sept., pp 251-258, 1995
- [6] L. Cheim, Arc temperature measurements in high breaking capacity fuses, PhD. Thesis, Univ. of Nottingham, Dpt. of Electrical & Electronic Engineering, December, 1992
- [7] M.A. Saqib, A.D. Stokes, B.W. James, I.S. Falconner, Measurement of electron density in a high voltage fuse arc, Proceedings of the 6th Icefa (IEN Galileo Ferraris, Torino, Italy), 20-22 Sept., pp 107-112, 1999

- [8] W. Bussière, Mesure des grandeurs (T,Ne,P) au sein du plasma d'arc des fusibles en moyenne tension, PhD. Thesis (in French), Univ. Blaise Pascal, D.U. 1258, December, 2000
- [9] W. Bussière, Influence of sand granulometry on electrical characteristics, temperature and electron density during high-voltage fuse arc, *J.Phys.D:Appl. Phys.* 34, pp 925-935, 2001
- [10] Lakshminarashima C S, Barrault M R and Oliver R, Factors influencing the formation and structure of fuse fulgurites, *IEE Proc., Sci. Meas. Technol.*, 125, 391-399, 1978
- [11] Wilkins R, Gnanalingam S, Burn-back rates of silver, fuse elements, 5th Int. Conf. on Gas Discharges (University of Liverpool), 195-198, 1978
- [12] W. Bussière, Estimation of the burn-back rate in high breaking capacity fuses using fast imagery, *J.Phys.D:Appl. Phys.* 34, 1-10, 2001
- [13] M.A. Saqib, A.D. Stokes, P.J. Seebacher, Pressure inside the arc channel of a high-voltage fuse, *Proceedings of the 6th Icefa (IEN Galileo Ferraris, Torino, Italy)*, 20-22 Sept., pp 83-88, 1999
- [14] D. Rochette, W. Bussière, Pressure evolution during HBC fuse operation, *Plasma Sources Sci. and Technol.*, 13, pp 293-302, 2004.
- [15] W. Bussière, P. André, Evaluation of the composition, the pressure, the thermodynamic properties and the monoatomic spectral lines at fixed volume for a SiO₂_Ag plasma in the temperature range 5000-25000 K, *J.Phys.D: Appl. Phys.* 34, pp 1665-1674, 2001
- [16] O. Bouilliez, J.C. Perez-Quesada, Conception et utilisation de fusibles limiteurs MT, *Cahier Technique n°128*, Ed. Schneider Electric, Collection Technique, Novembre 2002.
- [17] A. Lesage, R.A. Rathore, I.S. Lakicevic, J. Puric, Stark widths and shifts of singly ionized silicon spectral lines, *Phys. Rev. A* 28, pp 2264-2268, 1983
- [18] NIST Atomic Spectra Database Lines Form, http://physics.nist.gov/PhysRefData/ASD/lines_form.html
- [19] J. Menart, J. Herbelein, E. Pfender, Line-by-line method of calculating emission coefficients for thermal plasmas consisting of monatomic species, *J. Quant. Spectrosc. Radiat. Transfer*, Vol. 56, N°3, pp 377-398, 1996
- [20] F. Cabannes, J. Chapelle, Reactions under plasmas conditions, Chap. VII, *Spectroscopic plasma diagnostic*, Ed. M. Venugopalan (Wiley Interscience, NY), Vol. 1, 367-469, 1971
- [21] E.E. Whiting, An empirical approximation to the Voigt profile, *J. Quant. Spectrosc. Radiat. Transfer*, Vol. 56, N°3, pp 377-398, 1996
- [22] G. Traving, *Plasma Diagnostics*, Ed. by W. Lochte-Holtgreven, Wiley NY, 66-134, 1968
- [23] J. Richter, *Plasma Diagnostics*, Ed. by W. Lochte-Holtgreven, Wiley NY, 1-65, 1968
- [24] H.R. Griem, *Spectral Line Broadening by Plasmas*, Academic Press, NY, 1974
- [25] H.R. Griem, *Principles of Plasma Spectroscopy*, Cambridge University Press, 1997
- [26] L.G. D'yachkov, The calculation of continuous radiative spectra, Translated from *Teplofizika Vysokikh Temperatur*, Vol. 30, N°5, 868-875, Sept-Oct, 1992
- [27] M.I. Boulos, P. Fauchais, E. Pfender, *Thermal plasmas – Fundamentals and applications*, Vol. 1, Ed. Plenum Press (N.Y. and London), 1994
- [28] S.E. Schnehage, M. Kock, E. Schulz-Gulde, The continuous emission of an argon arc, *J. Phys. B: At. Mol. Phys.*, 15, 1131-1135, 1982
- [29] H. Kafrouni, S. Vacquie, Study of the recombination continuum in an SF₆ arc discharge, *J. Quant. Spectrosc. Radiat. Transfer*, Vol. 32, N°3, 219-224, 1984
- [30] D. Hofsaess, Emission continua of rare gas plasmas, *J. Quant. Spectrosc. Radiat. Transfer*, Vol. 19, 339-352, 1978
- [31] L.G. D'yachkov, G.A. Kobzev, P.M. Pankratov, Continuous radiation of a dense plasma on inert gases: analysis of experimental data, *High Temperature*, Vol. 34, N°6, 855-863, 1996
- [32] Y. Vitel, L.G. D'yachkov, Yu K. Kurilenkov, Radiation continuum of dense krypton plasma, *J. Phys. B: At. Mol. Phys.*, 30, 2021-2031, 1997.
- [33] A Gleizes, J J Gonzalez, P Freton, Thermal plasma modelling, *J. Phys. D: Appl. Phys.*, 38, N°9, R153-R183, 2005
- [34] A Gleizes, J J Gonzalez, B Liani, G Raynal, Calculation of net emission coefficient of thermal plasmas in mixtures of gas with metallic vapour, *J. Phys. D: Appl. Phys.*, 26, N°11, 1921-1927, 1993
- [35] D. Hofsaess, Photoionization cross sections calculated by the scaled Thomas-Fermi method, *Atomic Data and Nuclear Data Tables*, 24, 285-321, 1979
- [36] D. H. Menzel, C.L. Pekeris, *Monthly Notices of the Royal Astronomy Society*, 96, 77-?, 1935
- [37] P. André, W. Bussière, D. Rochette, Transport coefficients of Ag-SiO₂ plasmas, *Plasma Chemistry and Plasma Processing*, To be published, DOI. 10.1007/s11090-007-9086-y
- [38] D. Rochette, W. Bussière, P. André, Composition, enthalpy and vaporization temperature calculation of Ag-SiO₂ plasmas with air in the temperature range from 1000 to 6000 K and for pressure included between 1 to 50 bars, *Plasma Chemistry and Plasma Processing*, Vol. 24, N°3, 475-491, 2004
- [39] W. Bussière, E. Duffour, P. André, R. Pellet, L. Brunet, Experimental assessment of temperature in plasma wall interaction. Application to PE and POM., *Eur. Phys. J. D* 28, 79-90, 2004
- [40] D. Rochette, S. Clain, W. Bussière, Mathematical model using macroscopic and microscopic scales of an electrical arc discharge through a porous medium in HBC fuses, *Proceedings of the 7th Icefa (Gdansk Univ. of Tech., Gdansk, Poland)*, 8-10 Sept., pp 188-193, 2003

MEASUREMENT OF THE PRE-ARCING TIME AND THE FULGURITE LENGTH IN HBC FUSE IN THE CASE OF TESTS PERFORMED WITH AN A.C. 100 KVA STATION

William Bussière¹, David Rochette², Steeve Memiaghe¹, Gérard Velleaud², Thierry Latchimy¹ and Pascal André¹

¹ LAEPT CNRS UMR 6069, Phys. Bât. 5, Université Blaise Pascal, 24 Avenue des Landais, F63177 AUBIERE Cedex, France, Phone: +33 4 73 40 77 04, william.bussiere@univ-bpclermont.fr, steeve.memiaghe@univ-bpclermont.fr, thierry.latchimy@univ-bpclermont.fr, pascal.andre@univ-bpclermont.fr

² LAEPT CNRS UMR 6069, Université Blaise Pascal, IUT de Montluçon, Avenue Aristide Briand, BP 2235, F03101 Montluçon Cedex, France, rochette@moniut.univ-bpclermont.fr, gerard.velleaud@moniut.univ-bpclermont.fr

Abstract: This study deals with a specific test device especially designed to perform tests on HBC fuse on a scale of a non industrial laboratory. In fact it is not possible for most of academic laboratories to build up a device supplying the same current and voltage ranges as in an industrial test station. Moreover the capacitor bank discharges are often used in academic laboratories to test electric fuses. But the main drawback of the capacitor bank is to supply a non 50 Hz-sinusoidal current waveform for one half period only. We present the first measurements performed on experimental HBC fuses using a 100 kVA station built up from a single phase transformer. These first measurements are performed using various fuse elements with the same geometries as in industrial fuses of the middle voltage range. The filling material is silica sand or quartz sand and it is chosen with the same properties as in industrial fuses.

The fuse working is studied experimentally on the whole duration of the fuse working which depends on the values chosen for the power factor and the closing angle. The results are given for the pre-arcing time and the fulgurite length. The power factor put in the tests is equal to $\cos \varphi \sim 0.9$ and $\cos \varphi \sim 0.1$, and the closing angle is increased from 0° to 180° . The results are discussed by taking into account the influence of the energy to dissipate, namely the Joule energy and the inductive energy.

Keywords: closing angle, power factor, fulgurite, energy, experiment.

1. Introduction

This paper deals with the first measurements obtained with a novel supplying device built up from a 100 kVA single phase transformer. Up to now our experimental study of the fuse working has

been performed using a capacitor bank discharge with fitted resistive and inductive constants to obtain a current waveform close to the 50 Hz-waveform [1-5]. For modelling and experimental purposes an A.C power station is now used with a power factor varying in the range from $\cos \varphi \sim 0.9$ down to $\cos \varphi \sim 0.1$, and a closing angle varying in the range from 0° to 180° [6].

The current study concerns High Breaking Capacity (HBC) fuses that usually comprise: two metal electrodes of high conductivity ending, a helicoidal core in insulating material, around which a fuse element or fuse strip in silver of high purity with reduced sections is coiled, and the filling cavity filled with the arc quenching material, silica sand or quartz sand of high purity.

Whatever the type of the electrical supply a specific experimental fuse has been designed according to the electrical and/or physical properties studied. This is detailed in Section 2. The characteristics of the power station are given in Section 3. In Section 4 the experimental results are given and discussed, mainly for two properties, the pre-arcing time and the fulgurite characteristics. Finally we conclude in Section 5.

2. Experimental fuse for measurements

The fuse working can be briefly summarized as follows. The appearance of the fault current implies the fusion and the vaporization of the fuse element around the reduced sections because the electrical resistivity is higher. The temperature rise of the fuse element is caused by the energy brought by the fault current. Once the enthalpy necessary to obtain the vaporization of the melted silver is provided, an electric arc is initiated because of the disruption of the fuse element [7]. First this electric arc is mainly composed of metallic vapours [8]. Second, due to the surrounding silica sand grains, the silver plasma interacts with the sand grains and the plasma becomes a silica plasma [9]. The plasma

temperature increases up to around 20,000 K, the plasma electron density is around 10^{18}cm^{-3} to 10^{19}cm^{-3} at the most, and the plasma pressure is in the range of tens of atm [5,10-11]. Whatever the assessed properties the experimental fuse is always designed: to allow the measurement of the electrical and physical properties, and to avoid the edge effects during the packing operation and the fuse test. In each experiment the industrial sand is used with given values for the mean granulometry and the packing density. The measurement of the electrical properties is helpful to check the reproducibility of the fuse tests.

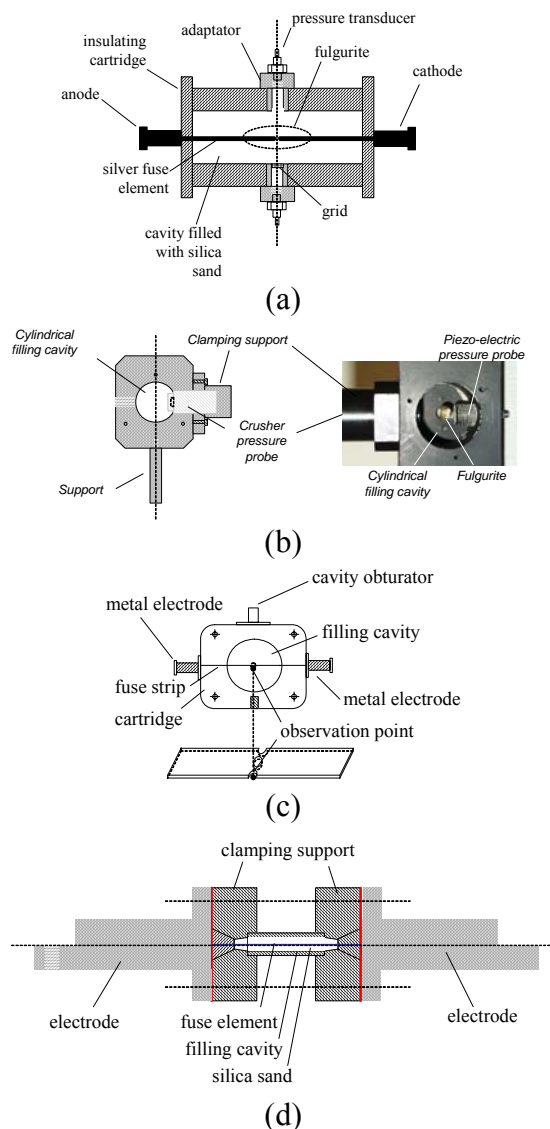
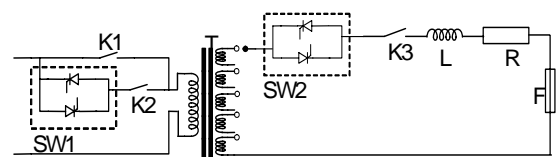


Fig. 1: Different experimental fuses. (a) Measurement of the pressure due to the filler and due to the air in the interstices with piezo-electric sensor [5]. (b) Measurement of the pressure due to the filler with a Crusher probe. (c) Study of the radiation emitted by the plasma [1]. (d) Experimental fuse in this study.

A HBC fuse of industrial type is naturally opaque to the radiation emitted by the plasma due to the cartridge. Two techniques can be used to collect the light: either by inserting an optical fibre close to the reduced section area [12], either by fitting a quartz window close to the fuse element reduced section to collect the light directly via an optical device integrating a focussing lens [3]. The experimental fuse given on Fig. 1(d) has been especially designed to be used in the fuse tests performed with the 100 kVA station. A specific care has been focussed on the interference resistances, the gas tightness, and the reproducibility of the packing operation. Such an experimental fuse can be equipped with several fuse elements in parallel, each of them being equipped with several reduced sections.



F: experimental fuse ; K1: power switch ; K2: security switch ; K3: security switch ; L: inductive load ; R: resistive load ; SW1: primary static switch ; SW2 : secondary static switch ; T: 100 kVA single phase transformer.

Fig. 2: Diagram of the 100 kVA single power station.

3. Power station

The diagram of the 100 kVA power station is given on Fig. 2. It is built from a single phase transformer with a 100 kVA true power which can be supplied with 230 V.A.C. or 400 V.A.C. at the primary. The secondary can be supplied from 100 V.A.C. to 500 V.A.C. The corresponding nominal current is 200 A. Moreover the whole of the electrical device, that is to say the magnetic circuit and the electrical circuit, is designed to allow a secondary A.C. current of 2000 A for 500 ms. The load is composed of a set of coils up to 2860 μH . By using fitted electrical resistances the power factor $\cos \varphi$ can vary in the range from 0.1 to 0.9 with loading A.C. currents up to 2000 A.

The fuse test is performed in two steps. Firstly the calibration of the test circuit is done with a given set of resistive and inductive loads to obtain the experimental values of the closing angle and the power factor, and the waveform corresponding to the prospective current. Secondly the experimental fuse is inserted in the test circuit and the fuse test is performed with a calibrated load.

Due to the A.C. power supply the prospective current is written as:

$$I(t) = \frac{\hat{V}}{\sqrt{R^2 + L^2\omega^2}} \times \left(\sin(\omega t + \theta - \varphi) - \sin(\theta - \varphi) \times e^{-\frac{R}{L}t} \right)$$

where \hat{V} is the supplied voltage peak, R is the resistive load, L is the inductive load, ω is the pulsation at 50 Hz, θ is the closing angle, $\cos \varphi$ is the power factor, t is the time. The calibration allows the measurement of the resistive load and the inductive load for the given prospective current.

Table 1: Experimental values of the closing angle θ .

Presumed closing angle θ ($^\circ$)	θ ($^\circ$) for $\cos \varphi \sim 0.9$	θ ($^\circ$) for $\cos \varphi \sim 0.1$
0	6.7	12.1
90	87.4	90.3
160	157.2	160.7

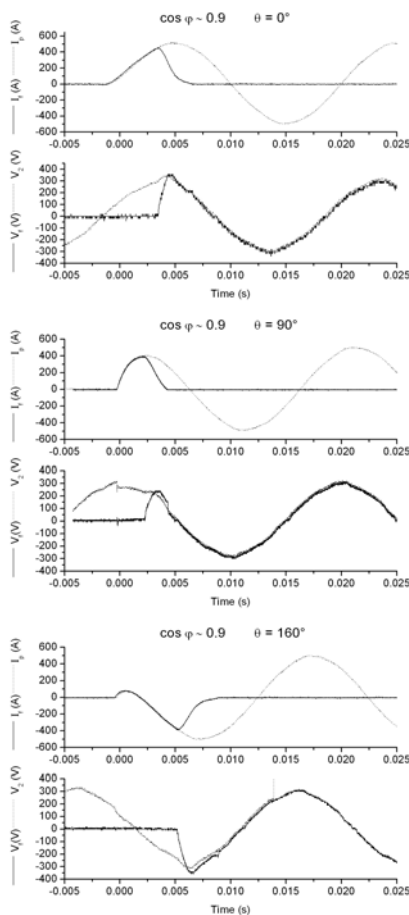


Fig. 3: Evolutions versus time of current and voltage for $\cos \varphi \sim 0.9$ and $\theta = 0^\circ, 90^\circ, 160^\circ$.

4. Measurements

4.1 Conditions of the tests. Prospective currents

Whatever the case, namely calibration or fuse test, the experimental conditions are given in Table 1. The first column gives the presumed closing angle, and the two last columns correspond to the experimental value obtained for the test of the fuse.

These conditions are chosen to scan the experimental domain accessible and to study the influence of the closing angle and the power factor on the quoted properties. The discrepancy between the presumed values and the experimental values is linked to a first version of our numerical control. It has been improved now. The whole conditions allow us to study the fuse working for various cases between the symmetrical and the asymmetrical case.

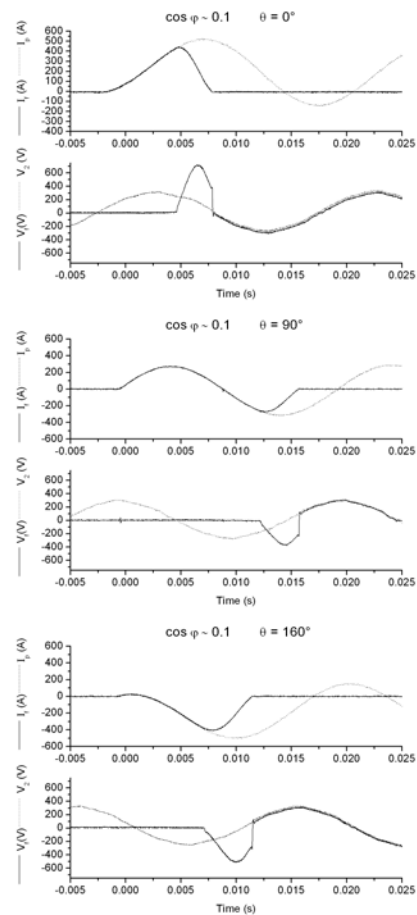


Fig. 4: Evolutions versus time of current and voltage for $\cos \varphi \sim 0.1$ and $\theta = 0^\circ, 90^\circ, 160^\circ$.

The evolutions versus time of the prospective current I_p , the voltage of the supply V_2 , the current in the fuse I_f , and the voltage across the fuse V_f are given in Fig. 3 and Fig 4 respectively for the power

factors $\cos \varphi \sim 0.9$ and $\cos \varphi \sim 0.1$ and the quoted values of the closing angle (Table 1).

4.2 Fuse tests

The fuse tests performed with the conditions defined in Section 4.1 are given in Fig. 3 and 4, with the evolutions versus time of the current in the fuse I_f and the voltage across the fuse V_f . The fuse tests have been performed from $\theta = 0^\circ$ to $\theta = 160^\circ$ by step of 30° and the results can be found in [6]. As it can be seen from Fig. 3 and 4 the total duration of the fuse working, namely the pre-arcing time plus the arcing time defining the extinction time, varies from one to around two half-periods of the 50 Hz supply.

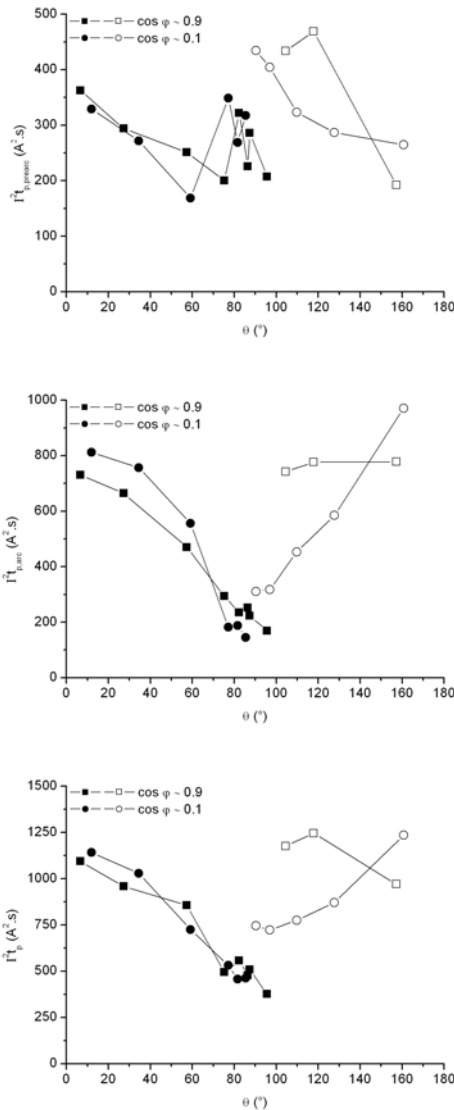


Fig. 5: Experimental Joule integral for the pre-arcing time, the arcing time, the total duration of the fuse working, for the two power factors, versus the closing angle.

This is quite logical in so far as the prospective current peak is not high enough to work with high fault current conditions.

The various conditions of the tests can be compared using the Joule integral calculated for the prospective current. The I^2t values are calculated for the pre-arcing stage, the arcing stage, and the total duration of the fuse working. From Fig. 5 we see that $I^2t_{p,prearc}$ decreases from $\theta = 0^\circ$ to $\theta \sim 90^\circ$ for $\cos \varphi \sim 0.9$ and to $\theta \sim 100^\circ$ for $\cos \varphi \sim 0.1$. We observe strong fluctuations around these latter θ values.

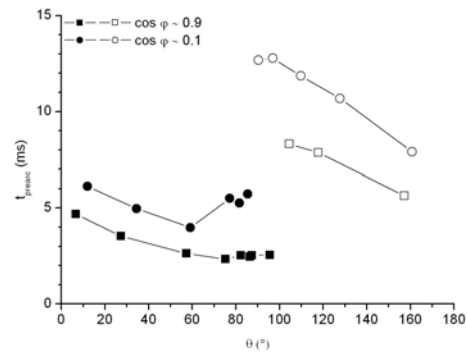


Fig. 6: Influence of the closing angle and the power factor on the pre-arcing time.

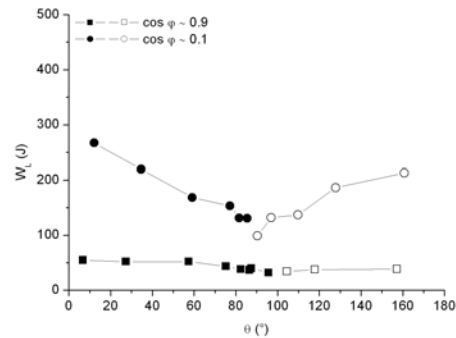


Fig. 7: Evolution versus the closing angle of the electromagnetic energy stored in the coil.

The values are in the range from ~ 160 A².s to ~ 360 A².s. For higher θ values there is a strong increase up to values more than 400 A².s followed by a decrease for $\theta > 90^\circ$ and 100° . There is a gap between the lower and the higher values of θ for which the test can not be performed. This is due to the supplied voltage close to around 0. This particular value of the closing angle is defined as the limit closing angle or θ_l .

The evolution of the pre-arcing time is given on Fig. 6 versus the closing angle. We observe a

decrease up to θ_l . The pre-arcing time decreases from 6.13 ms to 3.98 ms for $\cos \varphi \sim 0.9$ and from 4.67 ms to 2.33 ms for $\cos \varphi \sim 0.1$. Around $\theta < \theta_l$ there is a slight increase. On the whole θ -values defined by $\theta < \theta_l$, the pre-arcing stage lasts longer in the case $\cos \varphi \sim 0.1$. For $\theta > \theta_l$, there is a strong increase of the pre-arcing time up to around 8.30 ms for $\cos \varphi \sim 0.9$ and around 12.68 ms for $\cos \varphi \sim 0.1$. And for higher θ -values up to 160° the values of the pre-arcing time decrease regularly. The discrepancy between $\cos \varphi \sim 0.9$ and $\cos \varphi \sim 0.1$ can be explained by: the prospective current peak inferior in the case $\cos \varphi \sim 0.1$, and the energy brought by the inductive load (Fig. 7).

The influence of the two parameters, $\cos \varphi$ and θ , on the fulgurite characteristics is of great importance from the industrial point of view. In the case of a HBC industrial fuse the fuse element is equipped with many reduced sections in series. The gap between each reduced section is chosen carefully to avoid the merging of two consecutive arcs. In this latter case the fuse is conductive on its whole length and the fault current is not interrupt. Thus the influence of $\cos \varphi$ and θ on the fulgurite characteristics has to be known. The evolutions of the mass and the length of the fulgurite are given on Fig. 8 versus the closing angle. The evolution of the length versus the mass is also given. The two parameters, $L_{fulgurite}$ and $m_{fulgurite}$, decrease with increasing θ up to θ_l . For $\theta > \theta_l$ and $\cos \varphi \sim 0.9$ the mass and the length do not vary significantly. On the contrary for $\cos \varphi \sim 0.1$, $L_{fulgurite}$ and $m_{fulgurite}$ increase strongly up to 160° by a factor roughly estimated around 2. The trends observed for the length and the mass are very similar to the ones of the Joule integral calculated for the arcing stage on one side, and to the ones of the energy dissipated during the fuse working on the other side.

The discrepancy observed for $L_{fulgurite}$ and $m_{fulgurite}$ between the two power factors on the whole θ range is clearly visible for $\theta \ll \theta_l$ and $\theta \gg \theta_l$. These domains correspond to the higher discrepancies observed for the arcing stage Joule integral and the energy dissipated by the fuse, this latter being linked to the energy of the inductive load.

The results given on Fig. 8 clearly show that strong variations can be observed for the fulgurite characteristics according to the conditions of working. These results have to be explained by taking into account the energy point of view more precisely. Moreover some previous experimental

studies [2,4] have clearly shown that the common morphometric properties, namely the packing density and the mean granulometry, play a great role on the plasma properties on one side, and on the fulgurite mass, length, and weight on the other side. Therefore the control of these properties could be very useful to influence the resulting fulgurite characteristics obtained after the fuse operation.

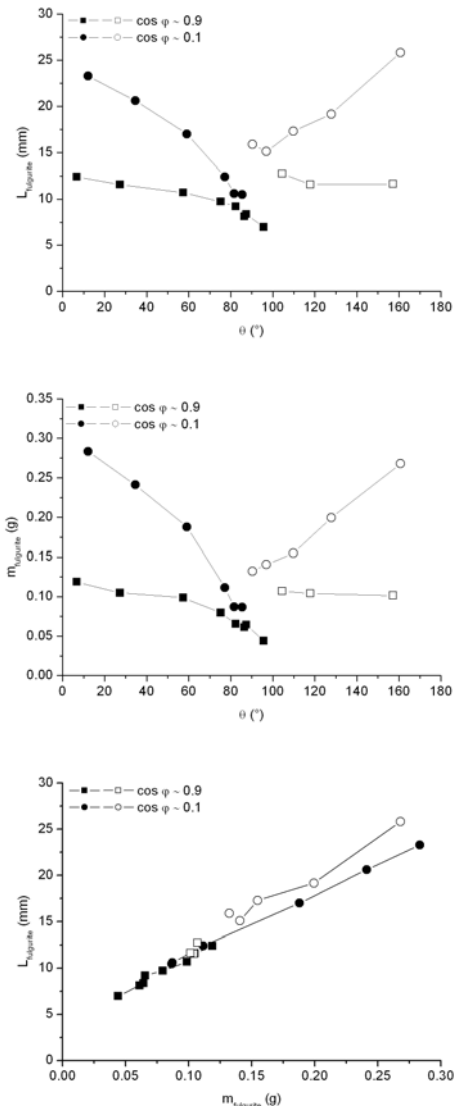


Fig. 8: Evolution of the length and the mass of the fulgurite versus the closing angle and for the two power factors.

5. Conclusion

We have given the first results obtained with an A.C. 100 kVA power station appropriate to perform fuse tests inside an academic laboratory. These results clearly show that fuse tests can be performed with the same conditions as for industrial ones at the condition that the experimental fuse is fitted by

taking into account the specificities on the industrial fuse.

The influence of the closing angle has been shown for two power factors, $\cos \varphi \sim 0.9$ and $\cos \varphi \sim 0.1$. These values have been chosen to test our power station in the case of two limit cases, respectively the resistive and the inductive case.

The analysis of these measurements must be improved by taking into account the energy (Joule, inductive) as far as it has been shown that for example the morphometric properties can strongly influence the dissipation of the energy brought by the fault current.

Acknowledgements

We thank both for their financial support and their help through many discussions, Mr. J.L. Gelet and Mr. T. Rambaud from Ferraz Shawmut, Mr. J.C. Perez Quesada from Mesa, and Mr. F. Gentils from Schneider Electric.

References

- [1] W. Bussière, P. Bezborodko, Measurement of time-resolved spectra using a new experimental arrangement, *J. Phys. D: Appl. Phys.*, 32, 1693-1701, 1999
- [2] W. Bussière, Influence of sand granulometry on electrical characteristics, temperature and electron density during high-voltage fuse arc, *J.Phys.D:Appl. Phys.* 34, pp 925-935, 2001
- [3] W. Bussière, P. Bezborodko, R. Pellet, Spectroscopic study of a cutting electrical arc in HBC fuse, Proceedings of the 6th Icefa (IEN Galileo Ferraris, Torino, Italy), 20-22 Sept., pp 113-118, 1999
- [4] W. Bussière, Estimation of the burn-back rate in high breaking capacity fuses using fast imagery, *J.Phys.D:Appl. Phys.* 34, 1-10, 2001
- [5] D. Rochette, W. Bussière, Pressure evolution during HBC fuse operation, *Plasma Sources Science and Technology*, 13, 293-302, 2004
- [6] W. Bussière, D. Rochette, G. Velleaud, T. Latchimy, J.L. Gelet, F. Gentils, J.C. Perez Quesada, T. Rambaud, and P. André, A specific test device for HBC fuses. Influence of the closing angle and the power factor, Submitted to *IEEE Trans. Mag*, Ref. TMAG-07-07-0225, 2007
- [7] D. Rochette, W. Bussière, R. Touzani, S. Memiaghe. G. Velleaud, P. André, Modelling of the pre-arcing period in HBC fuses including solid-liquid-vapour phase changes of the fuse element, Proceedings of the 8th Icefa (Blaise Pascal University, Clermont-Ferrand, France), 10-12 Sept., Session III, Part I, 2007
- [8] P. André, J. Aubreton, W. Bussière, M.F. Elchinger, S. Memiaghe, D. Rochette, Basic Data: Composition, Thermodynamic Properties and transport Coefficients applied to fuses, Proceedings of the 8th Int. Conf. on Electric Fuses and their Applications (Blaise Pascal University, Clermont-Ferrand, France), 10-12 Sept., Session III, Part I, 2007
- [9] P. André, W. Bussière, D. Rochette, Transport coefficients of Ag-SiO₂ plasmas, To be published in *Plasma Chemistry and Plasma Processing*, DOI. 10.1007/s11090-007-9086-y, 2007
- [10] W. Bussière, P. André, Evaluation of the composition, the pressure, the thermodynamic properties and the monatomic spectral lines at fixed volume for a SiO₂-Ag plasma in the temperature range 5,000 K – 25,000 K, *J. Phys. D: Appl. Phys.*, 34, 1657-1664, 2001.
- [11] M.A. Saqib, A.D. Stokes, P.J. Seebacher, Pressure inside the arc channel of a high-voltage fuse, Proceedings of the 6th Int. Conf. on Electric Fuses and their Applications (IEN, Torino, Italy), 20-22 Sept., 83-88, 1999.
- [12] M.A. Saqib, A.D. Stokes, B.W. James, I.S. Falconner, Arc temperature measurement in a high-voltage fuse, Proceedings of the 6th Int. Conf. on Electric Fuses and their Applications (IEN, Torino, Italy), 20-22 Sept., 107-112, 1999

USING A PARALLEL RESONANCE CIRCUIT TO MEASURE TIME-CURRENT CHARACTERISTICS OF HIGH VOLTAGE CURRENT-LIMITING FUSES

Cai Jiong^[1], Wang Jimei^[2]

Hangzhou Boda Electrical Co.Ltd^[1], Hangzhou P.R.China, cjiell@163.com
Xi'an Jiaotong University^[2], Xi'an P.R.China, jmwang@mail.xjtu.edu.cn

Abstract: This paper describes the peculiarities of a parallel resonance circuit to measure time-current characteristics of high voltage current-limiting fuses. The principle of construction of this circuit and the method of measuring time-current characteristics of fuse are introduced. Finally, how to design power condensers and high-current reactor is described.

Keywords: parallel resonance circuit, current-limiting fuse.

1. Introduction

In general, fuse manufacturers may necessarily have a large capacity of single-phase power transformer for determining the pre-arc time-current characteristics of current-limiting fuses. In addition at the same time they correspondingly need a large power source. By using the new test equipment for high-voltage current-limiting fuses not only produce a low price with using a low capacity single-phase power transformer, but also doesn't need a large power source. The manufacturer can easily undertake the pre-arc time-current characteristics of current-limiting fuses.

2. Basic Circuit of Parallel Resonance

The basic circuit of parallel resonance is shown in Fig.1 consists of two parts: AC power source U and a parallel resonance circuit that is composed by capacitor C and inductor L . The peculiarity of the parallel resonance circuit would be as follows. Fig.2 shows the vector diagram of currents of capacitor C and inductor L . I_c is a capacitive current vector which is leading the voltage vector U , an angle 90° and I_l is an inductive current vector which is

lagging the voltage vector U , an angle of 90° . Due to the inductive impedance Z_l is equal to the capacitive impedance Z_c , namely resonance occurs to the circuit, the current of the capacitor is equal to the current of inductor L . Because their vector is in opposite, so no current comes from source. Due to they're being some dielectric loss in the capacitive and some resistance loss in the inductor. In this time, there is a small amount current supplying from source only.

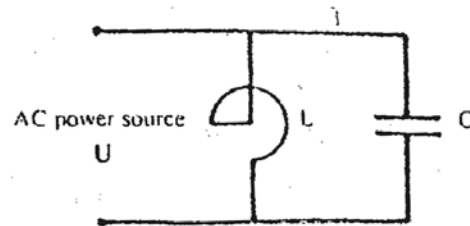


Fig. 1: Basic circuit of parallel resonance

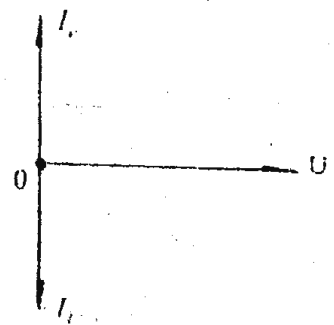


Fig. 2: Vector diagram

3. Test Circuit and Procedure

(a) Test Circuit

The test circuit of pre-arc time vs. prospective current characteristics of high-voltage current-limiting fuses

are as shown in Fig.3. In this Figure. U—A.C. Source of 50Hz, 220/380V selecting current 50~100A; A—low voltage automat circuit breaker, 220/380V, 30~40A; T_1 —voltage regulating transformer, input 220/380V, output 0~1200V; C—capacitor, rated voltage 1200V, 18000 μ F, L—inductor, 1200V, 0.56mh; F—fuse sample, K—link switch, A—ammeter with current transformer of 5000/5; FL—shunt with a

(b) Testing Procedure

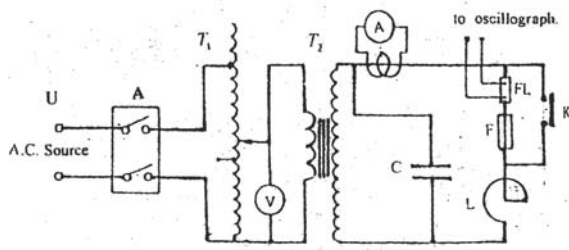


Fig .3: Test circuit for prearc time v.s. prospective current characteristics of high voltage current-limiting fuses

(1) Set voltage regulating transformer T_1 to zero voltage position, link switch K in closed position, and connect fuse sample F.

(2) On low voltage automat circuit breaker A and observe voltmeter V, indicate in zero voltage.

(3) Increase voltage to a given value. (For example. if a rated current of fuse sample is 250A, look at Table 1. or Fig.4 when prearc time is at 0.1s and the prospective current is 3100A, then rise up voltage by voltage regulating transformer to 3100A which is read from ammeter, and open link-switch immediately. We can read actual values of prearc time against prospective current from oscillograph.

(4) All switches and control devices return to original position, then for preparing next test of a same rated current new fuse sample.

Table 1. Prearc time v.s. prospective current datum from Fig.4

Time	Rated current of fuse element									
	40A	50A	63A	80A	100A	125A	160A	200A	250A	400A
0.1 s	320	420	560	770	970	1250	1600	2450	3100	5300
1s	200	270	330	460	560	700	920	1400	1800	3900
10s	150	200	250	330	390	490	620	890	1150	2700

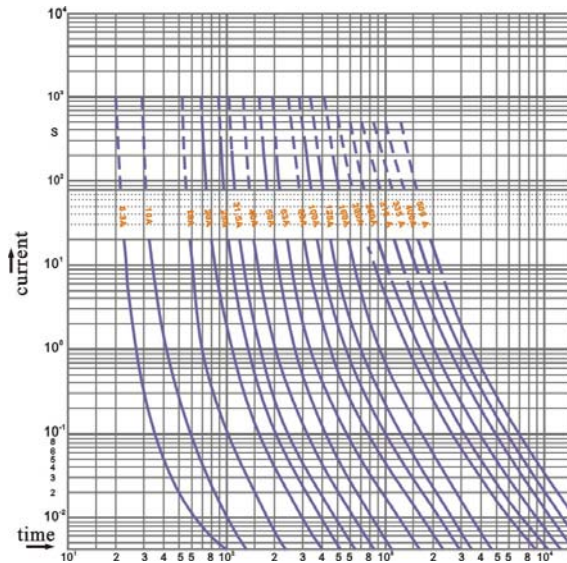


Fig. 4 “Prearc time v.s. prospective current curves” from SIBA

4. Determination of Parameters of Testing Devices

According to 400A rated current of SIBA fuse to estimate the parameters of testing devices for prearc time v.s. prospective current characteristics as follows

(1) Parameters of Power Capacitor

The capacity of power capacitor is

$$C = \frac{I_c}{2\pi f \cdot U_c} = \frac{5300}{2\pi(50)(1000)} = 0.1687F = 16870\mu F$$

where

I_c —Discharge current, 5300A (prearc time=0.1s)

U_c —Applied voltage, 1000V

Selected 100 units of power capacitors in parallel. Each of them is 180 μ F. Now we select the discharging current to

$$5300 \times (180.0/168.7) = 5650A$$

(2) Parameter of Reactor

Reactance of reactor is

$$L = \frac{U_1}{2\pi f \cdot I_1} = \frac{1000}{2\pi(50) \cdot (5650)} = 0.000563H = 0.56mh$$

The construction of reactor is a dry type non-iron core.

(3) Link-switch

Link-switch is a single-phase vacuum contactor of 5000V and 1000A.

(4) Low voltage automat circuit breaker is a single or three phase mold-circuit breaker of 380V or 500V, 100A.

(5) Voltage regulating transformer is a single-phase of input 220/380V, output 0~380V or 450V.

(6) Voltmeter

Voltmeter is a panel type of 100V~124V with 1000/100 potential transformers.

(7) High voltage oil-immersed power transformer

A single-phase oil-immersed power transformer of input voltage 220/440V. output voltage 0~1100V with 15kVA is used.

(8) Ammeter

An ammeter is a panel type of 7.5A with low voltage current transformer 5000/5 is used.

(9) Memorize oscilloscope

Two canals memorize oscilloscope with printed device.

5. Design and Calculation of Reactor

In the most saturation, reactor is designed and manufactured by the manufacture it-self.

The process of design and calculation steps are as follows. According to basic parameters, the construction and dimensions are shown in Fig.5. The calculation formula is from U.S.S.R reference^[1].

The average diameter and hight of each coil respectively D=50cm, W=4.5cm. turns of coil

$n=5$, total turns $N=5 \times 8=40$ gap between coils $d=1\text{cm}$, thickness of coil. $B=(0.5+0.2) \times 5=3.5\text{cm}$, Total height of reactor is $h=7 \times d+8 \times w=7 \times 1+8 \times 4.5=7+36=43\text{cm}$.

$$L_1 = 10.5 N^2 D \left[\frac{D}{2(h+d)} \right]^{3/4} \times 10^{-6} = 0.681 \text{mH}$$

The calculation value 0.681mH is large than original given value 0.53mh, it may be regulated by gaps distance d between reactor coils to satisfy given value of 0.53mh.

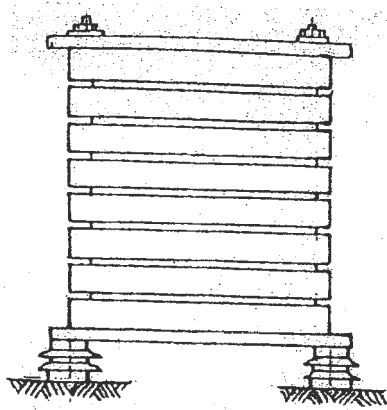


Fig. 5 Lay out of reactor

(1) Calculation of reactor coil

Sketch of coil is shown in Fig.6. Outer diameter of coil is $D_w=53.5\text{cm}$, Inner diameter of coil is $D_n=46.5\text{cm}$. Section of coil is $A=5\text{mm} \times 40\text{mm}$. Current density of coil is

$$J = I_n/S = 5650/200 = 28.25 \text{a/mm}^2.$$

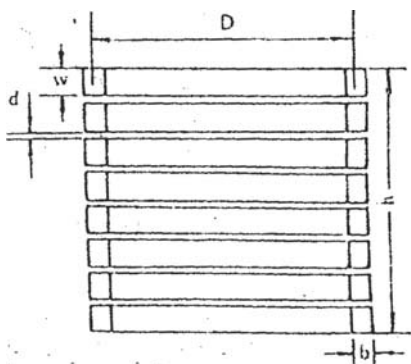


Fig. 6 Sketch of coil

Length of reactor coil is $L = (50\pi \times 5 + 14) = 799.4 \approx 800\text{cm} = 8\text{m}$

Weight of coil is $W = 800 \times 0.5 \times 4 \times 8.9 \times 10^{-3} = 14.5\text{kg}$. Total weight of 8 coils is $W_T = 14.5 \times 8 = 116\text{kg}$

(2) Insulation of coil arrangement

Fig.7 shows a section view of reactor coil insulation between turns of reactor coil is 0.1mm of PTPE trap with 5 layers.

The total thickness is 1mm. Then this 5 layers coil is tied by white cotton trap with 2 over lap layers, the thickness about 1.5mm. Final this coil is treated by varnish in vacuum oven.

(3) Check by Dynamic force

To prevent reactor coil deformation under large current passing through coil, laying out 8 rods around in coil as shown In Fig.8.

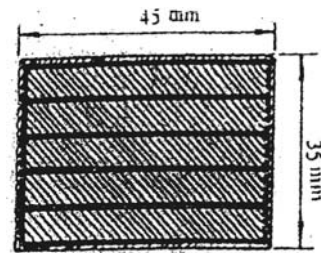


Fig. 7 Section view of coil

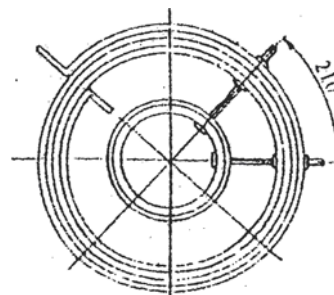


Fig. 8 Supporting of reactor coil

According to reference^[1], we can calculate dynamic force per cm. As using following formular

$$F = \frac{q}{L} \sqrt{\frac{24\sigma^3}{E}}$$

where

q —section area of outer layer turn of reactor coil, $4 \times 0.5 \text{ cm}^2$

L —distance between outer layer turn of reactor coil, $L = 53.5\pi/8 = 21 \text{ cm}$

σ —permit tensile strength of copper, 1600 kg/cm^2

E —modulus of elasticity of copper, $1.13 \times 10^6 \text{ kg/cm}^2$

The dynamic force under coil turn is

$$F = \frac{4 \times 0.5}{21} \sqrt{\frac{24 \times 1600^3}{1.13 \times 10^6}} = 28.1 \text{ kg/cm}$$

According to reference^[1], we can calculate max. current under above dynamic force, 28.1 kg/cm .

$$\begin{aligned} I_m &= 10^4 \sqrt{\frac{F \times h}{\beta}} = 10^4 \sqrt{\frac{28.1 \times 43}{10}} \\ &= 110 \text{ kA (peak)} \end{aligned}$$

h — height of reactor.

β — from reference[1], Table 12-8.

The value of 110 kA is more than the actual value of $5.65 \times \sqrt{2} = 8 \text{ kA}$

6. Conclusion

Parallel resonance circuit method is a best way to obtain pre-arc time against prospective current characteristics curve. Manufacturers of fuses can easily set up this installation.

References

- [1] MUAUAOB B.B. "Calculation and design of high voltage apparatus" U.S.S.R. 1950
- [2] CUPOTHOKUU A.U "High voltage Technique" U.S.S.R 1951
- [3] Wang Jimei, "High voltage A.C. Fuses" Xi'an Jiaotong University Publishing House. China. 2000

FAULT CURRENT LIMITERS BASED ON HIGH TEMPERATURE SUPERCONDUCTORS

Eleonora DARIE⁽¹⁾, Emanuel DARIE⁽²⁾

⁽¹⁾ Technical University of Civil Engineering Electrotechnical Department, Pache Protopopescu 66, Sector 2, Bucharest, Romania, eleonora_darie@yahoo.com

⁽²⁾ Police Academy, Privighetorilor 1-2, Sector 1, Bucharest, Romania, edarie@yahoo.com

Abstract: The Fault-current limiters based on high temperature superconductors offer a solution for controlling fault-current levels on utility distribution and transmission networks. These fault current limiters, unlike reactors or high-impedance transformers, will limit fault currents without adding impedance to the circuit during normal operation. Development of superconducting fault-current limiters is pursued by several utilities.

Keywords: high-temperature superconductors, faults, feeder, current limitation, system protection, fault current limiter.

1. Introduction

The Fault current limiter (FCL) is a power apparatus suppressing the fault current by generating the limiting impedance when the fault occurs into electric power system. For fault current limiter, it is important to choose the optimum limiting impedance properly according to the purpose of the introduction of FCL, the installed location of the fault current limiter in the power system [2], [3]. Electric power system designers often face fault-current problems when expanding existing buses. Larger transformers result in higher fault-duty levels, forcing the replacement of existing bus work and switchgear not rated for the new fault duty. Alternatively, the existing bus can be broken and served by two or more smaller transformers. Another alternative is use of a single, large, high-impedance transformer, resulting in degraded voltage regulation for all the customers on the bus. The classic trade off between fault control, bus capacity, and system stiffness has persisted for decades.

Superconductors offer a way to break through system design constraints by presenting the impedance to the electrical system that varies depending on operating conditions. The development of high temperature superconductors (HTS) enables the development of economical FCL. Superconducting fault current limiters were first studied over twenty years ago. The earliest designs used low temperature superconductors, materials that

lose all resistance at temperatures a few degrees above absolute zero.

Operating characteristics of superconducting fault current limiter (SFCL) are shown in Figure 1, where: i_1 – expected fault current without limiter, i_2 – current limited by SFCL without limiter, i_n – nominal current, t_1 – fault, t_2 – the operation of conventional switch, t_3 – SFCL operation.

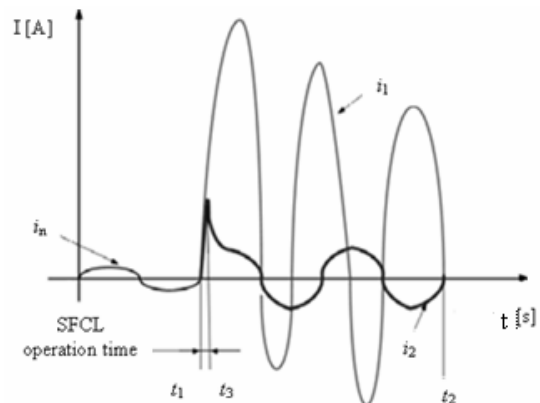


Fig. 1: Operating and currents characteristics of SFCL.

The superconductors' materials are generally cooled with liquid helium, a substance both expensive and difficult to handle.

2. Fault Current Limiter Applications

Fault-current limiters can be applied in a number of distribution or transmission areas. The most direct application of a fault-current limiter is in the main position on a bus (Fig. 2). Benefits of an fault current limiter in this application include the following: the larger transformer can be used to meet increased demand on a bus without breaker upgrades, the low impedance transformer can be used to maintain voltage regulation at the new power level, reduced fault-current flows in the high voltage circuit that feeds the transformer, which minimizes the voltage dip on the upstream high-voltage bus during a fault on the medium-voltage bus.

The fault current limiter can be used to protect individual loads on the bus (Fig. 3). The selective application of small and less expensive limiters can

be used to protect old or overstressed equipment that is difficult to replace, such as underground cables or transformers in vaults.

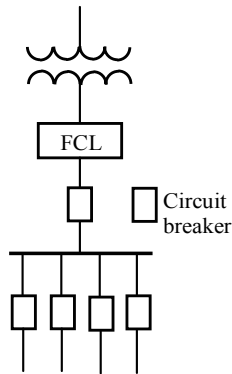


Fig. 2: Fault-current limiter in the main position. The fault-current limiter FCL protects the entire bus.

Such a limiter would require only a small load current rating but would deliver the following benefits: separate buses can be tied together without a large increase in the fault duty on either bus, during a fault, a large voltage drop across the limiter maintains voltage level on the unfaulted bus, the paralleled transformers result in low system impedance and good voltage regulation; tap-changing transformers can be avoided, excess capacity of each bus is available to both buses, thus making better use of the transformer rating.

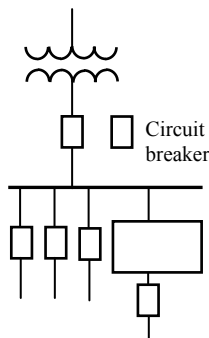


Fig. 3: Fault-current limiter in the feeder position. The fault-current limiter FCL protects an individual circuit on the bus. Underrated equipment can be selectively protected as needed in this manner.

The FCL find numerous applications as it offers these benefits: avoid equipment damage; avoid equipment replacement, higher breaker rating; use lower fault rated equipment, avoid series reactors; avoid split buses, opening bus-tie breakers; higher system reliability when bus tie breakers are

closed; use lower impedance transformers; reduce voltage dip on adjacent feeders; enhance grid stability.

3. Fault-Current Limiter concepts

3.1. The Series Resistive Limiter

The simplest superconducting limiter concept, the series resistive limiter, exploits the nonlinear resistance of superconductors in a direct way. The superconductor is inserted in the circuit. For a full-load current of I_{FL} , the superconductor would be designed to have a critical current of $2I_{FL}$ or $3I_{FL}$. During a fault, the fault current pushes the superconductor into a resistive state and resistance R appears in the circuit.

The superconductor in its resistive state can also be used as a trigger coil, pushing the bulk of the fault current through a resistor or inductor. The advantage of this configuration, shown in Fig. 4, is that it limits the energy that must be absorbed by the superconductor.

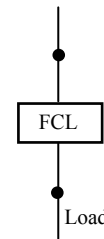


Fig. 4: Fault-current limiter with HTS trigger coil.

The fault-current limiter (FCL) normally is a short across the copper inductive or resistive element Z . During a fault, the resistance developed in the limiter shunts the current through Z , which absorbs most of the fault energy.

The trigger coil approach is appropriate for transmission line applications, where tens of megawatt-seconds would be absorbed in a series resistive limiter. The trigger coil configuration also allows an impedance of any phase angle, from purely resistive to almost purely inductive, to be inserted in the line.

A resistive FCL limits the fault current by its increased resistance when the HTS wire transitions to its normal state during a fault. The key parameters impacting the resistive FCL design are fault current (I_{lim}), fault duration (Δt) and permissible temperature rise (ΔT) of the HTS elements. These variables are related in through the following equations:

$$R = \frac{V_0}{I_{lim}} = \frac{\rho \cdot L}{t \cdot w}; \quad I_{lim} = t \cdot w \sqrt{\frac{C_p \cdot \Delta T}{\rho \cdot \Delta t}} \quad (1)$$

where: R is FCL resistance during fault, V_0 is system rms voltage, L - length of HTS current limiting elements, ΔT - maximum permissible temperature rise, Δt - maximum fault duration (hold time) ρ , t , w - resistivity, thickness and width of HTS, C_p - effective specific heat of HTS and stabilizer.

Solving these equations, one can derive the minimum conductor volume given below for a series FCL. The required conductor volume (Vol) is independent of conductor resistivity.

$$Vol = \frac{I_{lim} \cdot V_0 \cdot dt}{C_p \cdot \Delta T} \quad (2)$$

The series limiter employs a coil in series with the load and limits current by its increased resistance during the current limiting phase. This design is best for a single fault current limiting action, with resetting after the several minutes required cooling it down to its pre-fault temperature.

This FCL requires wire current density, high resistively stabilizer and higher heat removal capability and the cold temperature. It is most suitable for a single fault limiting event with recovery after multiple minutes of cool-down.

3.2. The Inductive Limiter

This concept uses a resistive limiter on a transformer secondary, with the primary in series in the circuit. This concept, illustrated in Fig. 5, yields a limiter suitable for high-current circuits ($I_L > 1000$ A). One phase of the limiter is shown. A copper winding (W_{Cu}) is inserted in the circuit and is coupled to an HTS winding W_{HTS} . During normal operation, the zero impedance is reflected to the primary.

Resistance developed in the HTS winding during a fault is reflected to the primary and limits the fault. The inductive limiter can be modeled as a transformer.

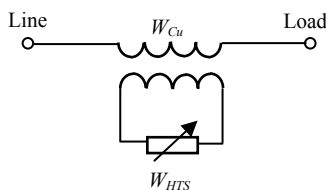


Fig. 5: Inductive fault current limiter.

The impedance of this limiter in the steady state is nearly zero, since the zero impedance of the secondary (HTS) winding is reflected to the primary. In the event of a fault, the large current in the circuit induces a large current in the secondary and the winding loses superconductivity. The resistance in the secondary is reflected into the circuit and limits the fault.

3.3. The Shunt Resistive Limiter

The shunt limiter concept uses a warm resistor (or inductor) in parallel with the HTS coil and this can be bulky. During normal operation, the resistance of the HTS coil is essentially zero and steady-state current flows through it. However, during a fault, if the resistance of the HTS coil increases to a high enough value, most of the current is diverted through the warm resistor. This limiter could be designed to withstand several fault limiting events within a safe upper limit of the HTS coil temperature. Once the fault is cleared, steady-state current can continue to flow without excessive heating in the HTS coil because it remains in the superconducting temperature range. Preliminary analysis shows that the shunt limiter HTS coil requires about 10 % more HTS wire than the series limiter.

The shunt limiter employs an inductor in parallel with the HTS coils. Once the HTS coil transitions to its normal state, fault current is limited by the impedance of the external inductor. An advantage of the shunt limiter is that with proper design, it could withstand multiple closely timed current limiting events.

3.4. The Series-Parallel Resistive Limiter

As shown in Figure 6, the fault-current limiter is formed by connecting four superconducting coils in a series-parallel configuration so the total inductance is minimized.

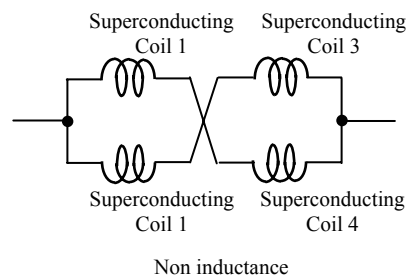


Fig. 6: Configuration of superconducting coils.

One set of coils is used for each phase of the device, and limiting is accomplished by quenching the coils.

4. Modelling

4.1. Generalities

The model uses data from superconducting YBCO samples thick films on YSZ substrate. The data takes the form of E (electric field) - J (current densities) as well R (Resistivity) - T (Temperature) characteristics to room temperature and beyond.

The current waveform and other system parameters such as superconductor temperature and magnetic field are calculated by an iterative process. Due to the nature of FCL devices, thermal conduction into the substrate is considered and a prediction of the material temperature throughout the limiting period is made. The superconductor is considered as a single homogenous element at present; future revisions will include some degree of inhomogeneity into the model in order to ascertain the significance of manufacturing imperfections. Additionally, depending on configuration, the magnetic field applied to the material may change. Both factors influence the voltage drop across the FCL and hence the current through it. Thus one limiting cycle involves an excursion over the E - J - B - T plane. To attempt to predict the current-time waveform analytically would be difficult if not impossible. The superconductor is modeled in Matlab - Simulink within the overall model as a single block with three inputs: J , B and T (corresponding to the current density, magnetic field and temperature) and two outputs corresponding to the specific heat capacity (modeled as a function of temperature) and electric field strength E appearing across the sample. The line and load impedances are modelled as lumped parameter models using Laplace transform to represent the transfer functions relating to the imaginary and real parts of their impedances [1].

For example, a line with 0,1 ohms resistance and 1 mH inductance will have an impedance of $0,1+0,001 j\omega$, where j is the complex operator. The laplacian operator $s=\sigma+j\omega$ allow us to model the line transfer function as:

$$\frac{1}{sL + R} \quad (3)$$

4.2. Heat flow

Heat flow through the FCL is modelled in two ways: Heat flow from top surface of film and Heat flow into substrate.

The first term is modelled by a simple function relating to the temperature difference between the film and the liquid nitrogen cryogen. The equations vary according to the nucleate or film boiling regime, which can be predicted from the temperature difference between the material surface and the cryogen [3].

The flow into the substrate is modelled as a 20 element diffusion model. This is achieved in Simulink by the use of a state space representation in order to fit in with the laplacian derivative block format expected in Simulink [4].

The addition of an external magnetic field is used in practice to overcome material non-

homogeneity by helping the whole material past the superconducting to normal transition (non-homogeneity is a major problem in some designs of limiter). The signal can be derived from other points in the model for a proportional connection (B proportional to I for series connected coil, or B proportional to E across the superconductor for a coil connected in parallel with the FCL element.). A switch element can be introduced in the case of a triggered coil type design (where external field is turned on suddenly as soon as a fault is sensed).

Coil inductance is, as in the case of line inductance, modelled by the complex term of a Laplace transform.

4.3. Results of the model

The fault simulation begins with the current I_n flowing for at least one whole cycle. This is 20ms for a 50Hz supply frequency. The fault is then initiated by instantly lowering the load impedance to that expected for a short line fault (SLF). In this case the SLF condition corresponds to $I_f = 200$ A peak. Figure 7 shows the current – time waveforms for the first 50 ms of the simulation. The cross sectional area has been kept constant and the limiter lengths are between 3,2 cm (short limiter) and 400 m (long limiter).

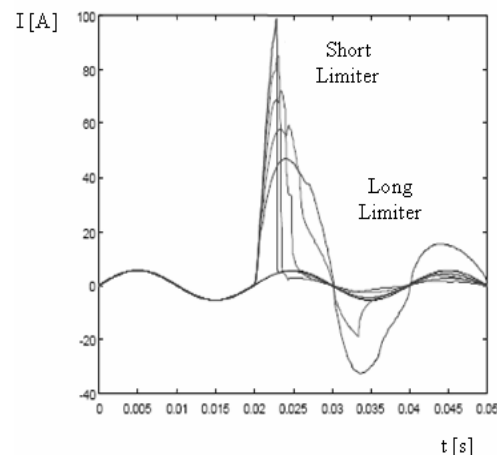


Fig. 7: Current and time for different limiter lengths.

From Figure 8 shows the resultant temperature rise for the same range of limiter sizes.

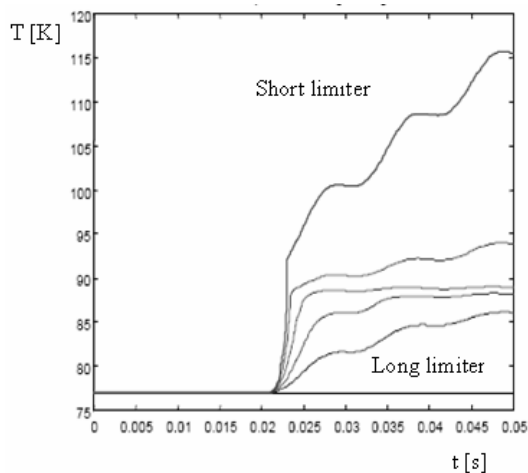


Fig. 8: Predicted temperature rise over fault period.

5. Conclusions

Superconductors offer a way to break through system design constraints by presenting the impedance to the electrical system that varies depending on operating conditions [3].

Resistive fault current limiter limits the fault current by its increased resistance when the high temperature superconductors wire transitions to its normal state during a fault.

The series limiter employs a coil in series with the load and limits current by its increased resistance during the current limiting phase. This FCL requires wire current density, high resistively stabilizer and higher heat removal capability and the cold temperature. This FCL is best for a single fault current limiting action, with resetting after the several minutes.

The shunt limiter employs an inductor in parallel with the high temperature superconducting coils. Once the high temperature superconducting coil transitions to its normal state, fault current is limited by the impedance of the external inductor. The shunt limiter could withstand multiple closely timed current limiting events.

The computer model provides useful information about the predicted current-time waveforms for homogenous film type limiters. The problems associated with material in homogeneity will be addressed in the very near future.

References

- [1] T. Jankowski, S. Kozak. "Properties comparison of superconducting fault current limiters with closed and open core", IEEE Trans. Appl. Superconduct. Vol. 13, pp. 2072-2075, 2003.
- [2] H. Kim M., H. Kang. "A variation of impedance of a high - T_c superconducting fault limiter with an open core", IEEE Trans. Appl. Superconduct. Vol. 12, pp. 446-489, 2002.
- [3] S Kozak., "Measurement of static characteristics of inductive superconducting fault current limiter". Seminar, Applications of Superconductors, Lublin, 2001, p. 111-120.
- [2] L Salasoo: "Superconducting fault current limiters". Electronics Eng., Vol. 20, pp. 710-717, 2000.

FACING GLOBAL-WARMING, MANUFACTURERS ARE INVITED TO THINK TO ECO-DESIGN. ENVIRONMENTAL PRODUCT DECLARATION ALSO CONCERNS FUSES

Jean-Louis GELET⁽¹⁾, Joël GAUCHON⁽²⁾

(1) FERRAZ-SHAWMUT, Rue Vaucanson, 69720-St-Bonnet de Mure. France.
Tel. 33 (0)4 72 22 66 30. jean.louis.gelet@fr.ferrazshawmut.com

(2) FERRAZ-SHAWMUT, Rue Vaucanson, 69720-St-Bonnet de Mure. France.
Tel. 33 (0)4 72 22 69 92. joel.gauchon@fr.ferrazshawmut.com

Abstract :

Global-warming doesn't suffer any doubt today. Nevertheless important are the debates concerning its amplitude, effects and causes. In front of this problem, International Authorities make efforts for a global legislation. In 1992, conclusion of the Summit of Rio on behalf of United Nations was a Declaration on Environment and Development. Later, in 1998, the Kyoto-Protocol to United Nations Framework Convention on Climate Change was adopted by most of industrial countries. In despite of this, some stay as opponents. Anybody knows who they are.

As a follow up of Kyoto-protocol, European Community stated three orientations for electrical products. First is WEEE, which specifies conditions for the end of life of electrical products. Second is RoHS, which gives rules for restriction of hazardous substances. And third concerns directives for eco-design.

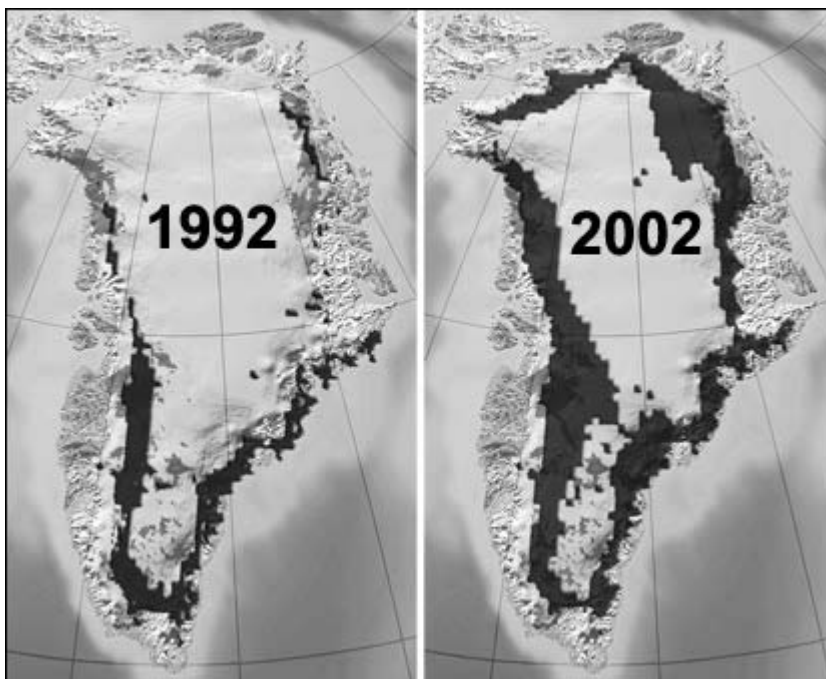
EC-economical experts estimated that 80% of global environmental impacts of products are deterred as soon as design-phase. Then, it has been proposed to define a method for carrying out this estimation at the level of each single product. This should take the concrete form of an Environmental Product Declaration (EPD), based upon several criteria such as use of renewable or non-renewable resources, electricity consumption, emission related impacts and waste.

For the time being eco-design is not subjected to legal obligations. But manufacturers could have great interest to follow this way. FERRAZ-SHAWMUT uses the help of a so called software "EIME", from CODDE-company for the determination of Environmental-Profiles of his products. The purpose of this paper is to come back to the environmental considerations from legislation-point of view and to compare the Environmental Profiles of two fuse-ranges.

1. ECO-CONCEPTION AS A PART OF A GLOBAL ANSWER TO EARTH-WARMING :

An Unquestionable Statement

Numerous figures may illustrate how much today's human activities impact the Earth. For example, man today burns within one single day, resources that nature took 10 000 days for building up. In France, statistics demonstrate that each inhabitant thoughts out 1 kg of waste per day, which is twice what he did 40 years ago, and equivalent figures are available for all industrial countries. As a consequence, our planet is under the menace of a global heating. Estimations have been carried out, announcing that during the 20th century, the mean-temperature of the earth increased of about 0.6°C. For the 21st century, the less alarmist forecasts concern temperature-increase of 2°C, with dramatic effects on the polar ice-pack and mountain-glaciers leading to an elevation of the see-levels.



First comes to the mind the fuel-consumption during the life of the product. But this is not the only impact over the environment. Indeed raw material-consumption, water-consumption, through out in water, through out in air, various kinds of wastes, also modification of natural environment and life-conditions are very significant impacts. And they will occur at any stage of the life-cycle of the product, from manufacturing to disassembling.

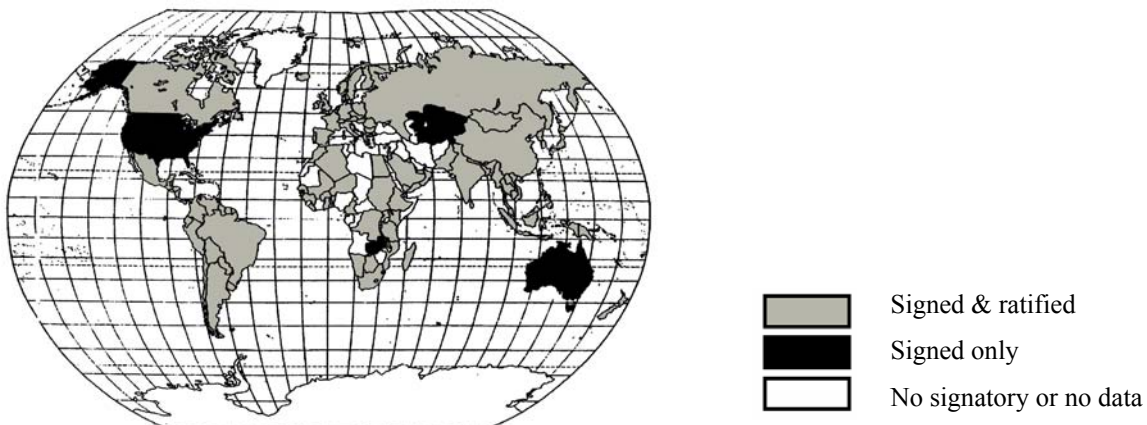
Earth-Summit of Rio –1992

From 3rd to 14th June 1992 took place at Rio de Janeiro, in Brazil, the United Nations Conference on Environment and Development (UNCED), commonly known as Earth-Summit of Rio. More than 2,400 senior officials from 179 governments attended to the meeting. They were joined by hundreds of officials from United Nations organizations, municipal governments, business, scientific, non-government and other groups. Nearby, the '92 Global Forum held a series of meetings, lectures, seminars and exhibits on environment and development issues for the public. This drew 18,000 participants from 166 countries, as well as 400,000 visitors. There were 8,000 journalists covering the Rio meetings, and the results were seen, heard and read about around the world.

This Conference has been concluded by the adoption of 27 principles, called “Rio Declaration on Environment and Development” which introduced the idea of sustainable development, i.e. *development that meets the needs of the present without compromising the ability of future generations to meet their own needs*. Moreover the Conference gave the opportunity to adopt an actions-plan for the 21st century, called “Action 21” or “Agenda 21”, which enumerate some 2500 recommendations for the concrete setting of the principles of the declaration.

Kyoto Protocol – 1998

Five years later, from December 1 through 11, 1997, more than 160 nations met in Kyoto, Japan, to negotiate binding limitations on greenhouse gases for the developed nations, pursuant to the objectives of the Framework Convention on Climate Change of 1992. The outcome of the meeting was the Kyoto Protocol, in which the developed nations agreed to limit their greenhouse gas emissions, relative to the levels emitted in 1990. Only Parties to the Convention that have also become Parties to the Protocol (i.e. by ratifying, accepting, approving, or acceding to it) will be bound by the Protocol’s commitments. 171 Parties have ratified the Protocol to date. Of these, 35 countries and the EEC are required to reduce greenhouse gas emissions below levels specified for each of them in the treaty. The Convention on Climate Change sets an overall framework for intergovernmental efforts to tackle the challenge posed by climate change. It recognizes that the climate system is a shared resource whose stability can be affected by industrial and other emissions of carbon dioxide and other greenhouse gases. The Convention enjoys near universal membership, with 189 countries having ratified, even if a polemic is still running with USA and Australia denying to ratify the protocol.



European Community Directives :

Respect of commitments taken through the Kyoto Protocol is one of European Economic Community prerogatives. EEC rules establish that directives are edited by the Community and then turned to laws by each of the twenty-five members. Then, EEC stated three orientations for electrical products. First is WEEE (Waste of Electrical and Electronic Equipments), which specifies conditions for the end of live of electrical products. Second is RoHS (Restriction of use of Hazardous Substances), which gives rules for restriction of six hazardous substances. And third concerns directives for eco-design of energy-using-products (EUP). Last directive will set the base for reduction of the environmental impact of products, for restriction of energy-consumption, and for information of consumers.

2. THE INS AND OUTS OF ECO-CONCEPTION :

Regulations and Economical Interests

At first, regulations could be considered as very compelling for industrials. This is true as long as they just look at the prohibition aspects of regulations. But, if they could admit that regulations bring a new cards-dealing,

especially within the over-concurrential globalisation-world, large opportunities for developments will be offered to them. Respect of regulations and economical interests are not inconsistent.

Global Impact

Studies carried out during last 10 years concluded that the most significant environmental aspect of electrical and electronic products obviously concerns their energy-consumption when in use. It has been calculated that energy-consumption may reach 80% of global environmental impacts. This ratio increases with high life-duration of the product. But other environmental impacts are not allowed to be neglected. Any product interacts with its environment because of its design. The choices of the materials, the manufacturing-processes and even the technological principals highly deter effects on environment. Also during manufacturing, because of energy-consumption, raw materials and wastes and during conditioning and transportation, effects are realities. And finally, when the product is at the end of its life-cycle, it has to be eliminated. Once again, it has effects on environment by the wastes, the rejected substances, the energy spent for treatment and eventually the place needed for storing hazardous or unreusable materials.

Then, it becomes very important to manage the problem from a global point of view, otherwise pollution should be transferred from one step of the life-cycle to another one. Systemic approach must be preferred in order to minimize the total impact of the product.

A New Syntagm : Eco-Conception

The syntagm “Eco-Conception” or “Eco-Design” has been introduced for underlining that from now, Conception or Design absolutely needs to involve Ecological considerations. Thanks to multicriteria approach of the “Eco-Conception”, manufacturers will investigate new progress-axies, according to available and up-to-date technologies.

A strong idea is that Ecological considerations have not to come after the Conception. But they are fully involved, as well as costs and quality.

Three main classes of impacts

As early as design-step, decisions have to be taken, keeping in mind what will be the impacts on environment all over the life-duration. Three main classes of impacts have to be considered:

- natural resources-consumption : both raw materials and energy have to be preserved,
- water- and air-pollution : emissions of greenhouses gas and ozone layer depletion are the most known of the all alterations of natural phenomena because of industrial activities,
- waste-production : manufacturing-wastes, conditioning-wares and end-of-life goods must be valued and upgraded for reducing disposal-volumes and resources withdrawals.

Ferraz-Shawmut’s Environmental Policy

The Ferraz-Shawmut’s management set internal policy for environmental saving. This policy consists of five axes, which are the frame for reaching and checking the environmental imperatives :

- to act as early as designing new products and processes for environment and personal safety,
- to deliver to customers quality and low environmental impact products,
- to fulfil regular, legal and all other environmental requirements, and contribute to develop them,
- to control and to reduce wastes and uses of toxic materials and to involve recycling-technologies,

- to permanently investigate for solutions which will reduce water-, energy -, raw-materials-consumption and conditioning-wares.

3. THE EIME-METHOD :

The Needs for a Simple and Complete Tool

The syntagm “Eco-Conception” involves the word “Conception”. It means that basically it is a “Conception”, but for being credited as “Eco”, it needs to be seriously fed by”Eco” considerations. The problem is that the specialist who owns the knowledge of “Conception”, whatever is the product, is not a specialist about environmental questions.

Hence, it has been necessary to think to a tool which can help people in charge of the development of products to also be able to take into account environmental aspects. The bill of requirements of such a tool should be briefly expressed as :

- to be usable by non-specialists of environment,
- to be compatible with any existing conception procedures,
- to cover a large range of products,
- at the same time, to be easy and simple to use, and to warrant a complete and exact approach.

Principles of EIME-Method

The EIME (for Environmental Information and Management Explorer or Evaluations des IMpacts Environnementaux)) is a simple and pragmatic tool to model any product. It is a compilation of three modules :

- a database of most representative electrical and electronic industry materials, components, processes which helps you to **model** any product.
- once the product architecture is built, routines which **calculate** the environmental contributions by impact and/or by sub-assembly.
- post-treatments using **graphs** which help to make the best eco-strategic choices.

Database

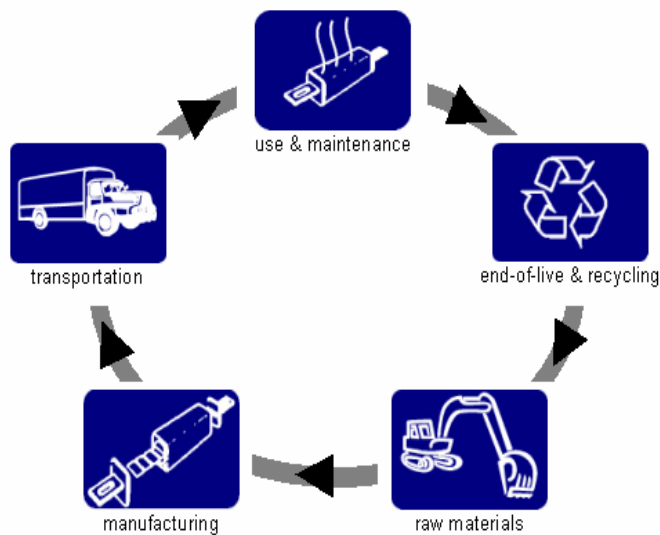
User will find within EIME a database which will help him to describe the product with numerous elementary bricks. These bricks may be :

- components or sub-assemblies, which offer any specific function such as diodes, bearings,...
- materials, such as metals, plastics, papers, filling materials,...
- additional chemical substances used for the manufacturing, but in small amounts, such as glues, lubricants,...
- transformation-processes, such as injection of plastics, machining, welding, plating,...
- connections or bonds, such as clippings, clampings,... without adding any material, these bricks contribute to the final architecture of the product.

For each one of these bricks, the environmental impacts have been evaluated : for example, impacts related to the manufacturing of a kilogram of copper or to the manufacturing of a diode or to the transportation of one ton of filler for one kilometre. By addition of all the impacts of all the bricks of the concerned product, it is possible to reach the potential impacts of the product. About 250 bricks are today available in the EIME-database.

Environmental Contributions

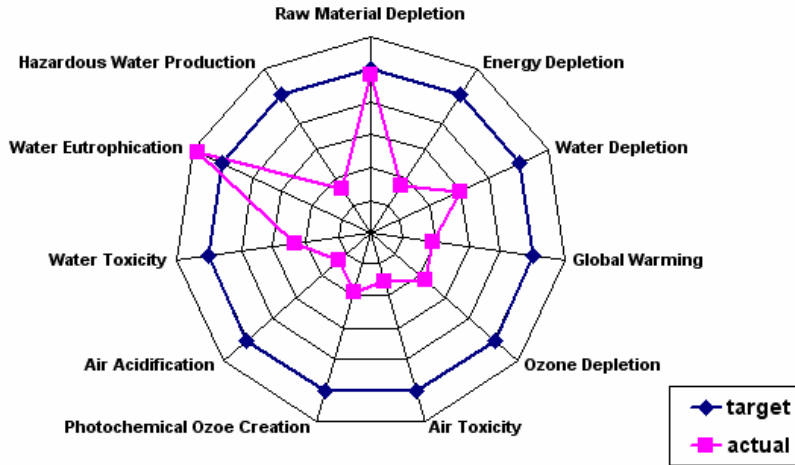
Nevertheless, environmental impacts of a product are not only the mere summation of the impacts of its components. Indeed, after manufacturing, the product will be transported, used, sometimes maintained, and finally eliminated. During each of these stages, there are consumption of material and energy and wastes. This has to be taken in consideration within impacts-evaluation.



- transportation : distance and way of transportation (rail, road, air, sea,...) and also conditioning-wares have to be precise.
- using : we have seen here-above that in general word, energy-consumption represents 80 % of the global impacts.
- end-of-live : the elimination-scenario has to be scheduled by the designer. For instance, some rules concerning the identification of the plastic-parts must be respected. One problem with electrical components such as fuses is that their life-duration is about 10 to 30 years, and it is not possible to know today what will be the recycling technologies at that time.

Environmental Indicators

The IEME-method will explicit the impacts of the products according 11 indicators, such as Raw Material Depletion and Energy Depletion. Afterwards, these impacts are drawn out on a spider-graph and can be compared to a target or to a previous version of the product.

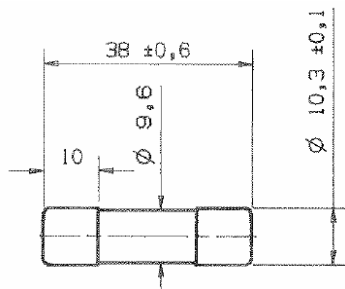


4. ENVIRONMENTAL PROFILES FOR FUSES :

The results of the EIME-method are difficult to analyze from an absolute point of view, specially for people who are not experts in environmental-science. Despite of that, it is possible and even easy to make comparisons between different solutions for a same level of functionalities and characteristics.

Cases of Cylindrical Fuses :

Here-after we will compare for two kinds of fuses, i.e. general purpose low-voltage fuses (gG) and general purpose ultra-fast fuses (gRB), two technologies of manufacturing, mainly regarding the way of connecting the fuse-element on the cup, i.e. soldering and spot-welding.



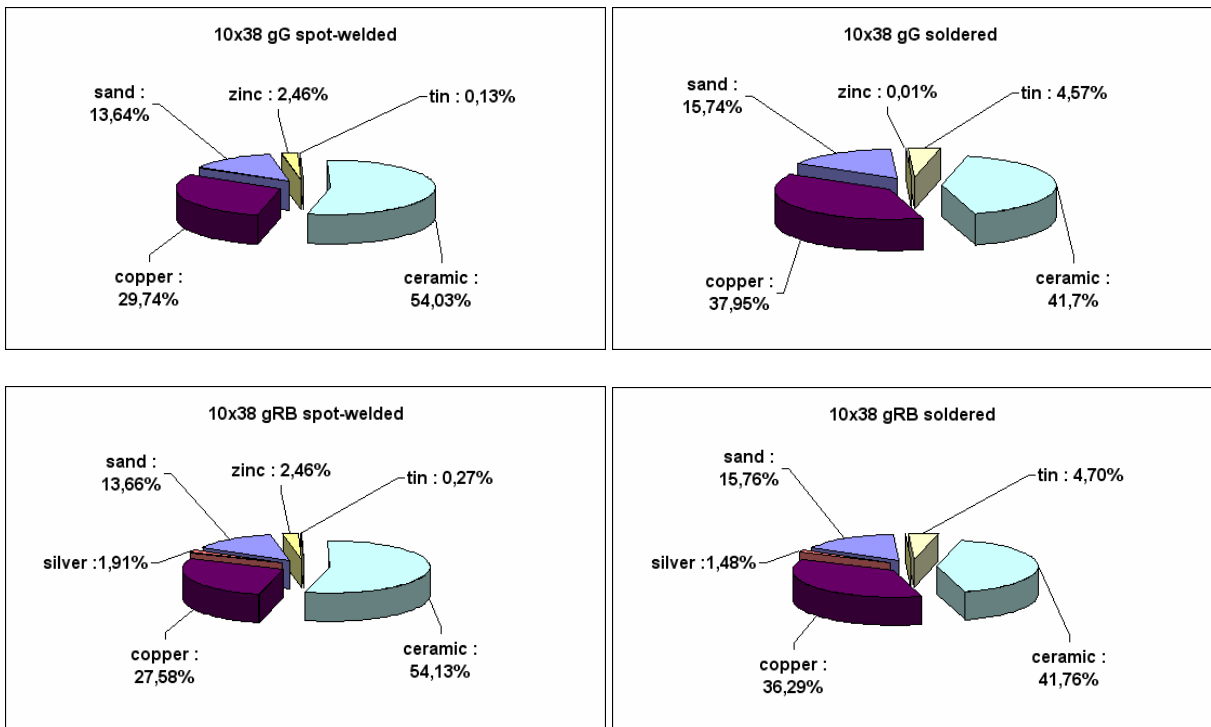
externally, the problem concerns same-size-fuses :

- diameter of ceramic body : 9.6 mm
- diameter of terminals : 10.3 ± 0.1 mm
- length : 38.0 ± 0.6 mm

Comparison of Watt-Losses :

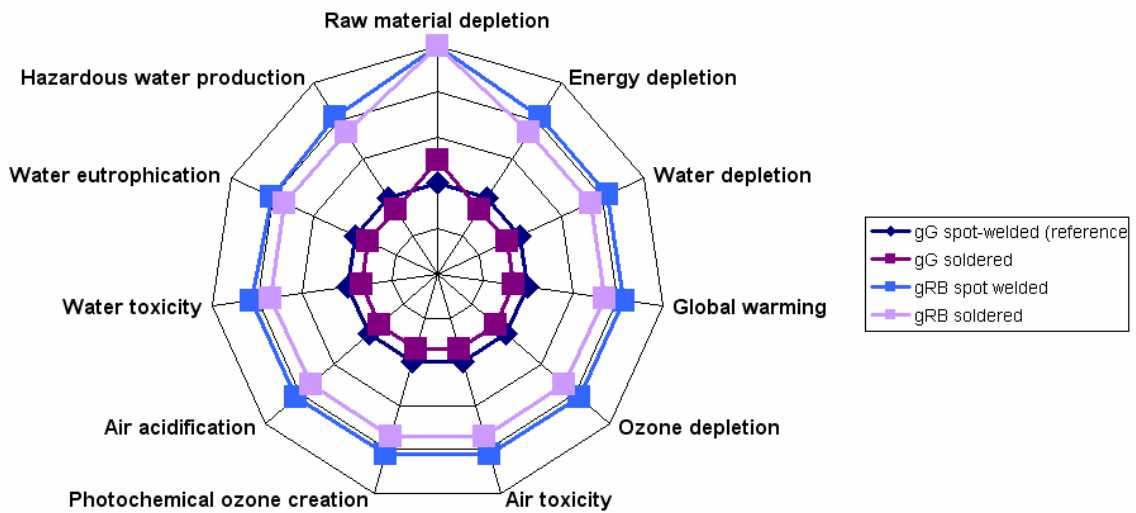
Fuses and Technologies	Watt-Losses at 0.5In
10x38 gG spot-welded	0,6 W
10x38 gG soldered	0,54 W
10x38 gRB spot-welded	1,12 W
10x38 gRB soldered	1,0 W

Comparison of quantities of materials :



Environmental Impacts Spider-Graphs :

Afterwards, EIME-method allows to draw out the environmental-impacts under spider-graphs.



It is clear that for gG-fuses, the soldered solution gives better results for all the points, except for raw material depletion, mainly explained by a higher quantity of copper for the studied solution.

gRB-fuses have bigger impacts. Once more the soldered solution gives better results except for raw material depletion.

5. CONCLUSIONS

The here-above example is very simple and it is clear that it can open large discussions, comparing fuse-solutions - here between low-voltage and ultra-fast fuses – and products offering the same functions, offered by different suppliers. Also interesting should be to compare protection-technologies, for example fuses and breakers.

Unfortunately, for the time being, industrials and especially industrials of electrical and electronic domains, have not achieved the publication of all the environmental profiles of their products. Maybe one reason for that is that they are not aware enough with the EIME-Method. However, this is a very positive way, for a continuous progress, taking an opposite view of compelling aspects of political regulations.

The database is promised to become a universal reference. In France, the GIMELEC (Groupement des Industries de l'Équipement Électrique) is promoting the EIME-Method. GIMELEC created and became the main financial partner of CODDE-company. CODDE is dedicated to be an expert structure for Eco-Conception. Its first aim is to distribute the EIME-software and also to make industrials sensitive to environment and to train them in this way. Through CODDE, companies can get a technical support for a better understanding and a better answer to regulations such as ROHS and WEEE-directives.

CODDE is engaged in an evolutive way, based on all his partners' experiments. Mutual sharing of these experiments will be profitable for any one of the partners, whatever will be his size, from the more little company to the largest group. And any one will be able to evaluate his environmental progresses through the same referential.

REFERENCES

1. Directive 2002/95/EC of the European Parliament and of the Council of 27 January 2003 on the restriction of the use of certain hazardous substances in electrical and electronic equipment (*Official Journal L 037 , 13/02/2003 P. 0019 – 0023*).
2. Directive 2002/96/EC of the European Parliament and of the Council of 27 January 2003 on waste electrical and electronic equipment (WEEE) - Joint declaration of the European Parliament, the Council and the Commission relating to Article 9 (*Official Journal L 037 , 13/02/2003 P. 0024 – 0039*).
3. Linda LESCUYER, Marc JANIN (Sté. CODDE). L'éco-conception de produits électriques et électroniques : enjeux, outils et exemples. (*La Revue 3EI n°43. Déc. 2005*).
4. EIME, an integrated information system for conscious environmental design. (available on www.codde.fr).

TO THE ORIGINS OF FUSES

Jean-Louis GELET

FERRAZ-SHAWMUT, Rue Vaucanson, 69720-St-Bonnet de Mure. France.
Tel. 33 (0)4 72 22 66 30. jean.louis.gelet@fr.ferrazshawmut.com

This paper will open the 8th ICEFA-conference organized by the LAEPT (Laboratoire Arc Electrique et Plasmas Thermiques) and hold in Clermont-Fd from 10th to 12th September 2007. No doubt that many papers of great interest for science and technology of fuses will be presented within the three-days-meetings. No doubt also that every authors and every members will work very conscientiously and very professionally and will make effort for continuing their predecessors' endeavour.

The Organization Committee thought that it could be appreciable for any member to begin the Conference by a general overview upon origin of the fuse and how it was necessarily related with the general history of electricity.

During ICEFA -Conference (International Conference on Electrical Fuses and their Applications) which was hold in Gdansk, in September 2003, Prof. Stokes from University of Sydney introduced his communication as follows :

“Modern electric fuses are marvellous devices for protecting life and equipment from potential power of uncontrolled electricity. Since the coming of electricity in the 1870s, they have been in front line for electrical defence. Indeed, it is fair to say that without the virtually fail-safe protection of the electric fuse there would be no modern electrical industry. Electricity would be regarded as far too dangerous for widespread use.”

Nowadays, the use of electricity and all the devices it makes move is so familiar for us that we are scarcely able to imagine how much difficult was the labour of the inventors who looked for the nature and the effects of electricity.

1.SHALL WE RE-MAKE HISTORY ? :

It is noticeable that between Franklin (1752) and Ampère (1820), seventy years have been necessary to pass from first relevant understandings of the nature of electricity to the formulation of the mathematical equations describing the fundamental laws, especially for that concerns the relationships with magnetism. This is both short and long. Short in comparison with the twenty odd centuries of the occidental civilisation. But long for people who needed improvements from electricity.

In another scope, many English engineers, such as William Murdock, William Symington and Robert Fourness built vapour-powered vehicles at the beginning of the 1780s. But apart from the road-machines manufactured by Trevithick et Vivian between 1802 and 1804, it is necessary to wait up to the middle of the 1820s for new sporadic attempts of vapour-carts or diligences. Wide diffusion of automotive actually started at the end of the 19th century.

Same notices can be drawn for flying machines which were in use in France in the early 1780. French Montgolfier brothers demonstrated their aerostat in 1783 and 1784. But actual progresses only began in the 1890s.

One explanation for these delays may perhaps be found in the French Revolution and the wars and troubles which followed. From 1789 to 1815, Europe permanently faced to instability and lavishly spent money, energy and lives. There was neither place nor time for science and technological development.



King of France Louis XVI and Queen Marie-Antoinette being arrested in Varennes, on 20th June 1791.

Politics fiction novelist could imagine that in 1791, Queen Marie-Antoinette should ask to her husband Louis XVI to leave France and take refuge with her father, King of Austria. In the case Louis XVI accepted, he would be arrested in Varennes and French Revolution would go on. But in the case he refused, he would never be arrested in Varennes and nation would continue to trust him. Maybe France would get a constitution and Revolution would stop.

Then, science and technology would go on with development...

This is a part of French History and also of European History. Anyone knows that King Louis XVI accepted his wife's requirements. And we have now to come back to the reality.

2. TO THE ORIGINS OF ELECTRICITY :

In order to make the things more simple, let say that the history of electricity covers three large periods, even if a 4th period could be mentioned, since the 1950s, with the fantastic possibilities of electronics:

1st period, mainly covering 17th and 18th century : electrostatic phenomena amazed people in the Curiosities Cabinets,

2nd period, from the early beginning of the 19th to the 1870s : chemical generators gave enough energy for carrying out scientific experiments and finding the actual nature and the laws of electricity,

3rd period, since 1870s: thanks to electromagnetic machine, it became possible to turn mechanical energy to electricity and the doors opened for universal uses.

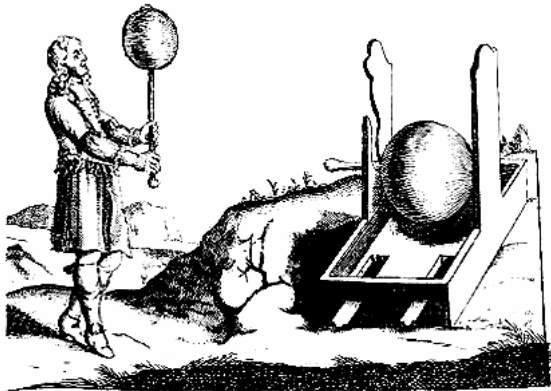
From Amber to Electrostatic, First Discoveries in the Curiosities Cabinets :

In the first times, scientists were captivated by the wonderful manifestations of electrostatic. Around the year 1600, the English Queen Elizabeth 1's own physician, William Gilbert [1] published a treaty about the magnetism of the Earth and proposed the word "*electricity*" to design the action of amber upon some light stuffs (amber is *elektron* in ancient Greek).

It was also the time for Curiosity Cabinets, where well-off people collected minerals, antiques, exotic wares and primitive physical instruments. These miniature museums were an attempt to classify science and civilization while the world was still amorphous. Many of these classifications were a strange hybrid of religion, science and superstition that are now considered obsolete.

Nevertheless, during this period, some interesting discoveries came to light. Around 1650, German Otto von Guericke built a crude friction generator with a sulphur ball that rotated fastly on a shaft. When Guericke held his hand against the ball and turned the shaft quickly, a static electric charge built up. In 1745, another German, Ewald Jürgen Georg von Kleist, found a method of storing this charge. He lined a glass jar with silver foil, and charged the foil with a friction machine. Kleist was convinced that a substantial charge could be collected when he received a significant shock from the device. This invention went on to be known as the Leyden jar because in

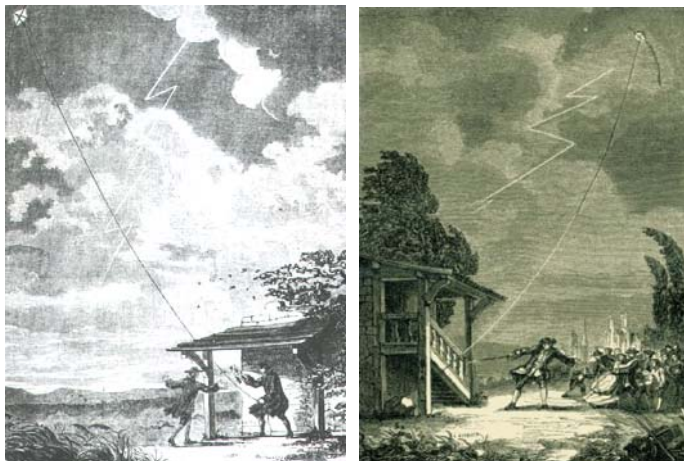
1746, Pieter van Musschenbroek of the University of Leiden, independently made the same discovery and let it know to the scientific world.



Guericke's machine (Germany, 1650).

During the second half of the 18th century, English Edward Nairne patented several electrical machines, including an electrostatic generator consisting of a glass cylinder mounted on glass insulators. The device was intended for medicinal use. Nairne recommended its use for nervous disorders, burns, scales, bloodshot eyes, toothache, sciatica, epilepsy, hysteria, agues and so on.

Also during this epoch, people began to make a parallel between electrostatic and thunder-lights. Most famous are the experiments carried out by American Benjamin Franklin and his son, with a kite in 1752. One year later, without any knowledge about Franklin's discovery, French Jacques de Romas did the same.



Experiments upon thunder :

left : by Benjamin Franklin and his son, in 1752.

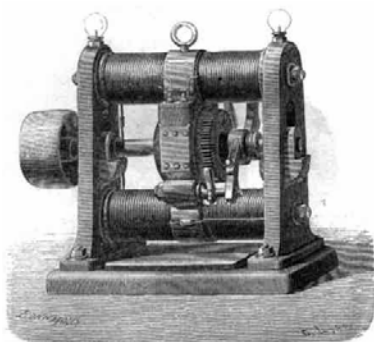
right : by Jacques de Romas in Nérac (France), in 1753

Thanks to Chemical Generators, Nature and Laws of Electricity are Explained :

Then, with the first Volta's batteries, it became possible to better understand the nature of electricity. For examples, Scotchman Prescott Joule found the so called effect and Danish Ørsted observed the magnetic effect of an electrical current. The presentation by the French scientist Arago of Roster's works at the Académie des Sciences, in Paris, on 1820, September, 4th gave to physicist André-Marie Ampère a flash of inspiration. Within one month Ampère formulated the law of electromagnetism (commonly called Ampère's law) that describes mathematically the magnetic force between two electric currents.

Electro-Magnetic Machines Open the Door to Universal Uses:

Lastly, time went for machines able to turn mechanical energy to electricity. Generally, invention of the dynamo is attributed to the Belgian Zenobe Gramme who achieved an efficient machine in 1870. To be honest, he was continuing studies by French Hippolyte Pixii (1832), English Cooke and Wheatstone (1867) and Italian Antonio Pacinotti (1860). Gramme's machine was improved as soon as 1875 by American Charles Francis Brush. From this time, doors were open for multiple applications we know today and for their universal uses.



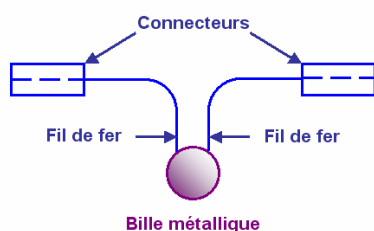
Zénobe Gramme's Machine (1870)

Only from this time started electricity's era.

3.THE FUSE AS A KEY FOR UNIVERSAL USES OF ELECTRICITY :

According to A. Wright and P.G. Newbery [2], earliest references to electrical fuses concern discussions following the presentation of a paper by A.C. Cockburn [2] to the Society of Telegraph Engineers in 1887. In the comments about this, W.H. Preece stated that platinum wires had been used as fuses to protect submarine cables since 1864 and Sir David Salomons referred to the use of fuses in 1874.

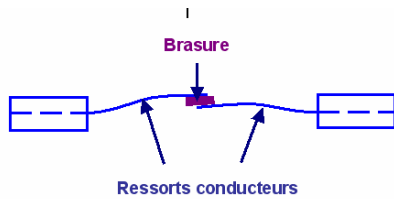
According again to A. Wright et P.G. Newberry, significant quantities of fuses must have been in use since 1879 and even, the simple wire-construction was not adequate enough for some applications because in that year Professor S. P. Thomson produced an "improved" fuse. It consisted of two iron wires connected together by a metallic ball of lead-tin alloy or any other low melting-temperature alloy.



Fuse with lead-tin alloy ball by Prof. S.P. Thompson(1879)

We may assume that action of gravity on the ball at the time it melted, allowed to get a faster and larger opening of the electrical circuit and then a better interruption of the electrical arc. Let us keep in mind that up to about 1890, electricians quite exclusively used direct current, that we know today is more difficult to cut than alternative one.

An evolution to Thomson's fuse occurred and was patented in 1883 by C.V. Boys et H.H. Cunyngham. They soldered two flat conductors having a spring ability. Above a sufficient current, the solder melted and made the conductors free to move in opposite directions.



Fuse patented by Boys and Cunyngham (1883).

Other physical arrangements based on this principle followed, one of them being attributed to Sir W. Thomson.

But, use of fuses actually arrived because of the large interest for electrical lightning in the years 1880-1882. Mentioned by the same A. Wright et P.G. Newbery, J. H. Holmes remembers in a letter to Clothier [4] that earliest lightning installations with incandescent filament lamps were built in 1878, almost simultaneously in England by Swan and in the United States by Edison. In order to protect the lamps against over-running, more than against short-circuit-currents, both Swan and Edison used fuses.



Thomas Edison (1847 - 1931)

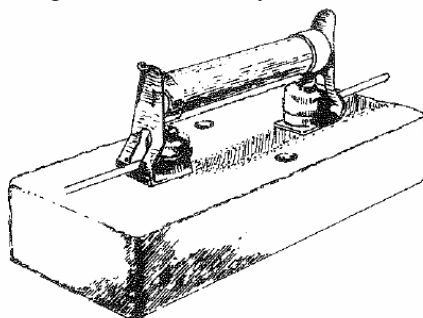
A British patent attributed to Thomas Edison on April 1881 is probably the first official notification of the use of lead-wire as over current protection. It can be read that Edison's disposal is named "safety-guard".

Nevertheless, some information – a lightning installation at Armstrong Works in December 1880 – tend to demonstrate that Swan owns the anteriority of the invention of fuses.

Swan and Edison went to Court in England and in United States, not only for the priority of fuses but also for lamps-patent. In 1883, after legal actions on both sides of the Ocean, Swan and Edison found a commercial solution in a common company : "The Edison & Swan United Electric Light Co". Each lamp produced by this new company were fitted with an additional fuse, consisting in a tin-strips.

Fuse for electrical protection against over-currents was born.

In addition, it is here necessary to bring some information about the invention of the filling of fuses. This is attributed to W.M. Mordey who took a patent in 1890. According to A. Wright et P.G. Newbery, this patent describes a fuse link with a fusible copper conductor enclosed in a glass tube or similar vessel. The tube was completely or partially filled with finely divided, badly conducting materials, preferably incombustible or non-flammable. Mordey suggested dry chalk, marble, sand, mica, emery or asbestos as filling materials. For anyone who experimented fuses, solutions concerning ability to interrupt the arc are as attention-grabbing as conduction and melting. So, W.M. Mordey does merit so much consideration as Edison and others.



Cartridge fuse patented by W.M. Mordey (1890)

4. YES, BUT BEFORE EDISON ? :

The French Electrical Telegraph :

Beside, and also before efforts from engineers working on large electrical installations such as lightning, others have used the same principle consisting on the melting of a conductive wire. According to credible references, fusing-wires have been early used for the protection of telegraphic lines against thunderbolts. The idea is attributed to French Louis-François-Clément Bréguet as soon as 1846.

The story is worth being told.



*Louis-François-Clément
Bréguet (1804-1883)*

In the years 1830-40s, France was equipped with a large net of Chappe's optical telegraphs. For that time, it was an efficient medium, and for example, a message could be transmitted from Paris to Toulouse (ca. 700 kms) within twenty minutes.

At the same time, the English, under Wheastone's leadership, were working on an electrical telegraph.

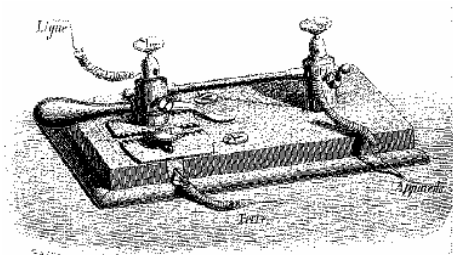
This application of electricity was compliant with the low capacities of the electro-chemical available generators.

The great scientist Arago, who also was a member of the Chamber, succeeded in persuading king Louis-Philippe to install an electrical telegraph line between Paris and Rouen. The Director of the Administration of Telegraphs prescribed that the new system must keep the encoding of the ancient. Operators, wont to read signals of the articulated arms of the Chappe's telegraph would not have to learn a new code. Because of the precision required for the mechanism, the manufacturing of the gear was committed to a famous clock- and scientific device-maker : Louis-François-Clément Bréguet.

This one would write later how came the necessity of the fuse [3]:

“In June 1846, because of a fierce thunderstorm over Saint-Germain village, all the wires of Le Vesinet-station were burnt and the apparatus were destroyed. This accident let us think that we had to protect the operators. We imagine to insert in the electrical circuit a very small and resistant wire, which should burn before the copper-wires of the electro-magnets.”

We called that a "paratonnerre" (Thunder-rod). It consisted as main part of a 0^m,00011 diameter wire, set inside a small wooden or glass-tube in order to preserve it against strokes. This "paratonnerre" was located in the electrical circuit outside the station.”



Bréguet fuse (1846)

About Dangers to be a Scientist:

Another "old story" is related by W. Bussière [4] from Fraunberger [4, 5]:

"On 6 August 1783, in St-Petersburg, Professor Georg Richman and his assistant were struck by lightning while charging capacitors (The Leyde Jar was invented by Ewald Jürgen von Kleist in 1745). The assistant escaped almost unharmed, whereas Richman was dead immediately. The pathologic analysis revealed that "he only had a small hole in his forehead, a burnt left shoe and a blue spot at his foot. [...] the brain being safe, the front part of the lung sane, but the rear being brown and black of blood." The conclusion was that the electric discharge had taken its way through Richman's body. The scientific community was shocked".



Prof. Richman's dramatic accident (Russia, 1783)

W. Bussière also relates that English scientist Edward Nairne [9-11], well-known for having built an electrostatic machine in 1774, is told to have used metallic wires, connected to the potential, in order to make a safety during capacitor-discharge. These wires, because of their electrical resistance and thanks to their adapted lengths were supposed to behave like fuses in case of over currents.



Edward Nairne's machine (England, 1774)

Nairne didn't the commit the same mistake as Prof. Richman. He used fuses!

5.CONCLUSION :

During the all history of electricity, have been the fuses present. Moreover, each time that electricity stepped progress and brought up new dangers, these were cleared by solution including fuses. Edward Nairne used wire-fuses, Louis-François-Clément Bréguet used wire-fuses and also Swan and Edison. Professor Richman who didn't think to protect himself paid with his life.

Beside the evidence of fuses to face the electrical protection-problems, there is the necessity of an adaptation of the fuse to the actual applications. In other words, beside the principle of conductor-melting under Joule's effect, are the adjusted technologies. Our job is there. Perhaps more than Swan or Edison, or Bréguet, or Nairne, the genuine father of our fuse-community is W.M. Mordey who went farther in the understanding of the needs, pointed out the arc-extinguishing and found a technological solution.

Today, because of new applications, because of globalisation, because of environmental regulations, bills of requirements for fuses are changing. And any one of us is asked for improving, and adapting the technologies. Nevertheless always based on the same fundamental principle.

Surely, the 8th ICEFA will demonstrate that the fuse is always able to adapt its simple principle to nowadays environment. The Organization-Committee sincerely hopes that this Conference will bring a better perception of this essential consideration. He will also be very proud to contribute to keep the community which is gathered around the fuse as enthusiastic and dynamic as in the previous time. The words "previous time" are referring to the forerunners of the 19th century as well as engineers who created ICEFA just 30 years ago.

REFERENCES:

- [1] William Gilbert. De Magnete, Magneticisque Corporibus, et de Magno Magnete Tellure (On the Magnet and Magnetic Bodies, and on That Great Magnet the Earth) , anno 1600.
- [2] A. Wright, P.G. Newbery. Electric Fuses. *Peter Peregrinus Ltd, on behalf of the Institution of Electrical Engineers. Stevenage, UK, 1982.*
- [3] A.C. Cockburn. On safety fuses for electric light circuits and on the behaviour of the various metals usually employed in their construction. *J. Soc. Teleg. Eng. 16 pp 650-665, anno 1887.*
- [4] H. W. Clothier. Switchgear Stages. *G.F. Laybourne & Unwin Brothers, 1933.*
- [5] L. Bréguet. Manuel de télégraphie électrique, quatrième édition, ornée de 80 gravures sur bois placées dans le texte et de 4 planches gravées sur acier. *Paris, Librairie de L. Hachette et Cie, 1862.*
- [6] W. Bussière, T. Latchimy. Fonctionnement des fusibles MT, Etudes expérimentales et théoriques. *5° Journées du Réseau Plasma Froid. Bonascre. LAEPT Clermont-Fd, 2006.*
- [7] Fritz Fraunberger. Ueber das elektromotorische Verhalten von Metallen, *Buchdruckerei von J. Fuller, München, 1904.*
- [8] Fritz Fraunberger. Elektrizität im Barock. *Aulis Verlag Deubner und Co, s. d. , Köln.*
- [9] Edward Nairne. The description and use of Nairne's patent electrical machine : with the addition of some philosophical experiments and medical observations, 1787.
- [10] E. Nairne, The description and use of Nairne's patent electrical machine [*Document électronique*] : with the addition of some philosophical experiments and medical observations, 1995.
- [11] Caullet de Veumorel. Description de la machine électrique négative et positive de M. Nairne, avec les détails de ses applications à la physique, et principalement à la médecine ; *traduit de l'anglais, 1784.*

IMPROVED TECHNOLOGY FOR MANUFACTURING OF THE HIGH-VOLTAGE FUSE-LINKS

Valer GIURGIU¹ and Gheorghe OARGA²

^{1,2} Electrical Engineering Co.-ICPE SA, 313 Splaiul Unirii, 030138-Bucharest, ROMANIA, hvfuses@icpe.ro

Abstract: The new patented design solution and corresponding technology for manufacturing high-voltage fuse-links reduces to the minimum the number of parts in the area of the contact between the fuse-elements and the contacts of the fuse-link. The electric contact between these parts is realized on the outer size of the isolating tube, utilising magnetoforming method, that being the base modification in technology, conducting to a great productivity and high savings. As regards the striker construction, there are eliminated tinning operations and the new solution is simple, cheap and environment-friendly. The tests made on the new fuse-links were conducted only for establishing of the temperature-rise and dissipated power and checking the time-current characteristics. The obtained values are in conformity with the imposed values by the international norms.

Keywords: fuse-link, fuse-element, technology, magnetoforming, striker.

1. Introduction

The time-current characteristics of the high-voltage fuse-links used in motor circuits must have a slow-fast specific feature, that is a relatively high operating current (slow operation) to give maximum withstand against motor starting current and relatively low operating current (fast operation) to give maximum short-circuit protection to associated switching apparatus, cables and motor.

The sizes of the fuse-links are high, therefore any modification in design or in technology can offer important reductions of the production costs, because the demand is of the order of thousand per year.

The new patented design solution and corresponding technology for manufacturing high-voltage fuse-links reduces to the minimum the number of parts in the area of electrical contacts between the fuse-elements and the contacts of the fuse-link.

The tests made on the new fuse-links were conducted only for establishing of the temperature-rise and dissipated power. The obtained values there are in conformity with the imposed values by the international norms.

2. The present stage in the manufacturing of the HV fuse-links for motor protection

The old technology of the HV fuse-links for motor protection implies many parts, Fig.1, and corresponding a high consumption of materials and electrical energy, a long execution time, therefore a small productivity and an unwholesome medium for execution personnel, because of the tinning operations, [1].

Contacts of the fuse-links there are executed in two parts: one which it is first assembled on isolating tube and another part, the proper contact which is fixed on the first part through screws.



Fig.1 – Old solution for contacts of the fuse-link

In order to obtain best technical results and an economical efficiency, it was selected the electromagnetic forming technique for assembling the first part of the contact on the isolating tube, which is deformed in high magnetic field, without mechanical contact, on a special device, based on the electromagnetic effect, Fig.2. Based on this technique, there are executed thousand of fuse-links with best results in comparison with another techniques: assembling with epoxy resins or by rolling. The principal advantages there are: reduced general cost of the assembling operation, minimal operator skill, a high productivity, no clearing or lubricants required (environmentally friendly process), the process can be easily automated and the forming energy can be precisely controlled.

Regarding the striker construction, the solution is expensive and implies many and great parts, assembled by tinning, which mean an unwholesome medium for operators and a great

consumption of the electric energy, in comparison with another solution, having smaller parts.



Fig. 2 - Electromagnetic forming equipment

The device for electromagnetic forming have a construction with many possibilities regarding the diameter of the piece which will be deformed, by simple change of the magnetic field concentrator.

3. The new solution for manufacturing of the HV fuse-links for motor protection

Motor type fuse-links [2-3], have the rated voltage of 7,2 kV and the rated currents in the range between 25 A to 250 A. The diameters of the fuse-links are divided in two sizes, according to rated currents:

- first diameter is about 74 mm, for rated currents between 25 A to 80 A;
- the second diameter is about 88 mm, for rated currents between 100 A to 250 A.

The rated currents of 315 A and 400 A, will be realized by connecting in parallel two fuse-links, two with rated current of 160 A for 315 A, respectively two with rated current of 200 A for 400 A.

The new solution for the manufacturing of the HV fuse-links for motor protection is based on a revision and a re-design of the many fuse-links parts, except the fuse-elements and the isolating tubes.

There were designed tools for manufacturing the new contacts and another new parts necessary for fixing of the fuse-elements by spot welding, to achieve an ensemble which is mounted between the contacts of the fuse-link.

To one end of the fuse-elements ensemble, the fuse-elements are welded on a part which will be pressed on isolated tube by the contact of the fuse-link, deformed by magnetoforming procedure, realizing a good electric contact between these pieces. To the other end of the fuse-elements ensemble, the fuse-elements are welded on a part which will be fixed, by screws, to the same type of

the piece as to the first end, over which will be deformed, by magnetoforming procedure, the second contact of the fuse-link, Fig. 3.



Fig.3 – Magnetoforming area

Also, it was re-designed the striker, classified as a medium type, by its mechanical characteristics. The new solution is simple, without tinning and with simple manufacturing operations.

4. Testing of the new solution and quality assurance

Because the new solution have not changed the fuse-elements, the tests were concentrated only on the measurement of temperature-rises and power dissipation, as well as the checking of some points on the time-current characteristics, to demonstrate that are not exceeded the limits imposed by the norms or by the technical specifications of the products.

The tests were made in conformity with the IEC 60282-1, [2]. Fig. 4 shown a testing circuit for the measurement of the temperature-rises and power dissipation.



Fig. 4 – Testing circuit

The temperature-rise in the hottest spots (middle of the isolated tubes) and on the contacts of the fuse-links were measured by thermocouples, utilising a Fluke device, and the values of the resistance of the fuse-link, before and after tests, were measured with a Chauvin Arnoux micro-ohmmeter type CA 10. In Table 1 are presented the results of the tests regarding the temperature-rise for each rated current of the fuse-links.

Table 1 – Measured values for temperature-rises

In [A]	Measured values			Imposed values [K]
	δT_1 [K]	δT_2 [K]	δT_3 [K]	
25	12	30	6	contacts: 65 isolated tube: 115
31.5	17	35	8	
40	19	40	10	
50	24	45	14	
63	29	63	20	
80	34	70	24	
100	22	30	17	
125	26	34	21	
160	34	38	27	
200	43	45	29	
250	59	50	36	

The tests were made with a vertical mounting of the fuse-link, and from the Table 1 it can be seen that the highest temperature-rises are measured approximate at the center of the isolated tube, except the case of the 250 A rated current, at which the highest temperature-rise is at the up contact of the fuse-link. This case can be explained by the fact that the tube reaches its limits regarding heat transfer by convection and radiation, the characteristic dimension being fuse's diameter.

The values measured for power dissipation are presented in Table 2.

Table 2 – Measured values for power dissipation

In [A]	Measured values [W]	Imposed values by technical specifications [W]
25	38	40
31.5	47	50
40	56	60
50	67	70
63	81	85
80	105	110
100	45	50
125	52	55
160	77	80
200	91	100
250	120	120

The value for rated current 250 A confirm the above supposition regarding the touching of the upper limit for heat transmission of the isolating tube.

Time-current characteristics for fuse-links were obtained in a low voltage test circuit, the same as for temperature-rise tests, with a constant value of the test current through the fuse-link.

The limits imposed in [3]:

$$I_{f_{10}} / I_n \geq 3 \text{ for } I_n \leq 100A$$

$$I_{f_{10}} / I_n \geq \text{for } I_n > 100A \quad (1)$$

$$I_{f_{0.1}} / I_n \leq 20(I_n / 100)^{0.25} \text{ for all current ratings}$$

provide slow and fast operation of fuse-links in the 10 s region and 0.1 s region respectively, and characteristics of our fuse-links are in accordance with these requirements.

In Table 3 are presented calculated values for these two currents, with equation (1).

Table 3 – Calculated currents with equation (1)

In [A]	25	31.5	40	50	63	80
$I_{f_{10}}$ [A]	75	95	120	150	190	240
$I_{f_{0.1}}$ [A]	350	470	630	840	1120	1500

In [A]	100	125	160	200	250
$I_{f_{10}}$ [A]	300	500	640	800	1000
$I_{f_{0.1}}$ [A]	2000	2650	3500	4760	6300

The time-current characteristics were checked for each rated current, by tests made on two fuse-links (two points on the characteristic), with currents for pre-arcing times in the neighbourhood of 10 s.

In Table 4 there are presented the pre-arcing times obtained for the testing currents corresponding to fuse-links with rated currents from 25 A to 80 A, and in Fig. 5 and Fig. 6 are shown examples where there are marked these points on the time-current characteristic for motor type fuse-links with 31.5 A, respectively 250 A rated current.

Table 4 – Measured values for pre-arcing times

In [A]	25	31.5	40	50	63	80
I_1 [A]	100	150	200	200	300	350
t_1 [s]	38	10	30	50	33	60
I_2 [A]	120	180	250	250	350	400
t_2 [s]	6.4	1.5	4	10	4	14

The points marked in Fig.5 and in Fig.6 are in a region of $\pm 20\%$ for the test current, using mean current values.

The manufacturing of the motor type fuse-links, and another HV fuse-links types (for capacitors or transformer protection), are made in an implemented quality assurance system, which takes in account,

firstly, all the conditions imposed by the international norms and secondly, the mechanical tolerances of the initial material (silver strips, for instance), parts or final assembly of fuse-link and thirdly, the tolerances regarding the electrical resistance of fuse-elements.

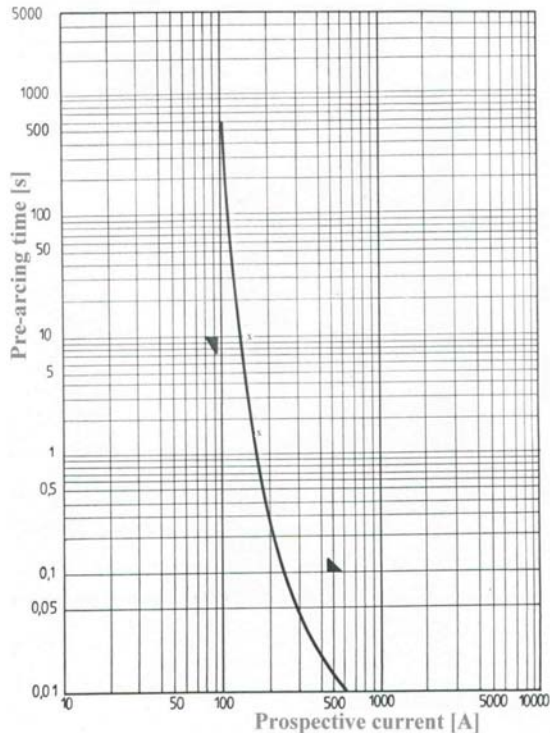


Fig. 5 – Time-current characteristic for a fuse-link with rated current of 31.5 A

There are imposed measurements in various stages of the production flux, to discover some irregularities in execution or assembly processes. The tolerance for electrical resistance is $\pm 10\%$ and the resistance is measured and recorded after consecutive execution operations, and naturally before and after the filling of the fuse-link with the sand, in order to detect any manufacturing influences, for instance damaged fuse-elements or poor welding. Each fuse-link has a serial number, very useful for identification, in case of any irregularities being observed later on. The fuse-links are marked with labels, having the following identifying data: manufacturer's name, type of the fuse-link, rated voltage, rated current, rated maximum breaking current, and serial number/year.

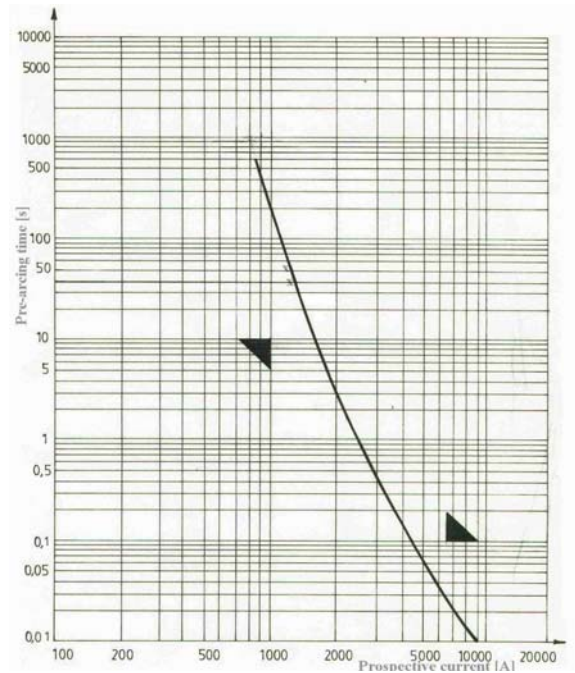


Fig. 6 – Time-current characteristic for a fuse-link with rated current of 250 A

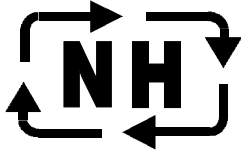
5. Conclusions

The authors describe a new solution for manufacturing of the fuse-links utilised for motor protection, having as a novelty application of a non-conventional technology in final assembling. Theoretically, electrical contacts between the fuse-elements and the contacts of the fuse-link are made by magnetofforming procedure, on the outer surface of the isolating tube, which reduces to the minimum the number of parts, and offer important reductions of the production costs.

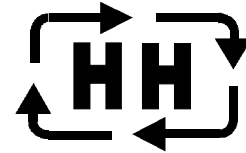
The tests were made only for checking the fact that the new technology doesn't modify significantly the values of the temperature-rises and power dissipation and that there are respected time-current characteristics. The obtained values are in conformity with the imposed values by the technical specification of the fuse-links.

References

- [1] Giurgiu V., Oarga Gh. and Purdel S.: "High-voltage fuse-links for motor circuits protections", Sixth International Conference on Electric Fuses and their Applications, Torino, 1999, pp 221-224.
- [2] IEC 60282-1: "High-voltage fuses – Part 1: Current-limiting fuses", 2002.
- [3] IEC 60644: "Specification for high-voltage fuse-links for motor circuit applications", 1979.



NH/HH-Recycling



Verein zur Förderung des umweltgerechten Recycling von abgeschalteten NH/HH-Sicherungseinsätzen e.V.

FUSE RECYCLING IN GERMANY – AN INITIATIVE FOR EUROPE

Martin Grote, Gerd Fink,

NH/HH-Recycling e.V., Association for the promotion of environmentally compatible recycling of disused LV HRC/HV HRC fuse links, Germany

Martin Grote, DRIESCHER WEGBERG, Tel. +49 (0) 2434 / 81 (1) 211, Fax +49 (0) 2434 81 446
martin.grote@driescher-wegberg.de

Gerd Fink, SIEMENS Regensburg, Germany, Tel. +49 (0) 941 790-2587, Fax +49 (0) 941 790-2766,
gerd.fink@siemens.com

The association NH-HH-Recycling e.V. is officially accredited as a non-profit association. It was founded in 1995 and since then the association is busy with the recycling of LV and HV HRC fuse-links in Germany and that on a non-profit basis.

The association was founded by German fuse manufacturers with the aim to return utilizable raw materials from LV and HV fuse links to the cycle of resources again.

In addition the target is, that only those fuses will be produced in future, which can be recycled without any problems.

The task of the Verein zur Förderung des umweltgerechten Recycling von abgeschalteten NH/HH-Sicherungseinsätzen e.V., a non-profit association established by German fuse manufacturers, is to process the various materials of which fuse links are made so that they can be returned to the cycle of manufacture for further use. In 2006, for example, the association collected and recycled more than 216 tonnes of materials.

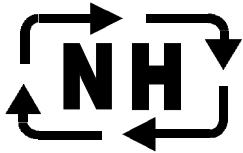
As far as the electrical industry is concerned, a ground-breaking initiative has been taken by the German manufacturers of low-voltage and high-voltage high-breaking-capacity fuse links. Even before the most recent German legislation on recycling came into force customers had begun asking the manufacturers of fuse links if they could set up a methodical system which would allow used fuse links to be returned for environmentally-compatible disposal. As a result, several fuse manufacturers began offering and charging for a disposal service for used fuse links.

Then, in 1995, with the aim of putting the subject of environmentally-compatible disposal on a regular footing, a number of the manufacturers involved (Fritz

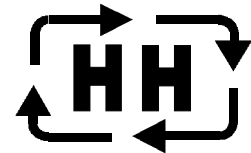
Driescher KG, EFEN GmbH, Lindner GmbH, Jean Müller GmbH, M. Schneider-Annaberg GmbH, Siba GmbH and Siemens AG) joined forces with the ZVEI (Zentralverband Elektrotechnik- und Elektronik-industrie) and, through an initial working party, established the non-profit-making "Verein zur Förderung des umweltgerechten Recycling von abgeschalteten NH/HH-Sicherungseinsätzen", otherwise known as "NH/HH-Recycling", registered in Regensburg and with its Head Office in Frankfurt.

Recycling the products and materials of 20 years ago

For many applications, fuse links represent a relatively cheap and safe way of providing protection for electrical systems and equipment. L.v. h.b.c. (NH) fuse links (low-voltage high-breaking-capacity) are used in low-voltage installations and h.v. h.b.c. (HH) (high-voltage high-breaking-capacity) fuse links in medium-voltage installations. The volume of the l.v. h.b.c. fuses varies between 45 and 900 cm³ (5 to 15 cm long and 3 to 10 cm wide). The h.v. h.b.c. fuses, on the other hand, are substantially larger: 20 to 65 cm long and 5 to 8.5 cm in diameter. The service life of these fuses, provided they are not called upon to blow, is approximately 20 years, which is well above the average life of most other types of electrical equipment. This means that, with these long-life products, recyclers are having to deal with materials that were in common use 20 years ago. In "old" fuse links, for example, asbestos was still being used as a jointing material. Fig. 1 shows a cross section through an l.v. h.b.c. fuse link and lists the other materials used in its construction; similarly Fig. 2 illustrates an h.v. h.b.c. fuse link.

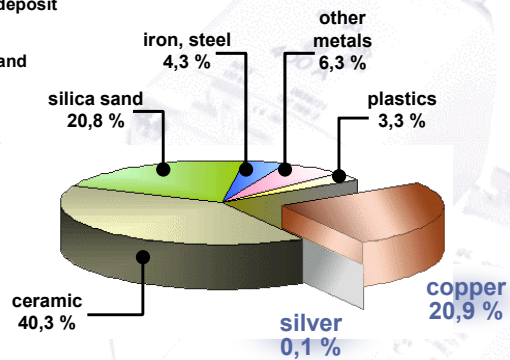
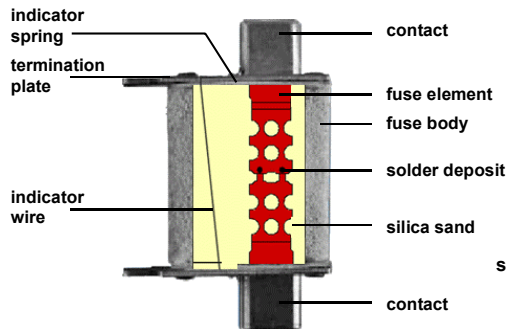


NH/HH-Recycling



Verein zur Förderung des umweltgerechten Recycling von abgeschalteten NH/HH-Sicherungseinsätzen e.V.

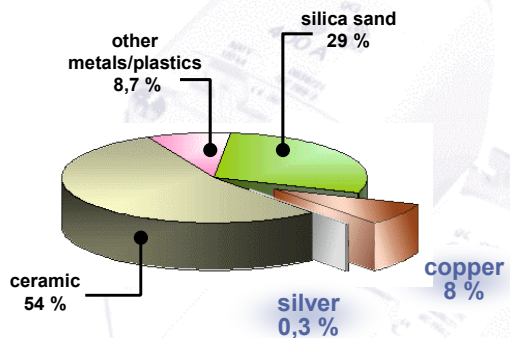
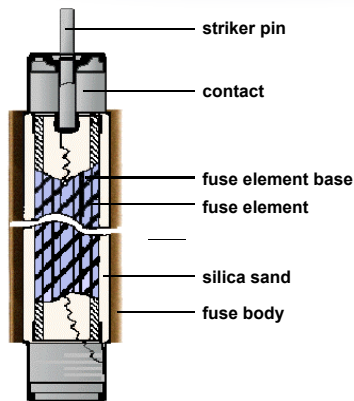
Structure of an LV HRC fuse link



- Values averaged over all sizes and types
- Depending on the year of construction and type, there may be slight amounts of cadmium (solder) and asbestos (seal)

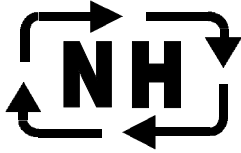
NH/HH-Recycling / 07/03 10

Structure of an HV HCR fuse link

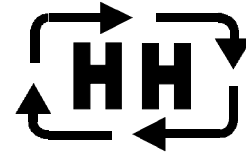


- Values averaged over all sizes and types
- Depending on the year of construction and type, there may be slight amounts of cadmium (solder) and asbestos (seal)

NH/HH-Recycling / 07/03 11



NH/HH-Recycling



Verein zur Förderung des umweltgerechten Recycling von abgeschalteten NH/HH-Sicherungseinsätzen e.V.

The result: copper, silver and materials for the building trade and the chemical industry

The percentages of different materials also listed in Fig. 1 show that the recycling and re-use of copper and silver is thoroughly worthwhile and, as "valuables", do not deserve to be included amongst the residual waste or dumped on the refuse tip. The classic alternatives of disassembly or shredding offer the possible means by which the materials can be recovered.

Although disassembling these fuse links is a labor-intensive process, some successful projects have been set up, e.g. with power utilities and disabled people's organizations working together, in which the fuses are disassembled and the valuable materials they contain recovered so that they can be returned to the manufacturing cycle. The actual cost of disassembly is not covered by the profit obtained from the raw materials so the disabled people's organizations have to make a small charge for each fuse. The asbestos joint gaskets mentioned previously also cause some problems with disassembly.

The strict rules that apply when working with asbestos make disassembly a complex and costly process - as also is shredding or processing by pan grinder (a crushing process producing coarser results than a shredder) with subsequent melting down in the blast furnace. This situation has led to further tests being carried out in conjunction with a copper smeltery which have demonstrated that fuse links can be processed directly in a converter without any pre-processing at all. Under normal circumstances it is necessary to add quartz sand during the process in order to produce slag and promote the precipitation of iron. Since the fuse links that are being melted down already contain around 30% quartz sand, however, this "waste product" actually helps in the process.

Following an inquiry among various copper smelters and recycling companies throughout the country, the Norddeutsche Affinerie in Hamburg was eventually chosen because of its capacity and environmental capabilities. As a second waste handler the NH/HH-Recycling entered into a contract with the copper smelter Brixlegg, Austria.

For direct processing in copper converters the fuse links must normally satisfy the following specification:

- Plastics content less than 3.5%
- Asbestos content less than 0.05%
- Cadmium content less than 0.005%

The plastics are utilized to produce heat with continuous monitoring of the flue gas. During the melting, any zinc that originates from, say, brass contact blades is converted into zinc dust and collects in the plant filters. However, this is not a problem provided the total amount of zinc remains below 50 tonnes per annum - as it will given the total amount of recycling anticipated. The ceramic body of the fuses and the quartz sand are converted to slag that can be used again for road building and in the concrete industry. Another end-product, sulfuric acid, can be re-utilized by the chemical industry. The asbestos is rendered harmless by being incorporated into the slag.

Research benefits from the profits

Most of the l.v. and h.v. h.b.c. fuse links come from the country's power utilities and general industry. They are usually collected in "egg box" pallets placed at specified collecting points. The various sales organizations, which also function as collecting points, provide information for smaller users, such as electrical contractors and installers, on the recycling facilities that are available. DHL, with branches all over Germany, has been awarded the contract for collecting the egg-box pallets when they are full and transporting them to the company's own buffer store. When a collecting point has full pallets to be collected it notifies the transport company by fax and the pallets are then collected within three days and replaced with new empty pallets.

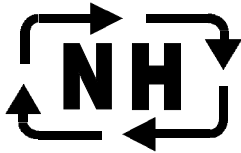
When a sufficient quantity of fuse links has accumulated in the buffer store, the haulier delivers them to the copper smeltery and invoices "NH/HH-Recycling" for its work. There are no charges to users for any aspect of the logistics involved or the recycling process.

After deduction of the costs for logistics, recycling and advertising etc., in accordance with the statutes of the association, the revenue is donated to a research agency to promote research in the area of fuse link technology and environmental compatibility. The agency is asked to publish results in appropriate manner.

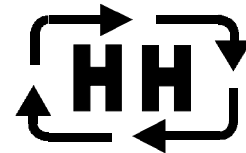
Spreading throughout Europe

In 2006, approximately 216 tonnes of used l.v. and h.v. h.b.c. fuse links were collected and recycled (Fig. 3).

"NH/HH-Recycling" intends to also enable foreign customers of the member companies to have their old fuse links disposed of by environmentally-compatible means. The organization's trade-marks have already



NH/HH-Recycling



Verein zur Förderung des umweltgerechten Recycling von abgeschalteten NH/HH-Sicherungseinsätzen e.V.

been registered in approximately 30 countries and inquiries about the concept of the recycling process have been received from Austria, Sweden and recently England.

Memorandum on the European activities of NH/HH Recycling (members' meeting resolution of 17.05.00)

1. The main tasks of NH/HH Recycling involve recycling fuse links that are manufactured or distributed either by members of the Association or by companies which use its sign. If these fuse links can be collected from foreign customers or at foreign production locations, they may also be included in the recycling concept.

2. Based on a legal assessment by ZVEI (German electrical industry), there are unlikely to be any benefits from operating NH/HH Recycling as a European association.

3. As a German nonprofit making association, it is not a primary objective of NH/HH Recycling to extend the system beyond Germany's borders.

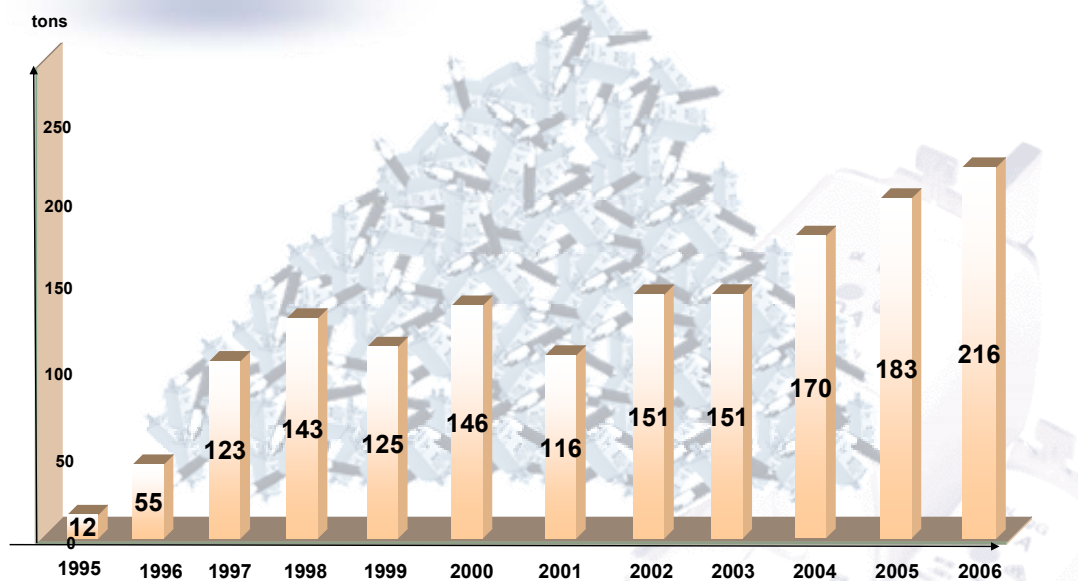
4. The legal opportunities of a German nonprofit making association are limited outside Germany.

5. It is part of NH/HH Recycling's basic philosophy to offer startup assistance for recycling systems in other countries under these countries' own leadership.

The manufacturers in Great Britain started also with a system like this. Colleagues from The Netherlands started and collecting fuses.

In a pilot phase the NH/HH – System, as we call it in Germany can be accommodated and extended to all European countries.

Recycling quantities



NH/HH-Recycling 03.2007

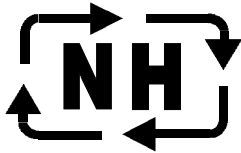
WEEE – Directive

The WEEE – Directive, it stands for “Waste electrical and electronic equipment” which became into force in August 2004 is the core of a taking back and recycling system.

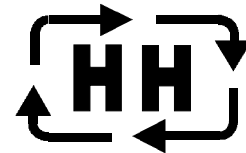
The countries have to install a collection and take back system free of charge for consumers that

ensures the return of the electronic equipment from August 2005.

The producers have to warrant financing of disposal take care for correct recycling and recovery of waste. In this case, the European legislation is the minimum for national legislation and it concerns also “... other



NH/HH-Recycling



Verein zur Förderung des umweltgerechten Recycling von abgeschalteten NH/HH-Sicherungseinsätzen e.V.

monitoring and control instruments used in industrial installations (e.g. in control panels)” (Cat. 9).

The “Restriction of use of certain hazardous substances in electrical and electronic equipment,” (RoHS) became into force in August 2004, valid in July 2006. There are no national differences or exemptions with material restrictions. Today, the equipment category 9 “monitoring and control instruments” is exempted from RoHS, but the reviews every 4 years may lead to the cancellation of all exemptions. The expected limits are (07/2003), e.g. 0,1 wt.% for Pb, Hg and 0,01 wt.% for Cd.

The third column has to guarantee the design and production in an environmentally more efficient way. The Eco-design requirements for energy using products (EuP) are estimated 2008 for coming into force. The first official draft of the European Community is in preparation.

What effects have all these arising requirements on the Fuse Industry and what is to do? First of all, the critical substances in fuses have to be recorded already, today ! What kind of substances which are probably included in fuses are concerned? Well known are Pb, Cr(VI), Cd, Halogenide, - the polyprominated biphenyls (PBB) and polyprominated diphenylethers (PBDE). For the most of these mentioned before are technical solutions which are existing or developing. The producers have to qualify and to use them. In the next step, when the critical substances are identified, the producers should design a plan for acting and changing to non-hazardous substances.

And what is the matter with a “Taking back and recycling system” the WEEE asked for?

With the above mentioned system we have already an existing system in Europe for fuse links.

The different countries or manufacturers can easily copy the principle of this system, which is well known in Germany as “Association for the promotion of environmentally-compatible recycling of disused LV HRC/HV HRC fuse links.”

A HIGH VOLTAGE VACUUM TYPE HYBRID CURRENT LIMITING FUSES FOR DOUBLE PROTECTION OF THE SHUNT POWER CAPACITORS

Hao He⁽¹⁾, Jimei Wang⁽²⁾

Xi'an Sielins Electric Co.Ltd⁽¹⁾, Xi'an P.R.China, sielins@126.com

Xi'an Jiaotong University⁽²⁾, Xi'an P.R.China, jmwang@mail.xjtu.edu.cn

Abstract: This paper is designed according to Chinese Standard of GB151665-94, GB110022, GB3988.2, and GB1661.1~5. The rated voltages are 3~35kV. The rated currents are 12.5~200A. The interrupting currents are for capacitive current 20~50 times of rated current and for inductive current 3.15~40kA. The paper gives design processing of high voltage vacuum type hybrid current limiting fuses for double protection characteristics.

Keywords: Chinese Standard. Vacuum, Hybrid, Current limiting, shunt power capacitor.

1 Introduction

The high voltage shunt power capacitor protection fuses are designed according to GB15166.5-94^[1]. (IEC standard, Publication-549^[2]) The rated voltages are 3~35kV as shown in Table 1 and the frequency is 50Hz. It protects single capacitor or parallel capacitors.

Table1 unit : kV

Rated voltage	3	6	10	15	20	35
Highest voltage	3.6	7.2	12	17.5	24	40.5

The rated currents are 12.5, 20, 25, 31.5, 50, 80, 100 and 200A. The insulation level is as GB110022 standard.

Capacitive current interrupting capacity (kA r.m.s.) of the fuse is 20 times or 50 times of rated current. Other parameters are defined by manufacture and users. Inductive current interrupting capacity (r.m.s.) are 3.15, 6.3, 8, 12.5, 16, 25, 31.5 and 40 kA.

The overload protection characteristics of the high voltage fuse are as following: at 1.5 times of rated current, melting time is less than 75s; at 2.0 times of rated current, melting time is less than 7.5s ; and conventional non-fusing current is 1.1 times of

rated current, where fuse element doesn't break in 4 hours.

Temperature rise of the high voltage fuse should be measured by alcohol thermometer as required by GB3988.2.

The interruption performance of the high voltage fuse is shown in Table 2.

The discharge withstanding performance of the high voltage fuse: it should withstand a rush current whose first half cycle amplitude exceeds 70 times of rated current in required procedures.

The anti-erosion layer of the high voltage fuse: all exposed metal surface should be protected that there is no erosion on the nice surface.

Indication device of the high voltage fuse: there should be obvious fused indication and it should work reliably.

Table 2

Interruption performance	
Inductive interruption test	Possibility passing through inductive current ¹⁾
	Nonpossibility passing through inductive current ²⁾
Capacitive current interrupting test ³⁾	
Discharge current interrupting test	

Note:1) This application examples are:

- Fuse for capacitors group
- Single fuse of delta connection group of nonseries unit
- Single fuse of star connection group with neutral ground of nonseries unit

2) This application examples are:

- Single fuse of star connection group of neutral without to ground
- Capacitors group of series unit

3) Star connection capacitors group of neutral point without ground is protected by fuse for capacitive current interrupting test

High voltage fuse in the same series products should have same installation size and can be replaced easily.

Basic requirements of discharge withstanding tests:

a. There are 5 discharges in 10 minutes for a fuse, discharge frequency is

i) For fuse whose rated current is less than 31.5A:

$$f(kHz) = 1.2U_m^{+20}_0\%$$

ii) For fuse whose rated current is greater than 31.5A:

$$f(kHz) = 0.8U_m^{+20}_0\%$$

where U_m —Maximum voltage (kV)

b. There is 100 discharges in a time interval defined by manufacture and discharge frequency is $8U_m^{+20}_0$ kHz.

For fuses in same series, the fuses with maximum rated current and minimum rated current should be tested.

The test can be done with any voltage level.

Current amplitude ratio of neighbor waves in the discharge test is 0.8~0.95.

In metal short circuit test, fuse can be replaced by a conductor whose impedance is much smaller negligible than that of test circuit.

The required first half cycle current amplitude, oscillation frequency and current decay coefficient can be gotten by adjusting test circuit and the parameters can be confirmed by oscillogram. The fuse should be in conductive state after tests.

2 Design of high voltage vacuum type Hybrid current limiting fuse with double protection characteristics.

So far there is no fuse that can meet the requirements of both overload protection and short circuit current protection for the external shunt power capacitor in all over the world.^[3]

To meet the requirements, a current-limiting fuse that can meet the requirements of both overload protection and short circuit current protection is developed by cooperation and short circuit current protection is developed by cooperation of Xi'an Jiaotong University, Hangzhou Boda Electrical Apparatus Company and Shanghai Kerui Vacuum Electrical Apparatus Company, which follows the GB15166.1 ~ 15166.5 standard. It is shown in Fig.1



Fig.1 A configuration of high-voltage vacuum type hybrid current-limiting fuse with double protection characteristics

There is only an expulsion fuse that is used for shunt capacitor protection in China now, which can only meet the overload requirements. There is a back-up fuse that can be used for short circuit current protection only. If both requirements are needed the 2 fuses should be used in series. But their cost are high and installation are not convenient.

According to Chinese National Standard for high voltage fuse, pre-arc time-current characteristics of expulsion fuse with overload protection should follow that in Table 3. And its conventional non-fusing time should be greater than 4 hours at 1.1 times rated current.

Table 3

Times of rated current	1.5	2.0
Melting time, s	75	7.5

(1) Design ideas

Generally high voltage current-limiting fuse is belong to back-up fuse as shown in Fig.2. It only meets the requirements of short circuit current protection. For overload current, only current over 3.5 times rated current can be interrupted reliably. For example, a current-limiting fuse with rated current 100A can interrupt current when it exceeds 350A.

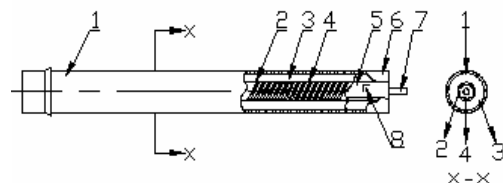


Fig.2 General configuration of high voltage current-limiting fuse

In addition, there is an explosion hazard, when back-up fuse is used for single capacitor protection. We designed a high speed interrupting fuse element. Many years experience shows that there is no fuse explosion to apply this novel fuse element.

Now let's analyze interrupting principle of expulsion fuse. It uses short fuse element. With overload current, a spring pulls the short fuse element and breaks and breaks it. When the short fuse element is broken, a high temperature arc is initiated, which makes gas-generating material in arc extinguish tube generates a lot of high temperature gas. The gas expulses the arc and makes the arc longer. Thus the arc is extinguished. The expulsion fuse is used for many years. It is reliable and simple. But its structure is open and its size is large. And it has fire hazard. We use vacuum fuse to replace it. Vacuum fuse has smaller size, high reliability and safety. It meets all requirements in standards and a novel design.

(2) Example of Design

Suppose a fuse for shunt power capacitor protection with rated voltage 6kV, rated current 50A and interrupting current 40kA^[4]

(a) Vacuum type fuse is used for overload current protection

Basic requirements: fuse element should be melted at 1.5 times rated current (1.5×50=75A) in less than 75s. It should be melted at 2 times rated current (2×50=100A) less than in 7.5s. It should not be melted at 1.1 times rated current (1.1×50=55A) in 4 hours. At first selecting (0.5×4=2mm²) copper is used to cut and try method for measuring pre-arc time-current characteristics. By adjusting design size of fuse element many times (0.5×3=1.5mm²) copper with length 10mm is chosen finally. Its pre-arc time-current characteristics is shown in Fig.3.

Configuration of vacuum fuse is shown in Fig 4, where 1 is output terminal to connect current fuse copper fuse element and 5 is linkage.

(b) High speed current-limiting fuse is used for high overload current and short circuit current protection

Pure silver is chosen as fuse element. Its total length is 300~320mm. Current density at neck is j=200A/mm². The configuration of high-speed current limiting fuse element is shown in Fig 5.

The length of fuse element is L=2×13+24×12=314mm. The cross-section area of the fuse element is

$$A = \frac{I_n}{j} = 25 / 200 = 0.125 \text{mm}^2 . \quad \text{The}$$

diameter of hole is 1.5mm and their separation distance is 0.2mm. Fuse element width is (1.5+0.2) ×5=8.5mm. Total hole separation distance is 0.2×5=1mm. Fuse element thickness is 0.125/1 = 0.125mm. There should be 2 fuse elements in parallel with rated current of 50A.

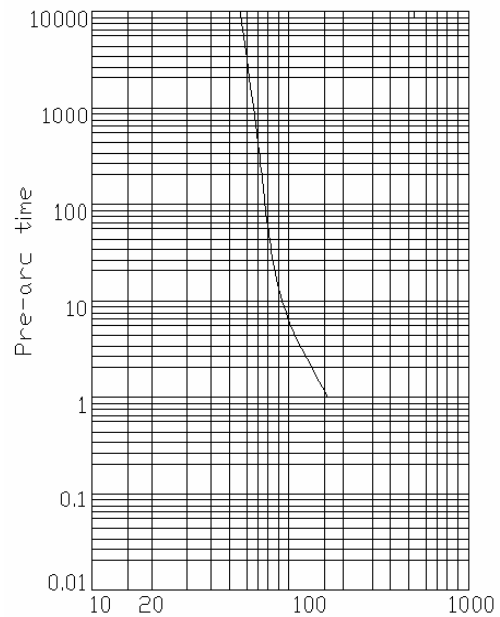


Fig.3 Time-current characteristics under vacuum condition of 5×10⁻⁴Pa

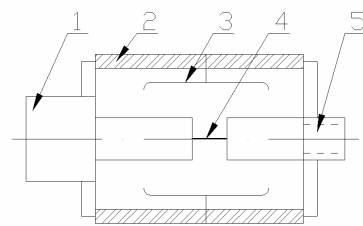


Fig.4 Configuration of vacuum fuse

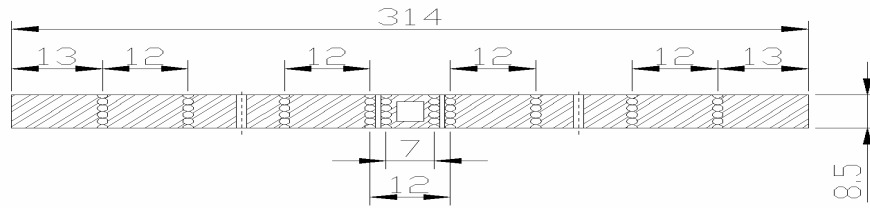


Fig.5 Configuration of high-speed current-limiting fuse element

Most of the available parts of back-up fuse except fuse element can be used in the new designed fuse for high overload current and short circuit current protection.

Fuse element of the high speed current-limiting fuse can be processed as wave shape, as shown in Fig.6.

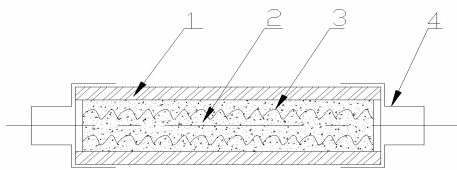


Fig.6 Cross-section configuration of high-speed current-limiting fuse

(c) The designed fuse for shunt capacitor with rated voltage 6kV, rated current 50A and

interrupting current 40 kA has passed interrupting capacity tests in test laboratory of XIHARI. The results show that it meets the requirements of Chinese Standard.

References

- [1] Chinese Standard GB15166.6-94
- [2] IEC Standard. Publication 549 First edition 1976.
- [3] Wang Jimei. "Study on special current-limiting fuse of protection shunt power capacitors", Electrical Technology No.1,2005
- [4] Wang Jimei, "High voltage vacuum type full-range current-limiting fuse", Electrical Technology, No.9, 2002

DEPENDENCE OF CURRENT INTERRUPTION PERFORMANCE ON THE ELEMENT PATTERNS OF ETCHED FUSES

Yuzo Ishikawa^{*}, Kengo Hirose^{**}, Mitsuo Asayama, Yasushi Yamano
and Shinichi Kobayashi

Graduate School of Science and Engineering, Saitama University
255 Shimo-Okubo, Sakura-ku, Saitama-shi, Saitama 338-8570, Japan
y-ishikawa@nemoto.co.jp, yamano@ees.saitama-u.ac.jp, s.kobayashi@ees.saitama-u.ac.jp

Abstract: This paper is about fuses for the protection of semiconductors. The pattern of their current-interruption area is composed of chemically etched copper plated on a ceramic substrate. Interruption tests revealed that the I^2t characteristics of these fuses are greatly influenced by the numbers P and S of parallel and series interruption points. The I^2t value of a $6S-32P$ fuse is 72 % that of a $6S-8P$ fuse, and the I^2t value of a $24S-8P$ fuse is 24 % that of a $6S-8P$ fuse. The synergy of these P and S effects reduces the I^2t value of a $24S-32P$ fuse to only 8.6 % that of a $6S-8P$ fuse.

Keywords: etched fuse, current-interruption, P effect, S effect.

1. Introduction

Etched fuses in which the fuse element is attached to ceramic substrate not only have excellent current-interruption performance but are durable and heat resistant. They have therefore been used ever since the first low-voltage semiconductor protection fuse composed of chemically etched copper plated on a ceramic substrate was presented in 1991 at the 4th ICEFA [1].

Semiconductor devices are increasingly being used in power control systems, and their operating voltages are getting higher. This trend is driving the development of fuses applicable to high-voltage semiconductors [2], and etched fuses are potentially able to provide the kind of protection that high-voltage semiconductors require [3-5].

We recently found experimentally that the current-interruption performance of etched fuses can be improved by making the element patterns smaller and that the I^2t value of a fuselink can be decreased by increasing the number of parallel interruption points [4]. In the work we report here we investigated the dependence of current-interruption performance

on the number of parallel interruption points, which is called the parallel effect (P effect), as well as the dependence of current-interruption performance on the number of interruption points arranged in series, which is called the series effect (S effect). We did this by experimentally evaluating the performance obtained with various numbers of parallel and series interruption points.

In these experiments we also investigated the effect of giving a fuse element three-dimensional structure, which means putting additional plating on the heat-radiating parts of the element while leaving the thickness of current-interruption parts as originally plated. This added structure reduces the resistance of the element, thereby increasing the current rating.

2. Fuse element for the tests

2-1. Interruption unit patterns

We used the two types of interruption unit patterns shown in Fig. 1.

We used the square type to clarify the effects of P and S on the current-interruption performance because the width b of the seed of an arc remains constant as the arc grows. After an arc forms where part of the narrow point melts, the width of the arc remains constant as the arc expands in the H direction.

Because the round type of pattern is likely to be used in actual fuses, we used this pattern for testing the rated current.

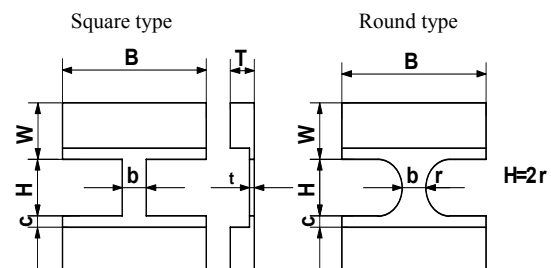


Fig. 1: Interruption unit patterns.

^{*}Also working with NEMOTO LTD., 4-10-9 Takaido-Higashi, Suginami-ku, Tokyo, 168-0072, Japan

^{**}Also working with FUJI RESEARCH INSTITUTE, 1-17-8 Matsubara, Setagaya-ku, Tokyo, 156-0043, Japan

2-2. Test fuses

Test fuses were constructed by connecting the interruption units as shown in Fig. 2, with S units in series and P units in parallel.

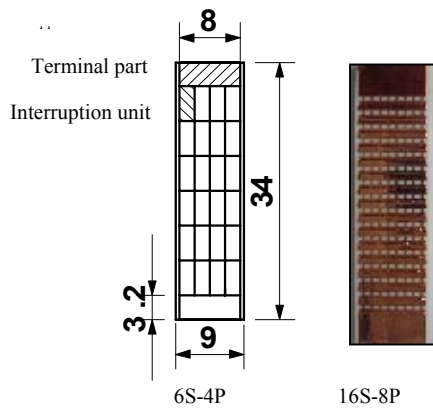


Fig. 2: Fuse structure (units in mm).

Interruption units were formed on ceramic substrates of 34 mm long, 9 mm wide, and 1 mm thick. Three-dimensional structure was formed by leaving the thickness t of the current-interrupting part 0.015 mm and increasing the thickness T of the heat-radiating part to 0.1 mm. In each fuse the sum of the lengths of two terminal parts was 6.4 mm and the sum of all the lengths designated W in Fig. 1 was 20.4 mm.

The sum of the widths b in the test fuses for the P -effect tests, for which the series number S was 6, was 3 mm. The dimensions of each part of the P effect test fuses, for which the target resistance was 3.62 m Ω , are listed in Table 1.

The sum of the lengths H in the test fuses for the S effect test, for which the parallel number P was either 8 or 32, was 7.2 mm. The dimensions of each part of the S effect test fuses, for which the target resistance was 5 m Ω , are listed in Table 2 (for $P=8$), and Table 3 (for $P=32$).

Table 1. Element dimensions (mm) of P effect test fuses

Type	b	Σb	H	ΣH	c
6S-4P	0.750	3.0	1.2	7.2	0.2
6S-8P	0.375	3.0	1.2	7.2	0.2
6S-16P	0.188	3.0	1.2	7.2	0.2
6S-32P	0.094	3.0	1.2	7.2	0.2

Table 2. Element dimensions (mm) of S effect test fuses with $P=8$

Type	b	Σb	H	ΣH	c
4S-8P	0.25	2	1.8	7.2	0.2
8S-8P	0.25	2	0.9	7.2	0.2
12S-8P	0.25	2	0.6	7.2	0.2
16S-8P	0.25	2	0.45	7.2	0.2
24S-8P	0.25	2	0.3	7.2	0.2

Table 3. Element dimensions (mm) of S effect test fuses with $P=32$

Type	b	Σb	H	ΣH	c
4S-32P	0.0625	2	1.8	7.2	0.2
8S-32P	0.0625	2	0.9	7.2	0.2
12S-32P	0.0625	2	0.6	7.2	0.2
16S-32P	0.0625	2	0.45	7.2	0.2
24S-32P	0.0625	2	0.3	7.2	0.2

3. The interruption test circuit

The principal part of the interruption test circuit (Fig. 3) is a resonance circuit having a 10 kV 14,000 μ F capacitor and an air-core inductor. The voltage in the resonance circuit is stepped down through the inductor. The test was done under conditions assuring a maximum resonance current of 100 kA (50 Hz) and a recovery voltage higher than 850 V.

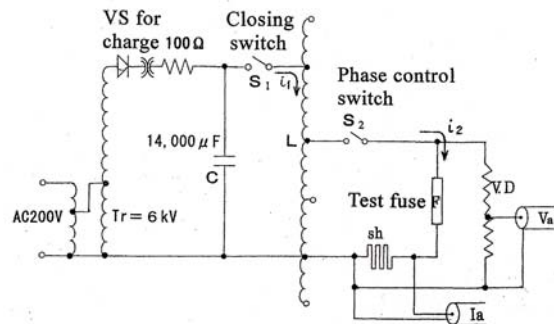


Fig. 3: Interruption test circuit.

4. Oscillograms of interruption tests

The S effect is demonstrated by the results shown in Fig. 4, which were obtained with of 8S, 16S, and 24S 8P fuses having square type interruptions. Note that the cut-off currents are approximately 2,000 A, while the maximum arc voltages became higher and the I^2t values became lower than the expected values inversely proportional to the increase of S .

The test results obtained with a 24S-32P fuse are shown in Fig. 5. Note that increasing P from 8 to 32 decreased the cut-off current from more than 1,500 A to about 1,300 A and decreased I^2t from 224 A²s to 79 A²s. From Figs. 4 and 5, we might think that before the current cut-off point P effect is more effective than the S effect in keeping the cut-off current low and that after the current cut-off point the S effect is more effective than the P effect in keeping the I^2t value low.

5. Experiment results on the P effect

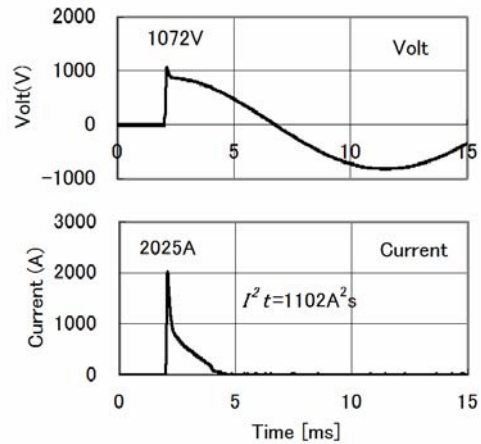
The P effect test results obtained with 4P, 8P, 16P, and 32P 6S fuses with square type interruption units are summarized in Table 4.

Table 4. P effect test results for 6S fuses

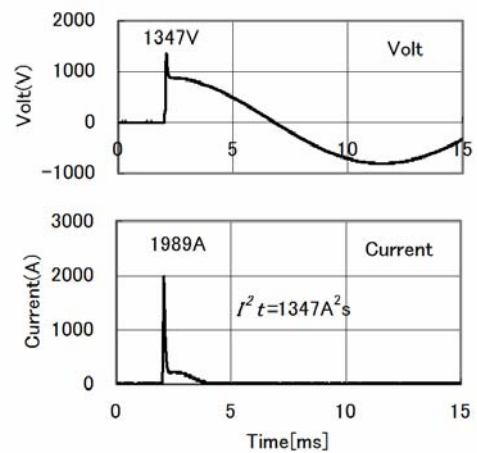
Type	I^2t [A ² s] (Resistance[mΩ])			
	Sample 1	Sample 2	Sample 3	Average
6S-4P	1,770 (4.2)	1,172 (4.9)	1,466 (4.6)	1,469 (4.6)
6S-8P	1,652 (3.9)	1,197 (4.5)	1,133 (4.6)	1,327 (4.3)
6S-16P	1,374 (3.8)	768 (4.7)	831 (4.6)	991 (4.4)
6S-32P	1,288 (4.2)	713 (5.1)	863 (5.1)	955 (4.8)

Analysis of variance was applied to evaluate their significance because the data in Table 1 showed much dispersion. It is confirmed that more than 95 % of data is accurate. The average I^2t values listed in Table 4 are plotted in Fig. 6.

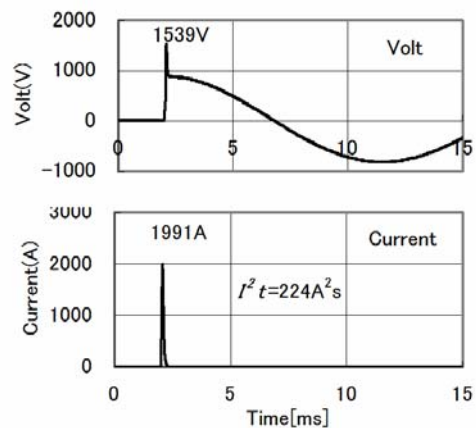
When the P effect is normalized by setting the I^2t value for the 6S-8P point in Fig. 6 to 100 %, the parameter r (the resistance of the fuse) is eliminated and the P effect without the influence of r can be expressed by the percentage change. The normalized P effect is shown in Fig. 7, which shows that the I^2t for a 6S-32P fuse is only 72 % that for a 6S-8P fuse.



(a) 8S-8P



(b) 16S-8P



(c) 24S-8P

Fig. 4: Oscillograms of interruption tests obtained with 8P fuses.

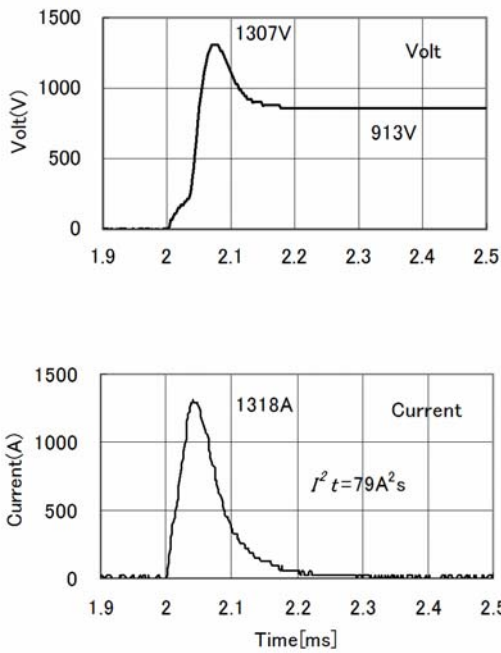


Fig. 5: Oscillograms of interruption tests of 24S-32P.

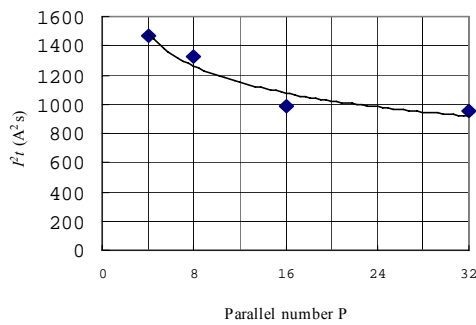


Fig. 6: Parallel number P - I^2t characteristic (6S series).

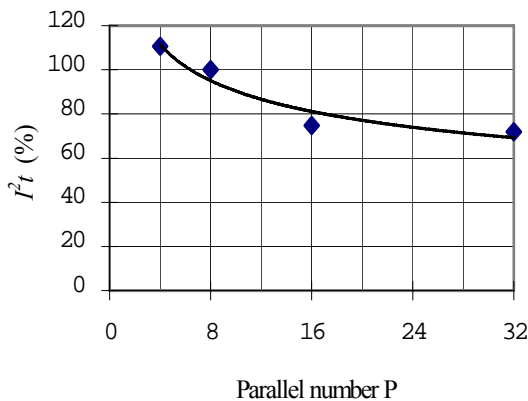


Fig. 7: Normalized P effect.

Increasing the number of parallel interruption points in a fuse element divides an arc into smaller ones, and thus makes the pre-arcing time shorter and the cutoff current smaller. This is why I^2t initially decreases with increasing P . As shown in Fig. 7, however, when there are too many parallel interruption points the likelihood of interaction between adjacent arcs and thus of restriking increases and limits the decrease in I^2t . To obtain further improvement of current-interruption performance, we need to arrange the interruption points in a pattern that prevents restriking. One way to do this is to adjust the number of interruption points arranged in series.

6. Experiment results on the S effect

6-1. Test fuse element patterns

The test fuses for the S-effect tests were 4S, 8S, 12S, 16S, and 24S 8P and 32P fuses with $t \times \sum b \square$ 0.03 mm².

6-2. Results of experiments with the 8P series

The experimental results and estimated I^2t values are listed in Table 5.

To evaluate the dependence of I^2t on parameters such as the series number S , we need to take into account the relation between I^2t and resistance. As we can see from the data listed in Table 5, resistance increases with increasing S . The corresponding I^2t values for fuses with the target resistance were estimated as follows. The I^2t values calculated from the test result listed in Table 5 were plotted on log-log paper as shown in Fig. 8. Then straight lines having a slope inversely proportional to the square of resistance were drawn through the points plotted for each value of S . According to our experiments I^2t values were inversely proportional to the square to the 2.5th power of resistance. In this experiment former relation was applied.

Table 5. S effect test results for 8P fuses

Type	Test result		Presumed value
	Resistance(mΩ)	$I^2t(A^2s)$	$I^2t(A^2s)$ at 5 mΩ
4S-8P	4.3	4,604	3,405
8S-8P	5.0	1,012	1,012
12S-8P	5.4	403	470
16S-8P	5.8	329	443
24S-8P	6.6	224	390

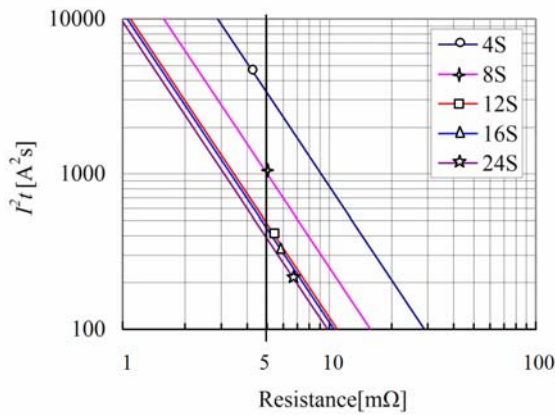


Fig. 8: Resistance - I^2t characteristics (8P series).

The I^2t values at the intersections of the 5 mΩ line in Fig. 8 and each of the straight lines we drew in that figure give are listed in Table 5 as presumed values and are plotted in Fig. 9, showing the S effect at 5 mΩ. From Fig. 9 the I^2t value for a 6S-8P fuse is estimate to be 1650 A²s. The I^2t value of the 24S-8P fuse (390 A²s) is thus only about 24 % that of the 6S-8P fuse.

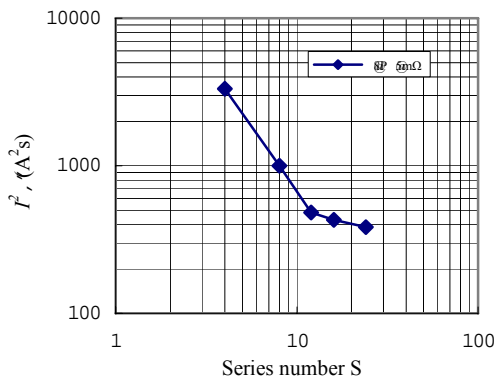


Fig. 9: S - I^2t characteristics (for the 8P series).

The total arc voltage of a fuse element can be calculated as the product of the arc voltage of one interruption point and the series number S , because the arc voltage of each arc is almost the same. Since increasing the series number S makes the arc voltage of the fuse higher. It decreases I^2t as shown in Fig. 9. When S is too large, however, isolated arcs between terminals can degrade current-interruption performance. For the element pattern used in the present experiments, currents were successfully interrupted by fuses with S numbers as large as 32 (described in the next subsection). Additional plating between interruption points might block the expansion of an arc and prevent arcs from unifying.

6-3. Results of experiments with the 32P series

The experimental results and presumed I^2t values are listed in Table 6. Presumed I^2t values were obtained by the same process described in subsection 6.2. The relation between presumed I^2t values at 5 mΩ and series number S is shown in Fig. 10, where one sees that the decrease of I^2t with increasing S is greater than that seen in Fig. 9. This may be due to synergy of the P and S effects.

Table 6. S effect test results and presumed I^2t values at 5mΩ for 32P fuses

type	Test result		Presumed value
	Resistance(mΩ)	$I^2t(A^2s)$	$I^2t(A^2s)$
4S-32P	4.4	4,166	3,226
8S-32P	5.6	538	675
12S-32P	6.1	167	249
16S-32P	5.8	123	166
24S-32P	6.0	79	114

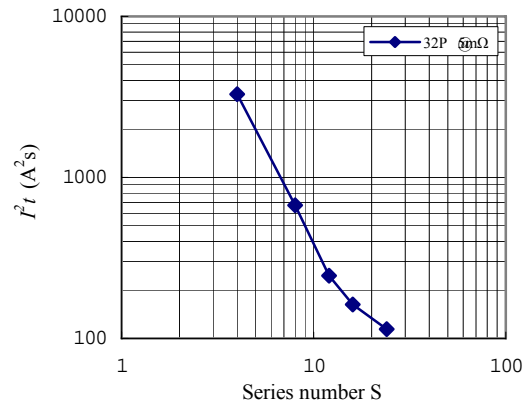


Fig. 10: S - I^2t characteristics (for the 32P series).

7. Synergy of S and P effects

The characteristic curves shown in Figs. 9 and 10 are plotted together in Fig. 11 for comparison. The I^2t value for the 24S-8P fuse is 390 A²s (Table 5 and Fig. 9). If the S and P effects were independent of each other, we can see from Fig. 7 that the P-effect would reduce the I^2t value for the 24S-32P fuse by about 28 %, or from 390 to 280.8 A²s. The experimental results obtained with the 24S-32P fuse, however, showed that its I^2t was actually 114 A²s, or only 8.6% that of the 24S-8P fuse. This much smaller value than expected decrease in the I^2t value reflects the synergy of the S and P effects.

The cause of this synergy is not clear, but it could be that current-interruption performance deteriorates because the P effect becomes ineffective when the parallel number P is greater than 16. If this deterioration were due to the restriking of arcs and the S effect suppressed this restriking, the current-interruption performance would be improved much

more than expected from P and S effects independently. Identifying the cause of this synergistic effect will require further experimental investigation.

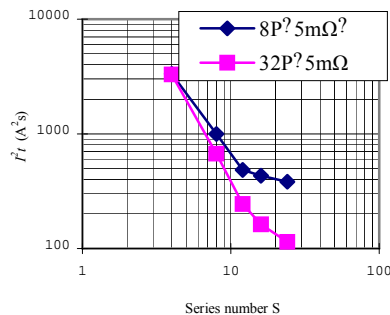


Fig. 11: $S - I^2t$ characteristics for 8P and 32P series.

8. Rated current test

We carried out a temperature-rise test on a 16S-16P fuse having the round type of interruption units and a resistance of 4.9 mΩ. The test yielded a rated current of 45 A.

9. Conclusion

An advantage of etched fuses is that the patterns of their interruption units can easily be made extremely small, so their numbers S and P of series and parallel interruption points can be large. This is important because the I^2t value for a 24S-32P fuse, with a resistance of 4.9 mΩ, is only 8.6% that of a 6S-8P fuse.

Highly serial and parallel fuses for practical use cannot be made without reducing the cost of their production and the decreasing the resistance of their elements, but we think that the low I^2t values of these fuses justifies their higher production cost. We also think that because the patterns in these fuses are so small, it will be necessary to repeatedly carry out such reliability tests as tests of deterioration due to oxidization, repeated overload tests, and continued turning-on -off- electricity tests.

References

- [1] Takahashi H. and Hirose K.: "A semiconductor fuse-link on a ceramic substrate", *Proc. of the 4th International Conference on Electric Fuses and their Applications (ICEFA), Nottingham (UK), 1991*, pp.92-95.
- [2] Flat fuse range for IGBT case protection, Ferraz Shawmut publication no. 06/2001 Ref.J601021A, edition 06/2001.
- [3] Wright A. and Newbery P.G.: "Electric Fuses", 2nd edition, The Institution of Electrical Engineers, London, UK, p.94, 1995.

- [4] Asayama M., Ishikawa Y., Hirose K., Kobayashi S., and Yamano Y., "Improvement of etching fuse performance by element pattern design", *IEEJ Trans. on Power and Energy*, Vol. 127-B, No.3, pp.522-530, 2007 (in Japanese).
- [5] Asayama M., Ishikawa Y., Hirose K., Yamano Y., and Kobayashi S.: "Breakdown characteristic of the high voltage etching fuse", *Proc. of the 5th International Workshop on High Voltage Engineering, Hamamatsu (Japan), March, 2007*, pp.65-70.

COMPARISON OF ELECTRICAL BEHAVIOUR BETWEEN THE LIQUID METAL CURRENT LIMITER AND THE LOW VOLTAGE MELTING FUSE

Mitja Koprivšek

ETI Elektroelement d.d.,
Obrezija 5, SI-1411 Izlake, Slovenija,
mitja.koprivsek@eti.si

Abstract: Liquid Metal Current Limiter (LMCL) is in previous literature shown as a possible way how to realize a protection device which can break the short circuit current for several times. This article analyses the behaviour of LMCL and his functional principles under short circuit current conditions. The main part of this article consists of analysis of electrical behaviour of a melting fuse and LMCL under same testing conditions. At the end, the conclusions are made regarding future research.

Keywords: Liquid Metal Current Limiter, Low Voltage melting fuse, short circuit current.

1. Introduction

Switchgear devices in general are made for following functions:

- Distribution of electrical energy
- Control of electrical consumers
- Protection of people, animal and equipment against electrical shock

Main functions are:

- Connecting
- Switching
- Disconnecting
of circuits

To fulfil various demands, many different devices with main functions were developed. A lot of switching principles have been developed to fulfil demands from different switching processes.

From electro technical point of view, switching event is a process where impedance is changed for a large scale, e.g. from $1\text{m}\Omega$ to $10\text{M}\Omega$ in a time of milliseconds. This fact requires use of different switching principles according to different parameters of the circuit.

Switching devices, where the switching event is concluded with current zero within normal sinus wave, has no protective function. Protective function in such a case is connected with the capability of a device to reduce the thermal effect due to I^2t let-

through energy and dynamic effect due to the let-through current I^2 .

Switching devices with current limitation as protective function are:

- Circuit breakers
- Current limiters
- Fuses

It is true that not all Circuit breakers has current limitation properties. Those with "current zero" arc quenching principle cannot be counted in above mentioned switching devices. Nowadays, more and more circuit breakers are designed as current limiting devices. On the other hand fuses and current limiters has strong current limitation property

This article will show functional principles of Melting Fuses and Liquid Metal Current Limiter (LMCL) and comparison of electrical behaviour of Melting fuse and LMCL, where LMCL is self-restoring current limiter, with another words, LMCL has reproducible and repeatable current limitation behaviour.

2. Melting fuses, functional principles

Following Figure Fig1 shows a diagram of electrical behaviour of melting fuse under short circuit condition. It is known from the literature, that short circuit current limitation is provided by arc voltage, which is higher than network voltage. Melting and arcing phases are also clearly shown on Fig1 [1]

On one hand, the fuse is very economic and efficient short circuit protective device, on the other hand it has only one main disadvantage, namely, the fuse link has to be replaced by the maintenance crew and in the mean time this part of installation is without supply of energy. The question is, how to create a short circuit protection device, which is able to cut the short circuit fault current for several times without replacement. One of the possible answers is Liquid Metal Current Limiter.

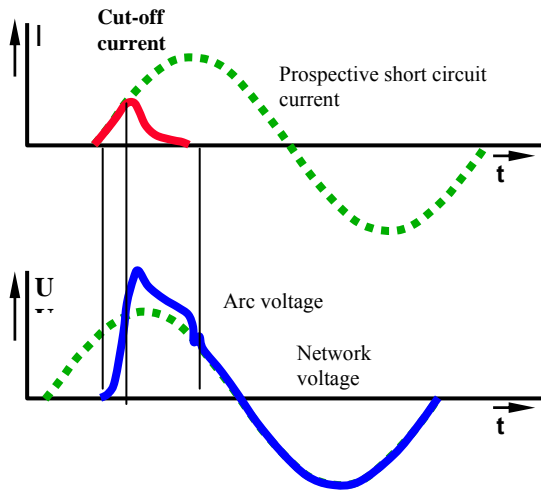


Fig 1: diagram of electrical behaviour of melting fuse under short circuit condition

3. Liquid Metal Current Limiter

Nowadays there is an increasing demand of use of electrical energy, especially in industrial sector. These demands are shown through the following criteria:

- Higher short circuit power available
- Higher system voltages (specially in industry)

On the other hand, a demand for selectivity has to be considered in case of several protective devices connected down stream in the installation. In case of an error, only the last protective device has to break the current. Thus, the higher availability level of an electrical energy is provided.

Another demand is more and more important in low voltage installation, and that is how to prevent the exhaust of hot gases out of the breaker. In the future, all switching devices, which are working on the principle of contacts, will have to be closed in housings. On the fig.2 above we can see the principle of LMCL, consisting from enclosure where liquid metal is separated with several spacers. In each spacer there is at least one spacer channel. On both ends there are electrodes and terminals for electrical connection of LMCL.

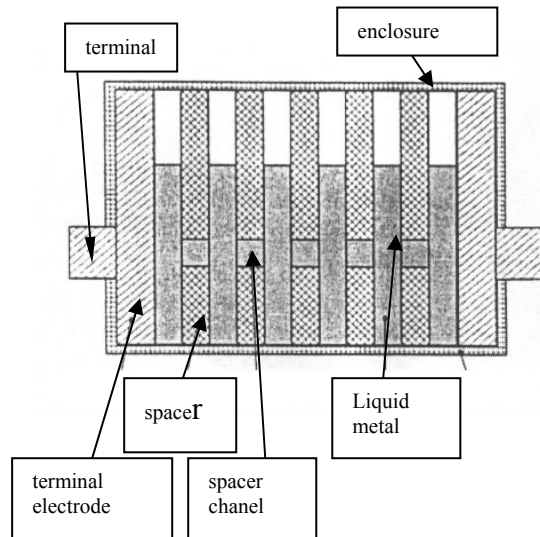


Fig 2: Construction of LMCL

3.1 Material behaviour and functional principle:

Liquid metal is very interesting conductive Gallium-Indium-Tin alloy (GaInSn). This alloy is non-toxic and is also used in various medical applications. In investigations [3] an eutectic alloy was used, with lowest melting point. The most important physical properties given at 20°C are shown in table 1.

Table 1: physical properties of GaInSn alloy

Melting point	g_M	10.5°C
Boiling point	g_E	> 2000°C
Density	ρ	6.4 g/cm ³
Electrical conductivity	σ	3571(Ω mm) ⁻¹
Thermal coefficient (el.)	α	0.00088 K ⁻¹
Specific heat capacity	c	320 J/kgK
Heat of evaporation	h_E	3337 kJ/kg
Thermal conductivity	λ	35 W/mK

»Self pinch-off« effect is a consequence of electromagnetic forces in liquid metal. Usually, it appears between contacts in classical switchgear devices when contact material is melted. The cause of pinch effect is geometrical instability of magnetic field. This instability in LMCL, is caused by spacers and spacer channels. Fig 3 shows the current density and magnetic field instability. The model on Fig 3 is described in [5].

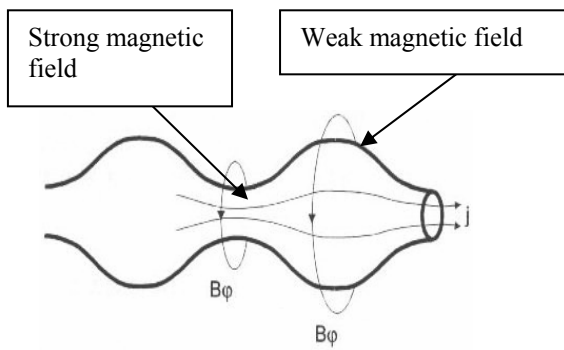


Fig 3. Geometrically unstable magnetic field

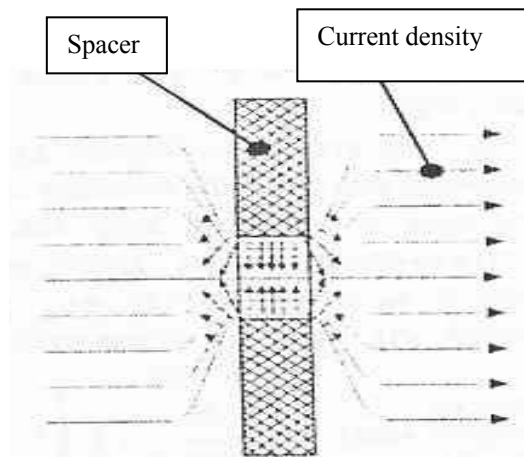


Fig 4. Pinching of liquid metal

Fig 4 shows one spacer channel and direction of magnetic forces, which are the cause of liquid metal separation and arc ignition [2]. According to [3] the highest pressure is in the axis of the channel. In [5] following equation is presented:

$$p(r) = \mu_0 \frac{I^2}{4\pi^2 r^2} \left[1 - \left(\frac{r}{R} \right)^2 \right] \quad (1)$$

Where

$p(r)$: Is pressure in liquid metal related to the radius in the channel

R : Radius of the channel

4. Comparison of electrical behaviour between the low voltage melting fuse and the LMCL

First of all, the construction of both devices was compared.

4.1. Comparison of construction features:

A construction of LV melting fuses type NH00 with rated current 100A and some data are presented in [4].

Current density

- Melting element NH00 100A
 - o Copper strip: width=18mm, thickness=0.18mm, cross-section = 3.24mm²
 - o Length: 38mm
 - o Constriction: width=2.4mm, thickness=0.18mm, cross-section=0.432mm²
 - o Length of each constriction: 2.0 mm
 - o Cross-section ratio between melting element and constriction: 3.24/0.432= 7.5: 1
 - o Number of constrictions: 5
 - o Specific conductivity of basic material: E-Cu: 58 (m/Ωmm²)
- LMCL:
 - o In [3] the number 15 of spacer channels are recognized. The contribution to arc voltage is given only by 6 or 7 spacer channels which can be compared with constrictions on melting element.
 - o Ratio between spacer channel and the rest of current path in LMCL: 7: 1 [2]
 - o Exact dimensions of LMCL are not presented.
 - o Resistance of LMCL before the test is not presented in the literature.
- Comparison of conductivity and dimensions between the melting element of the fuse and the LMCL:
 - o Comparison of conductivity:
 - Specific conductivity of copper: 58000 (Ωmm)⁻¹
 - conductivity of copper is 16.2 greater than GaInSn alloy,
 - specific conductivity of GaInSn alloy: 3571 (Ωmm)⁻¹

Comparison of melting fuse and LMCL shows very good similarity of both constructions, especially in ratio of constriction and normal current path.

4.2 Comparison of pre-arcing process in melting fuse and LMCL:

Melting Fuse: Pre-arcing time depends on quantity of thermal energy I^2t , caused by the current through the melting element. It also depends on the construction of constriction and material behaviour, namely, on melting point.

LMCL: From literature [3] it is known that the pressure in liquid metal depends on I^2 . In the same literature the time for liquid metal separation is also calculated. In principle, this pre-arcing time can be compared with melting time in fuses. It is estimated that the pre-arcing time in LMCL depends also viscosity of the liquid metal, especially at high currents where the liquid metal flow speed is higher. It is also estimated that the pre-arcing time depends on the pressure in the volume between the liquid metal and the enclosure (see Fig.2)

4.3. Diagram of short circuit breaking in LMCL

[2]:

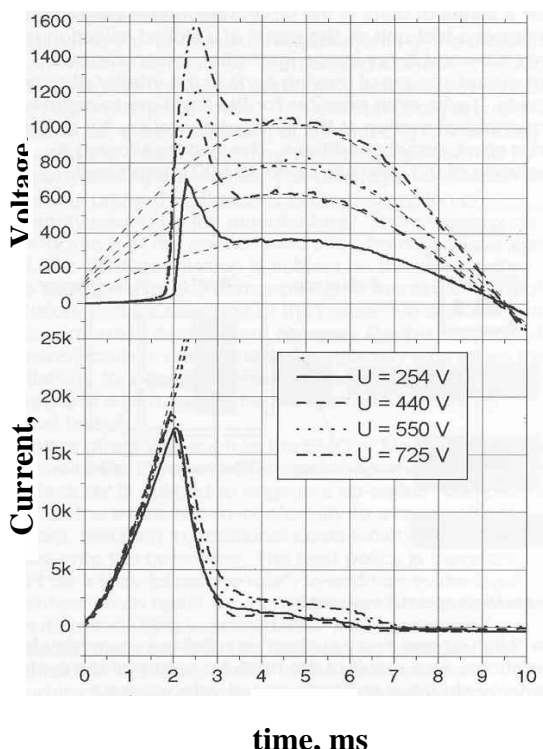


Fig 5: Diagram for voltage and current in LMCL

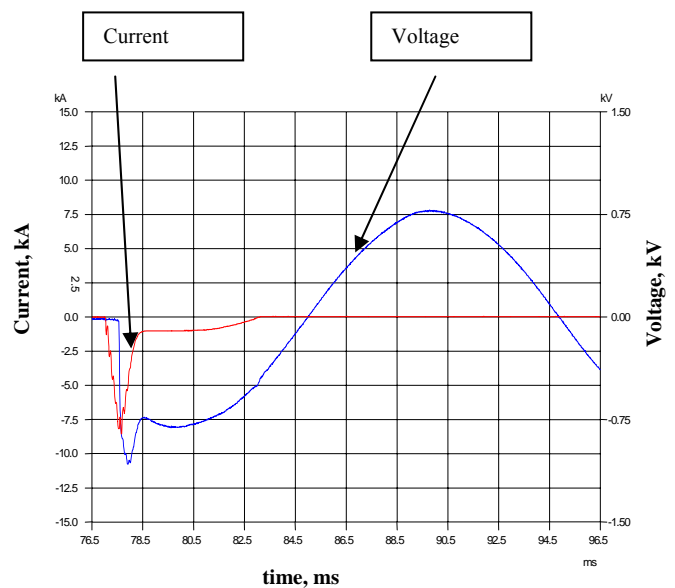
Testing Voltage $U_p = 550$ V
 Prospective short circuit current $I_p = 50000$ A
 Cos fi: 0.22
 Switching angle according to voltage: 5°
 Let-through current I_d : 16.000 A
 Arc Voltage U_{obl} : 1.200 V
 Pre-arcing time: 1.8 ms

4.4. Diagram of short circuit breaking in Low Voltage melting fuse type NH00 [4]:

Testing voltage $U_p = 554$ V
 Prospective short circuit current $I_p = 50500$ A
 Cos fi: 0.18
 Switching angle: 0°
 Let-through current I_d : 8.200 A
 Arc Voltage U_{obl} : 1.050 V
 Melting time: 0.6 msec
 Other data:

- Resistance in cold status: 1.2 m Ω
- melting integral: 6.870 A²s
- switching integral: 24.460 A²s

Comparison of both diagrams on Fig 5 and Fig6 shows that the pre-arcing time in LMCL is longer than the one at the fuse.



4.5. Comparison of an arc phase in melting fuse and LMCL:

Melting fuse: from the literature the process of melting the copper strip is known. For the comparison with LMCL is important that also in the case of melting fuse Pinch-effect is mentioned as a cause for putting the melted metal apart which is followed by an arc. Metal vapours are present in the arc channel only for a very short time. Very soon arc channel is filled with silica sand vapours. Silica sand has lower point of evaporation than the copper. Arc

plasma in the rest of arcing phase has the properties defined by SiO₂ vapours.

LMCL: in the literature there is no data about the heat transportation process to the surrounding and the cooling of an arc. But it is clear that in the LMCL liquid metal has also the role of cooling media. Arc channel is filled mainly with metal vapours [3].

5. Conclusions:

As a conclusion of presented work we can say the following:

- Electrical behaviour, that means current and voltage during the short circuit breaking in LMCL and melting fuse, are very similar at the same testing conditions,
- Presented comparison leads us to a conclusion that at further investigation on LMCL, experience from melting fuses could be used,
- There is no commercial product based on GaInSn alloy as liquid metal reported.
- GaInSn alloy as liquid conductor probably has no future in commercial use because of its price,

In low voltage switchgear technique laws of magnetohydrodynamics are used. One of the possible ways in future research could be serial connection of LMCL and LV breakers, where instead of liquid metal, other material, for instance materials on basis of nanotechnologies could be used.

References:

- [1] Mitja Koprivšek, Magistrsko delo, Univerza v Mariboru, marec 2005,
- [2] A.Kraetzschmar, F.Berger, P.Terhoeven, S.Rolle: *Liquid Metal Current Limiters*, Moeller Gmbh, Bonn,
- [3] F.Berger, O.Duehr, A.Kraetzschmar, P.Terhoeven: *Physical Effects and Arc Characteristics of Liquid Metal Current Limiters*, Moeller Gmbh, Bonn.
- [4] Technical data and test reports, ETI d.d., Izlake, 2003 - 2004.
- [5] F.Cap, *Lehrbuch der Plasmaphysik und Magnetohydrodynamik*, Springer Verlag 1994, stran 161.

INTRODUCTION TO ARC FLASH

M. Lang, T. Neal and R. Wilkins

Ferraz Shawmut, 374 Merrimac St, Newburyport, MA 01950, USA mike.lang@ferrazshawmut.com
Neal Associates Ltd., 106 Leetes Island Road, Guilford, CT 06437, USA nealassoc@earthlink.net

Abstract: Arc flash hazard calculations used to predict the magnitude of the heat hazard are based on tests with open-tip vertical electrodes in enclosures. Arc ratings for PPE are developed using opposing electrodes. Tests with electrode configurations that forced the arc plasma jets outward from the box yielded significantly higher heat energy measurements. When placed within this directional plasma flow, protective flame resistant (FR) fabrics yielded significantly lower arc ratings.

Keywords: arc flash hazard, current-limiting fuses, electric fuse, current limitation, arc rating, ATPV.

1. Introduction

The last 15 years have seen tremendous progress being made in protecting workers against the heat energy associated with arc flash. One major area of improvement has been the steps taken to get workers into safer clothing. The arc rating system developed by ASTM and the development of the predictive equations identified in NFPA70E and IEEE1584 have been instrumental in this effort.

At the center of these developments has been arc flash testing. The arc thermal performance value (ATPV) of electrical personal protective equipment (PPE) relies on arc flash tests performed in a high power test lab. The IEEE 1584 equations were developed empirically from arc flash tests performed in North American test labs from the late 1990s through 2002.

Recent research into arc flash phenomena, however, indicates that workers could be under-protected against the heat generated during an arc flash event. Test results presented at IEEE conferences [1-3] and at the 2007 IEEE Electrical Safety Workshop show that different configurations of electrodes (conductors) yielded heat energy higher than current predictions due to the directional nature of the arc development. Additionally, initial tests of PPE, when placed within this directional plasma flow, did not provide the level of thermal protection predicted by its ATPV.

2. Directional nature of arc development

Unrestricted high-current arcs move according to magnetic forces to increase the area of the current loop. Currents flowing in the opposite direction in parallel conductors give rise to forces that drive the arc away from the source to the end of the conductors where they typically burn off the tips of electrodes (busbars).

The behavior of a 3-phase arcing fault in equipment is very chaotic, involving rapid and irregular changes in arc geometry due to convection, plasma jets and electromagnetic forces. Arc extinction and re-ignition, changes in arc paths due to restriking and reconnection across electrodes and plasma parts and many other effects add to this chaotic nature and make it difficult to create equations for accurate predictions of its properties (e.g. impedance). Although it does not capture this chaotic behavior, Fig. 1 demonstrates an arc's general directional nature. The alternating 3-phase current creates successive attractive and repulsive magnetic forces, dramatically moving the plasma jets which feed an expanding plasma cloud. The cloud is driven outward, away from the tips, creating "plasma dust" as the highly energized molecules in the plasma cool, then recombine into various materials. The molten electrode material ejected off the tips also is in this flow.

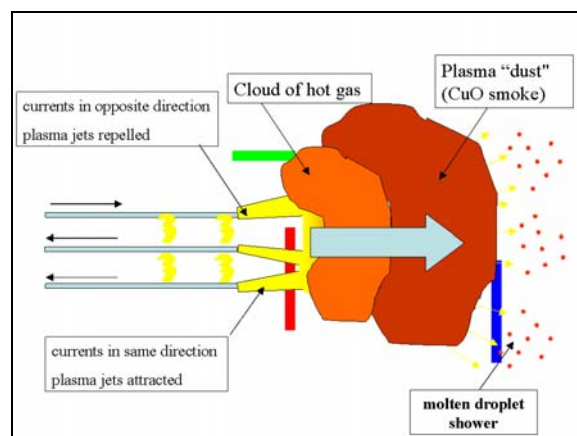


Fig. 1: The general directional nature of an arc; this depiction does not reflect chaotic behaviour.

3. Arc flash hazards

When the arc is being established, current begins passing through ionized air generating massive quantities of heat. Large volumes of ionized gases, along with metal from the vaporized conductors, are explosively expelled. As the arc runs its course electrical energy continues to be converted into extremely hazardous energy forms. Hazards include the immense heat of the plasma, radiated heat, large volumes of toxic smoke, molten droplets of conductor material, shrapnel, extremely intense light and a pressure wave from the rapidly expanding gases.

Recent tests have shown that an object in the expanding plasma cloud (refer to the red object in Fig. 1) is directly exposed to the highest heat of the event. Temperatures greater than 15,000 C have been cited for this area. In addition to the convective heat transfer from the plasma, this object is directly exposed to the molten metal ejected from the electrode tips and radiated heat from surrounding plasma.

Objects close to the arc but outside of the plasma jets (refer to the green object in Fig. 1) are not likely subjected to as high a quantity of heat. Exposure is predominately radiant heat, but includes convective flow from the thermal expansion of the gases. Objects in line with the electrodes but distant from the plasma jets (refer to the blue object in Fig. 1) receive lower convective heating and less radiant heat and molten metal spray.

The amount of heat absorbed varies with the method of heat transfer and receiving surface properties. For example, the amount of heat transferred from a mass of molten copper to a surface area would be greater if it adhered to the object instead of contacting it for a brief time.

4. Current test setups used for standards

Although the overriding principle of electrical safety is to de-energize equipment and place it into an electrically safe condition prior to work, there are numerous cases where companies put workers in PPE to perform tasks on energized equipment. The standards typically utilized to predict the magnitude of heat exposure and the protective ability of flame resistant (FR) fabric worn by exposed workers are based upon two unique electrode configurations in their test procedures as explained below. Heat transferred during tests with these orientations is most likely dominated by radiant heat.

4.1. NFPA 70E

First issued in 1979, NFPA 70E, Standard for Electrical Safety in the Workplace [4] covers the full range of electrical safety issues, from work practices to maintenance, special equipment requirements and

installation. In the 1995 edition, arc flash hazards were first addressed with the addition of "arc flash hazard boundaries," with the equations based on arcs in open air. "Arc-in-a-box" equations were added to the 2000 edition as options to calculate a worker's potential heat energy density exposure. These equations came from results of arc flash tests with a steel box and vertical electrodes with open tips [5-6] as shown in Fig. 2. The 2004 edition added the IEEE 1584 equations below.



Fig. 2: Open-tip vertical electrode configuration

4.2. IEEE 1584

Issued in 2002, IEEE 1584TM-2002, Guide for Arc Flash Hazard Calculations, [7] provides guidelines for an analysis to "identify the flash-protection boundary and the incident energy at assigned working distances throughout any position or level in the overall electrical system." The results from over 300 arc flash tests were incorporated into the low-voltage predictive equations for enclosed equipment contained within IEEE 1584. Three enclosure sizes were used in these tests, but all tests also used the vertical electrodes with open tips shown in Fig. 2.

4.3. ASTM 1959

The current edition of ASTM F1959, Standard Test Method for Determining the Arc Rating of Materials for Clothing, [8] uses a single phase opposing electrode orientation. This standard determines the ATPV rating of material used in arc rated PPE. The test procedure places materials in locations surrounding the area where the arc would occur. The majority of the heat transferred to the material is likely radiated from the arc. This open air arrangement from the 1980s would simulate flashovers on overhead power systems.

5. Effects on heat measurements with alternate test configurations

Research performed at Ferraz Shawmut's High Power Test Laboratory has uncovered electrode configurations that project significantly more heat energy out of enclosures toward worker locations

than currently predicted by the standards. To simulate components found in low-voltage electrical equipment, various setups were created for controlled testing. Heat was measured and compared with predictions of IEEE 1584 for switchgear. Results of these comparisons were published in two recent IEEE papers. [2-3] Configurations that forced the arc's plasma jets outward toward the worker produced heat measurements nearly twice those predicted by current IEEE 1584 equations when studied at typical working distances of 18 inches.

All arrangement described below are variations of an arrangement described in IEEE 1584 [1]. These test setups used a 508mm x 508mm x 508mm steel box with one side open. 3-phase arcing tests were conducted at 208V, 480 V and 600V. The gap between electrodes was 32mm and the distance between the electrodes and the back of the box was 102mm. Incident heat energy was measured with an array of 9 copper calorimeters as described in the IEEE 1584 test procedure. Photographs of the arcs were captured from video taken with a FASTCAM high-speed camera, at up to 10 000 frames per second. The station back up breaker was typically set at 6 cycles to limit arc duration.

5.1. Vertical Configuration

In the vertical configuration setup used in the IEEE1584 test program, the electrodes entered the box from the top. The electrode tips were open and 254 mm from the bottom of the box. This setup simulates equipment where bussing is vertical and open-ended such as a main-lugs panel.

The arc development, similar to that described for Fig. 1, will be downward toward the bottom of the box in this case. As described in [2], there is an outward convective flow due to the thermal expansion of the gases and not magnetic forces. Photo of the arc development is shown in Fig. 3. Most tests resulted in heat measurements consistent with the predicted levels of IEEE1584.



Fig. 3: Front view of arc development from vertical test 3ms into event.

5.2. Barrier Configuration

In the barrier configuration, the electrodes of the vertical setup are “terminated” into a block of

insulating material (barrier) as shown in Fig. 4. This setup represents conductors connected to equipment fed from the top.



Fig. 4: Barrier test configuration simulating the line side connections of top fed equipment.

With the barrier in place, the arc's downward motion is halted and plasma jets are formed along the plane of the barrier top surface (i.e. perpendicular to the plane of the electrode). [3] This significant finding is demonstrated in Fig. 5. The photo on the top shows a side view of arc development along the plane of the barrier in a setup without side panels. The photo at the bottom shows the same test but recessed in the box. This test shows the possibility of higher convective heat transfer toward workers than the open vertical setup. The barrier configuration also ejected significantly more molten electrode material.



Fig. 5: Side view of arc development from barrier tests 4ms into a 42kA, 480V event. Open configuration (Top) and in a enclosure (Bottom).

Chart I compares heat measurements (made with copper calorimeters) with the barrier setup to standard predictions. The black line represents predictions of IEEE 1584 equations for switchgear (508mm cubic box) for the available fault currents with a fixed 6-cycle clearing time. Alarmingly, the barrier test results almost always rose above the line—sometimes more than twice the prediction.

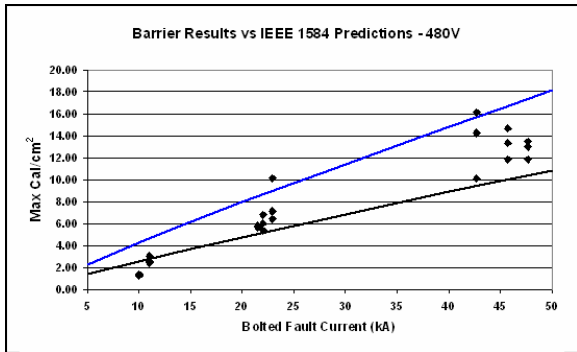


Chart I: Comparison of barrier results to predictions of IEEE 1584 equations for switchgear. The black line represents prediction; the blue line is 167% of the prediction.

5.3. Horizontal Configuration

Another configuration that deserves serious consideration is the “horizontal electrode configuration.” This setup simulates equipment where bussing is open-ended, but pointing toward the front of the enclosure, like that in the equipment shown in Fig. 6.



Fig. 6. The horizontal test setup was designed to simulate back-fed equipment like this unit (Left); side view of plasma flow at 8 milliseconds into a 44kA 600V arcing event for electrodes recessed in the horizontal setup test box (Right)

When the electrodes are horizontal and fed from the back, the arc development is very similar to that described for Fig. 1 and is shown in Fig. 7. In the top picture of Fig 7 the electrodes were brought to the front of the box, clearly showing the plasma jets formed on the tips of the electrodes. In the bottom picture, the electrodes were moved to 104 mm from the back of the box. Although the plasma jets are not

visible there is a greater outward flow, since the walls of the enclosure give a more focused expansion of the plasma.

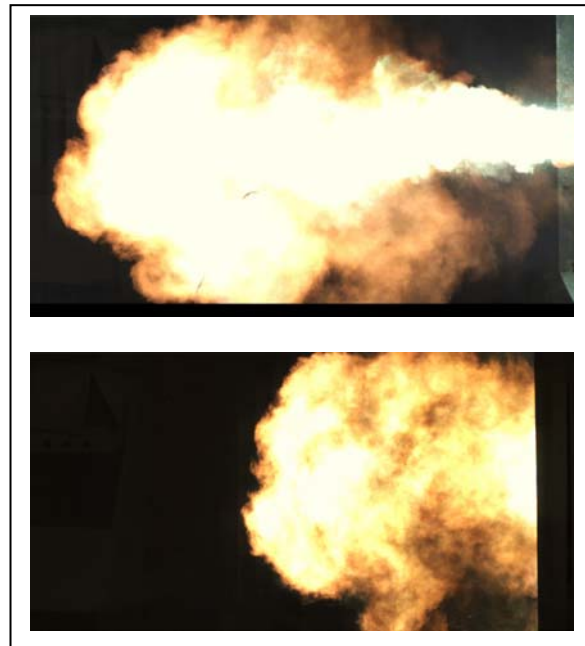


Fig. 7. Side view of plasma flow at 8 milliseconds into a 44kA 600V arcing event for horizontal electrodes. Electrode tips are flush with the front of the box (T) and recessed to 104mm from the back of the horizontal setup test box.

Like the barrier configuration, all tests resulted in heat measurements significantly above the predicted levels. In some case, the incident heat energy density was near three times that of the vertical tests.

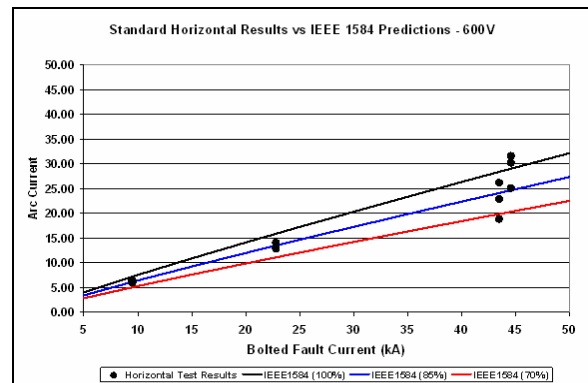


Chart II: Comparison of arc currents from horizontal tests to predictions of IEEE 1584 equations for switchgear. Note that some of the test results were below even the 85% value recommended by the standard.

Of equal concern is the fact that arcing currents were below predicted levels for this configuration (see Chart II). In some applications, clearing times will be significantly longer than expected if the arcing current is too low to operate the short circuit element of the upstream overcurrent protective

device (OCPD). In these applications, the increase in arc flash heat energies will be far greater than the differences obtained in tests with a fixed clearing time of six cycles.

5.4. Tests with current-limiting fuses.

A number of tests with current-limiting fuses showed, with proper fuse selection, that workers will be exposed to far less heat energy even when standing in locations subject to the plasma flow (Fig. 8). The results were very close to those predicted by current IEEE 1584 equations for all configurations. Plants currently employing this conservative method of protection will still need to recalculate arc fault currents and determine if fuses will be operating in their current-limiting modes for arc faults on equipment with horizontal electrodes.

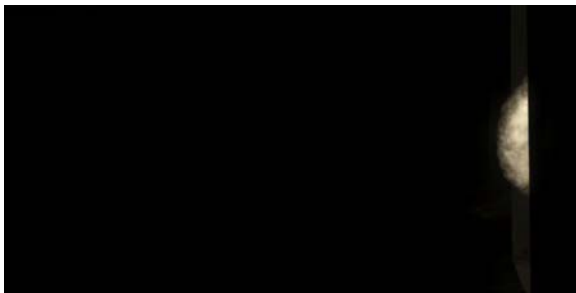


Fig. 8: Photo of maximum reach of plasma with current-limiting effect of 600A UL Class RK1 fuses. Test conditions are the same as those described in Fig. 7.

6. Effects of alternate configuration tests on PPE

Preliminary investigations showed that many protective FR fabrics did not yield the same level of thermal protection when placed within the directional plasma flow for the barrier configuration. Tests were performed with FR fabric placed at 18 inches from the electrodes of the vertical, barrier and horizontal configurations (Fig. 9) for fabric test setup. A variety of currents and clearing times were used in these 480V tests to generate a range of heat energies for the tests.



Fig. 9: Fabric test setup with barrier test (Left); Front view of bare and fabric covered calorimeter (Right)

There were surprising results with the barrier and horizontal tests, as some fabrics performed at only 50% of their arc ratings. Initial testing of the vertical

configuration also indicated that the arc rating of FR fabrics is reduced. It is suspected that greater heat transfer through the material because of the increased convective energy component is responsible for its decreased performance in the plasma-rich region of the arc. Equally surprising results were obtained for arc rated faceshields, which exhibited an increased arc rating. This would be expected since, unlike the permeable FR fabrics, faceshields are impermeable to the increased convective energy component.

7. Moving forward

There are two major areas of improvement for better protection of workers against the heat of arc flash events. Both areas are related to the possibility that workers could be directly immersed in the developing plasma flow described in the foregoing text.

First, equipment configurations that would direct arc development outward need to be clearly identified and models developed to better predict the levels of heat energy that can be presented to workers from arc flashes in such equipment.

Second, the test method and a modified arc rating system for PPE need to be developed to address the reduced performance of PPE for hazards involving equipment configurations that would direct the plasma flow outward toward the worker.

Arc flash hazard analysis studies will be more important than ever. As better models of arc faults become available, users will be able to quickly update and assess situations where greater hazards will be expected.

For those who have already completed studies, it is strongly recommended that you review these studies and implement projects to mitigate the hazards wherever possible. Among other things, actions should include standardizing on UL Class J fuses and switching Class H, K and RK-5 fuses to RK-1s. Lower threshold currents provide the widest range of current-limiting operation and lowest energies. Tests with all configurations yielded results of 0.5 cal/cm² or less when fuses operated in their current-limiting modes.

Until further testing is done, consider modifying your PPE strategy as follows. If equipment is suspected to be similar to the alternate plasma flow configurations described above, then consider the rating of protective clothing to be half the listed arc rating. When using the NFPA 70E Tables 130.7(C)(9)(A) and 130.7(C)(10) to select protective clothing and PPE, add one Hazard Risk Category number to HRC0, HRC1, HRC2 and HRC3. For HRC4 hazards, avoid using the Tables or select PPE with a rating of at least 80 cal/cm².

8. Industry action

Leading organizations concerned with electrical safety are currently investigating the results of the research outlined in this article. The IEEE 1584 working group has joined with the NFPA 70E committee to form the IEEE/NFPA joint collaborative initiative on arc flash research. The goal of this research is to provide the information and knowledge needed to enhance safety standards that predict the hazards of arc flash events and improve safeguards for workers. The research and test planning committee has already developed a comprehensive test protocol to further quantify these findings and investigate the many other hazards of arcing events (e.g. pressure waves, sound, toxic smoke).

Additionally, the ASTM F18.65 subcommittee on Wearing Apparel has formed a task force to further study the performance of materials in the plasma flow. The task force will identify any needed modification or additions to the test protocols of ASTM F 1959F/ F1959M-06a for material performance.

References

- [1] Stokes, A.D. and Sweeting, D.K. "Electric Arcing Burn Hazards", IEEE PCIC Conference Record, 2004. Paper PCIC-2004-39, 9pp.
- [2] Wilkins, R., Allison, M. and Lang, M. "Effect of Electrode Orientation in Arc Flash Testing", IEEE Industry Applications Conference, 40th IAS Annual Meeting, Hong Kong, 2-6 October 2005, pp 459-465.
- [3] Wilkins, R., Lang, M. and Allison, M. "Effect Of Insulating Barriers In Arc Flash Testing" IEEE PCIC Conference Record, 2006. Paper PCIC-2006-6, 6pp
- [4] Standard for Electrical Safety in the Workplace, NFPA 70E, 2004 Edition. National Fire Protection Association
- [5] Neal, T.E., Bingham, A.H. and Doughty, R.L. "Protective Clothing Guidelines for Electric Arc Exposure." IEEE Transactions on Industry Applications, Vol. 33, No 4, July/August 1997, pgs. 1043-1054
- [6] Doughty, R.L., Neal, T.E., and Floyd II, H.L. "Predicting Incident Energy To Better Manage The Electric Arc Hazard On 600V Distribution Systems." Proc IEEE PCIC, Sept. 1998, pgs. 329-346
- [7] IEEE Guide for Performing Arc-Flash Hazard Calculations. IEEE Standard 1584, IEEE, September 2002.
- [8] ASTM F1959/F1959M-06a Standard Test Method for Determining the Arc Rating of Materials for Clothing

THEORETICAL AND EXPERIMENTAL DETERMINATION OF EROSION RATE FOR SILVER CONTACTS UNDER 14 VDC

A. Lefort⁽¹⁾, M. Abbaoui⁽¹⁾, D. Sallais⁽²⁾, N. Ben Jemaa⁽³⁾, E. Carvou⁽³⁾

University Blaise Pascal, LAEPT Laboratory, 63177 Aubière, France⁽¹⁾,
Andre.Lefort@univ-bpclermont.fr⁽¹⁾, Mhammed.ABBAOUI@univ-bpclermont.fr⁽¹⁾
Metalor Technologies (France) SAS, Contacts Division, BP 29, 28190 Courville-sur-Eure, France⁽²⁾,
damien.sallais@univ-rennes1.fr⁽²⁾
University of Rennes 1, PALMS Laboratory, 35042 Rennes, France⁽³⁾,
nouredine.ben-jemaa@univ-rennes1.fr⁽³⁾, erwann.carvou@univ-rennes1.fr⁽³⁾

Abstract: Erosion rate of electrical contacts is a fundamental parameter to understand and evaluate the performances of contact materials and their breaking devices such as the life time. In this study, we have focused our interest on the erosion in automobile applications under the 14 VDC power network.

The experimental apparatus, adapted to perform contact breaking in similar conditions to the automotive relays, ensures arc duration control by artificial quenching, with a constant arc current close to 40 A. Erosion rates of the electrodes were determined by weighing before and after 5000 breaking operations..

In parallel, theoretical study based on a finite element calculation is conducted. A three-dimension simulation gives erosion volumes and liquid volume evolution versus time.

To improve erosion resistance and avoid welding of the silver contacts at make, composites with additives, a one-dimension simulation was made to calculate erosion rate of such contact materials, except for AgSnO₂.

Keywords: silver contacts, erosion, contact material phase changes, silver metal-oxide alloys.

1. Introduction

Anode and cathode erosion rates in switches and relays are fundamental parameters to improve breaking device life time. The most common measurement of erosion is the mass change of the contacts, determined by weighing of the electrodes, before and after electrical tests. In this work, we attempt to determine erosion rate under 14 VDC, 40 A, by finite element simulation and by taking into account mass transfer between the anode and the cathode.

A time dependant anode thermal flux combined with a variable cathode spot repartition were considered to evaluate the mass exchanges between electrodes and liquid and vapor volumes evolution

versus time, and were compared to experimental results.

These calculations were led, first with a 3D axisymmetric geometry for Ag contacts, and then extended to metal oxides ZnO and CdO with a 1D model.

2. Experimental results

2.1. Test equipment and procedures

The experimental apparatus is a fully automated device which has been widely described in previous paper [1,2]. It is adapted to perform contact breaking in similar conditions to the industrial switches and relays. It is mainly composed of an electrical module (power supply, variable resistance and inductance) and of a mechanical part (stepping motor) which insures the separation between the moving contact (cathode) and the fixed contact (anode) with a controlled constant speed v in the range 1-50 cm/s. The main measuring instrument is a digital scope which samples and stores arc voltage V_a and arc current I_a during the break.

In addition, a parallel thyristor has been used to ensure arc duration control by artificial arc quenching. This latter component is gated at a given time T_d after arc ignition (figure 1) and stopped the arc discharge.

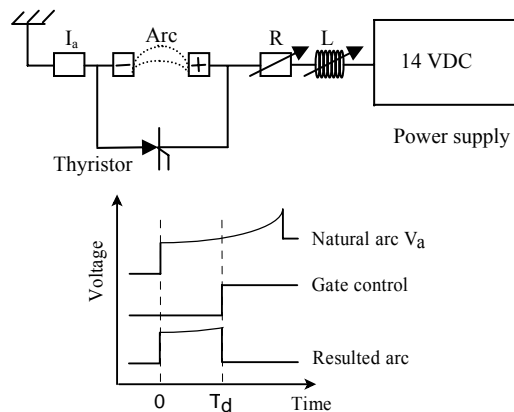


Fig. 1: Synoptic of the apparatus.

An high inductive load of 50 mH (time constant $L/R = 140 \text{ ms} \gg T_d$) keeps constant arc current close to 40 A, as it is shown in figure 2. This allows us to consider the field of bilateral erosion (bilateral losses of the anode and the cathode).

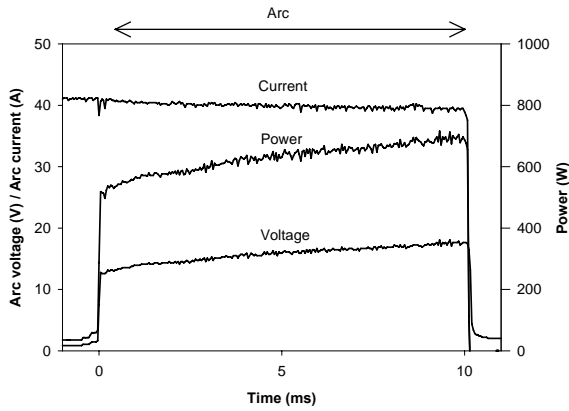


Fig. 2: Voltage, current and power characteristics of an arc adjusted to $T_d=10 \text{ ms}$, 14 VDC, 40 A, 20cm/s.

Contact materials used for this study are pure silver rivets (figure 3). The anode is flat while the cathode is bombed (10 mm radius).

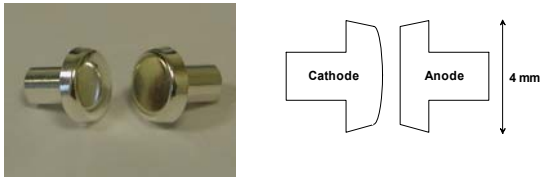


Fig. 3 : Silver rivets.

2.2. Silver erosion.

Experiments were performed for a wide arc length range (from 1 μm to 2000 μm). This allows us to consider the different fields of material transfer [3]: anodic (from the anode to the cathode), then in the reverse direction with a cathodic mass transfer (from the cathode to the anode), and at last the bilateral erosion for high arc lengths (bilateral losses of the both electrodes).

For each arc duration T_d , the same contacts pair performs 5000 operations under arc on break and null current on make in the following conditions: 14 VDC, 40A, opening speed of 20cm/s. Anodic and cathodic mass variations are determined by micro-weighing and averaged over three tests. Figure 4 shows the mass variations of anode and cathode versus arc length for pure silver.

3. Theoretical analysis and simulations

In this part, authors have focused their interest on the thermal flux received by the electrode surface at the junction with the electrical arc. For the anode,

energy is mainly transmitted by electrons, while for the cathode, metallic ions resulting for metallic vapour ionization, transfer energy to the electrode surface.

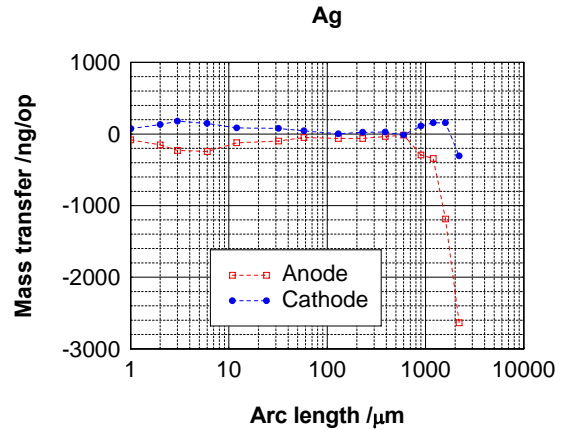


Fig. 4 : Mass transfer evolution versus arc length for pure silver contacts, 14 VDC, 40 A, 20cm/s.

3.1. Theoretical analysis

3.1.1. Anode energy flux

In the electric arc the anode spot collects the column electrons, JD Cobine and EE Burger [4] give an energy flux equation on the anode electrode surface:

$$P_{anode} = J_a \times (V_a + \varphi + V_T) + P_n + P_r \quad (1)$$

where J_a is the anode current density, V_a the anode voltage drop, φ the material work function, P_n the result of the energy of neutral atoms and P_r the radiant energy from the column. Usually the two last parts of equation 1 are negligible in comparison with the first part, V_T results of electron column flux. The incoming flux P_{anode} is transmitted to the anode surface, the part $P_{thermal}$ is transmitted to the electrode material, the part P_{es} is used to the emission of secondary electrons, and P_{rs} correspond to the photon emission so:

$$P_{anode} = P_{thermal} + P_{es} + P_{rs} \quad (2)$$

It is commonly admitted that the parts of the power used by the secondary electron emission, and by the material radiation are negligible comparatively to the power transmitted to the electrode. Approximations give:

$$P_{thermal} = J_a \times (V_a + \varphi + V_T) \quad (3)$$

3.1.2. Cathode energy flux

At the cathode, the energy flux balance [5] gives:

$$P_{cathode} = P_{ion} = P_{thermal} + P_{ec} + P_{rs} \quad (4)$$

where P_{ion} is the energy flux delivered to the cathode surface by the ions coming from the plasma

sheath. The energy flux P_{ec} is the result of the electron emission, but is negligible in comparison with $P_{thermal}$ [6]. Conclusions are similar for P_{rs} . The flux P_{ion} is given by [5]:

$$P_{ion} = (1-s) \times (V_c + V_i - \phi) \times J_c \quad (5)$$

V_c represents the cathode voltage fall, V_i the ionisation potential, J_c the total cathode current density and s represents the part of current resulting from the electron flux. With the approximations made above, the thermal power flux density $P_{thermal}$ directed on the cathode material surface is equal to the power flux P_{ion} given by the equation 5.

3.1.3. Conduction of heat in contacts

The electrode surface receives at the junction with the electric arc the thermal flux $P_{thermal}$. Energy is transmitted to the electrode material and dissipated by thermal conduction, by melting and vaporisation. To obtain the material solid-liquid-vapour and temperature evolution in each point, we solve, the enthalpy form heat equation contact, versus time t :

$$\frac{\partial H}{\partial t} = \text{div}(k\vec{\nabla}T) + \text{Source} \quad (6)$$

H , k and T represent respectively material enthalpy, thermal conductivity and temperature. The figure 5 precises the geometry used: the electrode is a Oz - axis cylinder; at time $t=0$, the thermal flux is applied on a circular surface whose centre is located at $z=0$ with a radius equal to r_a .

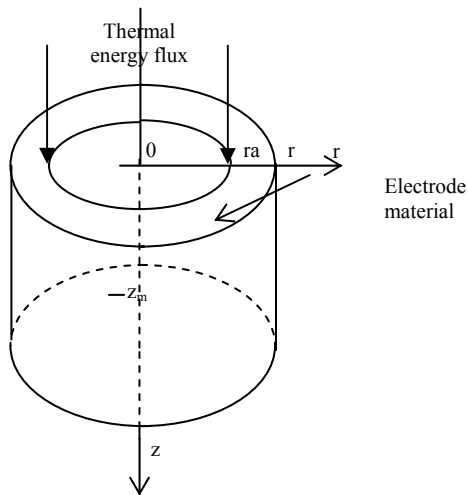


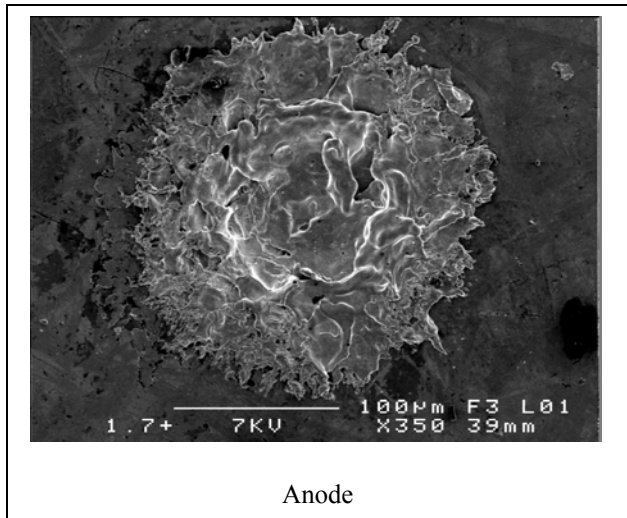
Fig. 5: The thermal energy flux is applied to the cylindrical electrode.

The numerical method is described in the paper of Rossignol [7] about 1D simulation. In 3D axisymmetric simulation, energy is transmitted in the Oz and Or directions instead of only in Oz direction. At $t=0$, each point is at room temperature with a specific enthalpy equal to H_0 . Then with the

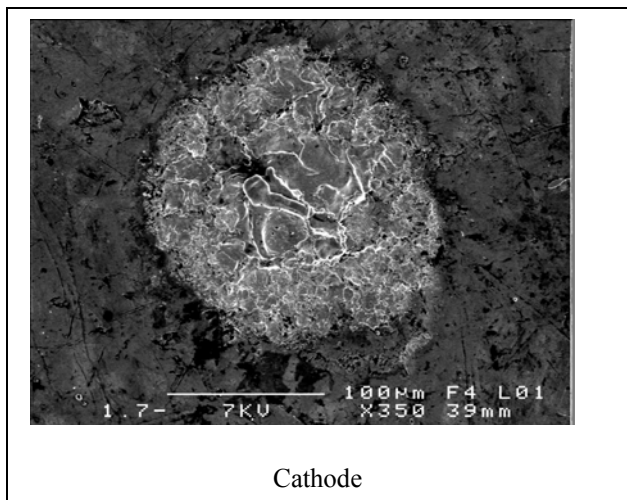
transmission of the energy by conduction starting from the surface circle, H involves to reach successively the specific liquefaction enthalpy and the specific vaporisation enthalpy liquid and vapour volumes appear. It gives versus time the liquid and the vapour volume evolution, erosion is defined by the vapour volume amount. Nevertheless this definition needs to be discussed in the comparison with experimental results. The studied domain is limited by the coordinate $z=z_m$ and $r=r_m$, the surfaces defined by these coordinates obey to the condition $H = H_0$.

3.2. Experimental results – Discussion

First, figure 4 shows that erosion and material transfer already occurs at the beginning of the contacts separation (for a few micrometers).



Anode



Cathode

Fig. 6: Anode and cathode spot surface for an arc length of 1.7 μm. Eroded areas exhibits a medium diameter of 109 μm for the anode and 91 μm for the cathode.

Microscopic observations, presented in figure 6, confirm this result. For such contacts separation values, we can't consider a single cathode spot, but a multispots distribution. The difference of surface area between the both eroded areas provides the influence radius of one cathode spot. With such a geometric analysis, we find 40 emission spots of 1 A each one. For the higher contacts separation distances, theoretical calculations are led with only one emission spot of 40 A.

To calculate the parameters defined in the paragraph 3.1, we consider, according experimental results shown in figure 4, that the anode erosion flux is equal to the cathode erosion flux. As the anode spot surface area does not evolve during the contacts separation, parameters for the anode are deduced from this assumption. Calculation gives then the erosion flux values. However, this method does not permit to determine the erosion rate presented in figure 9 for low time values (below $3.8 \times 10^{-4} s$). New cathode spot characteristics have also to be developed.

3.3. Parameters used for simulation

3.3.1. Anode parameters

With a defined anode surface area, a defined arc current value, and with T_e the medium temperature of electrons moving from the arc column towards the anode surface, the anode power flux is given by :

$$P_{thermal} = 1.07 \times 10^9 \times (V_a + 2kT_e + 4.63)$$

4.63 V corresponds to the extraction work of electrons for silver. To satisfy the conditions defined in the paragraph 3.2, it is necessary to impose : $V_a + 2kT_e = 2V$. In this case, the energy flux received by the anode spot is equal to $7.107 \times 10^9 Wm^{-2}$. However, this calculated energy flux value, uniform in time and space, leads to a vapor emission (responsible from material transfer) from the anode to the cathode starting from a time of $20 \times 10^{-6} s$. This result is not in good agreement with the experimental value (figure 4). Vaporization occurs earlier, so at the beginning of contacts separation, during the $40 \times 10^{-6} s$, the power density should be higher, time dependant and r-coordinates dependant, i.e. :

$$t \leq 3 \mu s$$

$$P_{thermal} = 4.4216 \times 10^{10} \times \left(1 - \frac{r^2}{1.881 \times 10^{-8}}\right)$$

$$3 \mu s \leq t \leq 4 \mu s$$

$$P_{thermal} = (1.34234 \times 10^{11} - 3.0006 \times 10^{16} \times t) \times \left(1 - \frac{r^2}{1.881 \times 10^{-8}}\right)$$

$$4 \mu s \leq t \leq 40 \mu s$$

$$P_{thermal} = 1.421 \times 10^{10} \times \left(1 - \frac{r^2}{1.881 \times 10^{-8}}\right)$$

$$t \geq 40 \mu s$$

$$P_{thermal} = 7.107 \times 10^9 Wm^{-2}$$

With such parameters, we consider that there is only a very few number of cathode spots (or no cathode spots) during the first microseconds (corresponding to an electrodes separation of about 1 μm). The main part of the dissipated power is received by the anode surface. After $40 \mu s$, the gap between the contacts, equal to $8 \mu m$, allows the development of cathode spots.

3.3.2. Cathode parameters

According to the equation 5 (paragraph 3.1.2) and to the following parameters for silver: electronic fraction ($s=0.8$), cathode fall ($V_c = 12.3V$), ionization potential ($V_i = 7.56V$), and electrons extraction work ($V_s = 4.63V$), the power flux transmitted to the cathode is only depending from current density J_c : $P_{ions} = 3.05 \times J_c$.

Erosion values defined in the paragraph 3.3.1 and results presented figure 4 lead to two kinds of cathode spots, allowing each one a current intensity of 1 A:

- in the contacts gap range : [0 μm (contacts closed) – 76 μm] :

$$J_c = 5 \times 10^{11} Am^{-2} ; r_c = 0.7979 \mu m ;$$

$$P_{ions} = 1.5246 \times 10^{12} Wm^{-2}$$

- in the contacts gap range : [76 μm – 240 μm] :

$$J_c = 1.3 \times 10^{12} Am^{-2} ; r_c = 0.4948 \mu m ;$$

$$P_{ions} = 3.9640 \times 10^{12} Wm^{-2}.$$

Calculations were not made for contacts gaps higher than 240 μm . In this case, the cathode spots number decreases up to one cathode spot, which insures the passage of a current of 40 A.

3.4 Simulation results

Figure 7 shows the solid-liquid and liquid-vapor transformed volumes versus arc duration, for a cathode spot with a current density equal to $J_c = 1.3 \times 10^{12} Am^{-2}$.

We can note on this figure, that anode and cathode exhibit similar behaviors: as the electrodes surfaces receive a thermal flux, first a liquid phase appears before vaporization. For short gaps, the emitted vapor is recovered by the opposite electrode. By using, for

exchanged flux, the results obtained with conditions described in paragraphs 3.3.1 and 3.3.2, we deduce the cathode mass profit. Theoretical and experimental results are presented figure 8. They are in good agreement.

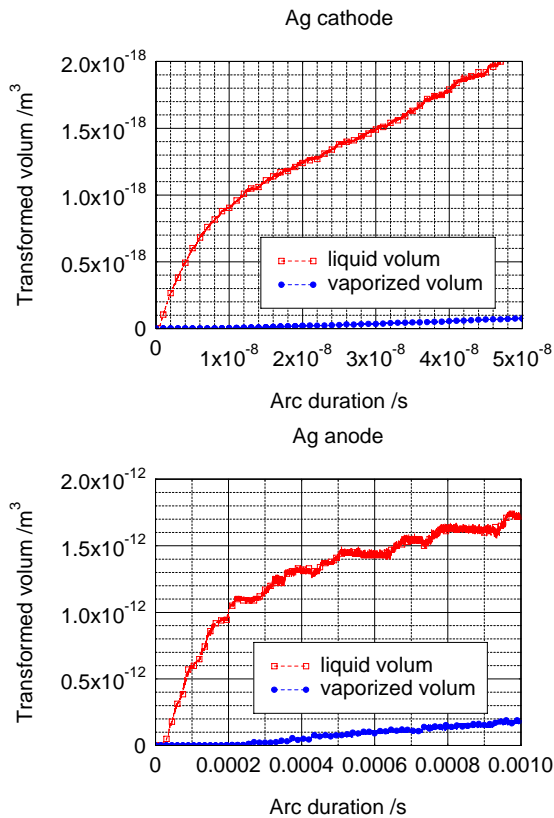


Fig. 7: Cathode and anode vaporized and liquefied volume evolution.

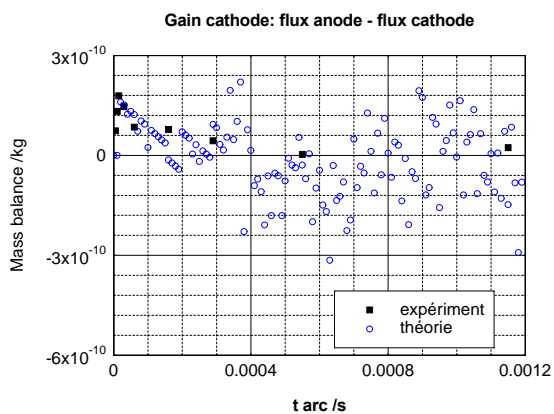


Fig.8: Comparison between theoretical and experimental results for the cathode.

4. Case of AgMeO

4.1 Simulation

Oxides grains disseminated in the Ag-matrix, exhibits an undefined form of a few micrometers,

whatever the elaboration process. In spite of their low electrical conductivity, they receive ions or electrons from the thermal flux transmitted to the electrodes, because of their small dimensions, either about arc root surface size for the cathode, or very lower than the anode spot area. By taking into account this assumption, a 3D-simulation of heating and phase changes for oxide grains is not necessary. In this work, a 1D-simulation was also realized to compare the both oxide ZnO and CdO with silver. Theoretical results are presented figure 9, for a thermal flux density in the range $[1.10^{11} \text{ W m}^{-2} - 5.10^{12} \text{ W m}^{-2}]$ for the cathode, and in the range $[5.10^8 \text{ W m}^{-2} - 1.10^{10} \text{ W m}^{-2}]$ for the anode.

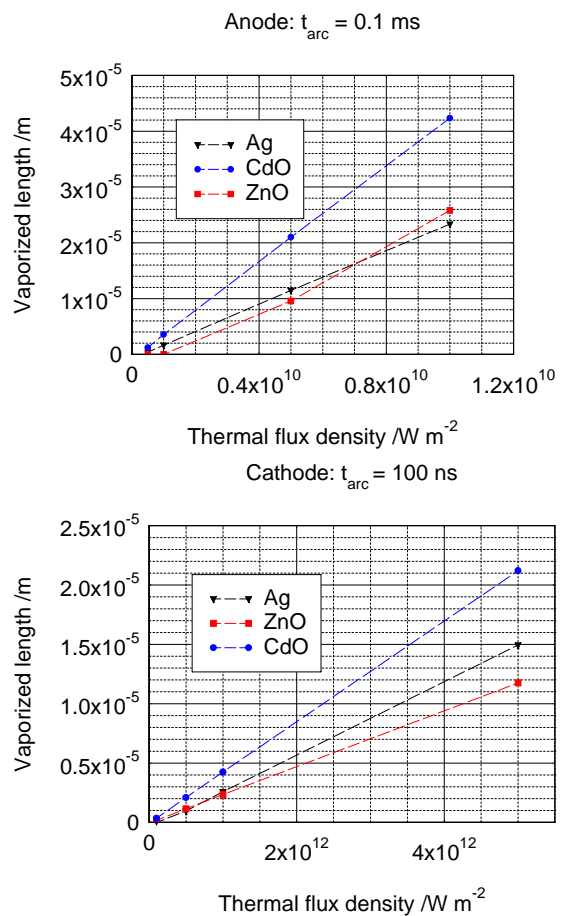


Fig. 9: Thickness of silver films and oxides films vaporized under arcing at the anode and the cathode.

First, we can note similar evolutions for oxides and silver. And the same behaviour is observed on the figure 10, which presents the vaporization speed versus thermal flux density, when only the vaporization is taken into account.

Simulation shows clearly, that the values obtained for silver are framed by those of both oxides. In addition, CdO exhibits a lower resistance against thermal flux in comparison with Ag and ZnO.

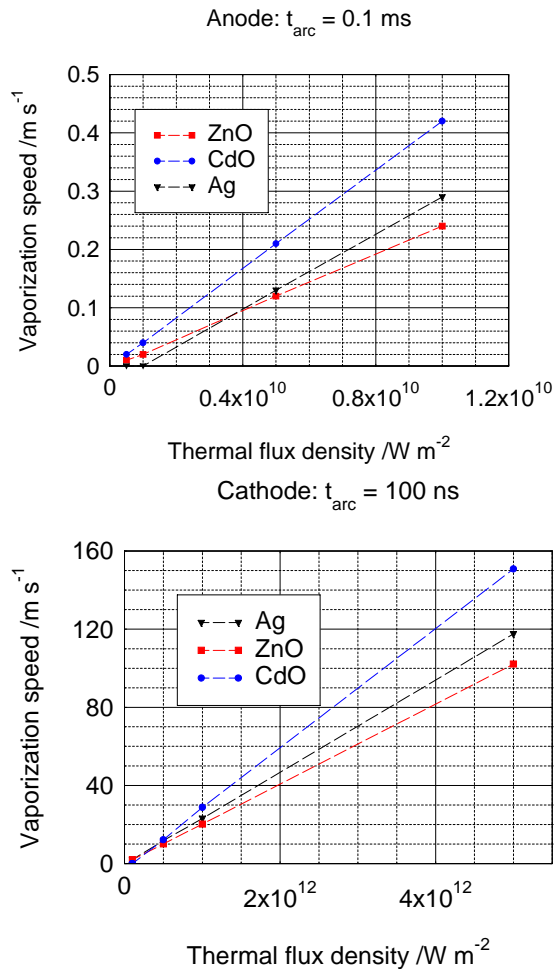


Fig. 10: Anode and cathode vaporization speed for Ag, CdO and ZnO.

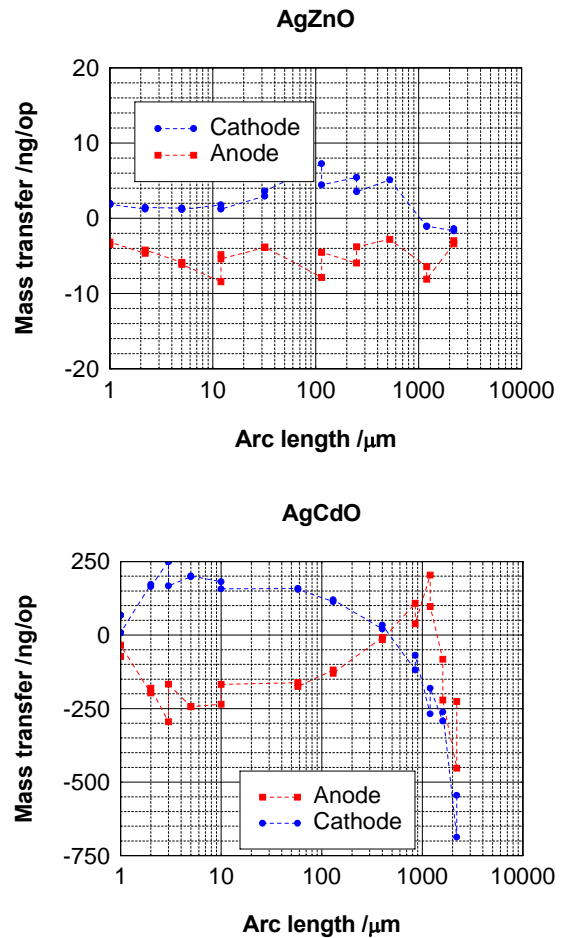


Fig. 11: Material transfer evolution versus arc length, for contacts in AgZnO and AgCdO.

4.2. Comparison with experimental results

Experimental results for pure silver and composites AgCdO and AgZnO are shown figures 9 and 10.

Experimental and theoretical results from figures 9, 10 and 11 show, that AgZnO exhibits the lowest transfer rates in comparison with Ag and AgCdO which transfers the largest amount of material.

5. Conclusion

The 3D finite element simulation for Ag contacts under 14 VDC and 40 A, leads to material transfer and erosion rates in good agreement with experimental results. To improve anti-welding properties, metal oxides, such as SnO_2 , ZnO, and CdO (nowadays forbidden for environmental requirements) are usually added to Ag-matrix in electrical contacts. Simulation for SnO_2 could not be carried out, because of the lack of physical constants for this oxide. However, a 1D calculation provide in this paper vaporization speed of ZnO and CdO, which bring response elements in the understanding of the behaviour of the composites AgMeO.

References

- [1] N. Ben Jemaa, L. Nedelec, S. Benhenda, "Break arc duration and contact erosion in automotive application", IEEE Trans. CPMT, vol.19, no.1, March 1996, pp.82-86.
- [2] N. Ben Jemaa, L. Doublet, L. Morin, D. Jeannot, "Break arc study for the new electrical level of 42 V in automotive applications", Proc. 47th IEEE Holm Conf. On EC, Montreal, Sept. 2001, pp.50-55.
- [3] N. Ben Jemaa, L. Morin, S. Benhenda, L. Nedelec, "Anodic to cathodic arc transition according to break arc lengthening", IEEE Trans. CPMT, vol.21, no.4, December 1998, pp.599-603.
- [4] Cobine J.D. and Burger E.E. "Analysis of Electrode Phenomena in the High-Current Arc", J. Appl. Phys., Vol 26, 1955, pp.895-8.
- [5] Lee T.H. and Greenwood A. "Theory of the Cathode Mechanism in Metal Vapour Arc", J. Appl. Phys. Vol 33, 1961, pp.916-23.
- [6] Lee T.H. "Energy Distribution and Cooling Effect of Electrons Emitted from an Arc Cathode", J. Appl. Phys., Vol. 31, 1960, pp. 924-7.
- [7] Rossignol J., Abbaoui M. and Clain S. "Numerical modelling of thermal ablation phenomena due to a cathodic spot", J. Phys. D : Appl. Phys. Vol. 33, 2000, pp. 2079-86.

NUMERICAL METHOD FOR PRE-ARCING TIMES: APPLICATION IN HBC FUSES WITH HEAVY FAULT-CURRENTS

S. Memiaghe, W. Bussière and D. Rochette

LAEPT, 24 av des Landais, 63177 Aubiere Cedex France, E-mail :steeve.memiaghe@univ-bpclermont.fr

Abstract: This work deals with calculations of pre-arcing time prediction for fuse links used in industrial protection circuits in case of heavy faults-currents. An enthalpy method to solve heat-transfer equation included two phase-changes is presented. The mathematical model couples thermal and electrical equations based on the principle of energy conservation and the Ohm's law respectively. In order to determine current density and temperature evolution in the fuses, three typical fuse links have been chosen for the calculations with circular, rectangular and trapezoidal reduced sections at their centre. Silver physical properties, mathematical equations and the numerical method are reported. Calculations results show that for the fuse link with rectangular reduced section a major heat-transfer mechanism took place compared to the other ones.

Keywords: High Breaking Capacity fuses, pre-arcing time, heavy fault-currents, Stefan problem, simulation.

1. Introduction

The fuses studied which common name is High Breaking Capacities fuses comprise four main elements: a fuse link (usually silver of high purity) with one or series reduced sections named notches in different checked shapes, the filling cavity (mechanically and thermally resistant), and the filling silica sand (or quartz) of high purity. HBC fuses operate in two stages, pre-arcing operation and arcing operation. The pre-arcing operation corresponds to the time from the apparition of a high fault current to the vaporization of the constricted sections and the disruption of the fuse link.

The modelling of the pre-arcing stage has been the object of several works until now. These theoretical works consist in semi-empirical modelling or physical modelling dedicated to the pre-arcing stage [1, 2]. The theoretical works dedicated to the pre-arcing stages proposed various models based on the heat transfer occurring into different fuses design [3-6]. In these models the end of pre-arcing operation is defined by the time to reach the melting temperature of the fuse element. Thus for pre-arcing time prediction calculations are

lead until melting temperature is reached. In this paper a model which considers the phase-changes to describe heat-transfer occurring in the fuse is presented. The model is based on the solution of the heat-transfer equation via an enthalpy formulation which allows taking into account two phase-change problems. This method also called *Stefan problem*, has been studied in [7] and it is useful in other thermal problems involving phase changes [8, 9]. Calculations are performed for three fuse elements with different reduced sections shapes located at their centre. In the case of short pre-arcing time (up to 10 ms), where the fuse-element temperature rising is almost adiabatic [8], a high overload current is applied, heat-loss is governed only by thermal conduction and other heat-loss mechanism are neglected. The heat-transfer equation is a mathematical equation coupling thermal and electrical equations.

We present in a first time, fuse-links geometries and physical properties of silver, following by the modelling equations, which stand for thermal and electrical phenomena, the imposed hypotheses of the model and the numerical procedure, are developed in section 3. In section 4 we show and discuss the numerical results.

2. Geometrical hypotheses and physical data

2.1. Fuse links description

The fuse links studied have circular, rectangular and trapezoidal reduced sections located at their centre.

The geometries of the three tested fuse elements are presented in figure 1. The fuse links have cross section and reduced section of respectively $le = 2.5 \times 0.105 \text{ mm}^2$ and $l'e = 0.5 \times 0.105 \text{ mm}^2$, where e is the thickness of the fuse link. The fuse links lengths are $L = 70 \text{ mm}$ and are made from pure silver strip (99.95%). The following areas are defined for the numerical treatment:

Ω fuse-element area, Γ_1 anode,
 Γ_2 cathode, $\Gamma_{3,4}$ fuse-boundaries

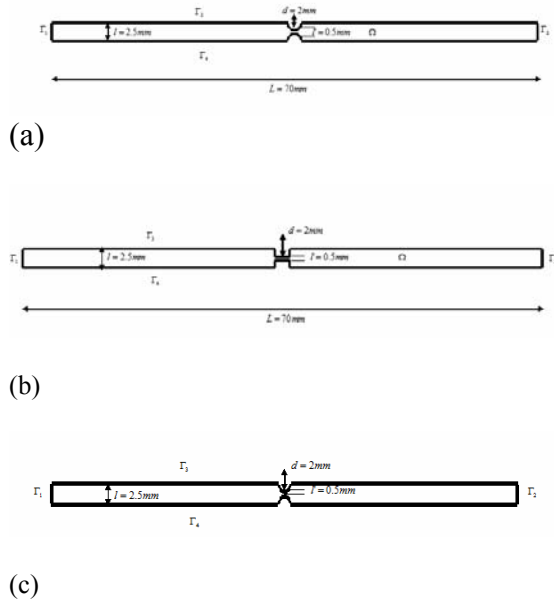


Fig. 1: 2-D geometries of the fuse links.

2.2. Physical properties of Silver

Table 1 presents thermodynamical data use in the computations; the parameters depending on temperature are given at reference temperature. The evolutions of the physical properties as functions of the temperature are in the following figures.

Table 1: Physical properties of the Silver

Silver density	$\rho = 10500 \text{ kg.m}^{-3}$ at 293 K
Thermal conductivity	$k = 452 \text{ W.m}^{-1}.K^{-1}$ at 293 K
Electrical conductivity	$\sigma = 64.17 \times 10^6 \text{ S.m}^{-1}$ at 293 K
Solid heat capacity	$c_s = 261.36 \text{ J.kg}^{-1}.K^{-1}$ at 293 K
Liquid heat capacity	$c_l = 310.4 \text{ J.kg}^{-1}.K^{-1}$ at 1235 K
Melting temperature	$T_m = 1235 \text{ K}$
Boiling temperature	$T_v = 2433 \text{ K}$
Melting latent heat	$L_f = 1.05 \times 10^5 \text{ J.kg}^{-1}$
Vaporization latent heat	$L_{vap} = 2.43 \times 10^6 \text{ J.kg}^{-1}$

The most used and complete thermal conductivities for silver are quoted in *Touloukian* tables [10]. Figure 2 presents silver thermal conductivity as a function of temperature for silver. It can be seen a strong decrease of thermal conductivity during the

solid to liquid phase-change. This thermal conductivity decrease is of :
 $k_s(T_m) - k_l(T_m) = 177.92 \text{ W.m}^{-1}.K^{-1}$.

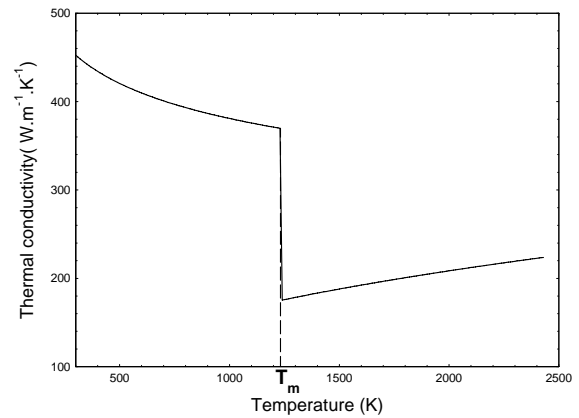


Fig. 2: Thermal conductivity versus temperature.

Figure 3 shows two type of data concerning electrical conductivity which occurs in the Joule heating term. The electrical conductivity has been measured (continuous lines) [11] and calculated (dashed lines) by means of *Wiedemann and Franz* law [12] which is written in terms of:

$$\frac{k}{\sigma} = L \times T, \quad (1)$$

where $L = 2.45 \times 10^{-8} \text{ V}^2 \text{K}^{-2}$ is the *Lorenz* coefficient, T is the temperature, k and σ are respectively the thermal and the electrical conductivity.

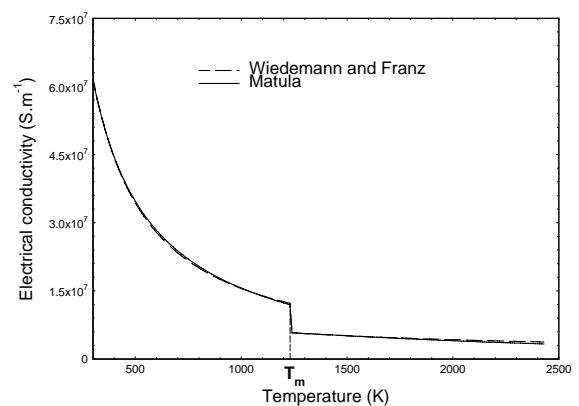


Fig. 2: Electrical conductivities versus temperature measured (dashed lines) calculated (continuous lines).

As electrical conductivity is concerned, it can be seen from the figure that an electrical conductivity

decreases of $\sigma_s(T_m) - \sigma_l(T_m) = 6.1037 \times 10^6 \text{ S.m}^{-1}$ when phase-change occurs.

A very good agreement is observed between the measured and the calculated values.

Figure 4 shows the enthalpy as a function of temperature. It can be seen from the figure two jumps named melting latent heat L_f and vaporisation latent heat L_v . This figure is an enthalpy formulation of the Stefan problem.

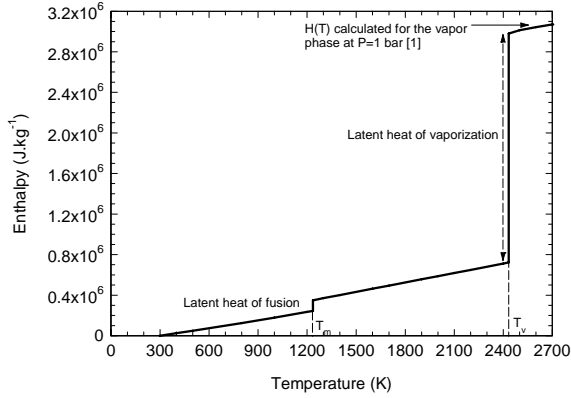


Fig. 3 : Enthalpy versus temperature [13].

3. Physical model of the fuse element heating and numerical method

Heat transfer equation is obtained by expressing heat balance equation, based on principle of energy conservation, expressing a balance between heat-loss mechanism and power injected:

$$\frac{\partial H}{\partial t} - \mathbf{div}.(k\mathbf{grad}T) = S, \quad (2)$$

Where H is the volumetric enthalpy, k is the thermal conductivity, T is the temperature. The source term representing the heat generated by Joule heating writes:

$$S = \frac{|\mathbf{J}|^2}{\sigma}, \quad (3)$$

where \mathbf{J} is the current density vector and σ is the electrical conductivity.

To solve numerically the heat equation, a reciprocal form of $H(T)$ is defined as $\beta(H(T)) = T$ [7], and the Stefan problem in enthalpy-temperature, with boundaries and initial conditions is given by the set of equations:

$$\begin{cases} \frac{\partial H}{\partial t} - \mathbf{div}.(k\mathbf{grad}T) = \frac{|\mathbf{J}|^2}{\sigma}, & \text{in } \Omega \times [0, t] \\ T = \beta(H), & \text{in } \Omega \times [0, t] \\ k(T) \frac{\partial T}{\partial \mathbf{n}} = 0, & \text{on } \Gamma_{1,2,3,4} \times [0, t] \\ H = H_0, & \text{in } \Omega, \text{ for } t = 0 \end{cases} \quad (4)$$

where H_0 is an initial condition stands for enthalpy at time $t=0$. The Joule heating in equation (3) is obtained by solving the following equations:

$$\begin{cases} \mathbf{div} . (\sigma \mathbf{grad} V) = 0, & \text{in } \Omega \\ \sigma(T) \frac{\partial V}{\partial \mathbf{n}} = \frac{I(t)}{|\Gamma_1|}, & \text{on } \Gamma_1 \times [0, t] \\ \sigma(T) \frac{\partial V}{\partial \mathbf{n}} = 0, & \text{on } \Gamma_{3,4} \\ V = 0, & \text{on } \Gamma_2 \\ \mathbf{E} = -\mathbf{grad} V, & \text{in } \Omega \\ \mathbf{J} = \sigma \mathbf{E}, & \text{in } \Omega \end{cases} \quad (5)$$

where V , \mathbf{E} and $I(t)$ are respectively the electric potential, the electric field vector and the electric current. \mathbf{n} is the outward unit normal to the boundary. We have prescribed the following boundary conditions:

- on Γ_1 defined as the anode, a Neumann condition is imposed for the current density flux;
- a Dirichlet condition for the potential in Γ_2 defined as the cathode;
- for the other boundaries a homogeneous Neumann condition is assumed.

To solve numerically the thermal electric problem (equations (4) and (5)), we use in the space discretization a standard finite element method [14], and the time integration of the heat equation (4) is performed by using a Chernoff scheme [7] which consists in the relaxation of the relation $H(T)$ (Figure 4).

4. Numerical results

Numerical results are given for the temperature, the Joule heating, the potential and the resistance evolutions for the three tested fuse links. For the evaluation of the pre-arcing time in fuse-links the calculations are led with the prospective current given by Equation (6) until the vaporization enthalpy is reached. For each fuse element the following voltage characteristics are used to remain in the short pre-arcing time domain: a maximum voltage of $\hat{V} = 300\sqrt{2} \text{ V}$.

The prospective current use in calculations is written as:

$$I(t) = \frac{\hat{V}}{\sqrt{R^2 + L^2 \omega^2}} \times \left(\sin(\alpha t + \theta - \varphi) - \sin(\theta - \varphi) \times e^{-\frac{R}{L}t} \right) \quad (6)$$

where \hat{V} is the supplied voltage, R is the resistive load, L is the inductive load, ω is the pulsation at 50 Hz, θ is the closing angle, $\cos \varphi$ is the power factor, t is the time.

The figure 5 shows examples of a non-structured 2-D meshes uses in calculations for the three tested fuse links, the mesh being performed using the mesh generator software *GMSH* [15]. The fuse elements meshes are composed of 7308 triangle cells and 3655 nodes for the circular notch (a), 7148 triangle cells and 3575 nodes for the rectangular notch (b) and of 7446 triangle cells and 3724 nodes for the trapezoidal notch (c); the reduced sections are meshed as more finely.

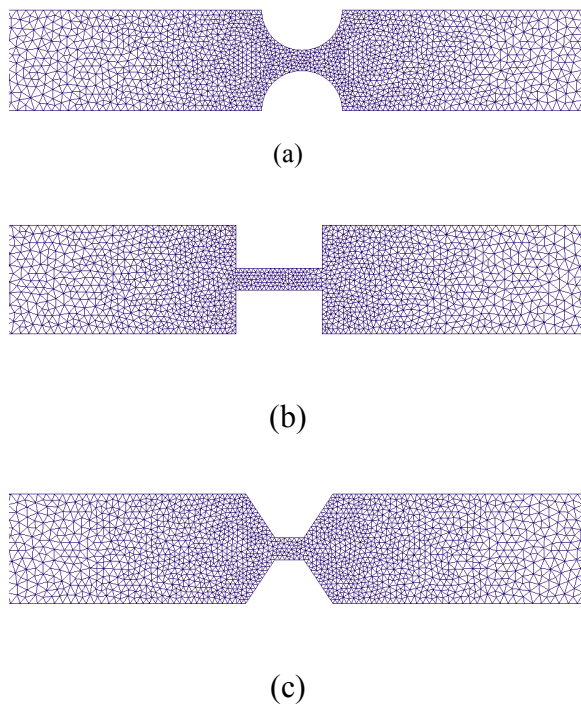


Fig. 4: Fuse links meshes.

Temperature at the initial time is fixed at $T_0=300K$, the time step is fixed at $\Delta t=10^{-5}s$ and calculations are stopped once the enthalpy of vaporization is reached.

Figure 6 illustrates an example of 2-D cartography of the temperature distribution in the fuse links at the end of pre-arcing time obtained at $t=3.9 ms$ for the three fuse links.

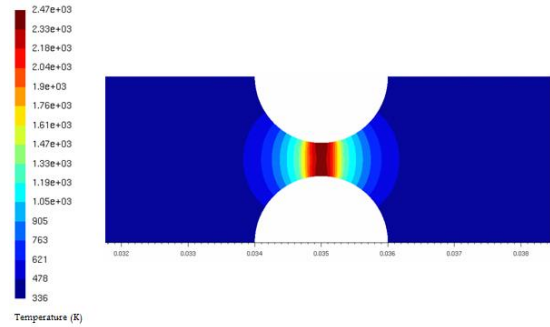


Fig. 5: Isothermal distributions in the fuse-element at the end of pre-arcing time.

It can be seen that the temperature rise takes place in the notch centre where isothermal contours are induced by the reduced sections shape. This is clearly demonstrated in figure 7 which presents temperature distribution along the fuse for the three reduced sections fuse links just before the creation of electric arc. The peak of temperature stand for the rectangular notch fuse link has a width of around 2 times the circular and the trapezoidal ones.

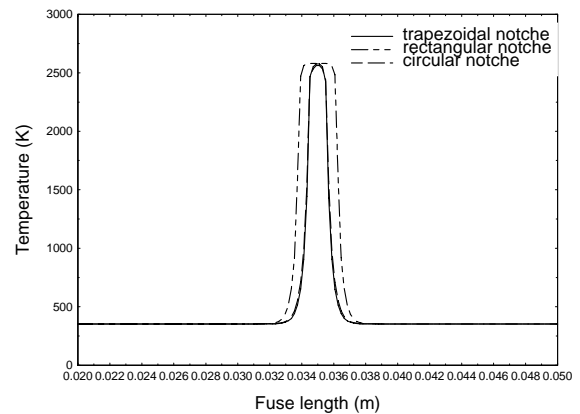


Fig. 6: Temperature distribution in the fuse-link following the x-direction at $y=1.25mm$.

Figure 8 presents the temperature history during the pre-arcing time for the three considered fuse links. The temperature of the fuse links evolve according to four stages: a gradual increase up to the melting temperature, followed by the phase change at constant temperature during a lapse time. The third stage which corresponds to the strong temperature rise due to the high resistivity of the fuse links and the last stage corresponds to liquid vapour transition. The time necessary to this transition is longer due to the latent heat of vaporization which is about 20 times the latent heat of fusion as previously given in Table 1.

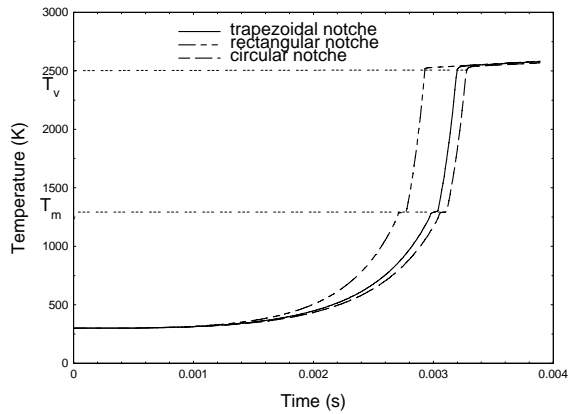


Fig 7: Temperature history at positions $x = 35 \text{ mm}$ for $y = 1.25 \text{ mm}$ for the three fuse links.

It is noteworthy to note that for the rectangular notch fuse link, the temperature rise up to the vaporization temperature is faster than the two others fuse links and the liquid vapour transition time is longer than the other ones. Indeed due to the abrupt constricted section at the centre of the rectangular notch fuse link, a fast and strong increase of Joule effect induced by a maximum of current density is observed in figure 9.

The joule heating history versus time has the four stages previously quoted. Concerning the last stage a joule heating increase is observed due only to the current density rise. Indeed the electrical resistivity is almost constant after the vaporization temperature.

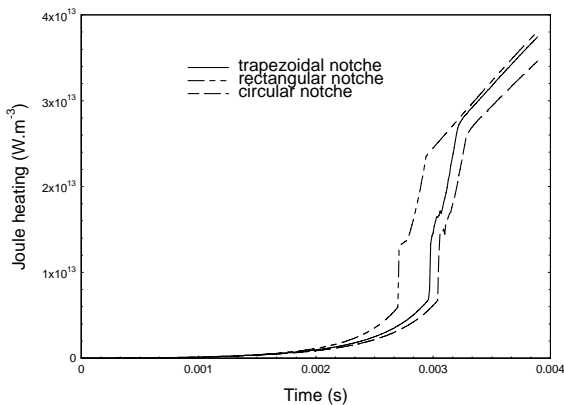


Fig. 8: Joule heating rise of the three fuse links during the pre-arcing time, at positions $x = 35 \text{ mm}$ for $y = 1.25 \text{ mm}$.

Figure 10a and figure 10b presents respectively the calculated evolutions of resistance and voltage of the three fuse links as functions of time.

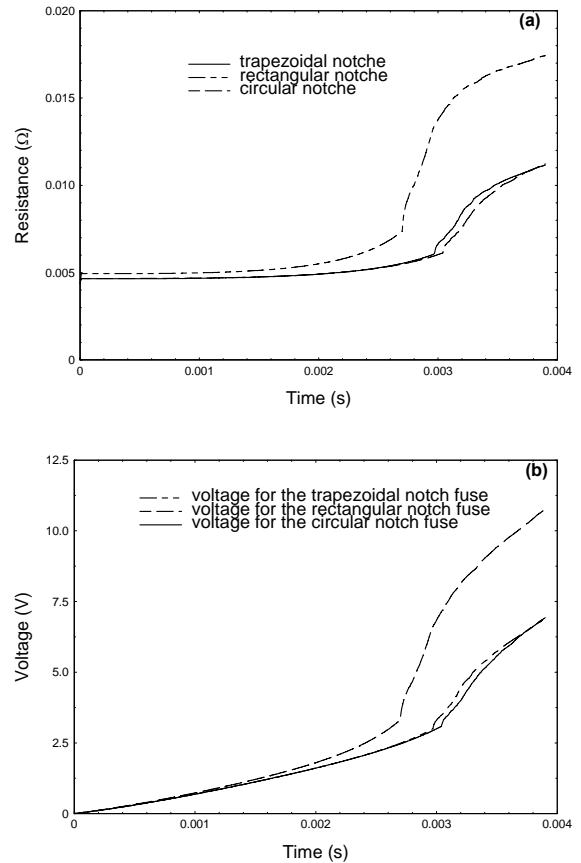


Fig. 9: Voltage and resistance histories versus time for three fuse links.

The voltage curves and the resistance curves show a two-step evolution: the first step is characterized by a slow increase and the second step is characterized by a fast increase. This is due to the silver resistivity which is 2 times more important in the liquid state than in the solid state and consequently the voltage evolution has same characteristics.

5. Conclusion

A model to predict pre-arcing time in heavy fault currents applied to HBC fuses has been presented. The model is based on the solution of heat-transfer equation including two phase-changes. Thermal conduction and Joule heating are respectively, the major heat-loss and heat source. The enthalpy method is used of calculating short pre-arcing times in three silver typical fuse links. A comparison between the numerical results shows that for the fuse link with rectangular notch a fast and strong Joule heating due to a highest resistivity than the two others. A maximum of energy correspond to the latent heat of vaporization is necessary to

vaporize and to allow the disruption of the fuse links.

Acknowledgments

We thank both for their help through many discussions and their financial support MM. T. Rambaud and JL. Gelet from Ferraz Shawmut, M. JC. Perez-Quesada from Mesa. and M. F. Gentils from Schneider Electric.

References

- [1] J.G. Leach, P.G. Newbery, A. Wright, "Analysis of high-rupturing-capacity fuse-link prearcing phenomena by a finite-difference method", Proceedings of the IEE, vol. 120, n°9, September, 987-993 (1973).
- [2] L.A.V. Cheim, A.F. Howe, "Calculating fuse pre-arcing times by transmission-line modelling (TLM)", Proceedings of the 4th International Conference on Electric Fuses and their Applications, Nottingham, 162-167 (1991).
- [3] M. S. Agarwal, A D Stokes and P Kovitya, "Pre-arcing behaviour of open fuse wire", J. Phys. D: Appl. Phys 20, 1237-1242 (1987).
- [4] M. Sasu and G. Oarga, "Simulation of the heat transfer phenomena in variable section fusible elements in non-adiabatic regime", Archiv für Elektrotechnik, 75, 425-431 (1992).
- [5] C. Garrido and J. Cidras, "A method for predicting time-current characteristics of fuselinks", Electric Machines and Power Systems, 26, 685-698 (1998).
- [6] Y. Kawase, T. Miyatake, and S. Ito, "Heat Analysis of a Fuse for Semiconductor Devices Protection Using 3-D Finite Element Method", IEEE TRANSACTIONS ON MAGNETICS, vol. 36, no.4 (July 2000).
- [7] G. Amiez, P.A. Greneau, "On a numerical approach to Stefan-like problems". Numerische Mathematik, 59, 71-89 (1991).
- [8] D. Rochette, R. Touzani, W. Bussiere, "Numerical study of the short pre-arcing time in HBC fuses via an enthalpy formulation", J. Phys. D: Appl. Phys. 40 (2007) 4544-4551.
- [9] Y. Safa, "Simulation numérique des phénomènes thermiques et magnétohydrodynamiques dans une cellule de Hall-Héroult", Thèse EPFL no 3185 (2005).
- [10] Y.S.Touloukian, R.W. Powell and C.Y. Ho, "Thermal conductivity - metallic elements and alloys", Vol. 1 of Thermophysical properties of Matter – the TPRC Data Series, ed. IFI/Plenum New York Washington (1970).
- [11] R.A. Matula, "Electrical Resistivity of Copper, Gold, Palladium, and Silver", JPCRD 8(4), 1147-1298 (1979).
- [12] J.L. Bretonnet, "Conductivité électrique des métaux liquides", Techniques de l'ingénieur MB2 (2005).
- [13] I. Bahrin, "Thermochemical Data of Pure Substances", 3rd ed. in collaboration with G. Platzki, vol. 1. Ag-Kr and vol. 2. La-Zr, VCH Weinheim, Federal Republic of Germany, New York (1995).
- [14] J-M. Bergheau, "Simulation numérique des transferts thermiques par éléments finis", © LAVOISIER (2004).
- [15] C. Geuzaine and J.F. Remacle, GMSH, <http://www.geuz.org/gmsh/>.

A COMPLETE 3D THERMAL MODEL FOR FAST FUSES

Adrian Plesca

Gh. Asachi Technical University of Iasi, Bld. D.Mangeron, 51-53, Iasi - 700050, Romania, aplesca@ee.tuiasi.ro

Abstract: It is important to know the thermal behaviour of a fast fuse for an optimized design as well as for a right choice of the fuse rating with the aim to protect the power semiconductor device. A 3D thermal model was developed in order to study the temperature distribution at a fast fuse. In this model the thermal behaviour of the fast fuse depends on the design of the fuselink elements, the material parameters and the ambient conditions. It was shown the temperature distribution through all fuselink elements. The simulated temperatures were compared with measured temperatures at defined points on the fuse.

Keywords: 3D thermal model, simulation, fast fuse, temperature distribution.

1. Introduction

Semiconductor power diodes were first marketed in 1953. It was realised from the outset that these devices had very limited overload capacities and, as they were expensive, the fuse manufacturers attempted to produce fuses which were more sensitive to overloads and which would operate more quickly than their conventional designs. As a result, the first applications were filed in 1955 for patents on fuses specifically designed to protect semiconductor rectifiers. The invention of the thyristor and the subsequent rapid expansion of the power electronics industry which it initiated, made the need for semiconductor fuses even more apparent.

Today, semiconductor devices are being manufactured with maximum continuous current ratings up to 4kA and peak inverse voltages of 6kV. Unfortunately, the devices still have poor overload capacities and continue to need sensitive and fast-acting protection.

2. Fuses for power semiconductor devices

The underlying principle associated with fuses is that a relatively short piece of conducting material, with cross-sectional area insufficient to carry currents quite as high as those which may be permitted to flow in the protected circuit, is sacrificed, when necessary, to prevent healthy parts of the circuit being damaged and to limit the damage to faulty sections or items to the lowest possible level. Fuses incorporate one or more current-carrying elements,

depending on their current ratings, and melting of these, followed by arcing, occurs when excessive overcurrents flow through them. They can be designed to safely interrupt the very highest fault currents that may be encountered in service, and, because of the rapidity of their operation in these circumstances, they limit the energy dissipated during fault periods. This enables the fuses to be of relatively small overall dimensions and may also lead to economies in the cost and size of the protected equipment.

From power semiconductor devices' overcurrent protection point of view a special fuses were made, so called fast fuses. These kind of fuses have a distinct construction of the fuselinks because of their specific geometry.

Taking into account the thermal phenomena complexity for a fuse it is very difficult to study the heating processes both in steady-state or transitory operating conditions, using the traditional analytical equations. Approaches to simulate these processes have already been made in earlier work. In [1] the temperature distribution, and the thermal and electrical resistances of basic elements of the fuses are described by exact or semi-empirical analytical equations, and combined with iterative solution procedures. In [2, 3, 4] the fuselink is represented by an equivalent R-C network. Other simulations discretize the fuselink including its conductor according to Finite Element, in [5, 6, 7], or Finite Difference schemes, like in [8]. Because of the typical geometry of fuses a three-dimensional discretization is generally necessary, at least for the heat diffusion problem. In [9] a commercial FEM package has been used to model heating of relatively simple fuse geometries without notches and with one single notch, respectively. Other FEM work has been reported in [10, 11, 12]. In [13] a Windows based program code for modeling complete fuses, including M-Effect, using the Finite Volume Method, has been developed.

3. 3D thermal model of a fast fuse

During former work, because of limited computer capabilities, the authors had to concentrate on partial problems or on parts of the fuse geometry. The progress in computer technology enables the modelling and simulation of more and more complex structures in less time. It has therefore been the aim of this work to develop a 3D model of a complete fast fuse used for power semiconductor devices

protection. The starting point is the power balance equation for each volume element dV , in the integral formulation:

$$\iiint \frac{j^2}{\sigma} dV = \iiint \rho c \frac{\partial T}{\partial t} dV - \iiint \text{div}(\lambda \cdot \text{grad}T) dV \quad (1)$$

where:

- T means the temperature of element [$^{\circ}\text{C}$];
- j – current density [A/m^2];
- σ – electrical conductivity [$1/\Omega\text{m}$];
- ρ – material density [kg/m^3];
- c – specific heat [$\text{J}/\text{kg}^{\circ}\text{C}$];
- λ – thermal conductivity [$\text{W}/\text{m}^{\circ}\text{C}$].

The left term of before equation (it exists only in the fuse conductor elements), denotes the heating power from the current flow. It is in balance with the heat stored by temporal change of temperature, and the power removed from the element by thermal conduction. For the steady state temperature calculation, the heat storage term is zero, and the equation (1) becomes,

$$\iiint \frac{j^2}{\sigma} dV = -\iiint \text{div}(\lambda \cdot \text{grad}T) dV \quad (2)$$

The above equations are valuable only for internal volume elements because they don't take into account the surface convection.

A 3D model for a fast fuse has been developed using a specific software, the Pro-ENGINEER, an integrated thermal design tool for all type of accurate thermal analysis on devices. The subject was a fast fuse type aR with rated current by 400A, rated voltage about 700V and rated power losses of 65W. The 3D model had taken into consideration all the component parts of a fast fuse: outer cap, end tag, rivet, inner cap, ceramic body, fuselink and granular quartz, as shown in Fig. 1. It was considered a simplified geometry for the rivets.

The granular quartz which is filling up inside the ceramic body of the fuse have been modelled by a solid. This allow to use many small solid parts to fill all the gaps from the fuselinks.

4. 3D thermal simulation of the fuse

It was considered a typical application when this type of fast fuse is used to protect against overcurrents a three-phase power semiconductor rectifier. The current which flows through the converter branches and therefore through the fast fuses is about 315A. Taking into account that the rated power losses for the fuse is about 65W and the rated current is 400A, the rated resistance will be,

$$R_n = \frac{P_n}{I_n^2} = 0.4\text{m}\Omega \quad (3)$$

Hence, at a current with the value of 315A results a power losses by,

$$P = R_n \cdot I^2 = 39.69\text{W} \quad (4)$$

In this case, because the fuse has three fuselink elements and assuming an equal distribution of the current flow, every fuselink will dissipate 13.23W.

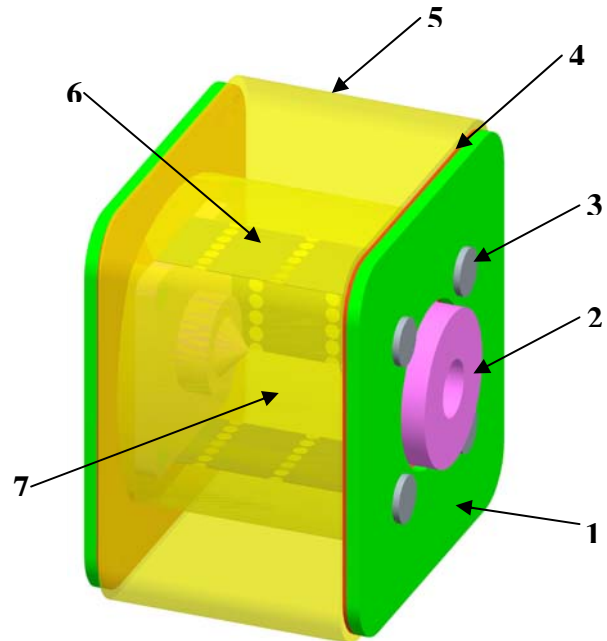


Fig. 1: Thermal model of the fast fuse (1 – outer cap; 2 – end tag; 3 – rivet; 4 – inner cap; 5 - ceramic body; 6 – fuselink; 7 – granular quartz).

For all thermal simulations a 3D finite elements Pro-MECHANICA software has been used. The material properties of every component part of the fuse are described in the table 1, according to Fig. 1.

The heat load has been applied on surfaces of the fuselink elements, 13.23W on every one. It is an uniform spatial distribution on these surfaces.

The mesh of this 3D fuse thermal model has been done using tetrahedron solids element types.

The analyzed fuse has the following overall dimensions: length: 50mm, square cross-section: 59mm x 59mm, end tag diameter: 24mm. The fuselink has a length of 38mm, width: 15mm, thickness: 0.15mm, notch diameter: 2.3mm. The ambient temperature was about 25 $^{\circ}\text{C}$.

From experimental tests [3], it was computed the convection coefficient value for this type of fast fuse, $k_t = 4.247$ [$\text{W}/\text{m}^2\text{C}$]. Hence, it was considered the convection condition like boundary condition for the outer boundaries such as outer caps, end tags, rivets.

Table 1. Material data and coefficients at 20°C

Parameter	Material					
	Ceramic body (5)	Copper (1, 2)	Iron FE40 (3)	granular quartz (7)	Silver (6)	Insulation material /pressed carton (4)
Density, ρ [kg/m ³]	2400	8900	7190	1500	8210	1400
Specific heat, c [J/kg°C]	1088	387	420.27	795	377	0.099
Thermal conductivity, λ [W/m°C]	1	385	52.028	0.325	121.22	0.063

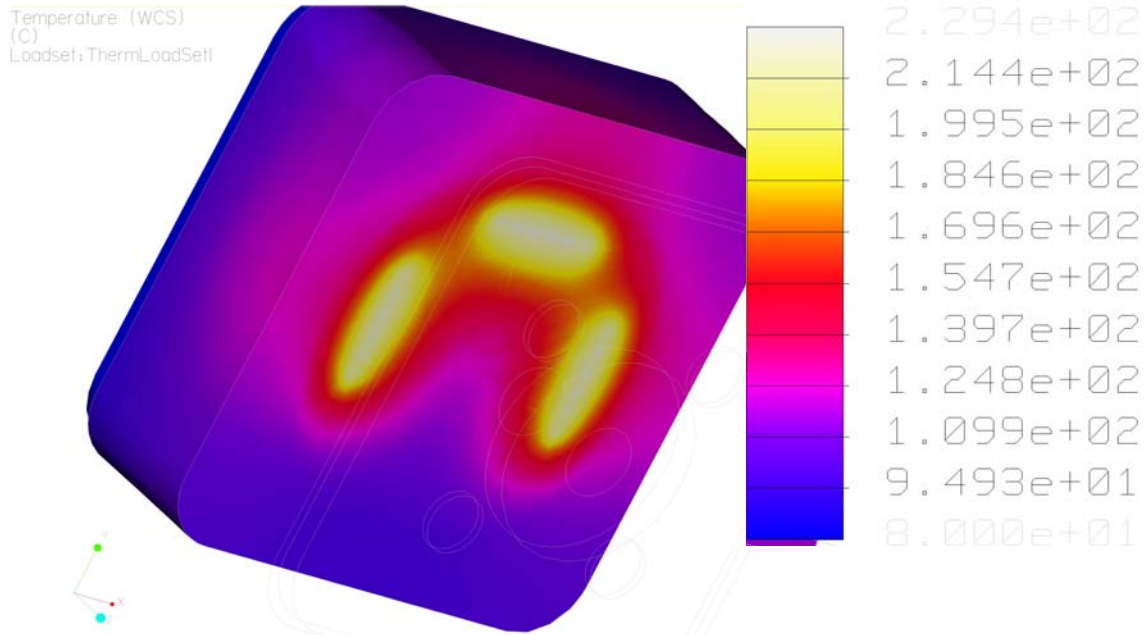


Fig. 2: Temperature distribution through the fuse at 50% cross section.

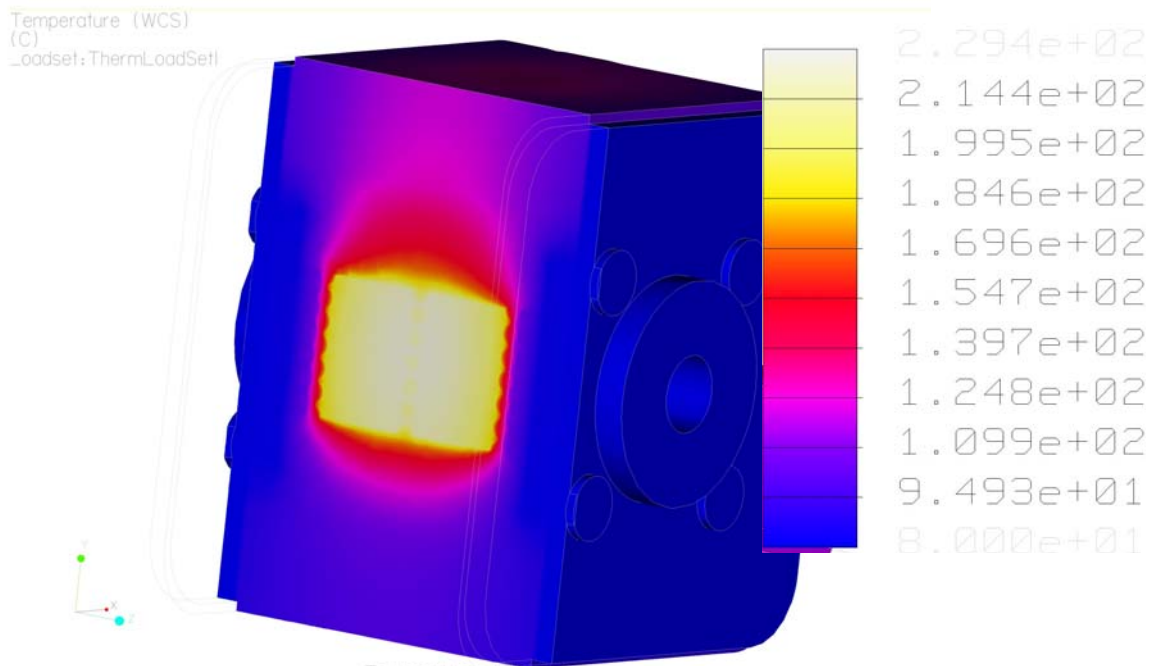


Fig. 3: Temperature distribution through left side fuselink at 24.45% cross section.

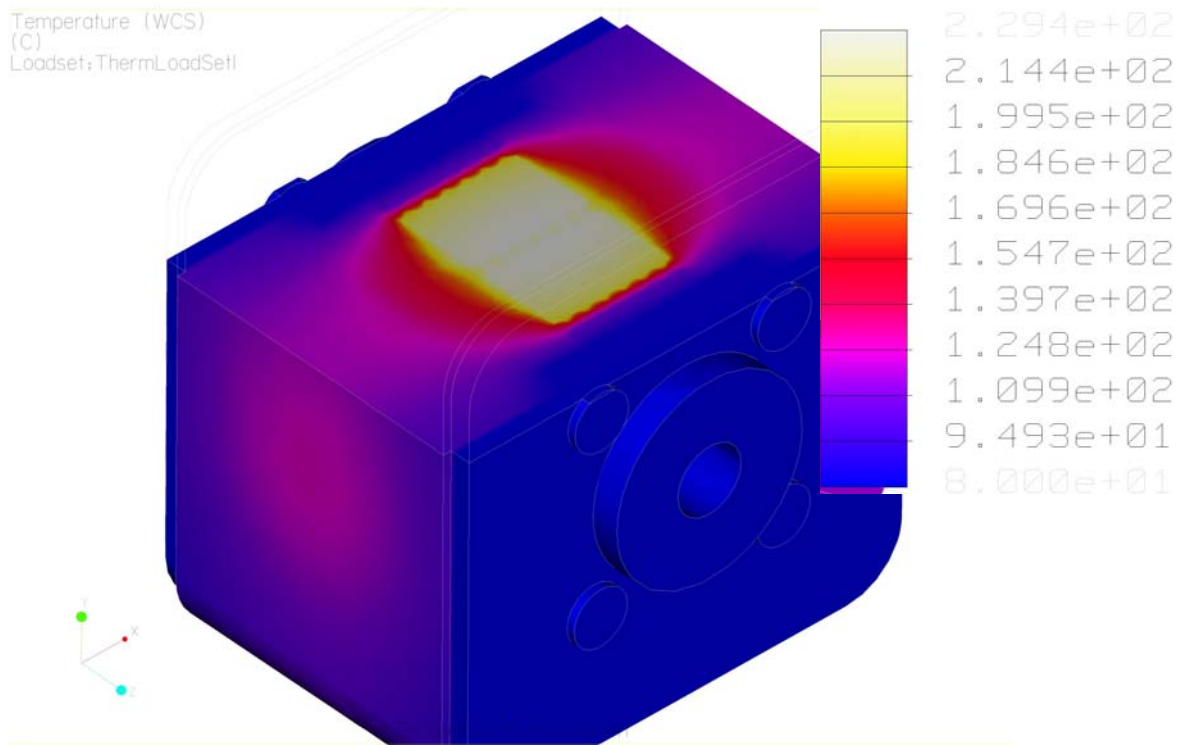


Fig. 4: Temperature distribution through upper side fuselink at 24.45% cross section.

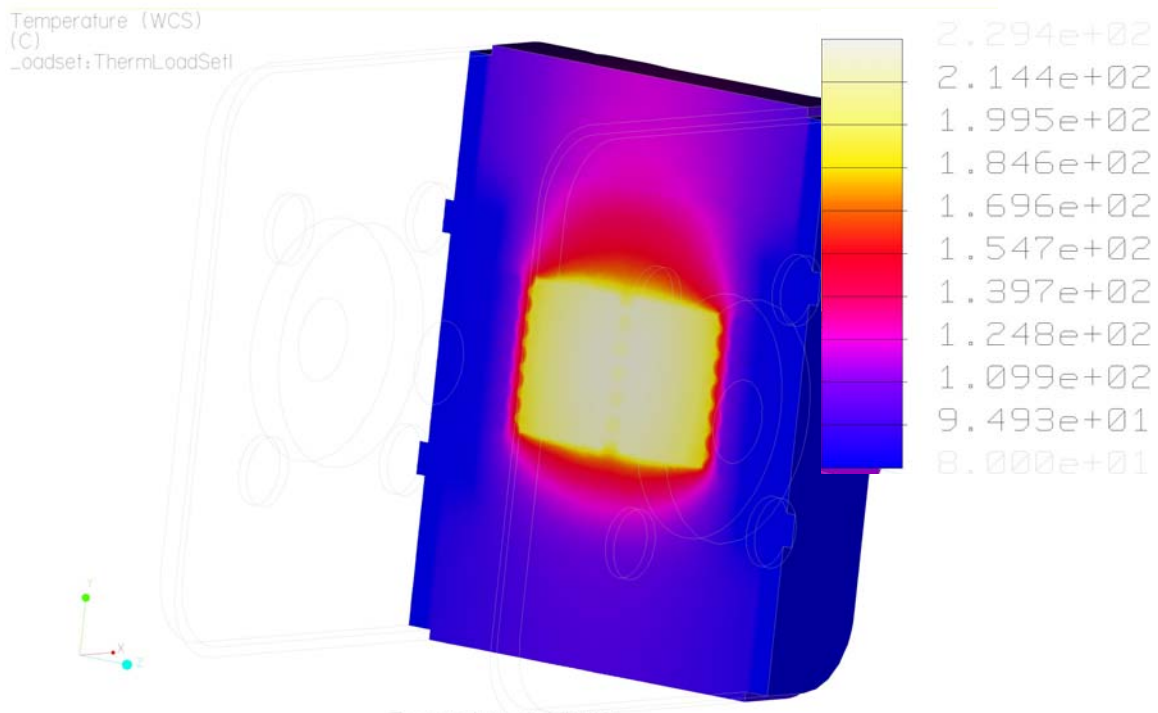


Fig. 5: Temperature distribution through right side fuselink at 75.55% cross section.

The convection coefficient has been applied on surfaces of outer caps, end tags and rivets, with an uniform spatial variation and a bulk temperature of 25°C.

Further on, some steady state thermal simulations have been done. The temperature distribution inside the fuse is shown in the figures 2 to 5. The maximum temperature, on the fuselinks is 229.4°C and the minimum, on the surface of the ceramic body, is about 80°C.

As it can see from the pictures, the maximum temperature is obtained on the fuselink elements in the centre. This is explained because of the notches made on the fuselinks in order to clear the fault current as soon as possible and to interrupt the electric circuit without high overvoltages. It was assumed that every fuselink element has to dissipates the same quantity of heat, hence the maximum temperature is the same for every one. Of course, there is a thermal influence among these fuselink elements because of their geometrical site, figure 2.

Therefore, there are high temperatures around these fuselinks with the maximum in the middle of them.

Hence, it can observe high temperatures on the center surface of the ceramic body of the fuse depending on thermal conductivity of the fuselink elements (silver), filling material (granular quartz) and ceramic body.

To validate the 3D thermal model some experimental tests have been done in the same conditions like in the case of thermal simulation. A diagram with the electric circuit used for experimental tests is shown in Fig. 6.

The switch K, allow to supply with low-voltage the auto-transformer ATR, which adjusts the input voltage for the current supply CS. The main current from CS, flows through the fast fuse F, and will warm it. The current value is measured by an ammeter A, through a current transformer CT. Using proper thermocouples Th, it has measured the temperature on the fuse ceramic body on the proximity sides of the fuselinks. The measurement points were placed on the lateral sides and upper side of the fuse body, Fig. 7. The voltage signals from all thermocouples have been acquired and processed by a data acquisition board and a PC.

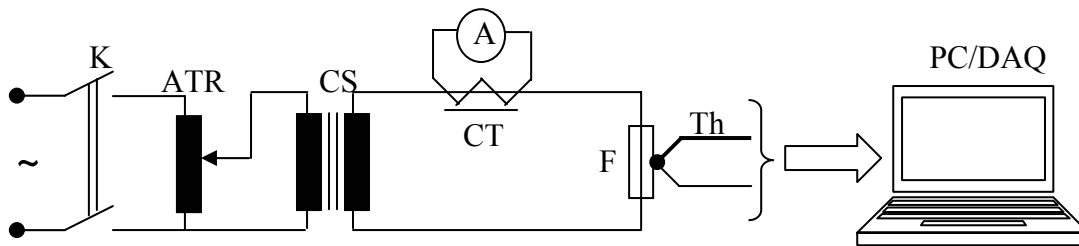


Fig. 6: Experimental tests electrical circuit

A comparison between experimental and simulation results is shown in the diagrams from figures 8 and 9. These represent the temperature variation on the body fuse surface against length of fuselinks (38mm). As it can observe from the graphics, there is a maximum temperature in the middle of the fuselinks and the minimum temperatures on the end-terminals of the fuse, because of the outer caps which act like simple heatsinks for the fuselink elements.

There are higher temperature values for the upper surface of the fuse (T_{expb}), as compared to lateral side (T_{expa}), because of the thermal influence of the lateral fuselinks. Of course, there are different temperature values resulted from experimental tests with respect to simulations (T_{sima} , T_{simb}), because of measurement errors, thermal model simplifications, unbalanced current distribution through fuselinks and mounting test conditions. The thermal model has not included different types of busbar connections from geometrical point of view.

Anyway, the maximum difference between experimental and simulation results is less than 3°C.

5. Conclusions

Further on, the main conclusions of the simulation study as regards temperature distribution at fast fuses are presented.

- because of very complex thermal phenomenon the analysis of fast fuses thermal field can be done using a specific 3D FEM software (Pro-ENGINEER and Pro-MECHANICA); in this way it can be calculated the temperatures anywhere inside or on the fuse;
- it can observe a maximum temperature in the middle of fuselinks and the minimum values at the ends; also, there is a thermal influence among fuselinks that leads to different temperature values on the fuse surfaces;
- there is a good correlation between experimental and simulation temperature values;

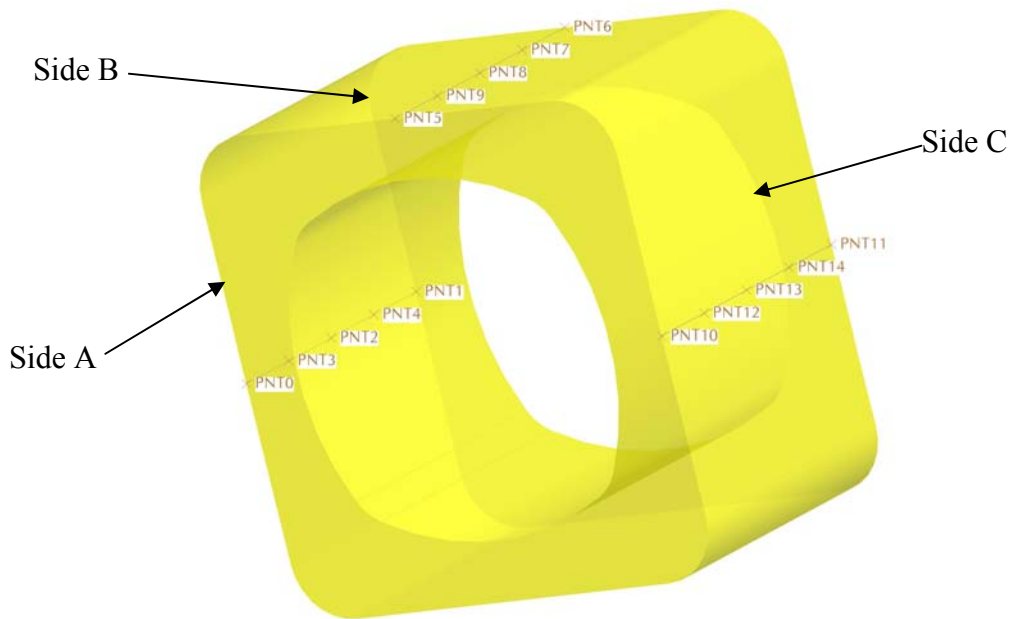


Fig. 7: Measurement points distribution on the surface of the fuse.

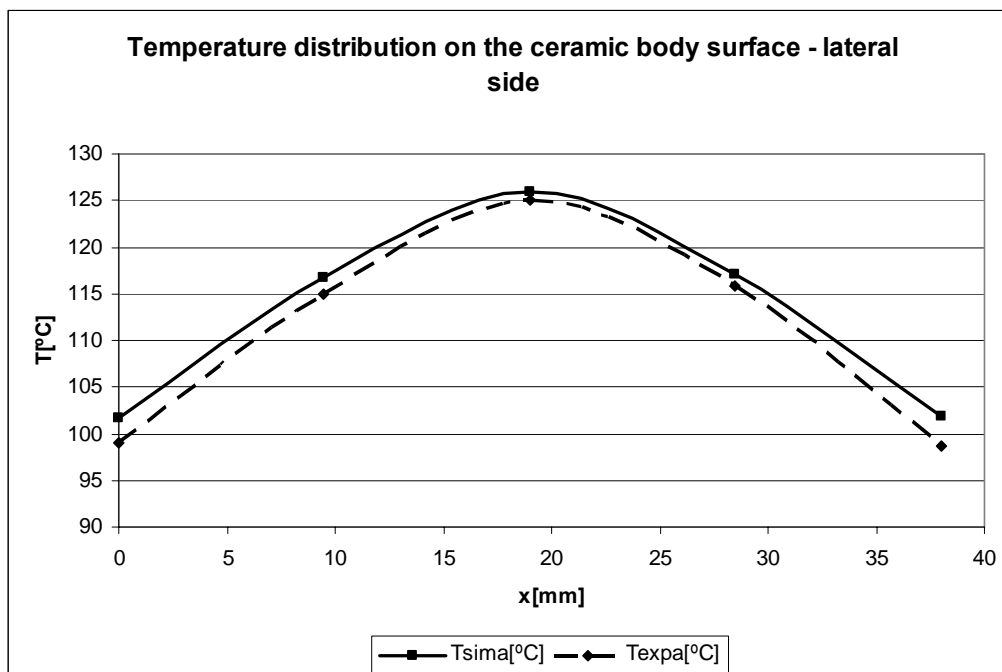


Fig. 8: Comparison between experimental and simulation temperatures vs. length of the ceramic body lateral side.

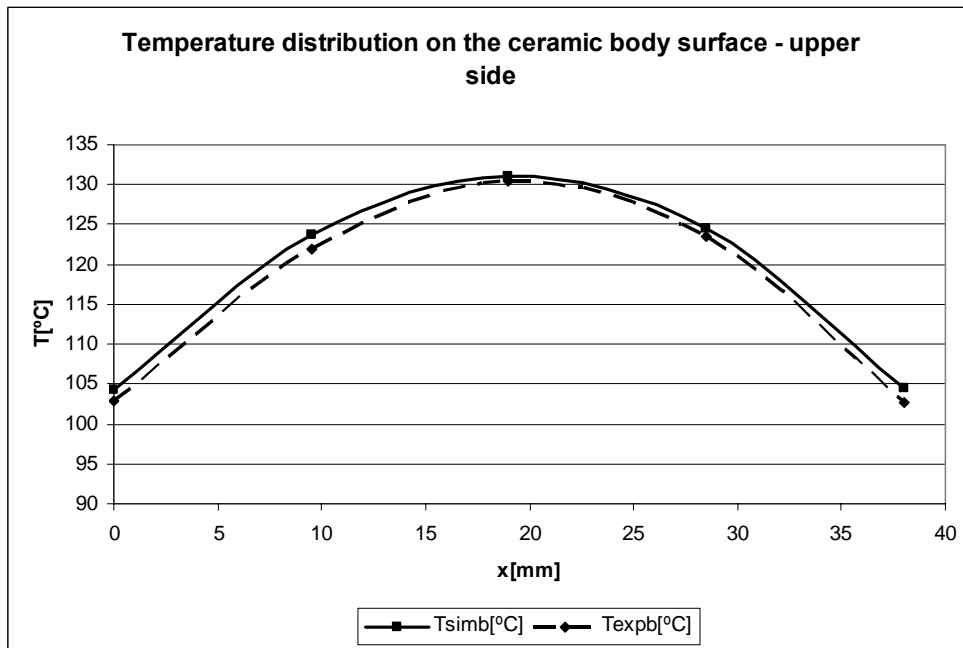


Fig. 9: Comparison between experimental and simulation temperatures vs. length of the ceramic body upper side.

- using the 3D simulation software it can improve the fast fuse designing and also there is the possibility to get new solutions.

Acknowledgements

The author has a pleasure to acknowledge that described investigations were carried out in the frame of CEEX National Programme, Funding Application for Excellences Research Projects, Code project: 5, Contract no: 1489/07.04.2006.

References

- [1] Wilkins R.: "Steady-state current sharing in fuses with asymmetrical arrangements". *Proc. of the 4th ICEFA Nottingham (UK), 1991*, pp. 28-33.
- [2] Gelet J., Tournier D. and Ruggiero M.: "Evaluation of thermal and electrical behaviour of fuses in case of paralleling and/or high frequencies". *Proc. of the 6th ICEFA, Torino (Italy), 1999*, pp. 49-53.
- [3] Pleşca A.: "Overcurrent protection systems for power semiconductor installations". *PhD Thesis*, Iaşi, Romania, 2001.
- [13] Lindmayer M.: "3D simulation of fusing characteristics including the "M-Effect". *Proc. of the 6th ICEFA, Torino (Italy), 1999*, pp. 13-20.
- [4] Hoffmann G. and Kaltenborn U.: "Thermal modelling of high voltage H.R.C. fuses and simulation of tripping characteristic". *Proc. of the 7th ICEFA, Gdansk (Poland), 2003*, pp. 174-180.
- [5] Kürschner H., Ehrhardt A. and Nutsch G.: "Calculation of prearcing times using the Finite Element Method". *Proc. of the 5th ICEFA, Ilmenau (Germany), 1995*, pp. 156-161.
- [6] Fernández L., Cañas C., Llobell J., Curiel J., Aspás J., Ruz J. and Cavallé F.: "A model for pre-arcing behaviour simulation of H.V. full-range fuse-links using the finite element method". *Proc. of the 5th ICEFA, Ilmenau (Germany), 1995*, pp. 162-168.
- [7] Wilniewczyk M., McEwan P.M. and Crellin D.: "Finite-element analysis of thermally-induced film de-bonding in single and two-layer thick-film substrate fuses". *Proc. of the 6th ICEFA, Torino (Italy), 1999*, pp. 29-33.
- [8] Garrido C. and Cidrás J.: "Study of fuselinks with different t-I curves using a mathematical model". *Proc. of the 6th ICEFA, Torino (Italy), 1999*, pp. 21-24.
- [9] Beaujean D.A., Newbery P.G. and Jayne M.G.: "Modelling fuse elements using a C.A.D. software package". *Proc. of the 5th ICEFA, Ilmenau (Germany), 1995*, pp. 133-142.
- [10] Cañas C., Fernández L. and González R.: "Minimum breaking current obtaining in fuses". *Proc. of the 6th ICEFA, Torino (Italy), 1999*, pp. 69-74.
- [11] Jakubiuk K. and Aftyka W.: "Heating of fuse-elements in transient and steady-state". *Proc. of the 7th ICEFA, Gdansk (Poland), 2003*, pp. 181-187.
- [12] Pleşca A.: "Thermal simulations of fast fuses for power semiconductor devices protection". *Proc. of the 7th ICEFA, Gdansk (Poland), 2003*, pp. 200-205.
- [14] Wright A., Newbery P.G.: "Electric Fuses". The Institution of Electrical Engineers, 1995.

EXPERIMENTAL INVESTIGATION OF THE FUSION IN CYLINDRICAL EXPLODING WIRES USING HIGH CURRENT DENSITIES WITH INDUSTRIAL FREQUENCY

C.S. Psomopoulos⁽¹⁾, D. Diamadopoulos⁽²⁾, C. Karras⁽³⁾, P. Karagiannopoulos⁽³⁾, E. Tsivlikas⁽³⁾

Ass. Professor⁽¹⁾, T.E.I. Piraeus, Dep. of Electr. Eng., High Voltage Laboratory, 250 Thivon & P. Rali str., GR-12244 Athens, GREECE, c-psomop@ath.forthnet.gr

Professor⁽²⁾, Research Associate⁽³⁾, T.E.I. Piraeus, Dep. of Electr. Eng., High Voltage Laboratory, 250 Thivon & P. Rali str., GR-12244 Athens, GREECE, diam@in.teipir.gr⁽²⁾

Abstract: The physicochemical process during the operation of fusible wires under high current densities presents complicity and seems not to be completely known. The work presented in this paper investigates the fusion process of exploding wires using common industrial power supply directly feed from the network of 50Hz. The measured magnitudes were the voltage drop and the current waveforms during the current interruption process and the total duration of the fusion. The measurements were performed through fast digital oscilloscopes connected with PC are presented and the observed phenomena are investigated. The total time duration (prearcing and arcing periods of fusion) of the fusion process was measured and the results for different current densities and lengths of the thin wire elements are presented and analysed.

Keywords: Fusion process, arc formation, exploding wire, high current densities, heavy ionised metal vapour column, arcs in air.

1. Introduction

The fusible wires and electrically exploded conductors are frequently used in fuses that protect the electrical installations of the low and medium voltage distribution network and in a wide variety of power applications. They generally operate either under a minus value of their nominal current or momentarily under excess or short-circuit currents. During the operation under nominal current or less the Joule heating produced on fuse element dissipates to the surrounding area of the element and thermal equilibrium is attained after a time period [1,2,3,4].

For the case of the operation under excess or heavy fault currents the design of fuses is based on the well known fundamental principle, that they must interrupt those currents in a very short time period. The phenomena developed are in brief as follows. The increase of the fuse elements resistance causes

the temperature to rise rapidly, until the melting point is reached. The latent heat of fusion is produced gradually by the current during the melting time until the material is completely vaporized [2,3,5]. When the material of the element vaporizes, electric arcs struck between the remaining solid parts of the element. This dynamic process gives rise to a rapid temperature increase, while the current decreases rapidly until its flow is interrupted. The fundamental fuse operation has been described extensively in the relevant literature [1÷12]. The understanding of this operation relies mainly on work on exploding wires and sand fuses mostly performed from 1960s to 1980s [3÷12]. Several theories have been developed to explain the disruption of fuse elements, but no conclusive proof has been found in favour of one of them. Hence new ideas on the exploding wires phenomenon and the sand fuse operation often appear [1÷3, 13÷16].

Present research activities are focused mostly in the arcing period and a number of models have been developed to simulate the fundamental operation. This operation is well understood in general, but all the physicochemical processes during the arcing period seem not to be completely known [12÷14]. However some models have been developed which can simulate fuses operation under fault current during the arcing period [1,6, 12÷14].

In this paper, measurements of the voltage drop across fuse elements and the current, using fast digital oscilloscopes connected with PC are presented. The fusion total duration is measured for a variety of thin wire elements lengths and different current densities. To our knowledge there are no similar measurements in the related bibliography especially considering the method used here were the fusion process was measured using actual industrial voltage (230V, 50Hz), which is simulating actual conditions for the circuit and the exposed fusible wire. In the related literature the experiments are carried out usually with pulse voltages or currents. The measurements in this work were performed in random position of the supply voltage curve. These measurements give the possibility to investigate the

physicochemical process during the pre-arcing and arcing periods. An identification of the existing knowledge in the measurements performed, and a further interpretation of the phenomena during sort-circuit is attempted.

2. Experimental Set-up and Measurement Results

2.1. Experimental Set-up

Fig. 1 shows the simplified schematic diagram of the experimental set-up, for the estimation of the voltage drop across a fuse element under sort-circuit conditions. Thin wires simulating the fuse elements, were connected to the circuit using appropriate terminals. A typical ohmic load of 0,5kW, connected in parallel with an open switch was used to simulate the nominal current operation and sort-circuit conditions respectively. A measuring resistance R_m was used to estimate the current through the fuse element. The material used for the measuring resistance had zero value coefficient of variation of resistivity with temperature ($\alpha \approx 0$). The variable resistance R was of a similar material as R_m and used to determine the peak current value during sort-circuit.

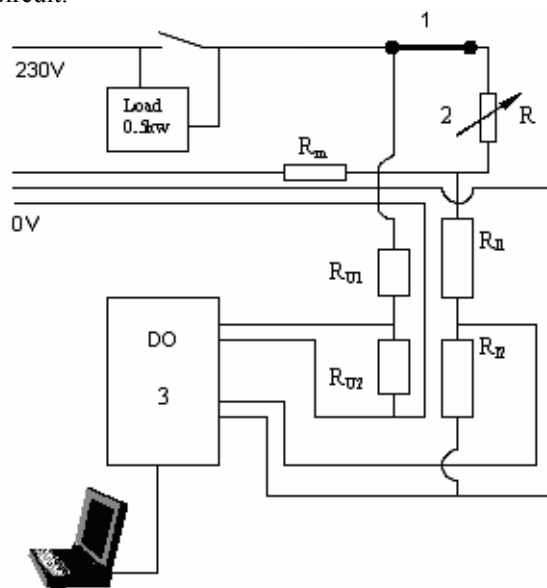


Fig. 1. Simplified schematic diagram of the used experimental set-up.

- 1) Thin-wire element
 - 2) R : variable resistance for determine the current peak value,
 - 3) Digital oscilloscope with an RS-232 connection to the PC,
- R_{U1} , R_{U2} voltage divider for the voltage across the element,
 R_{11} , R_{12} and R_m voltage divider and measuring resistance for the current through the element.

The measurements were performed through a digital oscilloscope with high sampling frequency up to 100MHz per channel and maximum voltage of 40V pick to pick (5V/div). The sampling frequency was 0,1MHz. The oscilloscope was directly connected to PC, via an RS232 port, for direct transfer of the measurements. The two voltage dividers were used in order to reduce the voltage peak value provided to the oscilloscope. The software of the interconnection could transfer the values and the curves in excel sheets (generally a spreadsheet software) directly with spreadsheet software format, and the measurement on the oscilloscope screen, as image independently inserted in the spreadsheet with common bmp format.

2.2. Measurements Results

Measurements were performed on conductors stretched in air. The conductors were thin cylindrical copper wires (99,9% Cu), with several diameters. Figures 2 and 3 show the voltage drop, the current and the resistance waveforms during the current interruption process in fuse elements with diameter of 0,14mm and 0,16mm and length which was varied between 35mm to 100mm with a step of 5mm. The current density was changed through the variable resistance (R) of the circuit.

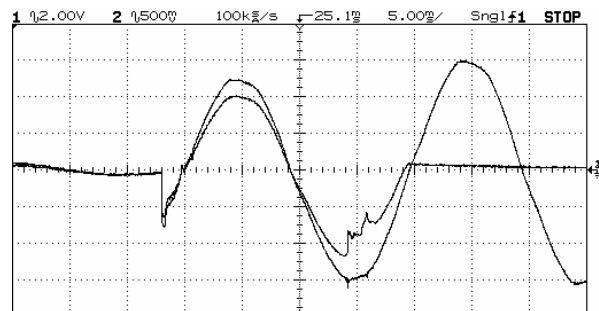


Fig. 2. Typical measurements of the fusion process in thin copper wire elements. Channel 1 is the voltage drop across the element (the sinus waveform), channel 2 is the current during fusion process (rapidly decreases to zero while voltage remains). The calculated maximum current density was 4,54kA/mm². The thin wire element had length 60mm, diameter 0.14mm.

3. Discussion

In figures 2 and 3, which present actual measurements from the oscilloscope's screen, it can be clearly seen the sort-circuit's duration, the voltage drop across the element, the current value (impulse and continuous sort-circuit currents). From the waveforms presented in this figures it can be notice that they follow the form of the ones in literature, and similar characteristics can be observed. Here the

difference that exists is that the measurements presented in this work were taken in random positions of the sinus curve of the voltage source.

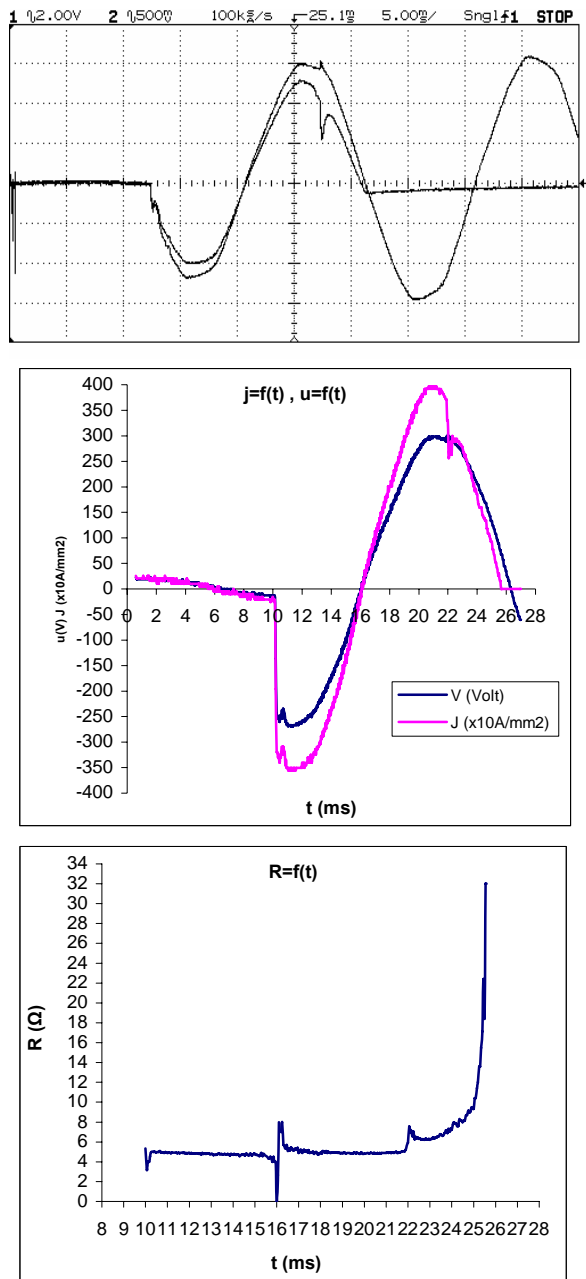


Fig. 3. Typical measurements and the respective actual values calculated from experimental set up characteristics, of the fusion process in thin copper wire elements. The waveform of the of the fusion process $R=f(t)$ is also presented. Channel 1 is the voltage drop across the element (the sinus waveform), channel 2 is the current during fusion process (rapidly decreases to zero while voltage remains). The calculated maximum current density is $4,54\text{kA/mm}^2$. The thin wire element has a length 40mm, diameter 0.14mm.

Another difference concerned the voltage source, which was a common industrial sinus sapped waveform exactly the same one with the one that the equipment it is supplied, and not a laboratory produced voltage. With these two mentioned here basic conditions the fusible wire is exposed to the actual conditions of a network and thus the phenomena observed are closer to the actual ones in practical applications.

General, the waveforms observed in the literature can be divided in two basic areas known as pre-arcing period and arcing period. In the measurements presented here the following can be observed: In the beginning of the pre-arcing period it can be seen the peak value of the sort-circuit current (impulse current). After few μsec , the current is almost stabilized (continuous sort-circuit current). The voltage across the element's edges, after a very fast rising period was also almost stabilized. This value was lower than the source peak value ($\approx 310\text{V}$).

During this period and after the first 0,5–1msec the waveforms presented the following behavior: The voltage drop was almost stabilized with increasing tense while the current although it was almost stabilized showed decreasing tense. These can be explained by the increasing of the specific resistance due to overheating. The graduated increase of the wire's specific resistance follows the well known relation $\rho = \rho_0(1 + a\Delta\theta + b\Delta\theta^2)$ and considering the sort-circuit conditions and the above mentioned, seems to give an explanation to the measured high voltage drop in the element's edges [8,12].

At the end of the prearcing period it can be observed a sinking of the voltage drop and the current for a sort time duration (0,25-0,75ms). This sinking may be explained from the accelerated temperature rise until the melting point of the fuse wire's material, and the changes from solid to liquid conditions (the wire starts to liquefy in the inner parts) [3,6,12,16]. During the sort times here in question and the surface tension, the gravitational forces do not play any role according to literature and thus the liquid wire material will remain in place and be heated further to the temperature of vaporization. At some instant before the material is completely vaporized, the metallic coherence within the fuse wire is interrupted and an arc is formed. [3,7,12]. However, it is doubtful whether this phenomenon will occur in a regular way or whether the liquid cylinder will explode under the mechanical action of the vapor pressure. [3,7,8,12].

According to the literature there is another action that could lead to arcs formation in fusible wires. A cylindrical wire completely melted by an electric current flowing through it, experiences a pressure in connection with the surface energy and a magnetic pressure created by the electric current. If the diameter of the melted wire shows small variations the magnetic pressure is largest at the smallest

diameter. As a consequence of the surface tension and the magnetic pressure, a cylindrical current-carrying liquid conductor stretched in air will deform into a number of globules (unduloids). If the source voltage of the circuit is sufficiently high, small arcs arise between these globules. This phenomenon is referred as “multiple arcing” and it has been observed [1,2,3,7,16].

With the volatilization and interruption of the metallic coherence, electric arcs are formed (arcing period) between the remaining solid parts of the conducting material, in an environment of metal vapors. In this complex environment, as the arcs expand produce both elevated temperature and pressure within the plasma and hence an active environment. In these conditions thermal ionization can be expected. There is a rapid change in arc dimensions, which is a function of the rate of burn-back of the metallic parts (arc elongation). This dynamic process gives rise to rapid increase in the electric resistance of the arc and its eventual extinction [1,2,3,6,12].

The metal vapor column, which arises during the evaporation process of a fusing wire surrounded by air, expands very rapidly due to the high pressure in this vapor, as has been made visible with cylindrical wires in the past [7]. The theoretical and experimental investigation concerning the exploding wires showed that fuse elements, after reaching the evaporation temperature under atmospheric conditions, could become highly superheated in the liquid state [9÷11,17]. At the actual evaporation temperatures the metal vapor column possesses a resistance which is much larger than that of the fuse element at the same temperature, but in liquid state. The fuse resistance in these circumstances is determined by the cross-section of the metal vapor column, the length of this column and the specific resistance of the ionised metal vapor. Experiments showed that the cross-section of the metal vapor column depends on the current [1,2,7,17]. In this metal vapor column the arcs are formed. In these conditions, to sustain a high electron density, a small electric field strength is needed and there is a small electrode fall (~10÷50V) [1÷3,17].

Figure 4 represents the total time duration of the fusion process in thin wire elements exposed in open air. It can be easily observed that the smallest is the length of the wire the higher is the time duration of the fusion process. This seems to be explained by the high volume of the metal structure that supports the element which operates as a heat dissipater and since the wire has small length the supporting absorbs a significant amount of the produced heat in the element [3,4,12,13,18]. Further more to this explanation, as it is mentioned above, during the interruption of the metallic coherence of the wire is followed by an electric arc. Thus the ionised metal vapor column has smaller length so its elongation is

very small considering higher lengths, and at the same time the current density presents high values (see fig. 3). During this process, the heavily ionised surrounding air is considered that is operating in the smaller gap (smaller length) [1,5,7,10,11,16, 17]. The development of the wire fragmentation in exploding wires and the plasma formation in experiments above mentioned have been observed, and described also in M.J. Taylor’s recent works. These experimental results presented the resistance change and the plasma formation and expansion through x-radiological image, photographic study and measurement of the current and voltage waveforms of the used pulses [19,20].

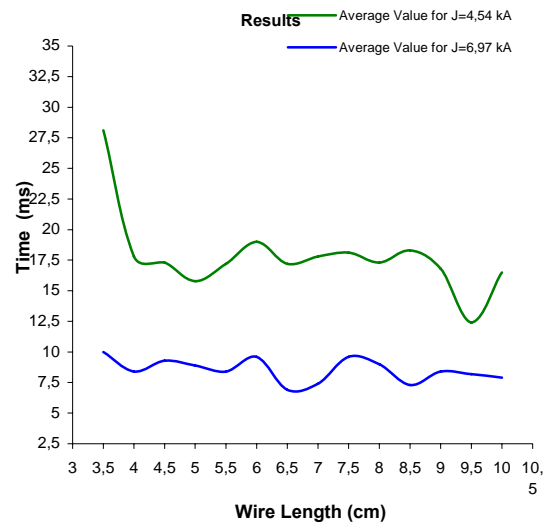


Fig. 4. Waveforms of the average mean value of the fusion process duration in relation with the wire length. The parameter of the current density is also presented. The copper fusible wire has a diameter of 0,14mm.

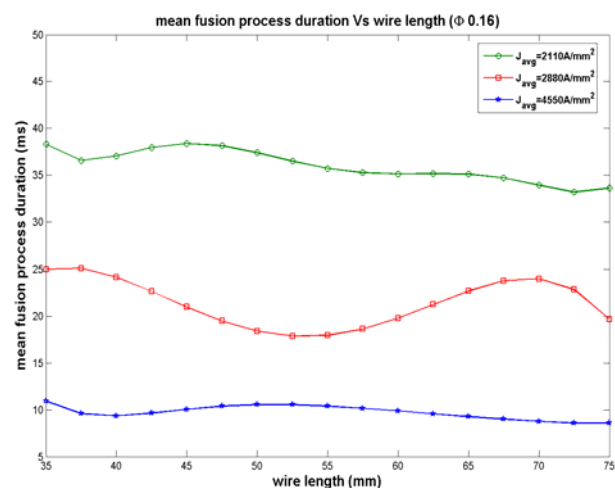


Fig. 5. Waveforms of the average mean value of the fusion process duration in relation with the wire length. The parameter of the current density is also presented. The copper fusible wire has a diameter of 0,16mm.

The resistance waveform in figure 3 present significant similarities with the ones in literature and especially with the ones of M.J. Taylor [19,20] even though the experimental procedures were completely different. The differences exist in the waveforms can be easily attribute to the different geometric characteristics and different waveforms. But the similarities provide strong evidence for the plasma formation and disruptions of the electrical coherence occur due to similar physicochemical procedures in both experiments.

In fig. 4 and 5 also it is observed that the higher the current density is the lower the fusion duration is. This could be easily explained from the above mentioned, since the produced heating power is analog to the term j^2 , where j is the current density (Joule relation) [3,4,16,18].

In these figures it can be easily observed also that in lower current densities the smaller the length is (lower than a threshold value) the higher is the duration of the fusion process. This seems that can be explained from the following assumptions: The heat from the produced Joule energy is lower per time interval. At the same time the energy that is transferred from the thin wire through the end tags is almost stable per time interval and depends from the materials and the volumes. Thus the energy used for melting and arc ignition is lower per time interval, and as a consequence the required time is rising [8,13,18]. Furthermore the lower current densities produced lower magnetic pressure values and thus the thin wire seems not to be exploded. In this smaller gap between the electrodes (smaller distance between the end tags, when the wire has smaller length) the metal vapour expands [7]. Here it must be notice that in small lengths of the gap between the end tags, the electric field is higher as it can be easily concluded from the abovementioned [1÷3,17]. Thus it seems that the metal vapours which are ionized expand not as rapidly as it has been observed in cylindrical wires with higher lengths where the field is lower and the metal vapours do not remain constrained [7]. These assumptions explain also the differences up 25% that can be observed in the total short circuit duration, in higher lengths of the wire elements and low current densities.

Similar observations have been made in all performed measurements, with differences concerning the fusion duration and the related current density. Important role in the fusion duration seems to have the time instant in which this occurs regarding the value of the source voltage. The lower was the source voltage in the starting of the short-circuit the longer was the duration. This can be explained from the resulted small current density in the beginning of the phenomenon which results a greater pre-arcing period, according to the aforementioned. Of course, differences existed because of the different geometric characteristics of

the fusible elements. Those differences, as it can be easily presumed are the consequences of [8,12,14] : Different wires' volumes which require different energy values to melt.

Different wires' resistance and thus different current densities in the elements.

The higher current densities have as a consequence smaller affect of the length in the fusion duration.

4. Conclusions

The measurements through fast digital oscilloscopes combined with PCs, can provide a more accurate approximation and understanding of the phenomena during the operation of the fuse elements. Another parameter that contributes to the above is the use of common industrial voltage source and random sinus values in the experiments. The resistance measurements combined with the voltage drop and current densities measurements can provide a more accurate approximation and understanding of the phenomena involved. The observed fast oscillations for different wire lengths and current densities provided useful information concerning the fusion process duration and thus for short-circuit, which fuse the thin wire. The fusible elements' geometric characteristics affect only the fusion's process duration and the values of the measured magnitudes, for small current densities. The results could be useful in fuses' design.

References

- [1] D.R. Barrow, A.F. Howe and N. Cook, "The chemistry of electric fuse arcing", IEE Proc. A., 138(1), pp. 83-88, 1991.
- [2] Cheim L.A.V. and Howe A.F., "Spectroscopic observation of high breaking capacity fuse arcs", IEE Proc. Sci. Meas. Technol., 141(2), pp.123-128, 1994.
- [3] Wright A., Newbery P.G.: "Electric fuses (2nd Edition)". London: IEE-Peter Peregrinus Ltd. 1995.
- [4] Leach J.G., Newbery P.G., and Wright A., "Analysis of high-rupturing-capacity fuselinks prearcing phenomena by a finite differential method", IEE Proc., 120(9), pp.987-993, 1973.
- [5] Narancic V.N., and Fecteau G., "Arc energy and critical tests for HV current-limiting fuse", *Ibid.*, pp. 236-251.
- [6] Chicata T., Ueda Y., Murai Y. and Miyamoto T., "Spectroscopic observations of arcs in current limiting fuse through sand", *Proc. of Inter. Conf. on Electric Fuses and their Applications, Liverpool (UK), 1976*, pp.114-121.
- [7] Vermij L., "The voltage across a fuse during the current interruption process", IEEE Trans. Plasma Sc., PS-8(4), p.p. 460-468, 1980.
- [8] Morgan V.T.: "Rating of conductors for sort-duration currents", Proc. IEE, 118(3/4), p.p. 555-570, 1971.
- [9] Lebedev D.V., "Explosion of a metal by an electric current", Sov. Phys. – JETP, 5(2), p.p. 243-252, 1957.
- [10] Vitkovitsky I.M. and Scherrer V.E., "Recovery characteristic of exploding wire fuses in air and vacuum", J. Appl. Phys., 52(4), p.p. 3012-3015, 1981.
- [11] Berger T.L., "Effects of surrounding medium on electrically exploded aluminum foil fuses", IEEE Trans. Plasma Scien., PS-8(3), p.p.213-216, 1980.

- [12] Reinhold Rüdénberg: *Transient Performance of Electric Power Systems*, (M.I.T. Press, 1970).
- [13] Chapman Alan J.: *“Heat Transfer, 4th Edition”*. New York: Maxwell Macmillan International. 1989.
- [14] M.A. Saqib and A.D. Stokes, “Time resolved spectrum of the fuse arc plasma”, *Thin Solid Films*, 345, p.p.151-155, 1999.
- [15] W. Bussière and P. Bezborodko, “Measurements of time-resolved spectra of fuse arcs using a new experimental arrangement”, *J. Phys. D: Appl. Phys.*, 32, p.p. 1693-1701, 1999.
- [16] C.S. Psomopoulos and C.G. Karagiannopoulos: Measurements of fusible elements during current interruption and interpretation of related phenomena, *Measurement, Journal of the International Measurement Confederation*, (32), p.p.15-22, 2002.
- [17] Yuri P. Raizer: *“Gas Discharge Physics”*. Germany - Heidelberg: Springer-Verlang. 1991.
- [18] C.S. Psomopoulos and C.G. Karagiannopoulos: “Temperature distribution of fuse elements during pre-arcing period”, *Electric Power Systems Research*, (61), p.p.161-167, 2002.
- [19] M.J. Taylor: “Formation of plasma around wire fragments created by electrically exploded copper wire”, *J. Phys. D.: Appl. Phys.*, (35), p.p.700-709, 2002.
- [20] M.J. Taylor, “Current diversion around a fragmenting wire during the voltage spike associated with exploding wires”, *Proc. of Inter. Conf. on Electric Fuses and their Applications, Gdansk (PL), 2003*, pp.1-9.

COMPACTION BY HORIZONTALLY VIBRATED 3D GRANULAR MATERIALS. APPLICATION TO SAND FILLING AND COMPACTION IN ELECTRICAL FUSES

A. Raihane⁽¹⁾, O. Bonnefoy⁽²⁾, J.-L. Gelet⁽³⁾, J.-M. Chaix⁽⁴⁾, G. Thomas⁽⁵⁾

Centre SPIN^(1,2,5) LPMG UMR CNRS 5148. Ecole Nationale Supérieure des Mines de Saint-Etienne.
158, Cours Fauriel. F-42023 Saint-Etienne. raihane@emse.fr⁽¹⁾, bonnefoy@emse.fr⁽²⁾, gthomas@emse.fr⁽⁵⁾

Ferraz-Shawmut⁽³⁾ 6, rue de Vaucanson. F-69720 Saint-Bonnet de Mure,
Jean.Louis.Gelet@fr.ferrazshawmut.com⁽³⁾,

SIMAP⁽⁴⁾ INPGrenoble-CNRS-UJF. BP 75, Domaine Universitaire, F-38402 Saint-Martin d'Hères,
Jean-Marc.Chaix@inpg.fr⁽⁴⁾

Abstract: Horizontal shaking of silica sand has been studied for the purpose of improving the efficiency and reliability of high breaking capacity fuses. An horizontal vibration device has been designed, which provides sinusoidal vibrations up to 300 Hz and enables the external observation of sand motion in 3D sand piles up to 4×8×5 cm³ in transparent boxes. At 50 Hz, with increasing relative acceleration Γ , the sand behaviour shows the onset and development of convective rolls in the upper part of the sand pile with 2-rolls organization, then the development of strong downwards motions at the four vertical corners of the box. An overall densification is observed in

dynamic conditions. When vibrations are stopped, the sand structure relaxes and further densification is observed. The relaxed density first increases with increasing acceleration, then tends to decrease to a plateau after having reached a maximum value.

Keywords: fuses, granular media, 3D horizontal vibrations, packing density, homogeneity.

To obtain the full paper, please contact J.-L. Gelet :
Jean.Louis.Gelet@fr.ferrazshawmut.com

SOME COMMON PERFORMANCE CHARACTERISTICS OF GAS-BLAST INTERRUPTERS AND POWER EXPULSION FUSES.

Alfonso Ávila Ramírez

Corporativo Arian, S.A. de C.V.
dirtec@arian.com.mx

Abstract: In this paper are described some common performance similarities of the medium voltage power expulsion fuses and gas-blast circuit breakers. Also is presented a short review of their mechanical operating characteristics paying attention to the movement of contacts and arcing electrodes in both type of devices. And their interaction with the power electric system. Finally is presented a shallow review through the time of the developments made by different researchers, adding a little more emphasis on the so-called conservation equations; the field of their scope and the improvements on the applied mathematics, for instance the change from ordinary to partial differential equations which are more adequate when studying the transient period after current zero on circuit breakers mainly.

Keywords: Arc plasma, nozzle, throat, clogging, ablation process, downstream region, upstream region, local thermodynamic equilibrium, self-pressure device, gas-blast device, stagnation pressure.

1. Introduction.

After melting the fuse wire in an expulsion fuse or after the contacts separation in a gas-blast circuit breaker, an electric arc appears. In power fuses the moving arcing rod or the moving arcing contact in self-pressurizing circuit breakers, both are enclosed within a chamber of insulating material which surface is partially vaporized by the ohmic heat input creating an overpressure inside the chamber that leads to an expansion flow through the open end in fuses or in the downstream region in circuit breakers, this pressure gradient act as momentum source and accelerates the flow of the arc plasma [1] and the surrounding vapor toward the outlet of fuses. Often that flow reach the choking points when it becomes supersonic in the above mentioned outlet in fuses or at the throat of nozzles of gas-blast interrupters.

The pattern of the plasma flow is very similar in gas blast circuit breakers in which the pressure gradient is externally imposed by a nozzle flow in the

gas blast arc, but in both cases the basic physical process is essentially the same.

When high magnitude currents are applied the arc diameter approaches that of the wall confining the arc and burns in a high pressure plasma formed by ablation of wall material [1] building up a strong axial flow of gas and hot plasma. The venting of the ablated vapors through the outlet can be choked as mentioned before, producing very high transient pressure [2] at the closed end of the chamber.

In order to illustrate the basic structure of a gas flow arc in both type of interrupting devices in the figure 1 is presented a single -flow arcing configuration for a circuit breaker: this structure consists of a plasma column consisting of hot gases species or may be contaminated by evaporated electrode material through which almost all current flows. A surrounding mantle of heated gas below that at which significant electrical conduction occurs, and an outer confining flow of gas whose properties are governed by aerodynamics considerations [3].

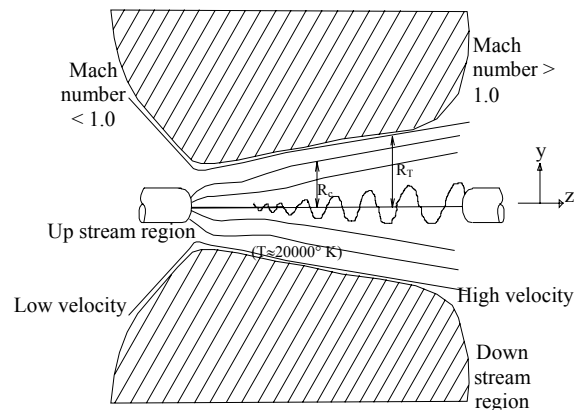


Fig. 1: Basic structure of a gas flow arc in the nozzle of a single-flow circuit breaker.

The interaction of the arc with the electric system when are applied current and voltage waveforms are very important for that devices. In the figure 2 is represented the discharge of a half sinusoid current pulse followed by the rise of recovery voltage across the gap after the current zero value.

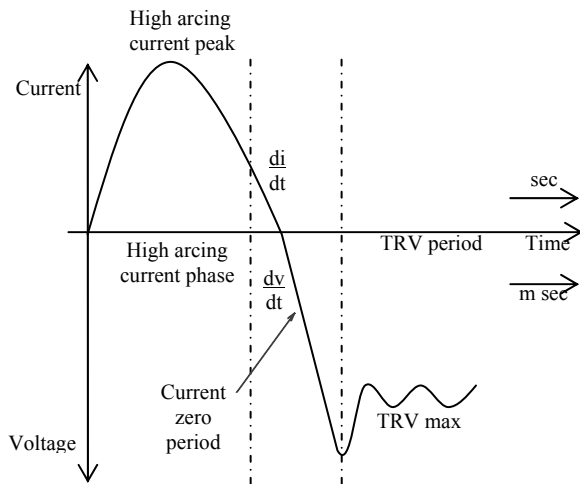


Fig. 2: Conditions of the electrical system.

The electrical energy is transformed in the arc and is dissipated as a stream of hot plasma and gas leaving in the open end of fuses or is the downstream region in circuit breakers. The production of vapor can be adjusted to the requirements choosing suitably: the geometry, dimensions and materials. In the figure 3 is shown a schematic representation of the axial variation of the transient pressure as a result of the ablation of the boric acid chamber of a power expulsion fuse for 25.8 kV of rated voltage after an arcing time of 4.4 ms and before the arcing rod have reached its resting position.

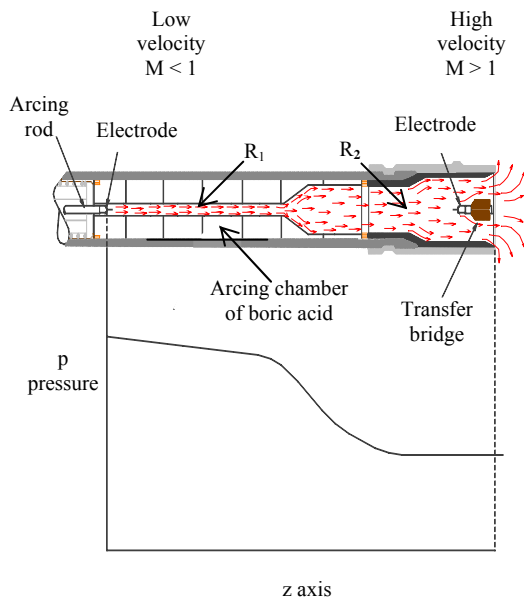


Fig. 3: Schematic representative of the axial variation of pressure for ablation of boric acid and in a power fuse of 25.8kV and rated current of 6A.

$$R_1 \ll R_2$$

The critical parameter that defines the magnitude of the maximum pressure is the ratio of channel (chamber) inside surface to the cross-sectional area [4].

$$\text{Area ratio} = \frac{2\pi Rl}{2l} = \frac{\pi R^2}{R}$$

Eliminating the constant multiplier, the critical parameter is $\frac{1}{R}$.

In the figure 3 we have $\frac{1}{R_1} \gg \frac{1}{R_2}$

2. Action of the system in both type of circuit breaking devices

As it was described before, after melting, during and following the instant of evaporation of the fuse wire or after the separation of the contacts in a gas-blast circuit breaker, the input current is carried by an arc of plasma that is a highly ionized gas from which it derives its conductivity.

- In circuit breakers the high pressure plasma reaches temperatures of the order of 20000 K.
- The conductivity at this temperature and the corresponding pressure inside of the interrupter is a fraction of an ohm-centimeter. Thus the current densities are in the order of several thousands amperes per square centimeter and the voltage gradients in the arc is of several hundred volts per cm [4].
- In such conditions in order to assure a successful interruption at a current zero, the quantity of energy extracted must be greater than the energy that is supplied by the system.
- The plasma must change from a conductor to a good insulator, bearing in mind that the transient recovery voltage (TRV) builds up across the residual plasma when the arcing current comes to zero.
- The dielectric strength between electrodes in fuses and circuit breakers must be regenerated at a rate greater than the TRV imposed by the system.
- In an fuse-unit of dropout type the opening process is the following: during the arcing time a compression or tension spring lengthen the arc path quickly, drawing apart the arcing contacts thereby stretching and finally breaking the arc. Immediately after the upper end of the arcing rod breaks the upper seal and releases the latch located in the upper contact assembly assuring the

dropout action by thrusting the fuse-unit outward to the fully open position. If the rate of rise of recovery voltage (RRRV) is very rapid the cooling time must be only tens of microseconds and the cooling rate of the order of 10^9 K/sec for a successful interruption. The RRRV gives a measure of the circuit severity from a switchgear point of view[5].

- When the decaying plasma has significant conductivity will flow a post-arc current as an indication that the system is applying more energy, but if the rate of energy extracted is bigger, the duration of such a current will be very short. See the figure 4.

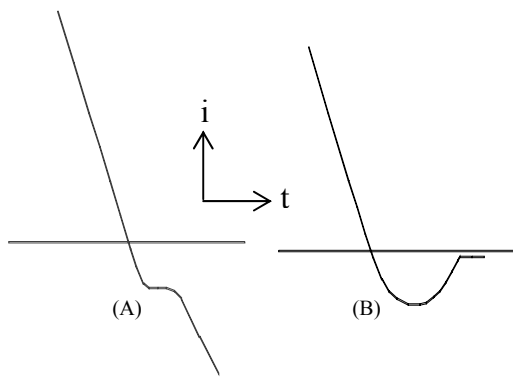


Fig. 4: Post-arc current (A) successful clearing (B) reignition.

In the figure 5 is shown the case of the presence of a small post-arc current when a power fuse unit interrupts satisfactorily a symmetric current of 11.5kA at 23 kV, 60 Hz. Its duration is approximately of 0.34 ms.

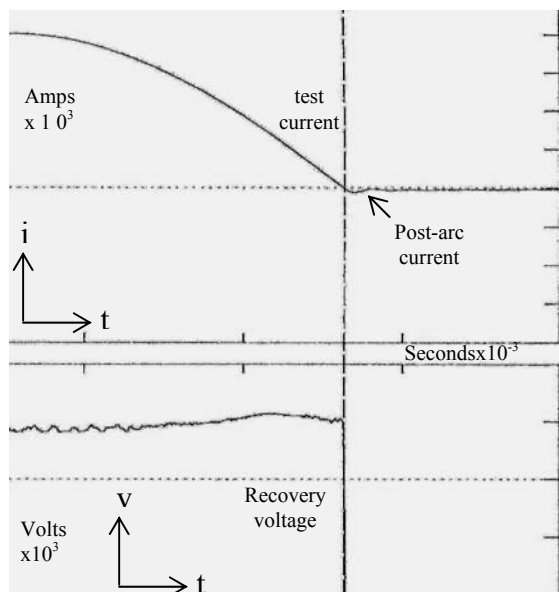


Fig. 5: Post-arc current in a fuse-unit tested with the 90 percent of its interrupting capacity.

- A circuit breaking device can be vulnerable to circuit conditions in which the TRV rises rapidly. When interrupts a secondary fault close to a transformer appears an arcing voltage with a high natural frequency with low damping. In the case of power expulsion fuses this case corresponds to the test series 6 of table 9 of the Std IEEE c37.41-2000. That establishes a TRV critically damped [6].

- In the figure 6 is presented the interruption with a power fuse of a current of 15 A at 23.2 kV in a circuit with a time to peak of 432μ sec and a equivalent frequency of 1.15 kHz.

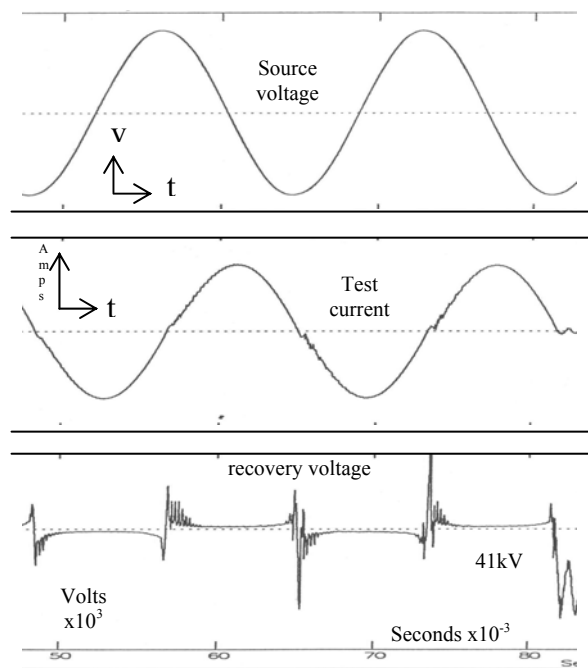


Fig. 6: Interruption of a current of 15 A with a power fuse-unit of 3A of rated current.

In medium voltage circuits a high arcing voltage can be advantageous because it can influence the magnitude of a fault current due its opposition of its flow. See the figure 6.

3. Requirements for circuit breakers and fuses.

The primary function of any of these two circuit breaking devices is the interruption, bearing in mind that they are interacting with the electrical power system.

In the case of circuit breakers, in addition to meeting their interruption functions, are these: to carry load currents, withstand voltage and energize

circuits. In the table 1 are shown the main functions of a circuit breaker [7].

Table 1

3.1 Interrupt faults.
Terminal faults up to the rated interrupting capability: <ul style="list-style-type: none"> - Isolated three-phase (or two-phase) faults. - Grounded three-phase (or two-phase) faults - Short line faults at any distance from the terminal, out of phase operations (optional).
3.2 Interrupt loads
<ul style="list-style-type: none"> - Normal loads up to the rated continuous currents - Capacitive loads. <ul style="list-style-type: none"> • Capacitor banks (optional) • Unloads lines • Cables - Small inductive loads - Magnetizing current of transformers - Reactors (optional) - Motors
3.3 Carry current.
<ul style="list-style-type: none"> - Rated continuous current - Short time fault current
3.4 Dielectric requirements in closed and open positions dry or wet.
<ul style="list-style-type: none"> - system voltage - Lightning surges - Switching surges
3.5 Energize loads
<ul style="list-style-type: none"> - Transformers (inrush currents) - Normal loads - Capacitor banks - Lines - Into faults (related to the short line fault current)

The basic functions of a power expulsion fuse are:

- To carry the load currents which magnitudes are as high as its nominal rated current
- To interrupt fault currents until its maximum interrupting capacity. These fuses are tested in accord with the standards, which should reflect as far as possible the operating conditions in the field. Another relationships between circuit breakers and fuses performance parameters are the mechanical and thermal constraints they impose. In circuit breakers with a given rating for which the performance demands are identical, individual mechanical designs will vary widely depending of the particular interrupting medium

employed [8] there is not possibility to define universal principles and consequently certain generally valid concepts are usually applied. In the table 2 are presented only those performance parameters corresponding to circuit breakers and fuses indistinctly.

Table 2

Circuit Breakers [8]
A. Continuous Current
<ul style="list-style-type: none"> - Contacts cross-section - Contact material - Number of contacts
B. Interrupting current
<ul style="list-style-type: none"> - Contact stroke - Minimum and maximum velocities limits - Number of series contacts - Opening resistor
Power expulsion fuses
A. Continuous Current.
<ul style="list-style-type: none"> - Cross section and material of the fuse wire - Time-current characteristic (both melting and total-clearing time)
B. Interrupting current
<ul style="list-style-type: none"> - Isolating distance between electrodes - Minimum velocity of the arcing rod imposed by the auxiliary spring of compression or tension type

In the figure 7 are presented the critical events in the time-story of the opening process in both type of the circuit breaking devices.

4. The theoretical investigation of arc properties in gas-blast circuit breakers and expulsion fuses.

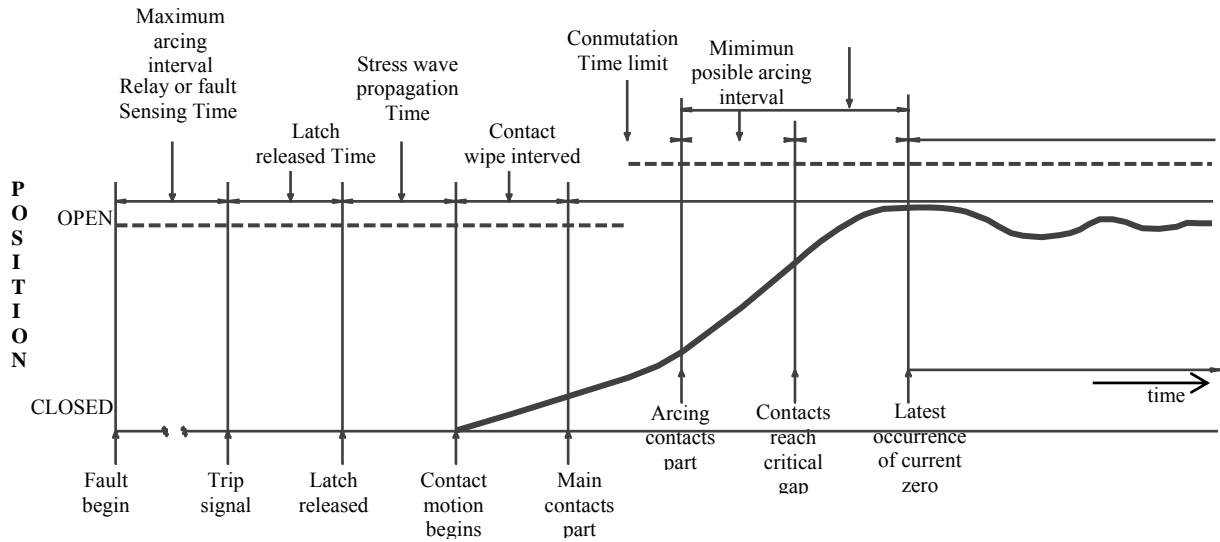
The purpose of this section is to present a brief description of the theoretical modeling of arc discharge in gas-blast circuit breakers and expulsion fuses and as far as possible a comparison of the results obtained by different researchers through the time.

During about thirty years the classical equations of Cassie and Mayr were or still are used in circuit breaking devices design.

In 1939, Cassie developed a differential equation for the arc resistance by assuming an arc column in which the arc temperature is constant and the arc area varies with the current. This model was intended to represent an arc in an air-blast circuit breaker

assuming that the air flow penetrated the whole cross-section of the arc, carrying away heat and making the dissipation per unit volume constant as well [9].

- Circuit breakers.



- Power expulsion fuses of dropout type.

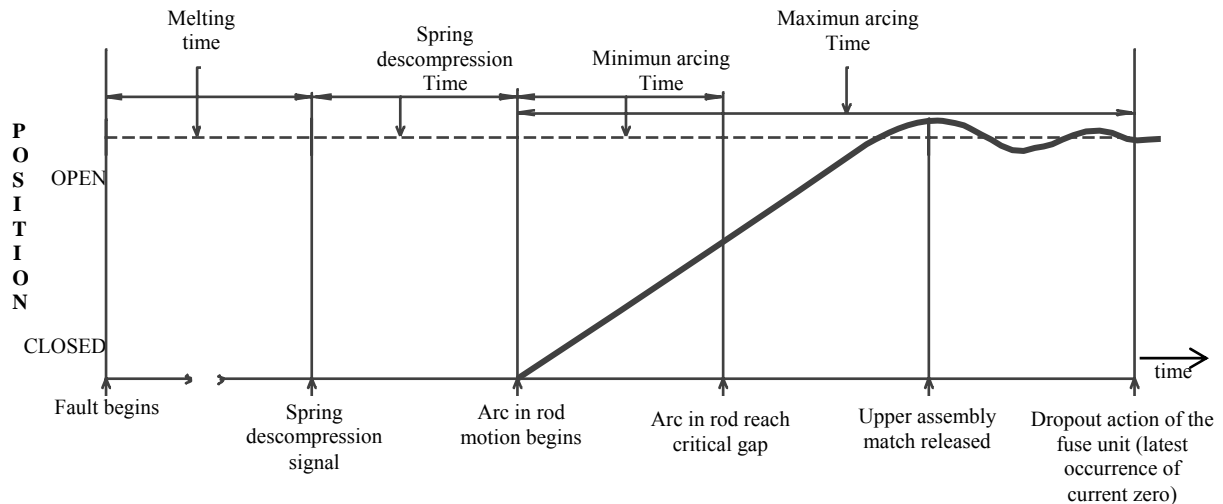


Fig. 7: Critical events in the time-history of the circuit breakers and fuses opening processes.

Such assumptions led to the following differential equation:

$$R \frac{d\left(\frac{1}{R}\right)}{dt} = -\frac{I}{\Theta} \left\{ \left(\frac{v}{v_0}\right)^2 - 1 \right\} \quad \text{where} \quad (1)$$

R= arc resistance

v= arc voltage an any instant

v₀= arc voltage in steady-state

Θ= Time constant =

Energy stored per unit volume

Energy loss rate per unit volume

The resistance increases exponentially as the stored energy is removed at a finite rate by the air flow.

In 1943 Mayr developed a differential equation for arc resistance by assuming an arc column in which the arc radius is constant and arc temperature varies with time. In this arc model energy is transferred only by radial conduction and the conductance of the arc varies exponentially with the energy stored in it. This is the differential equation developed

$$R \frac{d\left(\frac{1}{R}\right)}{dt} = -\frac{I}{\Theta} \left\{ \left(\frac{v_i}{w_0}\right) - 1 \right\} \quad (2)$$

This equation has certain advantages. In the steady state condition when currents and voltages are changing slowly

$$\frac{d\left(\frac{1}{R}\right)}{dt} = 0 \quad \text{and therefore} \quad v_i = w_0 \quad (3)$$

And the steady state characteristic arc hyperbolic being a good representation of what happens is an interrupter in the low current region [9].

In 1948 Browne developed a mathematical model of the arc that combined many features of the previous models, but without progress in numerically relating the terms of the equation with the physical properties of the interrupting medium. Due to the Cassie-Mayr arc models are described by ordinary differential equations there is a limit to the amount of information that can be obtained from them.

They cannot shed light on the physics of arc interruption because that is described by partial differential equations of gas dynamics.

Among the reasons for developing advanced models are these:

- Growth of short circuit current of power systems.
- Consequently the RRRV caused by a line fault that is proportional to the fault current.
- Nozzle clogging that occurs when the arc expands to fill the nozzle throat due to the high

plasma temperature and low density. Clogging the nozzle mass flow and limits the energy carried away by convection.

- The theoretical formulation of all determinant parameters is very useful to provide information of circuit interrupting devices performance, leaving behind the empirical design methods replaced by scientific analytical procedures.

Some decades ago (1950-1970) the difficulties for modeling circuit breakers arise from the complex nature of the equations describing nozzle arcs, the non-linear character of the thermodynamic and transport properties of interrupting gases, the complex flow fields generated with Laval nozzles with supersonic flow and shock waves, stability problems with numerical methods and the uncertainties in modeling arc turbulence and radiation.

Arc turbulence [10]

As has been mentioned before in the past there were little knowledge about turbulence in high pressure arcs but with the development of nozzle arc models it was understood the real need for turbulence information. The primary arc turbulence models were developed in base of aerodynamic turbulence.

In the momentum equation, the transfer of momentum in the y direction:

$$\frac{\partial}{\partial y} [(\eta + \eta_t) \frac{\partial v_z}{\partial y}] \quad (4)$$

Where η is the molecular viscosity and η_t is the turbulent viscosity defined by the equation

$$\eta_t = \rho \varepsilon_m$$

Where ρ is the gas density and ε_m is the eddy diffusivity of momentum. Similarly, in the energy equation the transfer of heat in the y direction is given by the term.

$$\frac{\partial}{\partial y} [(k + k_t) \frac{\partial T}{\partial y}] \quad (6)$$

k is the thermal conductivity

k_t is the turbulent thermal conductivity defined by the equation

$$k_t = \rho C_p \varepsilon_H \quad (7)$$

Where ε_H is the eddy diffusivity of heat and C_p is the specific heat. The eddy diffusivities of heat and momentum are related by equation

$$\varepsilon_H = \frac{\varepsilon_m}{\rho_{\tau t}} \quad (8)$$

Where ρ_{rt} is the turbulent Prandtl number assumed equal $\frac{1}{2}$. Therefore to estimate the effects of arc turbulence we must estimate the eddy diffusivity of momentum ϵ_m

In the inner region of a turbulent boundary layer the eddy diffusivity varies according to the equation

$$(\epsilon_m)_i = l \frac{\partial u}{\partial y} \quad \text{for } y_o \leq y \leq y_c \quad (9)$$

Where y_o is a small distance from the surface and l is the Prandtl mixing length which varies linearly with y in this region. In the outer region of the boundary layer, the velocity is fairly uniform and the eddy diffusivity varies according to the equation

$$(\epsilon_m)_o = \alpha_1 V_e \delta^* \quad \text{for } y_c \leq y \leq \delta \quad (10)$$

Where α_1 is a constant, δ is the boundary layer thickness, V_e is the free stream velocity of the boundary layer and δ^* is the displacement thickness which is proportional to δ and varies in the Z direction. From the equations (9) and (10) are inferred the following: within the core of a radiation dominated arc the flat temperature profile produces a fairly uniform core velocity and core turbulence may resemble turbulence in the outer region of the boundary layer where the velocity is also fairly uniform.

Arc radiation [11]

When the current exceeds 1000A, radiations is the most important loss mechanism at the arc centre Tuma and Lowke shown that nozzle arc models can be developed using two emission coefficients of radiation u and u_t as functions of temperature, pressure and arc radius assuming the arcs are approximately isothermal.

The coefficient u gives the radiation loss at the arc center and is dominated by ultraviolet radiation which is reabsorbed at the arc boundary.

The coefficient u_t gives the radiation which is reabsorbed at the arc boundary and gives the radiation which is completely lost from the arc and which is dominated by the visible region of the spectrum.

The thermal interrupting performance.

- In modeling this type of performance of an arc in a nozzle, the usual assumptions are: axial symmetry, constant gas pressure, local thermodynamic equilibrium (LTE) and no viscous or magnetic effects. Additionally axial variations and convection are assumed negligible in comparison with radial variations.

Arc models in cylindrical tubes and nozzles.

Choosing a cylindrical symmetric arc confinement, E.Z. Ibrahim [12] formulated the equation describing the physical behavior of the arc in the radial and axial directions. The equations for his arc model are:

- The energy conservation

$$\begin{aligned}
 & \text{J.E.} + \frac{\partial}{\partial z} (k_r \frac{\partial T}{\partial z}) + \frac{1}{r} \frac{\partial}{\partial r} (k_r r \frac{\partial T}{\partial r}) = \\
 & \text{ohmic power} \quad \text{axial conduction} \quad \text{radial conduction} \\
 & \text{Prad} + \rho C_p v_r \frac{\partial T}{\partial r} + \rho C_p v_z \frac{\partial T}{\partial z} + \rho C_p \frac{\partial T}{\partial t} \quad (11) \\
 & \text{radiated power} \quad \text{radial convection} \quad \text{axial convection} \quad \text{thermal inertia}
 \end{aligned}$$

- Conservation of momentum

Radial

$$\begin{aligned}
 & \frac{\partial p}{\partial r} + \rho v_z \frac{\partial v_r}{\partial z} + \rho v_r \frac{\partial v_r}{\partial r} + \frac{4}{3} \mu \frac{v_r}{r^2} = \\
 & \frac{4}{3} \frac{1}{r} \frac{\partial}{\partial r} (\mu r \frac{\partial v_r}{\partial r}) \quad (12)
 \end{aligned}$$

Axial

$$\begin{aligned}
 & \frac{\partial p}{\partial z} + \rho v_z \frac{\partial v_z}{\partial z} + \rho v_r \frac{\partial v_z}{\partial r} = \\
 & \frac{1}{r} \frac{\partial}{\partial r} (\mu r \frac{\partial v_z}{\partial r}) \quad (13)
 \end{aligned}$$

Conservation of mass is a balance between the radial influx of ablating wall material and the convective outflow of mass caused by pressure difference between the stagnation zone and tube exit

$$\begin{aligned}
 & \frac{\partial}{\partial z} (\rho v_z) + \frac{1}{r} \frac{\partial}{\partial r} (\rho v_r r) = 0 \quad (14) \\
 & \text{Axial variation of mass outflow} \quad \text{Radial variation of mass influx}
 \end{aligned}$$

Usual assumptions:

- Axial symmetry
- The arc is isothermal radially, i.e.

$$\frac{\partial T}{\partial r} = \frac{\partial T}{\partial z} = 0, \quad (15)$$

The temperature profile is rectangular / flat.

- The arc is isobaric, i.e. $\partial p / \partial r = 0$
- The arc core is in local thermodynamic equilibrium (LTE).
- The arc is quasi-stationary, i.e. $\frac{\partial}{\partial t} \approx 0$
- The arc core is radiation dominated.

The conclusions he found about analytical modeling of the ablation dominated confined arc in an cylindrical tube developed on the basis of an integral uni-dimensional formulation are:

- The temperature distribution in the ablation dominated, high current arc is almost flat radially and can be approximated by the central temperature.
- The arc's radiative behavior is a function of the formation of the heat.
- For any current density the pressure is a lineal function of tube half-length. He used a tube open in both ends.
- Turbulent plasma flow in the outer axial sections (tube with two open ends) of the confined arcs was established analytically.

The semi-empirically derived scaling laws/formulae, that link the relevant arc parameters are.

$$E_2 = 2.65 \times j^{0.4267} \text{ vcm}^{-1} \text{ Electric field gradient}$$

$$P_c = 6.375 \times 10^{-3} \times j^{0.955} \text{ bar kinetic stagnation pressure.}$$

$$T_1 = 1.641 \times 10 \times j^{0.238} \text{ K arc column temperature.}$$

$$T_2 = 3.63 \times 10 \times j^{0.308} \text{ K arc mantle temperature.}$$

Model developed by P. Kovitya and J.J. Lowke [13]

They assumed that if the energy losses from an optically arc are dominated by radiation, the radial temperature profile becomes flat at center and since the axial pressure and velocity gradients are much greater than the radial gradients, it is assumed that the radial variations in plasma temperature, pressure and velocity are negligible.

For instance the energy conservation equation for this arc model is:

$$\rho C_p \frac{\partial T}{\partial t} = \sigma E^2 - U - \rho C_p v_z \frac{\partial T}{\partial z} - \rho v_z^2 \frac{\partial v_z}{\partial z} \quad (16)$$

Making a comparison with the equation (11) here in the equation (16) are neglected the partial differential equations for radial convection and conduction.

The axial component of the equation describing the conservation of momentum of the arc is:

$$\frac{\partial(\rho v_z)}{\partial t} + \nabla \cdot \rho (v_z v) = - \frac{\partial p}{\partial z} \quad (17)$$

Where v is the vector velocity and P is the arc pressure

Integrating the equation (17) between cross-section at z and $z + \Delta z$ and arc boundary, after using the Gauss divergence theorem, and taking m as the rate of vapour entrainment into the arc and v_c is the axial vapour velocity, letting Δz approach to zero was obtained:

$$\frac{\partial}{\partial t} (\rho v_z A) + \frac{\partial}{\partial z} (\rho v_z^2 A) - \dot{m} v_c = -A \frac{\partial P}{\partial z} \quad (18)$$

The continuity equation for the arc

$$\frac{\partial(\rho A)}{\partial t} = \dot{m} - \frac{\partial}{\partial z} (\rho v_z A) \quad (19)$$

If equation (19) is substituted into equation (18), is obtained.

$$\rho \frac{\partial v_z}{\partial t} = -\rho v_z \frac{\partial v_z}{\partial z} - \frac{\partial P}{\partial z} - \frac{\dot{m}}{A} (v_z - v_c) \quad (20)$$

The term $m (v_z - v_c) / A$ was not included by Ibrahim, it represent deceleration by the entrained vapour.

Kovitya and Lowke developed a one-dimensional gas-dynamic model of ablation-stabilized arcs in uniform cylinders. They indicated that it was in good agreement with experiments.

In the above equations (11) to (20): ρ is plasma density, C_p is specific heat, T is plasma temperature. t is time σ is electrical conductivity, E is electric field, u is radiation emission coefficient, z is axial position, p is the arc pressure, μ is viscosity, v_z and v_r are the axial and radial velocities respectively, m is the rate of vapor entrainment into the arc.

Theoretical modeling of forced convection-stabilized arcs

In this section is presented a summary of a transients-two dimensional model of forced convection stabilized arc such as those found in gas-blast circuit breakers.

During the 1980-1990 decade Mitchell and Tuma [14] developed a computational model for solving the conservation equations along with

Ohm's Law and an equation of state. For a given current the working gas and information about the nozzle geometry, the model finds temperature and radial and axial mass velocities as functions of cylindrical coordinates r , z and time and also computes electric field as a function of axial position, all in the upstream region of the arc.

The pressure distribution is determined by; the stagnation and exit pressures, the shape of the nozzle and the type of gas. The three conservation equations for mass, axial momentum and energy are respectively:

$$\frac{\partial \rho}{\partial t} + \frac{\partial}{\partial z} (\rho v_z) + \frac{1}{r} \frac{\partial}{\partial r} (r \rho v_r) = 0 \quad (21)$$

$$\begin{aligned} \frac{\rho \partial v_z}{\partial t} + \rho v_z \frac{\partial v_z}{\partial z} + \rho v_r \frac{\partial v_z}{\partial r} = \\ - \frac{dp}{dz} + \frac{1}{r} \frac{\partial}{\partial r} (\eta r \frac{\partial v_z}{\partial r}) \end{aligned} \quad (22)$$

$$\begin{aligned} \rho C_p \frac{\partial T}{\partial t} + \rho C_p v_z \frac{\partial T}{\partial z} + \rho C_p v_r \frac{\partial T}{\partial r} = \\ \sigma E^2 - U + \frac{1}{r} \frac{\partial}{\partial r} (r k \frac{\partial T}{\partial r}) \end{aligned} \quad (23)$$

In these equations it is assumed that the axial second-order terms of viscosity and thermal conductivity can be neglected.

The model makes two simplifying assumptions which need to be justified.

These assumptions are:

- The axial pressure distribution is taken from the cold-gas potential flow solution, at the axis $r=0$ and.
- The radial momentum equation is approximated

$$\text{by } \frac{\partial p}{\partial r} = 0$$

When circuit breaker arcs carry very high currents operating with temperatures of the order of 20,000 K the radiation becomes the dominant mechanism of energy transport within the arc [14]. Losses at the arc centre are dominated by the radiation losses and the arc is approximately arc plasma rather than lost as radiation.

- The steady-state arc at high current.

Radiation Transport

For sulphur hexafluoride it is found experimentally that the radial temperature profile of the arc is nearly isothermal.

Thus convection and thermal conduction are no significant in this region the local power balance is $\sigma E^2 = u$

The radial temperature becomes flat-topped and 89% of the power input due to joulean heating is transported away from the arc core by radiation.

- Conduction, convection and the Arc Boundary.

A simplified analysis of the energy equation in the vicinity of the arc boundary shows a very sharp boundary which is observed experimentally in the double-nozzle flow geometry. In this region the joulean heating and radiation terms are relatively small

For steady-state the time term is zero and in the plane $z=0$ the axial convection is also zero the simplified energy equation is

$$- \frac{d^2}{dr^2} (kT) + \rho C_p v_r \left(\frac{dT}{dr} \right) = 0 \quad (24)$$

Neglecting the term $m \frac{dk}{dt}$ a denoting derivatives by primes

$$\epsilon T'' + T' \quad \text{where} \quad \epsilon = \frac{k}{\rho C_p v_r} \quad (25)$$

In the figure (8) are shown the solutions for four values of ϵ

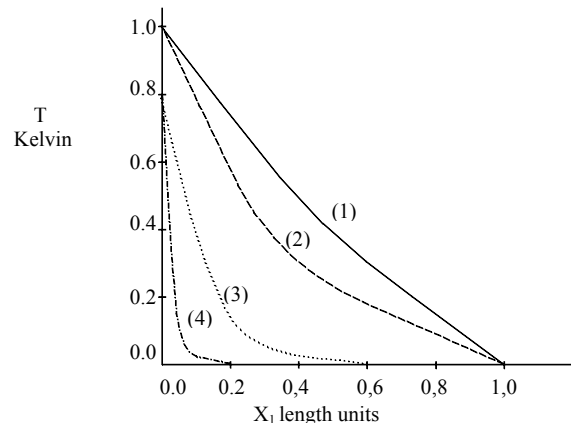


Fig. 8: Solutions to the convection-diffusion equation $\epsilon T'' + T' = 0$ for four values of ϵ - solid curve (1): $\epsilon=1.0$, dashed (2): $\epsilon=0.3$, dotted (3): $\epsilon=0.1$, chain (4): $\epsilon=0.03$ (Fig. 10, Mitchell & Tuma 1985, IEEE)

- Convection of Enthalpy

Due to the large axial mass velocities presented in a high-current stabilized arc, much of the arc power deposited by joulean heating is carried away by convection, Using a cylindrical control volume with radius R and a axial length L for representing a part of the arc between the nozzle throats. (model of Mitchell and Tuma):

The power lost by radiation from the arc core is deposited just inside the arc boundary and

consequently the power deposited is lost by convection and thermal conduction

Cold gas flows radially into the control volume with enthalpy $h_o = h$ ($T = 300K$). Hot gases flow axially out of the control volume in the positive z direction. In steady-state all the gas axially exiting enter the control volume radially by conservation of mass.

The mass flow is given by

$$\int_0^R \rho v_z 2\pi r dr \quad (26)$$

And the enthalpy flow exiting the control volume is:

$$F = \int_0^R \rho h v_z 2\pi r dr \quad (27)$$

Where $\rho h v_z$ is the enthalpy flux

This is the net power loss from the volume due to convection and account for about 95 percent of the power loss.

If the control volume radius is chosen at the 15000 K isotherm the plasma entering the volume has almost much enthalpy as the exiting axially.

- Transient differential Power Balance.

During the transient arc decay after current zero this balance is quite different from the steady-state when the arc is locally radiation dominated while radiation is absent from the decaying arc a few tens of microseconds after current zero.

- Upstream turbulence.

Ragaller et al introduced a large amount of turbulent thermal conductivity into their calculations in order to obtain agreement with the measured dielectric recovery characteristics of Schade and Ragaller [15]; they found that during 100-200 μs after current zero the temperature profile is flattened in the axial and radial direction due to the continue action of turbulence.

The results of Mitchell and Tuma along with the measurements of Graf [14] et al show that the radial temperature profile is constricted with a peak instead at the center

- Mitchell et al have applied a two-dimensional transient model of forced convection stabilized arc. It solves the LTE conservation equations for mass, momentum and energy, using an implicit finite-difference technique for marching in the axial and time dimensions and find the upstream values for temperature $T(r, z = 0, t)$ by using downstream information about the gas flow.

- This model has been used to simulate steady-state arcs in SF_6 and predicts that the arcs are cylindrical in the upstream region of single and double-flow model circuit breakers having parabolic axial distribution.
- The model also simulates the temperature and dielectric recovery of SF_6 arc in laboratory scale devices. It follows the arc from the steady state through the current ramp and during the subsequent free decay.
- Mitchell and Tuma conclude that the mechanism of convection and laminar conduction suffice to cool the upstream region of the decaying arc and that the turbulence has little influence on the upstream temperature recovery and hence on dielectric recovery

5. Conclusions.

It has been attempted to describe in few pages the most relevant performance characteristics of those type of circuit breaking (current zero) devices. Because their primary function of them is to interrupt overcurrents, this paper is focused to the heart of both: the arcing chamber that in fuses is composed by cylindrical chamber with different diameters and geometry and the nozzle of different shapes in circuit breakers without considering the type of arc quenching gas used or if they are self-pressurizing devices where the ablating dominated process is imposed by a given material.

Due to the intrinsic relationship between the interrupting process inside the arcing chamber, the type and shape of nozzles, if they are of single-flow or double flow and the geometry of the inside wall of outlets of fuses and the velocity of the moving contacts.

Finally are summarized several studies about this subject, beginning with the well known developments of Cassie, Mayr and Browne, to others more sophisticated in these fields: thermodynamic, mathematics and numerical methods mainly in the period 1970-1990, that has been applied to circuit-breakers design as well as for fuses.

References

- [1] L. Niemeyer "Evaporation dominated high current arcs in narrow channels". IEEE Transactions on power Apparatus and Systems, Vol. PAS -97, no. 3, May/June 1978.
- [2] P. Kovitya. "Ablation-stabilized arcs in nylon and boric acid tubes" IEEE Transactions on Plasma Science, Vol. P5-15. 0.3. June 1978.
- [3] A. Plessi, L. Niemeyer, F Perdoncin. "Research for medium-voltage SF_6 circuit-breakers" ABB Review 2/89.
- [4] G.R. Jones. "Fundamental arc property measurement in relation to gas-blast circuit breaker behaviour research on high-power interrupters using SF_6 and vacuum". Short course, Reenselaer Polytechnic Institute, Troy New York, July 23-24, 1981.

- [5] A. Greenwood. "Power system and circuit-breaker interactions". Short course Reenselaer Polytechnic Institute, Troy, New York, July 23-24, 1981.
- [6] IEEE Std. Design test for high-voltage fuses, distribution enclosed single pole air switches, fuse disconnecting switches and accessories. IEE Std. C37-41-2000.
- [7] J. Urbanek "Summary of requirements for circuits breakers and their impact on reliability". Short course at Reenselaer Polytechnic Institute, Troy New York, July 23-24, 1981.
- [8] P. Barkan, Physics and engineering of high power switching devices, T. H. Lee principal author, MIT Press, 1975.
- [9] C.H. Flurschein, Power circuit breaker, theory and design Peter Peregrinus LTP, London U.K. 1982.
- [10] B. W. Swanson, "Theoretical models for the arc in the current zero regime", Brown Boveri Symposium on current interruption in high-voltage networks, Baden Switzerland, 1977.
- [11] G. R. Jones, N. Y. Shamma and A. N. Prasad. "Radiated induced ablation in high power circuit interrupters. IEEE transactions on Plasma Science, Vol. P5-14, No. 14. August 1986.
- [12] E. Z. Ibrahim. "The ablation dominated polymethylmetacrylate arc". J. Phys D: Appl. Phys. 13 (1980) 2045-65.
- [13] P. Kovitya and J. J. Lowke "Theoretical predictions of ablation-stabilized arcs confined in cylindrical tubes" J. Phys. D: Appl. Phys; 17 (1989) 1197-1212.
- [14] R. R. Mitchell, D. T. Tuma. "Transient two-dimensional calculation of properties of forced convection-stabilized arcs" IEEE Transactions on plasma Science, Vol. P513, No. 4, August 1985.
- [15] E Schade, K. Ragaller "Dielectric recovery of an axially blown SF₆-arc after current zero: part 1- experimental investigations" IEEE transactions on Plasma science, Vol. p5to, No. 3, September 1982.

MODELLING OF THE PRE-ARCING PERIOD IN HBC FUSES INCLUDING SOLID - LIQUID - VAPOUR PHASE CHANGES OF THE FUSE ELEMENT

D. Rochette¹, W. Bussière², R. Touzani³, S. Memiaghe², G. Velleaud¹ and P. André²

¹ Laboratoire Arc Electrique et Plasmas Thermiques, CNRS UMR 6069, IUT de Montluçon, avenue Aristide Briand 03101 Montluçon, France.

rochette@moniu.univ-bpclermont.fr, velleaud@moniu.univ-bpclermont.fr.

² Laboratoire Arc Electrique et Plasmas Thermiques, CNRS UMR 6069, Université Blaise Pascal, 24 avenue des Landais, 63177 Aubière, France.

william.bussiere@univ-bpclermont.fr, steeve.memiaghe@univ-bpclermont.fr, pascal.andre@univ-bpclermont.fr

³ Laboratoire de Mathématiques, CNRS UMR 6620, Université Blaise Pascal, 24 avenue des Landais 63177 Aubière, France.

rachid.touzani@univ-bpclermont.fr.

Abstract: In this paper, we present a model and a numerical method of the fuse element heating including solid - liquid - vapour phase transitions in order to evaluate the pre-arcing time in HBC fuses. The mathematical model is based on the enthalpy formulation of the heat equation with a source term representing the Joule effect coupled with the Laplace equation for the potential and the Ohm's law. We obtain an approximation of the governing equations using a specific numerical scheme for time discretization and unstructured triangle or tetrahedral element grids are employed in spatial discretization using a standard piecewise linear finite element method. Numerical simulations of two fuse elements, used in industrial applications, are carried out and compared with experimental measurements obtained using a 100 kVA power station.

Keywords: Pre-arcing time, 3D Thermal/Electric model, Finite element method, Phase change.

1. Introduction

Numerous numerical investigations can be found in the literature on the study of the fuse pre-arcing regime [1-6] in order to evaluate the time/current characteristics and to be a useful tool for the fuse element design. This work relating once again to the study of the pre-arcing period in High Breaking Capacity (HBC) fuses is motivated by the aim at developing in future works a physical model of the fuse operation, *i.e.* pre-arcing and arcing models. To ensure the transition between the two regimes, we must extend the fuse element heating by Joule effect until vapour phase appears, *i.e.* initiation of the electric arc.

For this purpose, we have developed a 3D-model of the Joule heating of the fuse element. We use a set of equations coupling the thermal and the electrical

phenomena and the solid - liquid - vapour phase transitions are included using an enthalpy formulation. The physical parameters of the silver fuse element depending on the temperature are used. For the short pre-arcing times, we assume no heat transfer between the fuse element and the surrounding porous medium and for medium pre-arcing times, the heat exchanges with the porous medium are prescribed using appropriate boundary conditions. The model and the numerical method are tested with two fuse elements provided with one reduced section. Numerical results for short and medium pre-arcing times are compared with experimental measurements acquired using a 100 kVA power station.

2. Mathematical model

In a simplified approach, the study consists in modelling only the fuse-element where boundary conditions are supplemented to take into account the heat transfer, conductive and radiative, toward the porous medium. Consequently, no information is available on the porous environment.

We have tested two fuse elements provided with only one reduced section. The characteristics of the fuse element 1 are shown in Fig. 1. This one is used to test short pre-arcing time, consequently, we neglect heat transfer toward the porous medium and so a 2D-model is sufficient to describe the phenomenon.

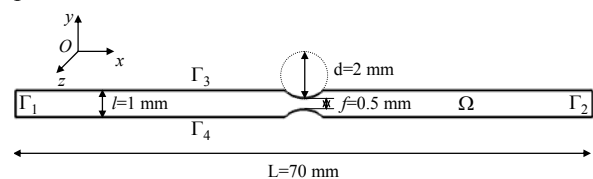


Fig. 1: 2D-geometry of the fuse element 1 of thickness $e = 0.105 \text{ mm}$.

Fig. 2 represents the 3D-geometry of the fuse element 2. This one is tested in the case of the medium pre-arcing time (> 10 ms) where heat exchanges between the fuse element and the porous medium are taken into account using boundary conditions on Γ .

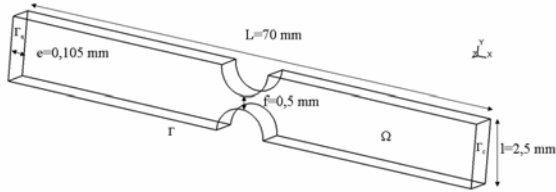


Fig. 2: 3D-geometry of the fuse-element 2.

The fundamental partial differential equation governing the transient Joule heating of the silver fuse element is described by the balance of energy:

$$\frac{\partial H}{\partial t} - \nabla \cdot (k \nabla T) = \frac{|\mathbf{J}|^2}{\sigma} \quad (1)$$

where T is the temperature field, H is enthalpy per unit volume, k and σ are respectively the thermal and electrical conductivities of the silver, all depending on temperature. \mathbf{J} denotes the vector of current density obtained in solving the Laplace equation and the Ohm's law:

$$\begin{cases} \nabla \cdot (\sigma \nabla V) = 0 \\ \mathbf{E} = -\nabla V \\ \mathbf{J} = \sigma \mathbf{E} \end{cases} \quad (2)$$

where V is the electric potential and \mathbf{E} is the electric field vector.

The enthalpy function versus temperature [7], illustrated in Fig. 3, is defined by the general form:

$$H(T) = \int_{T_{ref}}^T \rho c(s) ds \quad (3)$$

with

$$H(T) = \begin{cases} \int_{T_{ref}}^T \rho c(s) ds & \text{if } T < T_m \\ \int_{T_{ref}}^{T_m} \rho c(s) ds + \rho L_m & \text{if } T = T_m \\ \int_{T_{ref}}^{T_m} \rho c(s) ds + \rho L_m + \int_{T_m}^T \rho c(s) ds & \text{if } T > T_m \\ \int_{T_{ref}}^{T_m} \rho c(s) ds + \rho L_m + \int_{T_m}^{T_v} \rho c(s) ds & \text{if } T = T_v \\ \int_{T_{ref}}^{T_m} \rho c(s) ds + \rho L_m + \int_{T_m}^{T_v} \rho c(s) ds + \rho L_v & \text{if } T > T_v \end{cases} \quad (4)$$

where ρ is silver density [8], c is specific heat depending on temperature and T_{ref} is a reference temperature. L_m and L_v denote respectively the melting and boiling latent heats. T_m and T_v are respectively the melting and the boiling temperatures of silver. Notice that multivalued function (4) takes into account phase changes at temperature T_m (solid \rightarrow liquid) and T_v (liquid \rightarrow vapour) of the silver fuse element.

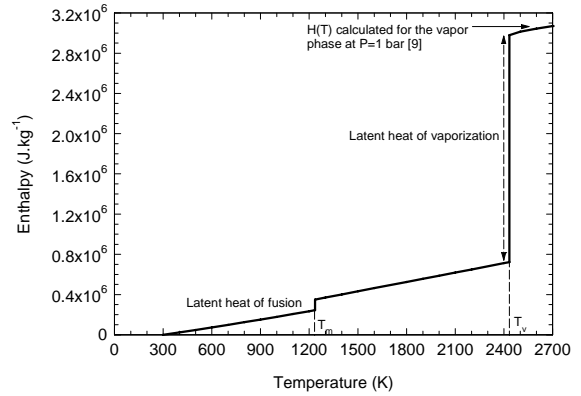


Fig. 3: Enthalpy versus temperature for silver [7].

To solve the transient electric-thermal problem, equations (1) and (2) must be supplemented by initial and boundary conditions.

The initial temperature is fixed at the value $T_0 = 300$ K and we impose the following boundary conditions:

- On boundary Γ_a (*i.e.* anode), we impose the current density flux through the fuse cross section $|\Gamma_a|$:

$$\sigma \frac{\partial V}{\partial \mathbf{n}} = \frac{I(t)}{|\Gamma_a|} \quad (5)$$

where \mathbf{n} is the outward unit normal to the boundary and $I(t)$ is the prospective current of the circuit as described hereafter (see equation (11)).

- On boundary Γ_c (*i.e.* cathode), a reference potential is prescribed $V = 0$.
- On boundary Γ , representing the other boundaries of the fuse element surrounded by silica sand, we have used two heat transfer conditions as:

$$k \frac{\partial T}{\partial \mathbf{n}} = k_{eff} \frac{(T - T_0)}{L} + \varepsilon \sigma_s (T^4 - T_0^4): \text{3D-model} \quad (6)$$

$$k \frac{\partial T}{\partial \mathbf{n}} = 0: \text{2D-model}$$

where k_{eff} is the thermal conductivity of the porous medium, $\varepsilon(T)$ is the silver emissivity, σ_s is the Stefan constant and L is the porous medium length. The first expression assumes that the porous medium is transparent (optically thin) and the second expression assumes no heat transfer.

The principal Silver properties used in the calculations are depicted in Table 1.

Table 1: Silver properties

Density (kg.m^{-3})	$\rho = 10490 \text{ kg.m}^{-3}$
Melting temperature	$T_m = 1235 \text{ K}$
Boiling temperature	$T_v = 2433 \text{ K}$
Latent heat of fusion	$L_m = 1.05 \times 10^5 \text{ J.kg}^{-1}$
Latent heat of boiling	$L_v = 2.26 \times 10^6 \text{ J.kg}^{-1}$

The thermal [10] and electric [11] conductivities depending on temperature are plotted in Fig. 4. For both, the ratio of thermal and electric conductivities at the melting temperature is slightly higher than 2.

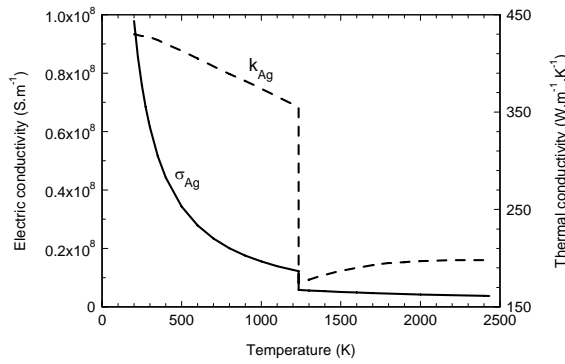


Fig. 4: Thermal [10] and electric [11] conductivities of Silver.

The total hemispherical emissivity of the silver fuse element is obtained by the formulation proposed by Parker and Abbott (Fig. 5):

$$\varepsilon(T) = 0.766 \sqrt{\frac{T}{\sigma}} - \left[0.309 - 0.0889 \ln\left(\frac{T}{\sigma}\right) \right] \left(\frac{T}{\sigma}\right) - 0.0175 \left(\frac{T}{\sigma}\right)^{3/2} \quad (7)$$

with T in K and σ in S.cm^{-1} .

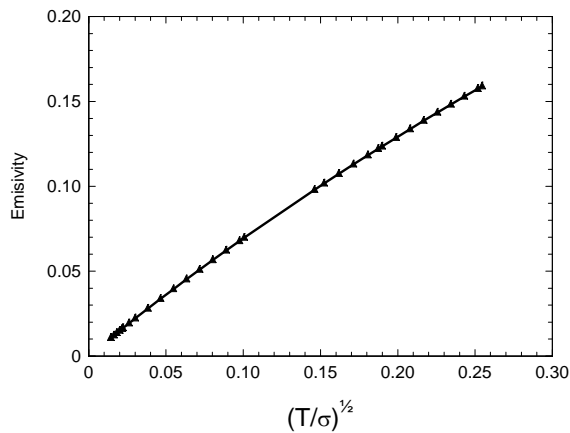


Fig. 5: Total hemispherical emissivity of Silver in function of $\sqrt{(T/\sigma)}$.

3. Numerical solution of the transient heat transfer and the steady potential equation

To obtain an approximation of equations (1)-(4), we consider space discretization by a standard piecewise linear finite element method and for time discretization we use a dedicated scheme for phase transition named ‘‘Chernoff scheme’’ [12]. The so called Chernoff scheme consists in a relaxation of the discontinuous relation enthalpy-temperature (Fig. 3) at the phase change temperatures (*i.e.* melting and boiling temperatures).

Let Δt denote the time step, and H^n , J^n , k^n and σ^n the approximations of the physical parameters at time t^n . We use the time integration scheme as follows:

$$\begin{aligned} \nabla \cdot (\sigma^n \nabla V^n) &= 0 \\ \mathbf{E}^n &= -\nabla V^n \\ \mathbf{J}^n &= \sigma^n \mathbf{E}^n \end{aligned} \quad (8)$$

$$\gamma \frac{T^{n+1} - \beta(H^n)}{\Delta t} - \nabla \cdot (k^n \nabla T^{n+1}) = \frac{|\mathbf{J}^n|^2}{\sigma^n}$$

$$H^{n+1} = H^n + \gamma (T^{n+1} - \beta(H^n))$$

with boundary conditions described in section 2. $\beta(H)$ is the reciprocal form of equation (3) and γ is a relaxation parameter, required to ensure the scheme stability, and satisfies:

$$0 \leq \gamma \leq \frac{1}{\max \beta'(H)} \quad (9)$$

The space discretization of equations (1)-(2) is made by a standard finite element method. Finite element approximation of the system (8) can be summarized as follows: We first consider a triangulation (finite element mesh) of the domain occupied by the fuse element Ω . We consider arbitrary continuous piecewise linear test functions ϕ and ψ and solve the variational system of equations:

$$\begin{aligned} \int_{\Omega} \sigma^n \nabla V^n \cdot \nabla \psi \, d\Omega &= \frac{I(t)}{|\Gamma_a|} \int_{\Gamma_a} \psi \, d\Gamma_a \\ \frac{\gamma}{\Delta t} \int_{\Omega} (T^{n+1} - \beta(H^n)) \phi \, d\Omega + \int_{\Omega} k^n \nabla T^{n+1} \cdot \nabla \phi \, d\Omega &= \int_{\Omega} |\nabla V^n|^2 \phi \, d\Omega \\ H^{n+1} &= H^n + \gamma (T^{n+1} - \beta(H^n)) \end{aligned} \quad (10)$$

Note that we have kept the same notation for the exact and the approximate solution.

Problem (10) can then written in the form of two linear systems of equations involving symmetric positive definite systems that we solve by a preconditioned conjugate gradient method at each time step n .

4. Experimental power supply

The experimental power supply is built from a single-phase transformer with a 100 kVA true power [13] and the prospective current delivered is given by:

$$I_p(t) = \frac{\hat{V}}{\sqrt{R^2 + L^2\omega^2}} \left(\sin(\omega t + \theta - \varphi) - \sin(\theta - \varphi) \exp\left(-\frac{R}{L}t\right) \right) \quad (11)$$

where \hat{V} is the supply voltage, R is the resistive load, L is the inductive load, ω is the pulsation at 50 Hz, θ is the closing angle, $\cos\varphi$ is the power factor, t is the time. The characteristics of the three experimental tests are given in Table 2. The fuse element 1 is tested to short pre-arcing times with two characteristic closing angles θ . The fuse element 2 is used to obtain medium pre-arcing time.

Table 2: Experimental test characteristics.

	Fuse 1 test 1	Fuse 1 test 2	Fuse 2 test 3
\hat{V} (V)	284.0	284.0	292.6
R (Ω)	0.52	0.54	1.07
L (μ H)	655	582	830
$\cos\varphi$	0.93	0.95	0.97
θ	84°	104°	0°
$I_{p, \max}$ (A)	503.6	496.0	265.6

5. Numerical results and experimental recordings

We have performed two experimental tests with the fuse element 1 described in Fig. 1 and one test with the fuse element 2 illustrated in Fig. 2. In this section, we present and compare numerical results to the measurements.

5.1. Fuse element 1 – Test 1

Fig. 6 gives recordings of the electrical parameters of the test 1, *i.e.* evolutions of the prospective current, the fuse current, the supply voltage and the fuse voltage during the fuse operation and the simulated current.

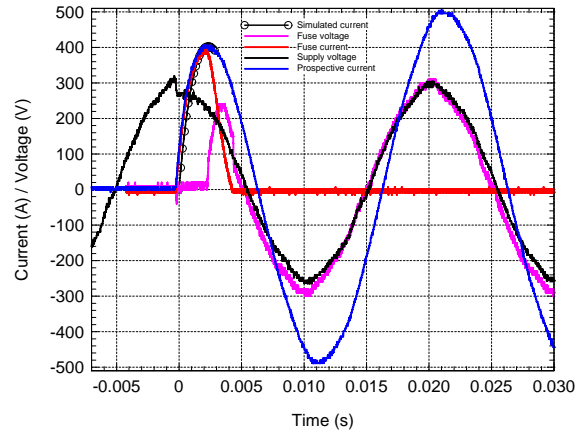


Fig. 6: Prospective and fuse current, supply and fuse voltage recordings and the simulated current during the test 1 for a power factor $\cos\varphi = 0.93$ and a closing angle $\theta = 84^\circ$.

The experimental pre-arcing time is evaluated at $t_{prearc} = 2.5 \text{ ms}$ and the arcing time around $t_{arc} = 2.2 \text{ ms}$. The fault current is interrupted at the middle of the first half 50 Hz-period. When the current is returned to zero, the voltage across the fuse reaches the supply voltage.

For numerical simulation, we use the 2D-model because we assume no heat transfer toward the porous medium for the pre-arcing times considered. The fuse element is discretized with an unstructured mesh of 12076 triangles and 6609 nodes where the reduced section is meshed more finely. At the initial time, the temperature is fixed at the ambient temperature and the time step is prescribed at $\Delta t = 10^{-5} \text{ s}$ in order to visualize the two constant stages of temperature. For all the simulations, we stop the calculation when the enthalpy of vaporization is reached.

Fig. 7 and 8 present the numerical results of the test 1 using the fuse element 1.

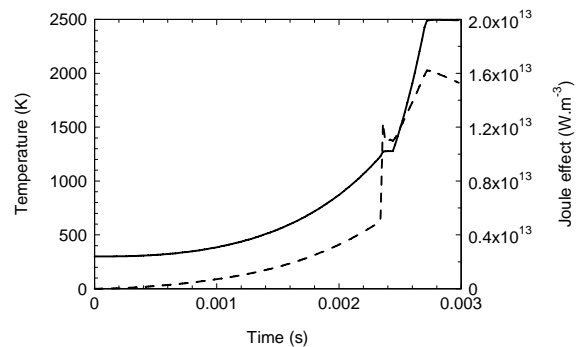


Fig. 7: Temperature (solid line) and Joule effect (dashed line) histories at the reduced section centre ($x = 35 \text{ mm}$, $y = 0.5 \text{ mm}$) during the pre-arcing time.

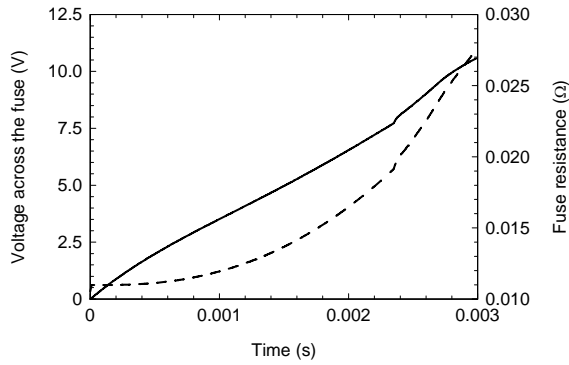


Fig. 8: Voltage across the fuse (solid line) and fuse resistance (dashed line) evolutions during the pre-arcing time.

The pre-arcing time simulated is about 3 ms compared to the 2.5 ms obtained by measurements. The temperature evolution can be divided in four steps:

- A gradual increase up to the melting temperature due to the Joule heating.
- A time lapse corresponding to the solid - liquid phase transition during which the melting latent heat energy is brought. We observe a discontinuous jump of the Joule effect due to the drop of the electric conductivity in liquid phase. The peak observed on the Joule effect curve is a numerical effect without physical explanation.
- An important temperature rise due to the maximum current density and the high resistivity of the fuse element.
- A time range carried out at constant boiling temperature during which liquid - vapour phase change occurs until the vaporization enthalpy is reached.

5.2. Fuse element 1 – Test 2

Fig. 9 gives the electrical parameters of the test 2 carried out with the fuse element 1.

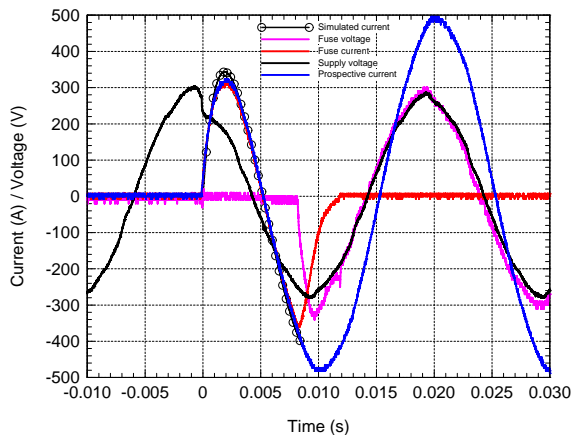


Fig. 9: Prospective and fuse current, supply and fuse voltage recordings and simulated fuse current during the experimental fuse test 2 for a power factor $\cos\varphi = 0.95$ and a closing angle $\theta = 104^\circ$.

The experimental pre-arcing time is evaluated at $t_{prearc} = 8.3\text{ms}$ and the arcing time around $t_{arc} = 4\text{ms}$. The fault current is interrupted at the second half 50 Hz-period.

Fig. 10 and 11 present the 2-D model numerical results carried out with the fuse element 1 and the characteristics of the test 2.

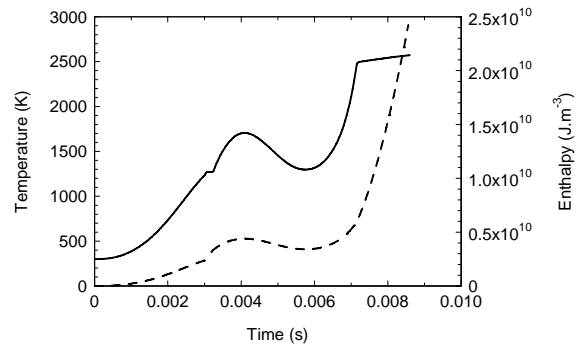


Fig. 10: Temperature (solid line) and enthalpy (dashed line) histories at the notch centre during the pre-arcing time.

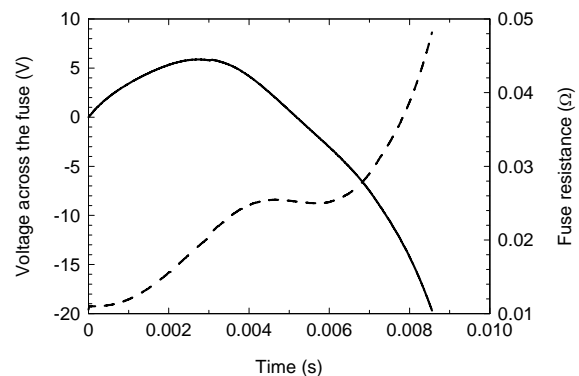


Fig. 11: Voltage across the fuse and fuse resistance evolutions during the pre-arcing time.

The simulated pre-arcing time is evaluated around 8.5 ms in agreement with the measured pre-arcing time. The shape of the temperature curve differs from the test 1. The melting stage of the temperature is clearly visible around 3 ms without an electric arc being initiated. Next, the temperature increases and decreases due to the combination of the Joule effect and the conduction heat transfer. Indeed, when the current return to zero, only heat transfer by conduction exists and the heat flow cools the hot area (reduced section) and heats the cold area (fuse ribbon). During the negative half-wave (Fig. 9), the Joule effect is sufficient to reach the vaporization enthalpy. We note in Fig. 11 that the fuse resistance gradually increases. Indeed, the notch temperature decreases but the heat energy is transferred to the fuse strip.

5.3. Fuse element 2 – Test 3

Fig. 12 gives the electrical parameters of the test 3 using the fuse element 2.

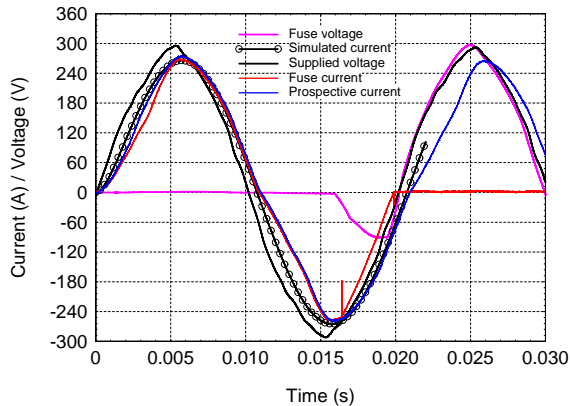


Fig. 12: Prospective and fuse current, supply and fuse voltage recordings and simulated current during the experimental fuse test 3 for a power factor $\cos\varphi = 0,97$ and a closing angle $\theta = 0^\circ$.

The pre-arcing time obtained by measurements is 16.5 ms and the arcing period is around 3.5 ms. The simulations have been performed with the 3D-model to take into account heat exchanges between the fuse element and the porous medium. In order to obtain reasonable computational times, we have simulated only one quarter of the fuse geometry and the time step is fixed at $\Delta t = 2 \cdot 10^{-5} s$. The fuse element is discretized with tetrahedral cells.

Fig. 13 shows isothermal contours in the fuse element close to the reduced section at the end of the pre-arcing time *i.e.* 22 ms. The temperature distribution is almost homogeneous in the fuse ribbon. As expected, the notch temperature is close to the boiling temperature.

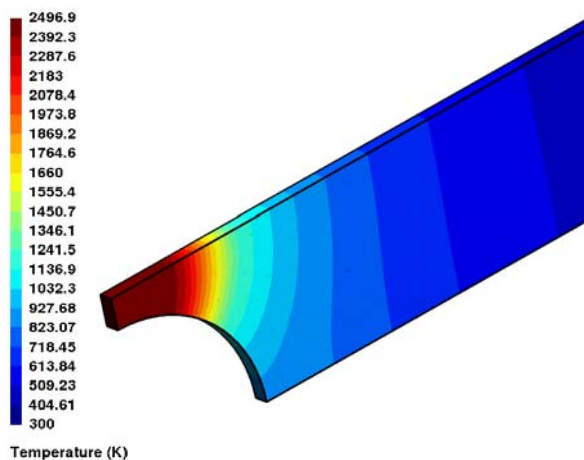


Fig. 13: Temperature distribution in the fuse element 2 at time $t = 22 ms$.

Fig. 14 represents the temperature evolution at the notch centre of fuse element 2 during medium pre-arcing.

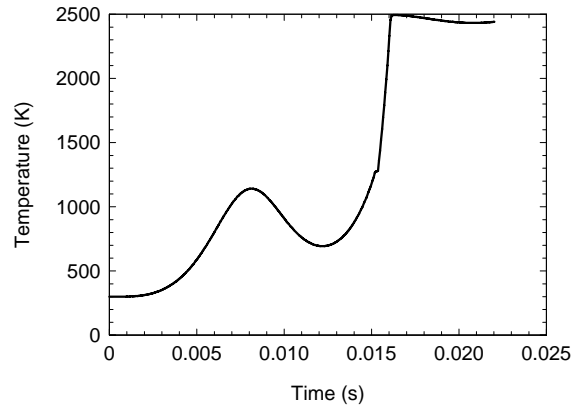


Fig. 14: Temperature evolution at the notch centre with conduction/radiation heat transfers between fuse element and the porous medium.

The simulated pre-arcing time is 22 ms compared to the 16.5 ms obtained by experiment. We have realized the same simulation without heat exchanges toward the porous medium and we have obtained a similar pre-arcing time.

6. Discussion and conclusion

The discrepancies observed between experiments and simulations pre-arcing times ($t_{pre-arc}^{experiment} > t_{pre-arc}^{simulation}$) can be explained as follows:

- By a microscopic visualization, we have observed that the real fuse element was not perfectly symmetric on the level of the reduced section.
- Silver electric conductivities of [11] are given until 1700 K in the liquid phase. So, we have extrapolated data until the boiling temperature. Moreover, when the boiling temperature is reached, the boiling stage temperature is rather long and during this stage the electric conductivity $\sigma(T_v)$ is constant. A significant drop of the electric conductivity probably happens during the contribution of the boiling latent heat.

In our opinion, these results must be taken with precaution. Indeed, it is surprising that the liquid phase in test 2 (Fig. 10) lasts also a long time (around 5 ms). An experimental measure which could be useful to validate the temperature evolution of Fig. 10 (the liquid phase lasts 5 ms) would be to measure with precision the voltage across the fuse during the pre-arcing time. Indeed, in liquid phase the fuse resistance increases significantly (Fig. 11) influencing the voltage across the fuse.

In spite of these remarks, the model allows to extend the pre-arcing time calculation until the vapour phase appears and from this moment a coupling with a gas flow model in porous medium would allow to investigate the beginning of the arcing period.

Acknowledgments

We thank for their financial support MM. T. Rambaud and JL. Gelet from Ferraz Shawmut, M. F. Gentils from Schneider Electric, and M. JC. Perez-Quesada from Mesa.

References

- [1] J.G. Leach, P.G. Newbery, A. Wright, Analysis of high-rupturing-capacity fuslink prearcing phenomena by a finite-difference method, *Proceedings of the IEE*, vol. 120, n°9, September, 987-993, 1973.
- [2] M.S. Agarwal, A.D. Stokes and P. Kovitya, pre-arcing behaviour of open fuse wire *J. Phys. D: Appl. Phys* 20, 1237-1242, 1987.
- [3] C. Garrido and J. Cidras, a method for predicting time-current characteristics of fuselinks, *Electric Machines and Power Systems*, 26: 685-698, 1998.
- [4] Y. Kawase, T. Miyatake, and S. Ito, Heat Analysis of a Fuse for Semiconductor Devices Protection Using 3-D Finite Element Method, *IEEE Transactions on Magnetics*, vol. 36, no.4, July 2000.
- [5] P.M. McEwan and R. Wilkins, A decoupled method for predicting time/current characteristics of H.R.C. fuses. Proceedings of ICEFA, Liverpool Polytechnic, 33-41, 1976.
- [6] A. Wright and P.G. Newberry, *Electric Fuses*, 3rd Edition, IEE Power & Energy series 49., 2004.
- [7] Bahrin, *Thermochemical Data of Pure Substances*, 3rd ed. in collaboration with G. Platzki, vol. 1. Ag-Kr and vol. 2. La-Zr, VCH Weinheim, Federal Republic of Germany, New York, 1995.
- [8] L-D. Lucas, Densité des principaux métaux et métalloïdes, *Techniques de l'ingénieur, Matériaux métalliques*, M. 65, MB. 2, in French, 1984.
- [9] D. Rochette, W. Bussière, P. André, Composition, enthalpy and vaporization temperature calculation of Ag-SiO₂ plasmas with air in the temperature range from 1000 to 6000 K and for pressure included between 1 to 50 bars, *Plasma Chemistry and Plasma Processing*, vol. 24, n°3, 475-491, 2004.
- [10] Y.S. Touloukian, *Thermal conductivity: metallic elements and alloys*, Series technical ed. IFI/Plenum New York Washington, 1970.
- [11] R.A. Matula, Electrical Resistivity of Copper, Gold, Palladium, and Silver *JPCRD* 8(4), 1147-1298, 1979.
- [12] A.E. Berger, H. Brézis and J.C.W. Rogers, A numerical method for solving the problem $u_t - \Delta f(u) = 0$, *R.A.I.R.O. Numerical analysis* 13 (4) 297-312, 1979.
- [13] W. Bussière, D. Rochette, C. Achard, P. André, T. Latchimy, A. Lefort and G. Velleaud, *Séminaire sur les Fusibles Moyenne Tension, SFMT* February 2006, <http://hal.archives-ouvertes.fr/hal-00019683> (in French).

EXPERIMENTAL APPROACH OF THE INTERACTION BETWEEN A SUB-MICROSCOPIC CATHODE TIP AND THE PLASMA

J. Rossignol¹, P. Testé², E. Bourillot¹, B. de Fonseca¹, J. Jouhannaud¹

¹Institut Carnot de Bourgogne, UMR 5209, Université de Bourgogne Mirande B.P. 47870 21078 Dijon Cedex – France, jerome.rossignol@u-bourgogne.fr

²Laboratoire de Génie Électrique de Paris, UMR 8507, Plateau de Moulon, 11 rue Joliot Curie, 91192 Gif-sur-Yvette Cedex – France, philippe.teste@lgep.supelec.fr

Abstract: The interaction between electrical arc and cathode represents a crucial problem in the conception of arc jet thrusters, circuit breakers, and plasma torch or arc heaters. At the cathode surface, the current and energy transfers are controlled by the current emitting site (cathodic spot). Theories and experimental observations, at macroscopic and mesoscopic scale, deal with the erosion of the cathodic surface. Under micrometer range, theories refer to the arc root to describe the erosion of the surface. The works presented here propose an original method to evaluate the arc-cathode interaction at micrometric scale. A nanotechnology is used in order to control the roughness of the electrode surface and to deposit the microscopic tip. After discharge, the influence of the tip in the cathodic erosion process is studied. Scanning Electron Microscopy images show that a good reproducibility of the erosion zone is obtained by using this experimental method.

Keywords: Nanotechnology; tip; cathode surface, cathode erosion.

1. Introduction

Electrical arc appear in relays, circuit breaker or plasma torch. Physic phenomena of the interaction between the plasma and the cathode are an important problem for industrial device. A large literature deals with this subject and is divided into two approaches.

The 'post-mortem' approach consists to observe the cathode surface after discharge extinction and highlights the existence of craters with dimensions 5 μm to 100 μm [1].

Post-mortem traces of a spotlight are characterized by a sudden high localised current going through the surface. Spotlights (current emitting site) play a major role in the electric arc. Indeed, they feed on the electrode neighbourhood plasma of atoms by electrode erosion [2-5] and of electrons by thermo-emission.

The 'in vivo' approach consists to observe the electrode surface using a high speed camera during the discharge. Oscilloscopes are used to monitor the

current and the voltage time evolution. Thus, Jüttner proposes a hierarchy of the spotlights associated to the current emitting site [6].

The paper presents the development of an experimental method to study the interaction plasma/surface at sub-microscopic scale. A nanotechnology is used in order to control the roughness of the electrode surface and to deposit the microscopic tip (on the middle of the surface). Then, this electrode contributes to obtain a reproducibility of the erosion space repartition.

The design of the tip and the set-up of the discharge apparatus are described. Then, the experimental results are exposed and discussed.

2. Design of the structured nano tips

The tips are deposited on the electrode surface by adsorption of carbon.

A sample is placed in the vacuum chamber of a Scanning Electron Microscope (SEM). Then, a spot of contamination is realized on the surface in order to adsorb carbon. The quantity of carbon deposited on the sample is characterized by the diminution of the current measured on the sample. A calibration is performed according to this diminution to quantify the size of the tip. To design the tip and locate the central site of the spot of contamination on the samples, an electron microscope JEOL 6500 is used. This apparatus has a turntable motorized with a precision of about 500 nm. It allows identifying precisely the site of release of the arc. Adsorptions carried out will be less important than with the SEM JEOL 840A because this one use a turbo-pump and not an oil-pump. This involves fewest carbons in the column and thus restricts adsorption.

In the first aspect of this experimental process, a Cu-layer is deposited on a glass substrate by cathode sputtering. Then, the sample is placed in the vacuum chamber of a SEM (JEOL 840A). After the development of a fine image, the mode "spot" is chosen to stop the scanning of the electron beam. The total energy of the electron beam (20 keV) is entirely focused on a precise point of the sample. This allows the adsorption of carbon. The height of the tip is then controlled by the measurement of the diminution of the current, expressed in pico-ampere. The time of

adsorption is variable according to the quantity of carbon present in the SEM column.

Table 1: Dimension of the tips obtained

Fall of current	Height of tip	Base of tip
45 pA	500 nm	450 nm
25 pA	400 nm	350 nm
20 pA	350 nm	285 nm
17 pA	345 nm	210 nm
15 pA	205 nm	208 nm
10 pA	110 nm	312 nm

Then the result can be observed and quantified as shown on figure 1. Thus, from smallest with largest, we obtain for a loss of 10 pA, a tip of 110 nm high for a base of 312 nm and we obtain for a loss of 45 pA a tip of 500 nm high for a base of 450 nm.

The whole of measurements is indexed in table 1. Thus, the profile of these tips is conical and their dimensions do not vary in a linear way with the loss of current. These results show that this technique is viable for the fabrication of tips. If the highest tips are not taking into account, it requires slightly rough copper substrates.

In this case, the diminution of the maximum current realized is about of 10 pA and the associated higher tip is about of 120 nm (figure 1). These values are limited but they are compatible with roughness obtained by polishing. Theoretically, the effect of tip should be sufficient and the electric arc is attracted by the carbon spots present on each electrode.

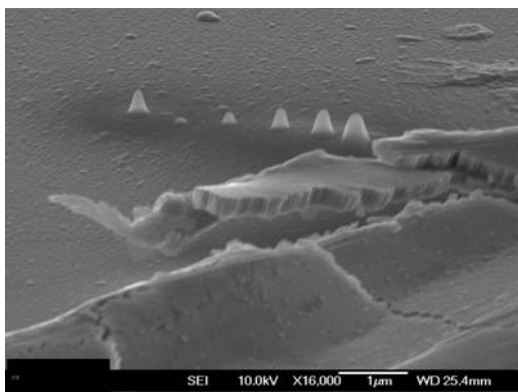


Figure 1: SEM image of several carbon tips (Magnification 16000)

In order to obtain a surface quality whose roughness is in adequacy with the height of the tip, we carried out a polishing of the copper electrodes. The copper sample is placed in an acrylic resin to allow good mechanical stability during polishing. The sample undergoes several stages of polishing of which the last is the use of an alumina felt of 1 μm .

A SEM observation (JEOL 6500) allows an evaluation of the roughness of produced surfaces (figure 2). The roughness of surface is about 30 nm and is quite lower than the dimension of the tip. The diminution of current being relatively difficult to maintain constant (fluctuation in order to 10 pA), a thin layer of gold is deposited (approximately 20 nm) by cathode sputtering. This increases the conductivity (without modifying the thermal properties of the layer) and thus increases the adsorption of carbon on the surface of the electrodes. In addition, the layer of gold allows “revealing” the zones where the electric arc struck. Thus, the fabrication of the electrodes led us to use the spots of contamination in order to deposit the tip. Experiments of electric arc were carried out on a copper electrode surmounted of a tip

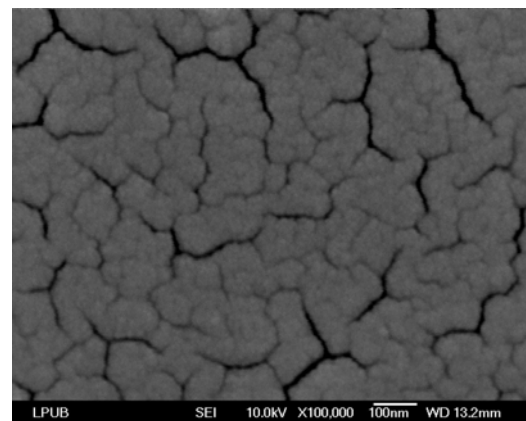


Figure 2: An observation with the SEM (JEOL 6500). Evaluation of the roughness of produced surfaces

of carbon of 110 nm high and three copper electrodes surmounted of a layer of gold with on each one a tip of 105 nm high. For the calibration of the distances from breakdown during the tests of electric arc, a polished electrode without tip is used.

3. Electrical apparatus

Figure 3 represents the electrical apparatus used to obtain the breakdown. It is composed of three stages. A high voltage transformer and a Graetz diode bridge allow the AC-DC conversion. The second stage consists to a capacitor bank with a load resistance R1. The discharge of the capacitor bank is controlled by a HV switch (denoted K_{HT}). The next element is a resistance R2 to control the intensity of

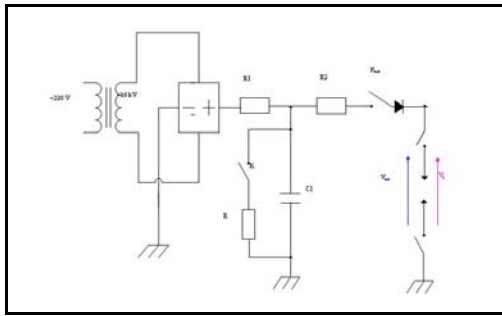


Figure 3: Scheme of the electrical apparatus

the current pulse and the current time.

This set up allows (in accordance with the electrode gap) to realize current pulses with a time in the range of 10 μ s-100 ms.

4. Results

The first experiment consists to define the duration of the discharge which assure the presence of multiple eroded zones without a large erode zone (macro-spot). The duration is estimated to 50 μ s. In this case, the distribution of the eroded zones on the surface indicates that the arc root moved by “jump” and not in a continuous way [7]. It is possible to return to the centre of the surface where the deposited cathodic point is located by following the discontinuous way of the arc.

In comparison with figure 4, which represents the cathodic surface of an electrode after arc, the deposition of gold ensures a more detailed description of the eroded zones. Thanks to that, the displacement of the arc along the surface can be followed.

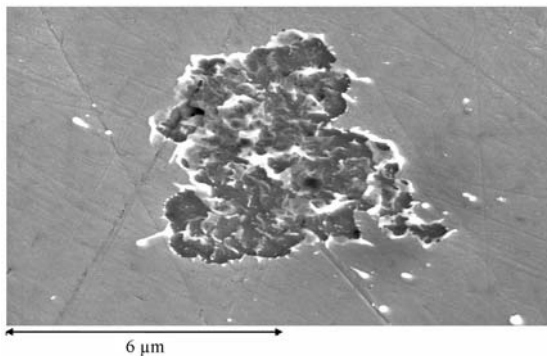


Figure 4: Example of eroded area

Fine SEM observations of the edge of one of these zones allow evaluating the importance of this layer of gold. The periphery of the eroded zone shows that the layer of gold was not vaporized but puffed up without liquefaction, leaving copper without any trace of erosion.

The analysis by photonic micro-probe of eroded surface (figure 5) indicates that there is only copper. While approaching the centre of eroded surface,

droplets are observed. The analysis indicates that they are made up of gold and copper. The weak difference between vaporization and liquefaction enthalpy of copper and gold leads us to suppose that the influence of gold on the erosion of the cathode is not significant. The blowing and the setback per pieces of plates of the layer of gold in periphery are explained by the effect of pressure applied by the arc foot on the gold depot. The observation of the central zone shows a consequent eroded zone lower 1 μ m. The presence of carbon must be due to the nano-structured point. Thus, the latter underwent erosion consequently to the vaporization of a part of carbon constituting it.

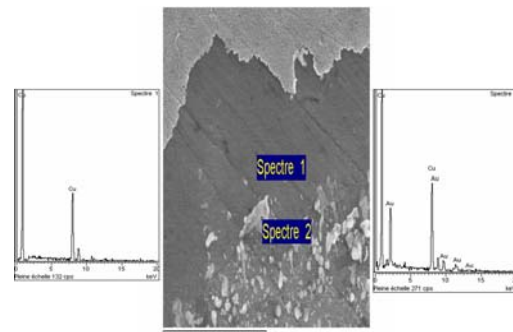


Figure 5: SEM observations with photonic survey of materials on the surface

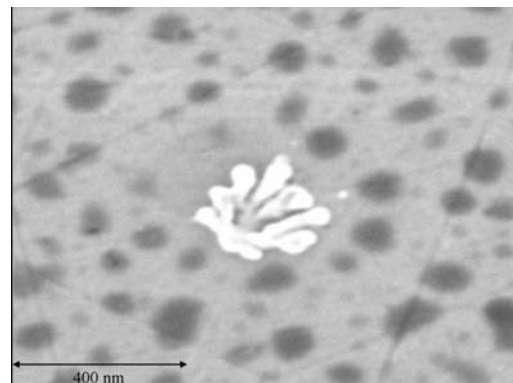


Figure 6: Observation of the central zone, place of the cathode tip

5. Short time of discharge

By means of discharges at short duration ($>20\mu$ s) the same experiment is renewed to obtain only one emissive site of current corresponding to the structured nano point.

The SEM observations of several surfaces (figures 7 and 8) subjected to the arc indicate the existence of only one emissive site of current via the setting in contrast by the layer of gold.

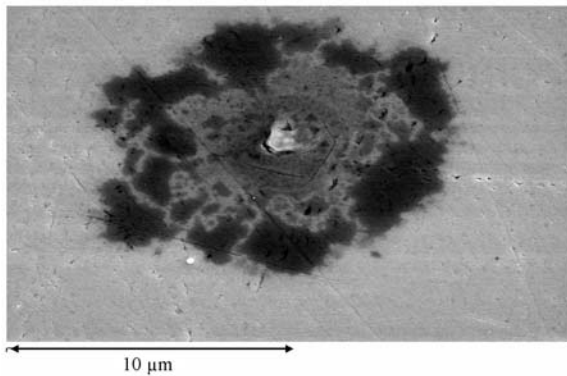


Figure 7: Image of the central eroded zone of the first electrode

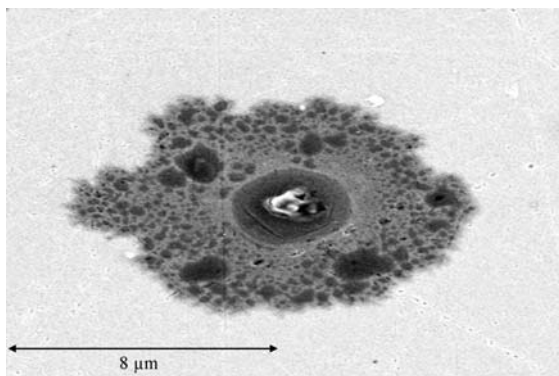


Figure 8: Image of the central eroded zone of the second electrode

Micro-probes measurements show that the site of the electrode (in the centre) corresponds to the site of a carbon cathodic point. The reproducibility is noted by the glance of the various tests. However, SEM image explains the surplus of energy of the discharge provided to obtain only one microspot: it is possible to start an arc with weaker energy and then have an emissive site of single current.

Future measurements require a device of discharge with a shorter time of discharge in order to

have a single microspot and not of a small group of microspots.

6. Conclusion

In this article, we proposed an original experimental method to study the interaction plasma/cathode at sub-microscopic scale. A nanotechnology is used to deposit a microscopic tip with a controlled design on the centre of a cathodic surface. To eliminate other possibilities of current ignition, the surface is treated with a gold layer (10 nm). Gold is chosen because of its thermophysical properties similar to the thermophysical properties of copper. The gold layer produces an appreciable contrast which allows SEM observations of the erosion on the cathode surface. The results demonstrate a reproducibility of the erosion trace with a short duration arc.

The present analysis should be continued with different sizes of tips and different materials. A numerical model of the cathodic heating by the arc will be also realized.

References

- [1] Daadler J.E., Cathode erosion of metal vapour arcs in vacuum, *Thesis*, Tech. univ. Eindhoven, 1978.
- [2] Essiptchouk A.M., Marotta A., Sharakhovsky L.I., The influence of the arc current on the cold electrode erosion, *Physics of Plasmas*, 10, 3770, 2003.
- [3] Sanders D., Boxman R.L., Martin P.J., *Handbook of vacuum arc science and technology*, ed Boxman & al Noyes publication, 1995.
- [4] Rossignol J., Clain S. and Abbaoui M., The modelling of the cathode sheath of an electrical arc in vacuum, *J. Phys. D: Appl. Phys.*, 36, pp. 1495-1503, 2003.
- [5] Miller G., Electrical Discharges in Vacuum *IEEE trans. on Electrical Insulation*, vol. 26, N°5, 1877-1979 and 1979-1990, p765 and p946.
- [6] Jüttner B., Cathode spots of electric arcs, *J. Phys. D: Appl. Phys.*, 34, pp. R103-R123, 2001.
- [7] Djakov B.E., Jüttner B., Random and directed components of arc spot motion in vacuum, *J. Phys. D: Appl. Phys.*, 35, pp. 2570-2577, 2002.

ESTIMATION OF THE PLASMA'S PARTICLE DENSITIES DURING THE ARCING PERIOD OF A HIGH-VOLTAGE FUSE

M.A. Saqib⁽¹⁾, A.D. Stokes⁽²⁾, I. S. Falconer⁽³⁾ and B.W. James⁽⁴⁾

⁽¹⁾Department of Electrical Engineering, University of Engineering and Technology, Lahore (Pakistan), Email: saqib@uet.edu.pk

⁽²⁾School of Electrical and Information Engineering, University of Sydney, NSW 2006, Australia, Email: stokes@ee.usyd.edu.au

^(3,4)School of Physics, University of Sydney, NSW 2006, Australia, Emails: falconer@physics.edu.au, b.james@physics.edu.au

Abstract: We report in this paper the results of the estimated number densities for the plasma species during the arcing period in a model sand-filled high-voltage fuse. The model fuse was energized at 6 kV, using synthetic test circuit, and a prospective current of 1.25 kA, 50 Hz, was passed through it. The arcing period has been investigated using spectroscopic means. The fuse arc is supposed to be composed of O I, O II, Si I, Si II and Si III particles. Using the estimated values of electron density and temperature, and assuming the plasma to be in Local Thermodynamic Equilibrium (LTE), Saha's and Brunner equations are applied to determine the particle densities of ionized and neutral particles in the plasma. The model high-breaking capacity high-voltage fuse, under the given testing conditions, shows that its arc remains highly ionised throughout the arcing period.

Keywords: Fuse arc, Saha's equation, Plasma species, Particle density, Plasma Ionisation.

1. Introduction

A high-voltage high breaking capacity fuse is the most effective and economical device for the protection against short-circuit currents in medium-voltage systems. It is preferred over a circuit breaker for the protection against such heavy currents because of its much faster response time: it can reliably operate even within 5 ms (i.e., quarter of the time period for a 50 Hz AC system) from the onset of a short-circuit current. When it is used with a circuit breaker the system can be protected against all fault currents; the circuit breaker providing the protection against over-load currents.

A large gap exists between the theory and practice as regards manufacturing and applications of high breaking capacity fuses are concerned. To bridge this gap, extensive testing is essential during the development stage of a new fuse. In spite of tens of years of research there still is a lot of uncertainty, and the mechanisms on the operation of HBC fuses are

unclear. Though the pre-arcing time in high-voltage HBC fuses is fully understood and good models exist to simulate the behaviour of the fuses [1]-[3], this is not the case with the arcing period. The dynamic behaviour of the arcing period in current-limiting high-voltage fuses is not yet known [4]. This is primarily due to the difficulty in experimentation of the arcing period for two reasons; first the arcing period is very short i.e., of the order of a few milliseconds during short-circuit currents and second that the arcing takes place inside an opaque fuse cartridge and is surrounded by silica sand thus providing no optical window for diagnostics. To have a better understanding of the operation of the fuses research is now being conducted to determine the physical parameters such as pressure, electron density and current during the arcing phenomenon [5].

For understanding the arc dynamics we have conducted the diagnostics on the arcing period inside an experimental model HBC fuse. The constructed fuse, shown in Fig. 1, had 112 mm long cartridge and inner diameter of the cartridge being 60 mm. A uniform silver wire of diameter 0.55 mm, used as fuse element, was stretched in the middle along the axis of the cartridge. An optical fibre, supported inside a glass capillary, was made to just touch the fuse element: a hole had been drilled in the centre of the fuse cartridge for this purpose. The other end of the optical fibre was brought to a rapidly scanning spectrograph which was coupled to an optical multichannel analyser (OMA). The fuse was then filled with silica sand under vibration. The fuse was tested using a synthetic test circuit: the circuit was charged to 6 kV, and a prospective current of 1.25 kA, 50 Hz, was passed through the fuse. The temporal resolution of the arc was achieved by gating an image intensifier in front of the OMA: the gating could be delayed to record spectrum at different times during the arcing period. The shot-to-shot based spectra could be considered as were taken from one testing of the fuse at different timings during the arcing phase as these shots were conducted under identical conditions.

The arc temperature was determined by measuring the relative intensity of Si II spectral lines, and the electron density from the Stark broadening of these lines. These investigations have been reported in references [6]-[8]. In fact we have used the results from these experimental studies to calculate the number densities of the arc species. Preliminary results of the number densities for arc species had also been reported earlier [9] using a number of simplifying assumptions.

2. The Use of Saha's and Brunner Equations

If electron density and temperature are known and the plasma can be assumed to be in Local Thermodynamic Equilibrium (LTE), Saha's equation [10] can be used to determine number densities of the ionised and neutral species in the plasma. The collision rates between the various species present in the fuse plasma are sufficiently high (particularly compared with the timescale of the discharge and diffusion times), that thermodynamic equilibrium is a good approximation for our discharge conditions. Saha's equation is:

$$\frac{n_{r+1}n_e}{n_r} = 2 \frac{u_{r+1}(T)}{u_r(T)} \times \frac{(6.28m_0kT)^{1.5}}{h^3} e^{-\frac{E_r - \Delta E_r}{kT}} \quad (1)$$

where

- n_r = number density of all r-fold ionised atoms (e.g., $r = 0$ for neutral particles);
- n_{r+1} = number density of all (r+1)-fold ionised atoms;
- n_e = number density of electrons;
- u_r = partition function of r-fold ionised atom;
- u_{r+1} = partition function of (r+1)-fold ionised atom;
- m_0 = electron rest mass, 0.9107×10^{-30} kg;
- h = Planck's constant, 6.626×10^{-34} J sec;
- k = Boltzmann's constant, 1.38×10^{-23} J/K;
- E_r = ionisation energy for ionisation process $r \rightarrow (r+1)$;
- T = absolute temperature [K];
- ΔE_r = lowering of ionisation energy.

The fuse arc is assumed to be composed of only Si I, Si II, Si III, O I and O II. These species were detected as reported in reference [11]. The mass of the SiO₂ evaporated by the arc discharge, as estimated in reference [8] was 2.8 g. The mass of the silver fuse wire (0.28 g) is 9% compared with the mass of the SiO₂ in the plasma and thus negligible. Furthermore, demixing processes [12] rapidly transfer the metal of the fusible fuse wire away from the hot plasma, so that the conducting medium in the arc is in effect a plasma in evaporated and dissociated SiO₂ filler material and any silver present in the arc was negligible as compared to that of Si and O and can be ignored.

The Saha's equation, for silicon and oxygen, can be written as:

$$(n_e n_{\text{Si II}})/n_{\text{Si I}} = f_1(T) \quad (2)$$

$$(n_e n_{\text{Si III}})/n_{\text{Si II}} = f_2(T) \quad (3)$$

$$(n_e n_{\text{O II}})/n_{\text{O I}} = f_3(T) \quad (4)$$

Since charge is conserved,

$$n_e = n_{\text{O II}} + n_{\text{Si II}} + 2 n_{\text{Si III}} \quad (5)$$

and assuming all O and Si atoms and ions are the result of decomposition of SiO₂,

$$(n_{\text{O I}} + n_{\text{O II}}) = 2 (n_{\text{Si I}} + n_{\text{Si II}} + n_{\text{Si III}}) \quad (6)$$

Equations (2)-(6) can be solved to obtain the number densities of the plasma species present for a known temperature and electron density. The term ΔE_r in Equation (1) can be calculated using the Brunner formula [10], which is:

$$\Delta E_r = 1.21 \times 10^{-6} \sqrt[3]{n_e [\text{cm}^{-3}]} + 2.5 \times 10^{-8} \sqrt{\frac{n_e [\text{cm}^{-3}]}{T [\text{K}]}} [\text{eV}] \quad (7)$$

3. Calculation of the Number Densities for the Arc Species

A computer program has been written in MATLAB which solves equations (2)-(7) and calculates the number densities of the fuse-arc species. It asks the user initially to provide the arc temperature [in K] and the electron density [in cm⁻³], and calculates ΔE_r – the lowering of ionisation energy – from equation (7). The program then asks the user to provide the partition functions of Si I, Si II, Si III, O I and O II corresponding to the initially given temperature and the calculated value of ΔE_r . These partition functions are given in reference [10]. The program then requires the values of ionisation energies for Si I (for transition from Si I to Si II), Si II (for Si II to Si III transition) and O I (for O I to O II transition): these values are also given in reference [10]. The program then prints the number densities of Si I, Si II, Si III, O I and O II.

The pressure in the arc could be calculated using the ideal gas law:

$$P = \Sigma n k T \quad (8)$$

Equation (8) was summed over all species including electrons and the temperature of all species could be approximated by the electron temperature.

Using these number densities, the percentage ionization of the arc is now calculated by:

$$\% \text{age ionisation} = 100 \times (n_{\text{O II}} + n_{\text{Si II}} + n_{\text{Si III}}) / (n_{\text{O II}} + n_{\text{Si II}} + n_{\text{Si III}} + n_{\text{O I}} + n_{\text{Si I}}) \quad (9)$$

The results are shown in Table 1 for the test fuse at 1.25 kA prospective current. The estimated values of electron density, given in reference [8], are reproduced in Table 1. The estimated temperatures as reported in references [6] and [8] were extrapolated to get the temperature values shown in Table 1 (the spectra were recorded at different timings for the temperature and electron density estimates e.g., the spectra for the temperature measurements were recorded at 0.368, 0.398, 1.203, 1.812, 2.148, 2.694, 4.138, 4.166 and 5.172 ms after the arc initiation).

4. Discussion

The number densities of Si I, Si II, Si III, O I and O II as a function of time in the arcing period of the fuse are shown in Figs. 2-6. The number density of Si I in the fuse arc is typically quite low – of the order of 10^{14} cm^{-3} – and thus these particles were not detected in the fuse arc as had been reported in reference [11]. We had studied the fuse-arc spectrum using photographic films there and had established that Si II lines were best suited for further investigation of the arc as they had been detected throughout the duration of the arc. This was also verified in our study of the fuse arc using a sensitive equipment - Jarrell-Ash monochromator and optical multichannel analyser - the response of the system being highly sensitive to radiation between 520 and 650 nm.

It is evident from Table 1 that the concentrations of Si II particles is of the order of 10^{17} cm^{-3} and as majority of the spectral lines of these particles fall under the sensitive region (520-650 nm) of the equipment the fuse spectra were dominated by Si II lines which were used for the investigation in references [4], [6]-[7]. The concentrations of the oxygen lines, particularly O II, is very high in the arc, and these lines – between 415 and 500 nm – were detected in the arc as reported in reference [11]. As the spectrum recording equipment is not very sensitive in this range (415-500 nm), it was difficult to identify these lines in the studies reported in references [4], [6]-[7].

The results reported in reference [9] were approximate as ΔE_r was ignored and average values of the partition functions at a temperature of 15000 K were used. The results of both these studies are slightly different; nevertheless they show similar trends.

The arc is highly ionised initially and for up to about 1 ms after the arc initiation: all the stored electrical energy of the circuit is suddenly dumped into the molten layer of silica sand (which results from this energy) and thus greatly ionises the arc. The ionisation of the arc then decreases as a function of time but still remains more than 50% toward the end when the last spectrum was recorded. The pre-arcing time of the fuse under these test conditions was 5.3 ms. Thus 4.1 ms time after the arc initiation - at which the last spectrum was recorded - refers to the point which is just 0.6 ms before the natural current zero (corresponding to 50 Hz). Toward natural current zero, the fuse arc is still highly ionised and this explains why the arc interruption did not take place under the given test conditions for the test fuse. The model fuse, unlike the commercial sand-filled current limiting fuses which are designed for automatic current interruption, was not intended for this purpose: it has been used to study the arcing dynamics in silica sand. To avoid a continuous flow of current through the arcing fuse, a crowbar – a pneumatically-operated switch which provided a parallel path for the current - was used. It started conducting between fifteen to twenty milliseconds after the fuse was provided electrical energy from the synthetic test circuit and the current had started flowing through it (i.e., at the beginning of the pre-arcing phase). This ensured that the test fuse remained in the arcing phase for a time between 10-15 ms (though we were only interested in the diagnostics of the arc before the first natural current zero).

The evolution of temperature and electron density (and hence the particle densities of the arc species) give useful information about the arc dynamics in high voltage sand-filled fuses. The plasma is highly ionised at the start of the arcing and should rapidly decrease its ionisation if the current interruption has to take place.

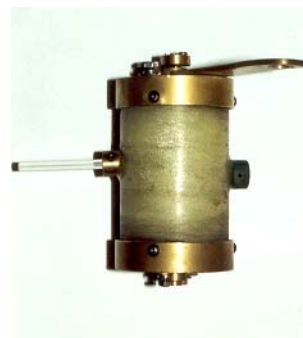


Fig. 1: Photograph of the model test fuse.

Table 1: The calculated plasma composition, corresponding to the estimated values of temperature and electron density, for the test fuse at 1.25 kA.

Time after arc initiation (ms)	0.157	1.121	2.105	2.470	2.673	3.360	4.100
Temperature (K)	21000	21000	18000	18000	18000	18000	15000
Electron density ($10^{17} \times \text{cm}^{-3}$)	3.5	2.1	3.0	2.5	2.0	2.7	1.2
$n_{\text{SiI}} (10^{17} \times \text{cm}^{-3})$	0.0068	0.0016	0.0250	0.0160	0.0092	0.0190	0.0180
$n_{\text{SiII}} (10^{17} \times \text{cm}^{-3})$	0.7300	0.3200	1.1400	0.8900	0.6500	0.9900	0.6500
$n_{\text{SiIII}} (10^{17} \times \text{cm}^{-3})$	0.3900	0.3100	0.1200	0.1100	0.1100	0.1100	0.0160
$n_{\text{OI}} (10^{17} \times \text{cm}^{-3})$	0.2700	0.0890	0.9300	0.6400	0.4000	0.7500	0.8400
$n_{\text{OII}} (10^{17} \times \text{cm}^{-3})$	2.0000	1.1700	1.6300	1.3900	1.1300	1.4900	0.5200
Pressure (bar)	2.0	1.2	1.7	1.4	1.1	1.5	0.7
%age ionisation	92	95	75	78	82	77	58

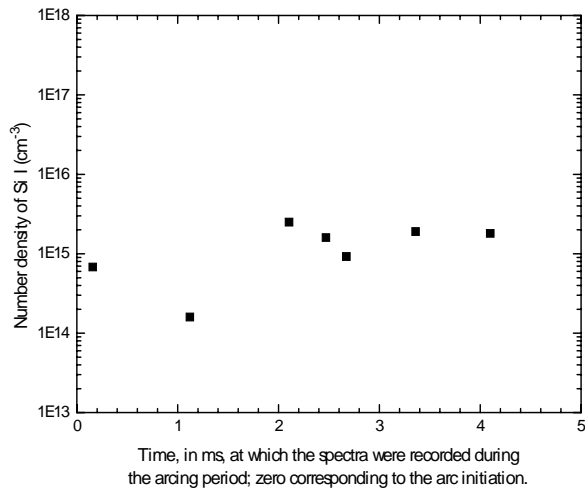


Fig. 2: Number density of Si I in the fuse arc as a function of time.

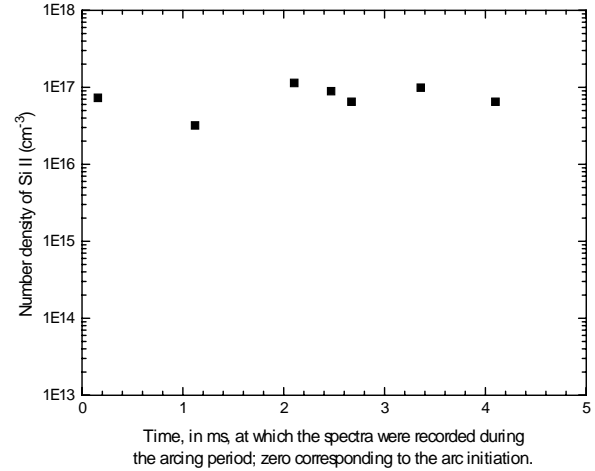


Fig. 3: Number density of Si II in the fuse arc as a function of time.

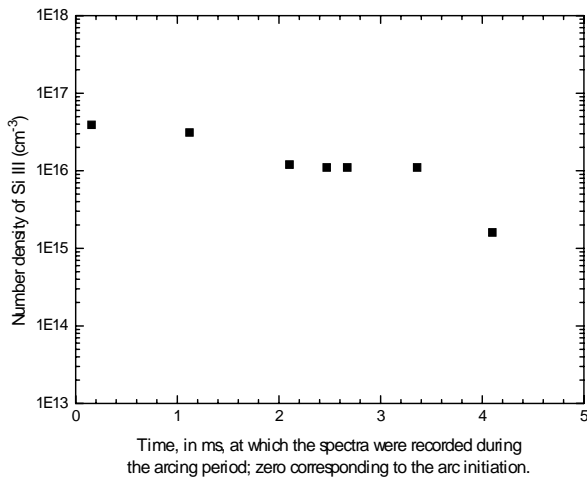


Fig. 4: Number density of Si III in the fuse arc as a function of time.

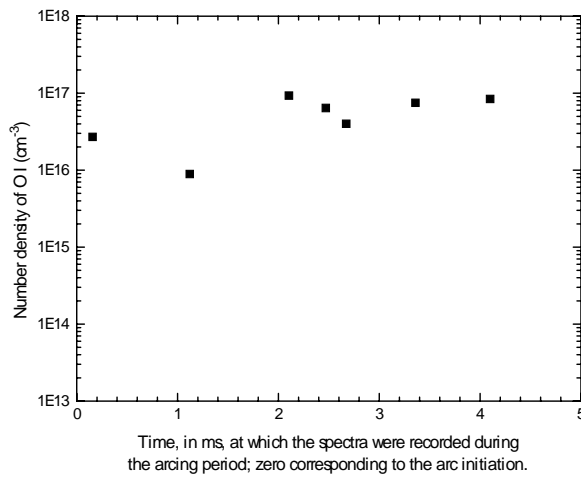


Fig. 5: Number density of O I in the fuse arc as a function of time.

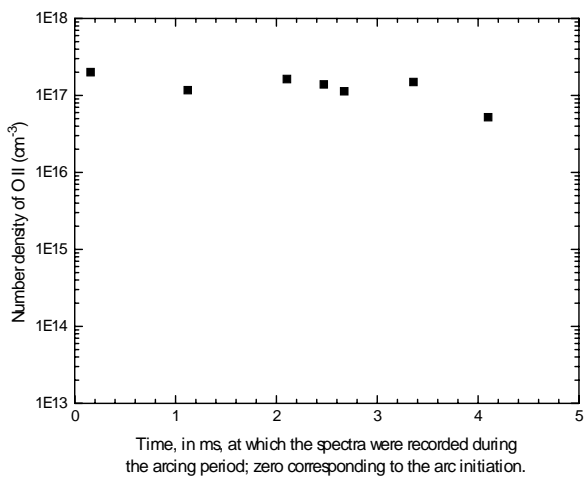


Fig. 6: Number density of O II in the fuse arc as a function of time.

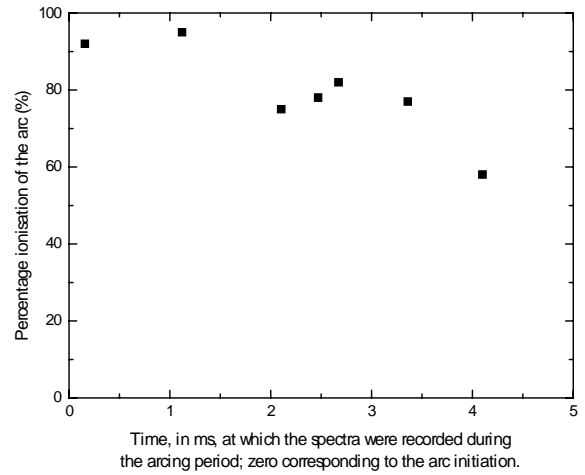


Fig. 7: Percentage ionisation of the fuse arc as a function of time.

References

- [1] McEwan P.M. and Wilkins R., "A decoupled method for predicting time-current characteristic of HRC fuse", Proceedings of the First International Conference on Electric Fuses and their Applications (ICEFA), Liverpool Polytechnic, England, pp.33-41, 7-9 April 1976.
- [2] Cheim L. and Howe A., "The use of transmission line modelling (TLM) for the solution of heat diffusion in electric fuses", International Journal of Numerical Modelling: Electronic Networks, Devices and Fields, Vol. 5, No. 4, pp. 289-295, 1992.
- [3] Kurschner H., Ehrhardt A., Nutsch G., Harrison I., Boerner A. and Mickley T., "Calculation of pre-arcing times using the finite element method", Proceedings of the Fifth ICEFA, Technical University of Ilmenau, Berlin, pp. 156-161, 25-27 September 1995.
- [4] Saqib M.A., Stokes A.D., James B.W. and Falconer I.S., "Estimating arc temperature in a model high breaking capacity fuse", Australian Journal of Electrical and Electronics Engineering, Vol. 1, No. 1, pp. 41-49, 2004.
- [5] Bussiere W., Rochette D. and Andre P., "Study of the SiO₂ plasma physical parameters: temperature, electron density, pressure, radiation", Proceedings of the Seventh ICEFA, Gdansk, Poland, 2003.
- [6] Saqib M.A., Stokes A.D., James B.W. and Falconer I.S., "Arc temperature measurement in a high-voltage fuse", Proceedings of the Sixth ICEFA, Turin (Italy), pp. 107-109, 20-22 September 1999.
- [7] Saqib M.A., Stokes A.D., James B.W. and Falconer I.S., "Measurement of electron density in a high-voltage fuse arc", Proceedings of the Sixth ICEFA, Turin (Italy), pp. 129-132, 20-22 September 1999.
- [8] Saqib M.A., "Arc behaviour and constriction in high-voltage fuses", PhD Thesis, School of Electrical and Information Engineering, University of Sydney, Australia, August 1999.
- [9] Saqib M.A., Stokes A.D., James B.W. and Falconer I.S., "Determination of the plasma ionisation for an HBC fuse during current interruption", Proceedings of the Fourth IEEE National Multi-topic Conference, Islamabad (Pakistan), pp. 216-221, 10-11 September 2000.
- [10] Drawin H. and Felenbok P., "Data for plasma in Local Thermodynamic Equilibrium (LTE)", Gauthier Villars, Paris, 1965.
- [11] Saqib M.A. and Stokes A.D., "Time resolved spectrum of the fuse arc plasma", Journal of Thin Solid Films, Elsevier Science, Vol. 345, pp. 151-155, 1999.
- [12] Murphy A.B., "Demixing in free-burning arcs", Phys. Rev. E, Stat. Phys. Plasmas Fluids Relat. Interdiscip. Top. 55 7473-94, 1997.

ENERGY TRANSFERS WITHIN ARCING FAULTS IN ELECTRICAL EQUIPMENT

Dr. David Sweeting, Professor A.D.Stokes

Sweeting Consulting, A1 Pindari Ave St. Ives 2075 Australia, david@sweeting.com.au

University of Sydney, PO Box 389 Newport 2106 Australia, stokes@ee.usyd.edu.au

Abstract: An arcing fault often develops from an insulation failure within electrical equipment. Arcing faults are substantially unconstrained free-burning arcs within electrical equipment.

In order to assess the hazards of arcing faults to personnel in the immediate vicinity of the fault it is necessary to understand their nature and be able to quantify the hazards.

This involves an understanding of the energy dissipation and the energy transfers in the near vicinity of these uncontrolled arcs.

This paper sets out to describe the physics of arcing faults and uses this to describe the energy transfers within an arcing fault.

This is the basis for describing the potential energy transfers to personnel in the vicinity of an arcing fault.

Keywords: arcing fault, energy transfer, line radiation, emission, absorption, electrode jets, restricted column, diffuse column, electrode-material column, air column, plasma cloud.

1. Introduction

When insulation fails in electrical power equipment, an arcing fault often develops within the electrical equipment. Whilst an arcing fault includes the equipment on which the fault arc is burning, the degraded insulation which allows re-ignitions and the fault arc itself, the terms arcing-fault and fault-arc will be used interchangeably in this paper. Arcing faults are substantially unconstrained free burning arcs but in some circumstances a limited amount of constraint is provided by the equipment in the vicinity of or containing the arcing fault.

This paper sets out to describe the physics of arcing faults in order to use this description to describe the energy transfers within fault arcs and in particular three-phase free burning arcs on parallel electrodes. This description is required to form the basis for assessing the arcing fault hazard to personnel, who work on or in the vicinity of high power electrical equipment.

This paper continues the work described in "Electric Arc Burn hazards" [1].

2. Research Background

The vast majority of the literature on arcs deals with arcs that have been constrained or stabilised either to study them or to make them useful.

Arcing faults are not constrained, they occur. They are not wanted and are extremely turbulent. The present task is to deal with what actually occurs in practice rather than what can be easily studied.

The bulk of the arc literature is based on single-phase opposing electrodes, where the current comes from one side and flows across to the other side. Useful devices such as circuit breakers and fuses have this characteristic.

Hazardous arcing faults in electrical equipment are virtually always on parallel electrodes.

The literature on parallel-electrode arcs has concentrated on measuring the velocity of arcs travelling along single-phase rail guns.

The available literature therefore needs interpretation for the present topic.

3. High Power Electrical Equipment

This paper only deals with electrical equipment connected to an electrical supply system, which can provide fault currents sufficient to cause significant injuries to personnel in the vicinity of an arcing fault. Such electrical installations consist of:

- Live Conductors (busbars/cables), which become electrodes for an arc,
- Neutral conductors, which become electrodes for an arc,
- Earth/ground conductors, which become electrodes for an arc
- Insulation between the live conductors and earth conductors

- Enclosures
- Electrical Protection Systems

The words (phase/neutral/earth/ground) describe the electrical potential of a conductor. The words (conductor/busbar/cable) describe how the conductor carries current. The word electrode describes the conductor from which current flows into an arc. Phase, conductor and electrode therefore describe different properties of the same thing and may be used interchangeably within this paper.

3.1 Arcing Fault Electrode Configuration

For faults in high power electrical equipment, the arc burns from up to three parallel live conductors. It is these three live-conductors that contain the fuses or circuit breaker contacts of the protection that is designed to clear the fault. The three live-electrodes are likely to have near to the minimum practical separation for the voltage level of the equipment.

When the neutral conductor follows a separate route to the live conductors, it is likely to not be involved in the fault due to the lack of a mechanism to get fault current into the neutral.

When the neutral runs parallel to the live conductors it can form a fourth parallel electrode.

It is harder to generalise the path of the earth/ground currents in the vicinity of the arc root.

Due to the magnetic influence on the arc behaviour, the earth/ground current is most likely to enter the earth/ground plane of switchgear enclosures in the plane of the three parallel live conductors. That is either beyond the end of the three live electrodes or outside the two outer electrodes in the same plane. What is important is the initial direction of current flow from the arc root. This determines the direction of travel of the arc root. There are the following possibilities.

(a) Earth/ground currents return parallel to the three parallel live conductors in the enclosure walls either side of the three parallel live conductors. This produces arcing in up to five parallel electrodes. This outcome is driven by inductance effects.

(b) Due to the arrangement of the earth/ground conductors in the enclosure, the earth/ground current flows in a distinct direction. This outcome is normally driven by resistance effects.

3.2 Fault Location and Movement

Arcing faults are initiated at a particular location because of some unwanted event. Either the insulation fails or a conductor is accidentally placed

across a potential difference. They rarely however remain at the initiation site.

The current enters the conductor at right angles to the surface and then flows back towards the source. This produces a magnetic driving force, which drives the arc root away from the source of supply.

As a result the arc will run away from the source of supply until it reaches something, which prevents it going further. This can be an end to the un-insulated conductor or a barrier.

Sometimes the arc voltage is sufficient to cause a breakdown of the insulation closer to the source of supply. This will cause a new arc to form at the breakdown point and the arc further down the conductor to extinguish. (Arcs will not burn in parallel for any length of time.)

The new arc will then run away from the source of supply.

Relatively stable arcing locations will therefore be found at the end of busbars, at gaps such as open contacts or before the conductors disappear inside insulation.

Highly mobile arcing locations often occur at the earth/ground electrode due to the influence of the self magnetic field of the current. They also occur on live busbars where there is nothing to provide stabilisation.

Highly mobile arcs behave differently to relatively stable arcs.

4. The Components of an Arcing Fault

An arcing fault within electrical equipment will be fed from up to three active (live) phases.

Depending on the source characteristics, the current from the active phases will return either on the other active phases or via a neutral or earth/ground system.

In general, the arcing fault will burn on,

Up to three parallel active (live) conductors,
With up to three mobile arc roots on the
neutral and/or earth/ground, conductors.

The arc roots on the neutral earth/ground conductors are likely to be outside the active conductors on the same plane as the active conductors due to the self-magnetic field influences on the arc columns.

Each live conductor, which becomes an electrode for an arc, is only likely to have one arc root and one cathode/anode jet coming off it most of the time.

There is only one arc root per conductor because arcs will not burn in parallel for more than a brief moment due to the negative voltage/current characteristic of atmospheric pressure arcs. Due to this characteristic, the smaller current arc or the longer arc will rapidly commutate into the other parallel arc and self extinguish. When an arc root is highly mobile more than one arc root can occur.



Fig. 1 One frame of a 5,000 frames per second movie of a 15,000Amp arcing fault on three live plus one surrounding earth electrodes.

Figure 1 shows an arcing fault on five-parallel conductors with the earth conductor surrounding the live conductors in the conductor plane. This shows that up to three extra arc roots can form on the earth/ground plane depending on the supply characteristics.

The arc roots on the live conductors move rapidly to relatively stable locations.

The arc roots on the earth/ground conductor are highly mobile and unstable. Even with a solidly connected surrounding ground/earth, the number of ground/earth arc roots oscillates between 0 and 3.

An arcing fault therefore consists of the following components:

- Cathodes, where electrons are emitted from the conductor and flow into the plasma,
- Anodes, where the electrons from the plasma re-enter a conductor (the cathodes and anodes are either highly mobile or relatively stable),
- Electrode material arc columns (these start at each stable electrode with a constricted arc column containing an axial plasma jet and tend to remain relatively straight.),
- Mainly air arc columns (these start at highly mobile electrodes and also connect between the constricted electrode-material jet columns),

- Some sections of constricted arc column in the plasma cloud can sometimes occur,
- Air which has not yet been contaminated by the electrode material,
- The plasma cloud generated by the arcs.

4.1 Cathodes and Anodes

At the cathode, electrons leave the crystalline structure of the conductor and enter the plasma of the arc core. At the anode, the electrons re-enter the conductor.

Both the cathode and anode spots have a cross sectional area, which is smaller than the neighbouring constricted arc column. As a result near to the cathode and anode spot the arc has a conical or hourglass shape.

The self magnetic field of the current in the column near to the electrode spot interacts with the current itself to draw air radially into the column, dissociate it, ionise it and drive the resultant plasma axially away from the cathode spot. This is what produces the electrode jets.

The same mechanism also increases the pressure inside the arc core above the surrounding air pressure.

Both the cathode and anode have a voltage drop of approximately 10 Volts over a distance of around a micrometer. Almost all of the energy from the 10 Volt electrode drop finishes up in the electrode material. For relatively stable arc roots on copper, aluminium and steel, this means it melts the metal and the pressure from under the electrode spot blows the molten droplets in all directions. With carbon electrodes (this includes carbonised insulation) the carbon does not go through a molten stage and it ablates from under the cathode spot. Carbon and steel electrodes can be heated to incandescence whereupon they become refractory electrodes that emit free electrons and are easy to restrike from.

Every time the current from a conductor changes sign, the cathode must change into an anode or the anode must change into a cathode. The creation of cathodes is the most difficult transition and requires sufficient voltage for it to occur.

The cathode consists of a positive ion space charge sitting of the order of a micrometer off the conductor surface. Every time a cathode is created this space charge must be created. This requires a minimum voltage of around 400Volts.

As a result the very small depth (in comparison to their cross section) of both the cathode and anode

space-charges, the current always enters the conductor perpendicular to the conductor surface at the location of the arc root (sometimes called an electrode spot).

4.2 Constricted Electrode-Jet Arc Columns

The small cross section of the electrode spots results in conical or hourglass shaped arc columns in the regions of the electrodes.

The self magnetic field of the current in the column interacts with the current itself (positive ions and free electrons) to drive the plasma axially away from the electrode spot. [2] (The axial current density produces a circumferential magnetic field, which together with the radially outwards component of the current density produces an axial force on the ions and electrons.) This produces the electrode jets. It also draws cool air radially into the arc column to replace the plasma being driven out axially. The energy required to heat, dissociate and ionise the radial air inflow, cools the surface of the arc column and produces a sharp temperature gradient on the boundary of the arc core in the radial inflow region.

The strong radial air inflow and the sharp radial temperature gradient will insulate the side of an electrode jet. Thus electrical connection between two electrode jets will be difficult until after the strong radial inflow has abated and the columns have become more diffuse. This will correspond to where the arc column starts to become cylindrical.

The high velocity axial flow in the electrode jets is also such that two jets hydraulically repel each other.

This would indicate that there is a minimum arc length between two electrodes. This would be the sum of the length of two constricted arc jets up until when the boundary of the arc-jets become diffuse enough to allow the current to cross over to the other electrode jet.

In the arc column from the electrode spot up until where the current and plasma jet starts to go in different directions, the diameter of the arc is increasing, which means the current density is decreasing.

The decreasing current density is likely to be associated with decreasing electric field gradient, lower electron temperature and lower plasma temperature. Roberts 1972 [3] reported the core temperature of a free burning arc dropping from around $30,000^{\circ}$ at the cathode to around $15,000^{\circ}$ five centimetres away.

This is consistent with the three orders of magnitude reduction in luminosity of the arc column from next to the electrode spot until the diffuse mainly air column connecting the three electrode jets reported by Stokes and Sweeting in 2004. It is also consistent with the photographs in this paper where radiation from the arc core next to relatively stable arc roots saturates the camera and the diffuse columns and plasma cloud are often black.

The mobility of the arc root has a strong influence on the luminosity of the constricted column. On highly mobile and new arc roots, where the arc has dwelled for less time than needed to melt the electrode material, the arc jet consists mainly of air and is not strongly dominated by the electrode material. As well as the lack of molten electrode material, the highly mobile arc has a magnetically driven cross flow.

On the other hand with relatively stable arc roots, where the arc dwells long enough to produce a spray of electrode droplets, the constricted arc column and the plasma jet contains entrained electrode material that after a while oozes out of and envelops the arc column. The resulting electrode material sheath then absorbs most of the electrode line emission.

The following photograph shows a single phase arc where the bottom arc root has migrated off the molten electrode material and is now burning in oxygen/nitrogen whilst the top arc root is burning in copper vapour. Notice the influence on colour and luminosity from identical current.

Highly mobile and new arc roots appear like the one on the lower electrode. Not only does the colour change, the luminosity drops off dramatically.



Fig. 2. A frame from a 15kA single phase arc where the lower arc root drifted off the molten copper and produced an air dominated arc jet.

This photograph was recorded using extra neutral density filters to minimise camera saturation at the arc root. As a result the diffuse core is very weak and the plasma cloud is black.

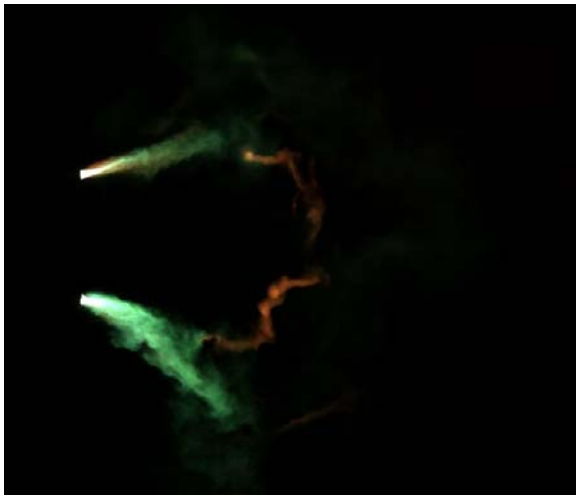


Fig. 3 A single-phase arcing fault showing the electrode vapour oozing out of the constricted column within centimetres of the electrode and an air dominated column connecting the copper dominated arc jets.

The electrode jet arc column up until where there is a divergence between the plasma jet and the current carrying core is therefore likely to be characterised by:

- A conical or hourglass variation in cross sectional area of the conducting core,
- The cross sectional area at any specific distance from the electrode proportional to current (a nearly constant current density with time or current),
- Radial inflow of air and axial outflow of plasma,
- A steep radial temperature profile at the electrode (due to radial cooling in-flow) becoming less steep as the jet is further from the electrode,
- A constant total voltage drop (as a function of both time and current) (the voltage drop given by one half of the minimum voltage between electrodes).

As you move away from the electrode,

- A drop in the electric field gradient (due to a drop in current density),
- A drop in plasma temperature (due to drop in electric field gradient and current density),
- A drop in luminosity of the arc by three orders of magnitude (measured),
- A drop in the intensity of emitted line radiation (lower field gradient/ electron temperature),

- A narrowing of the width of line radiation (lower atom/ion temperature),
- A broadening of the dark absorption band in the line radiation (due to a drop in the temperature gradient and therefore greater adsorption of line radiation),
- A drop in the intensity of the continuum radiation (due to a drop in the plasma temperature).

4.3 Arc Column Details

Whilst the electric field within an arc column acts on both the ions and the electrons, the vast majority of the energy is transferred to the lighter electrons. The electrons transfer their energy to the atoms and ions by collision.

In the arc core, the electron collisions with atoms and ions excite electrons attached to the atoms and ions and drive them to a higher energy state. When these electrons fall back to their normal energy level they emit light of a fixed frequency, which is determined by the difference between the two energy levels. This is the line radiation emitted by the arc. Line radiation dominates energy transfer within the core of atmospheric pressure arcs.

The temperature (thermal velocity) of the atoms/ions causes Doppler shifting of the line radiation. When added to Stark broadening, due to micro fields around each atom, the emitted line radiation is broadened.

Line radiation in the centre of an arc does not get very far however before it is adsorbed by another atom/ion. Near the edge of the arc, lines emitted with significant frequency shifting can escape from the arc because there are insufficient identical atoms/ions outside them to adsorb the radiation of that frequency. Thus the two edges of broadened lines with a dark adsorption band in the middle are often observed when studying the light emitted from electric arc columns.

In air, the oxygen and nitrogen molecules also adsorb all radiation in the vacuum ultraviolet. This is adsorbed by splitting the molecule and is not re-emitted when the molecule re-associates.

Arcs in air have their strongest line energy emitters in the vacuum ultraviolet. All of this energy is trapped when the radiation enters atmospheric air, which contains molecules. It therefore gets adsorbed at the molecular boundary of the hot plasma.

In the constricted arc columns with radial inflow of cooling air, all the vacuum ultraviolet radiation from the air flows out to the molecular boundary and some

is then sucked back into the arc core by the radial inflow of gas.

If the constricted arc column is attached to a relatively stable arc root electrode material is entrained in the constricted column. Close to the electrode, lines from the electrode material are not absorbed by the surrounding air. This region therefore emits far stronger radiation than anywhere else along the arc column.

A short distance from the arc root, electrode material begins to ooze out of the arc column and this material then absorbs line radiation emitted by electrode material inside the arc core. The electrode material line radiation therefore drops off dramatically after electrode material begins to ooze out of the arc column. This can be seen in figure 3.

If the constricted arc column is attached to a highly mobile arc root or in the first few 100 microseconds after a new arc establishes, significant electrode material is not entrained in the arc jet. There is then no electrode material line emission and the main oxygen/nitrogen lines are absorbed at the molecular boundary. The observed radiation from the constricted arc column is then significantly (factors) lower.

In the oxygen/nitrogen arc column without electrode material, the vacuum ultraviolet radiation will radiate out to the molecular boundary (boundary of the plasma cloud) where it will be adsorbed and taken away with the plasma cloud.

For an object inside the molecular boundary, the oxygen and nitrogen vacuum-ultraviolet lines will reach the surface of the object.

The line radiation from oxygen and nitrogen atoms, which is not broadened, will be adsorbed by atoms and molecules within the plasma cloud. Only the broadened edges of the lines can escape from the arc/plasma-cloud to be observed. A sharp temperature profile helps the broadened line edges to escape because there is less gas of the same temperature to pass through in order to escape the arc. As the temperature gradient falls however, it is anticipated that the intensity of radiation that escapes will also fall because of greater adsorption.

Line radiation from the electrode material, copper and/or aluminium, dominates the radiation which escapes from the arc core so that it can be measured and/or cause burns to people. This is because there are few atoms outside the core to adsorb any radiation that escapes. For an electrode material arc burning inside the plasma cloud however, there is a

source of electrode material vapour, which can adsorb the electrode-material radiation-lines.

Our photographs indicate that the intensity of line radiation from the arc column falls with distance from the electrode spot both due to lower emissions from lower temperatures and greater adsorption due to declining wall temperature gradients. When the column is inside the sheath and/or the cloud, the electrode-material lines are also adsorbed.

Continuum radiation that is a function of the plasma cloud temperature is likely to be the main radiation that escapes from the plasma cloud. The cloud beyond the arcing region is only however between 3000°K and 5000°K.

4.4 The Oxygen/Nitrogen or Diffuse Column

The arc column that connects the constricted arc jet columns to each other is mainly an oxygen/nitrogen column with little electrode material. It looks like a diffuse column because so much of the radiation is adsorbed. The lack of electrode material can be seen in the colour of the connecting column.

The arc current is flowing in a plasma core that is immersed inside the plasma cloud.

The luminosity of the diffuse arc columns is around three orders of magnitude smaller than that of the electrode-jet columns near to the electrodes.

This is likely to be due to both less emission due to a lower plasma temperature plus adsorption of the line-radiation by the surrounding plasma cloud. The plasma cloud contains electrode vapour, which allows it to adsorb line radiation emitted from any electrode material.

On three electrode systems, only one arc jet per electrode has been observed. This means the diffuse column has three ends, which must join somewhere in the middle. Whilst it is clear that the arc jet columns carry the same current as their electrode, the diffuse column current depends on where the join is.

Whilst the arc jet columns appear to have a reasonably constant length, the diffuse columns are blown out by the magnetic fields and continually restrike along shorter paths.

Arc voltage measurements with parallel electrodes indicate that the average length of the diffuse core is proportional to the instantaneous current. Arc voltages on parallel electrodes tend to be sinusoidal, whilst arc voltages on opposing electrodes tend to be constant with current. The difference is that arcs on

parallel electrodes change their length with the current.

4.5 Changes in arc length

As the current increases after a current zero, the increased self magnetic force due to the current interacting with its own magnetic field blows the arc out to a larger radius and therefore a larger voltage drop along the arc column.

Then an arc column appears across a shorter path and the longer arc path decays. The shorter arc paths are usually air dominated with little electrode material radiation. They often start and remain a straight line between the arc jets as they travel in the $j \times B$ direction. This indicates that they are probably in an existing plasma flow.

The shorter path is between two arc columns and does not involve creating a new cathode drop. The gap is only stressed by the arc column voltage drop along the longer arc path.

To achieve breakdown with this level of voltage stress the gas between the arc jets needs to be already ionised by a mechanism other than electron avalanche.

We believe that the air on the breakdown path has been heated and ionised by line radiation from the existing arc columns. It is unlikely to be in thermal equilibrium so it is difficult to assign it a temperature.

It is however almost certainly inside the molecular boundary, where all molecules have been split by the strong vacuum ultraviolet oxygen and nitrogen lines. Since recombination of the atoms produces heat, this is a strong heating process.

The oxygen/nitrogen lines produced by recombination of electrons and oxygen/nitrogen ions in the arc columns will produce ions and electrons inside the molecular boundary and in doing so provide a mechanism for electrical heating of the same space without requiring electron avalanche ionisation of the plasma.

Inside the molecular boundary, we therefore expect a current density determined by the voltage distribution along the arc columns and electrodes plus the conductivity created by the oxygen/nitrogen recombination lines.

This current distribution will be driven by the $j \times B$ forces created by the magnetic field of the current in the electrodes and main arc columns. This will drive

the plasma inside the molecular boundary and create a flow similar to what we observe in the movement of the new breakdown columns.

The arc shortening breakdowns therefore become an initiation of an electron avalanche mechanism inside bulk plasma travelling away from the electrodes and already carrying a much smaller current.

In some frames of our high speed videos more than one path breaking down into a constricted column can be seen. Also in some frames the breakdown is firstly to a bright highly constricted path decaying into a much less bright diffuse column within 100 to 200 microseconds.

This mechanism indicates that the molecular boundary is at least hundreds of millimetres away from the arc columns.

4.6 The Plasma Cloud

Once there is no current in the plasma, the temperature falls rapidly to around 5,000°K and then more slowly to around 3000°K. We anticipate that radiation, some of which is further adsorbed in the surrounding plasma is still the dominant mechanism.

Whilst turbulent mixing can be seen in the photographs, the glowing cloud maintains an identifiable structure as it moves away from the electrodes.

This limits the ability of turbulent mixing to play a significant role.

Within the plasma cloud line radiation is expected to play a less significant role and normal black body radiation due to the thermal motion of the particles is expected to dominate.

5. Energy Flows

5.1 Energy Dissipation

The voltage and current in the arc produces four distinct energy sources.

The energy from 10 Volt anode and cathode voltage drops is mainly dissipated in the electrode material.

The energy from the approximately 10 Volts/cm of arc column voltage drop is initially transferred to electron velocity within the arc core.

The voltage distribution along the electrodes and arc columns also produces a much lower current distribution in the plasma surrounding the arc and the lower energy from this is transferred initially to the electrons in the plasma surrounding the arc columns.

The interaction of the self magnetic field of the current in the electrodes and arc column produces electromagnetic forces on the arc column and diffuse plasma inside the molecular boundary.

5.2 Electrode Drop Energy

On highly mobile or new arc roots, the energy dissipated in the electrode does not have time to melt sufficient electrode material to cause an electrode spray or feed significant electrode material into the constricted column next to the electrode.

In part the mechanisms causing high mobility also causes cross flow on the arc column and the column therefore burns in the cross flow material rather than material close to or from the electrode.

On relatively stable arc roots on copper, aluminium and iron, the energy dissipated in the electrode produces a pool of molten material under the arc root.

This energy produces a spray of electrode material. On copper electrodes this consists of small droplets of 1080°C copper, which settle on nearby surfaces. On aluminium electrodes this produces droplets of aluminium, which burn to insulating aluminium oxide.

Our recent experiments show that this also produces a flow of electrode material into the constricted arc column next to the electrode. After a few centimetres, this electrode material oozes out of the column and then absorbs line radiation from the electrode material.

5.3 Arc Column Energy

The energy dissipated by the approximately 10V/cm voltage drop along the arc column is initially transferred mainly to electron velocity.

Electron collision with the atoms and ions of oxygen, nitrogen and the electrode material excite electrons in the atoms and ions.

Decay of the excited electrons to their natural energy level produces line radiation, which is then broadened by Doppler and Stark broadening. [4]

This line radiation is emitted in all directions until it is absorbed by another atom or ion of the same element with the same thermal and electric field properties. Another way of describing this is the absorbing atom/ion has to have the same broadening mechanisms as the emitting atom/ion or the radiation will pass by.

Within the arc core there are plenty of absorbing atom/ions and the energy is transferred to the boundary by repetitive emission and absorption.

Next to the anode/cathode, the air inflow driven by the electrode jets produces a steep temperature profile in air, which allows the outer wings of each broadened line to escape leaving a dark space in the centre of the line. The centre of each line is absorbed by the cooler air surrounding the arc column.

With little electrode gas in the inflow to the constricted arc column, the lines from the electrode material are able to escape all the way to the camera.

The electrode material lines are also strong in this region because the arc column is constricted by the anode/cathode and the current density and plasma temperature is higher.

Within a few centimetres of the anode/cathode on relatively stable arc roots we have observed electrode vapour oozing out of the electrode jet, which then absorbs some of the electrode material lines and significantly weakens them.

As a result the bulk of the radiated energy reaching the camera comes from the first few centimetres of constricted arc column next to relatively stable arc roots.

With highly mobile and new arc roots the anode/cathode heating of the electrode material is unable to feed electrode material into the constricted column so only oxygen/nitrogen lines are emitted by the constricted arc core.

The centre of the oxygen/nitrogen lines will also be absorbed near the arc core and some of these will also cause electrons to be split off atoms and dragged away in the electric field. This will create the diffuse current, which is the third form of energy dissipation.

The rest of the strong oxygen/nitrogen lines will pass through the inner layer of air until they reach oxygen/nitrogen molecules. Since the strong lines of oxygen and nitrogen are emitted in the vacuum ultra-violet they will be absorbed by the surrounding oxygen/nitrogen molecules, which will be split into atoms.

Recombination of the oxygen/nitrogen atoms into molecules will then transform the energy into heat or thermal velocity of the molecules.

In this way the strong oxygen/nitrogen lines heat the air at a distance from the arc column and together with the lines from ion/electron recombination in the

arc column core create a plasma cloud around the arc column core.

As a result of the above processes only the wings of oxygen/nitrogen lines in the visible spectrum reach the camera. These are much weaker than the electrode material lines, which reach the camera because the strong electrode material lines are in the visible spectrum and pass through air.

When plasma cloud containing significant electrode vapour comes between the arc column core and the camera, the intensity of electrode material radiation recorded by the camera also falls significantly due to absorption.

5.4 Diffuse Plasma Energy

The diffuse air plasma created by the absorption of the oxygen/nitrogen lines including those resulting from electron ion recombination in the arc column core is also subject to an electric field created by the electrodes and the arc column.

The current flowing in this diffuse plasma will also heat the plasma.

There are therefore two sources of heat for the air plasma within the molecular boundary.

Both of these energy supplies will stop after the molecular boundary and then the plasma will cool by the normal thermal radiation process, which follows a T^4 formula. This leads to an initial rapid cooling followed by a slower tail.

5.5 Electromagnetic Energy

The current through the electrodes and the arc column produces a magnetic field. This interacts with current density in the arc column and the diffuse plasma to produce electromagnetic forces on the electrons and ions.

These electromagnetic forces drive the electrode jets. They drive the arc column to expand in the form of an arc.

They also drive the diffuse plasma to move like a bulk flow in the same direction. This is evident in breakdowns which flow away as straight arc-columns instead of arc-shaped columns.

5.6 Other Energy transfers

As well as line radiation energy can be transferred by thermal conduction, turbulent mixing and continuum radiation due to the temperature of the gas/plasma.

Except on the steep sides of the constricted arc column, temperature gradients in the plasma cloud are not enough for significant conductive energy transfers.

When the camera is set to record radiation from the plasma cloud it maintains an identifiable pattern which means that the level of turbulence is also not large. In fact in the breakdown region it almost appears laminar.

Whilst we have yet to use a spectrometer on this arc, nearly all arc spectrographs show the lines as very much stronger than the continuum. We therefore think that the continuum will only dominate when line absorption and diffuse current heating have ceased.

6. Conclusion

Arcing faults in electrical equipment are normally supplied by three parallel active conductors.

An arcing fault will normally develop three relatively stable arc roots on the three parallel active electrodes.

On the ground/earth electrodes in the vicinity of the arcing fault highly mobile arc roots tend to form. These can vary over time between none and up to three separate arc roots.

The three relatively stable arc roots on the parallel active conductors will produce strong arc jets containing significant electrode material.

Sprays of molten (copper) or burning (aluminium) metal droplets are emitted from under the relatively stable arc roots.

The first few centimetres of the arc jets from relatively stable arc roots produce the vast majority of the radiation emitted from the arcing fault that reaches a camera or observer outside of the plasma cloud.

The electric field along the arc columns accelerates the free electrons in the arc column and these free electrons collide with the atoms and ions of oxygen, nitrogen and the electrode material.

These collisions raise the energy levels of the electrons in the three sets of atoms/ions causing some emission of free electrons.

The electrons falling back to their normal energy states emit line radiation which is Doppler and Stark broadened.

Due to absorption only the wings of the broadened lines in the visible spectrum reach an observer or camera.

The vast majority of the emitted lines are absorbed within the plasma cloud.

The electrode material lines are absorbed by electrode vapour that oozes out of the arc column and is left in the plasma cloud.

The strong oxygen and nitrogen lines are in the vacuum ultraviolet and are absorbed by oxygen and nitrogen molecules which are dissociated and heat the plasma on recombination. This leaves a molecular boundary around the arc column.

Inside the molecular boundary the lines from recombination of electrons and oxygen/nitrogen ions in the arc column cause ionisation and diffuse current flow in the surrounding plasma cloud.

When the arc column lengthens due to electromagnetic forces the increased arc column voltage drop causes arc columns to develop in the diffuse plasma cloud inside the molecular boundary. These new columns shorten the arc length.

These processes vary the arc length with current every cycle causing the arc voltage to follow something like a sine wave form.

Inside the molecular boundary the current in the diffuse plasma reacts with the magnetic field of the current in the electrodes and arc column to cause a magnetically driven flow of plasma.

As a result an unexpectedly uniform plasma cloud is driven away from the parallel electrodes.

References

- [1] A.D.Stokes and D.K.Sweeting, "Electric Arc Burn Hazards", 7th International Conference on Electric Fuses and their Applications, Jurata Poland September 2003
- [2] H. Maecker "Different types of arcs", Discharge and Plasma Physics edited by S.C.Hayden, University of New England Press 1964
- [3] G.R.Jones "Figure 4.24 in High pressure arcs in industrial devices", Cambridge University Press, 1988
- [4] R.G. Fowler "Radiation from gas discharges", Discharge and Plasma Physics edited by S.C.Hayden, University of New England Press 1964

THERMAL MODEL OF THE EVOLUTION OF FRAGMENTS INSIDE A MICROSCOPIC SPOT: A MULTISCALE APPROACH OF THE INTERACTION PLASMA/CATHODE

Ph. Teste¹, J. Rossignol²

1 Laboratoire de Génie Electrique de Paris, Plateau de Moulon, 11 rue Joliot Curie, SUPELEC, CNRS, France,
91192 Gif sur Yvette, teste@lgep.supelec.fr

2 Institut Carnot de Bourgogne, Bâtiment Mirande – Chimie, 9, avenue Alain Savary, BP 47870, 21078 Dijon
Cedex – France, jerome.rossignol@u-bourgogne.fr

Abstract: In this paper we propose an explanation for the great dispersion (several orders of magnitude) which exists in literature for the various values of essential parameters (such as surface power density or current density) of influence in the power balance at the surface of a copper cathode submitted to an electric arc. In this work this dispersion is explained by the difference in the space and time scales considered in the different works published. A simple model is proposed which constitutes a first step allowing to explain the difference in the values for the surface power density brought to the cathode surface.

Keywords: electric arc, cathode spot, multi-scale.

1. Introduction

For many applications (switching devices, plasma torches, study of lightning impact, arc welding...) the study of the electrode erosion under the action of an electric arc is of great importance. A great deal of literature concerning electrode erosion mechanisms for various experimental conditions is available. Many parameters are liable to influence the erosion phenomena. Among them, we can quote: the arc current intensity, the arcing time, the electrode material and polarity, the electrode gap and shape, the nature of the covering gas, the arc mobility on the electrodes... In these conditions, a theoretical predictive evaluation of the erosion caused by the electric arc action in given experimental conditions remains a very difficult work.

Another way to tackle the problem of electrode erosion is the assessment of the power balance at the electrodes. Many works concerning power balance at the cathode surface have already been published. However, in the case of low melting temperature electrodes (copper cathode for instance), there exists a great scattering (several orders of magnitude) in the values of several essential parameters such as the current density at the cathode surface or the surface

power density brought by the electric arc to the cathode surface.

The aim of his paper is to propose a possible explanation of the parameter value scattering. The root idea of this explanation is relative to different observations or modelling scales used for space as well as for time description.

In the first part of this paper the description of the power balance at the cathode is briefly recalled as well as the different values proposed in the literature.

In the second part of the paper a “multi-scale” approach of the cathode heating is proposed. This approach is based on the work of Jüttner [1] who observed different structures on the cathode surface. First results are then presented which may constitute a first step to explain the scattering which exists in the literature concerning the surface power density value brought by the arc to the electrode.

To finish, perspectives and remaining questions are presented.

2. Reminder of the power balance at the cathode and the various spot structures observed

The power flux brought by the arc to the cathode has several origins:

- the electrons (emitted or back scattered). The power « brought » by the emitted electrons to the cathode surface is usually written under the following form (Q_{ee}):

$$Q_{ee} = J_e \cdot F_N$$

where J_e is the emitted electron current density. For a given cathode material, J_e is a function of the macroscopic field in front of the cathode surface and of the surface temperature. F_N is called Nottingham potential. Several analytical expressions exist for J_e or F_N , which are obtained by making approximations according to the temperature and electric field range concerned [2,3]. Numerical calculations have also been carried out [4, 5].

- the ions impinging the surface, which bring to the cathode a fraction of their kinetic energy and which may bring also some energy provided by neutralisation phenomena that occur near the surface. Usually this power flux (denoted here Q_i) is written under the following form [6]:

$$Q_i = (1 - \alpha)(\varepsilon U_c + V_i - \phi_0)J$$

where α is the fraction of electron current density, ε is the fraction of kinetic ion energy transferred to the surface, U_c is the near-cathode voltage drop, V_i is the ionisation potential, ϕ_0 is the work function of the cathode material and J is the current density in the cathode root.

- the neutral species which bring a fraction of their kinetic energy to the surface and may also bring energy provided by excitation, ionisation phenomena that occur when they interact with the surface.

- the plasma radiation and the cathode surface radiation

- the various chemical reactions at the cathode surface

- the cathode Joule heating

In the case of “cold” cathodes (Cu, Ag, Ni, ...), many works have been done to assess essential parameters like the current density in the cathode spot and/or the surface power density brought by the arc to the cathode surface (these two parameters are linked). The proposed value ranges are quite large.

Concerning the current density determination, several experimental methods have been proposed: the observation of the tracks left by the arc root, the observation of the luminous zone over the cathode surface, spectroscopic study (Zeeman effect), the use of coils in the cathode, the measurement of the force exerted by the arc on the electrode...

All these studies lead in the case of « static » or moving arc to current density values in the range 10^8 - 10^{12} A/m² [7 to 13]. Moreover, modelling works [14 to 18] proposed values in the range $5 \cdot 10^9$ - $5 \cdot 10^{11}$ A/m².

Concerning the surface power density modelling works proposed values ranging from 10^{10} W/m² to 10^{12} W/m². Several experimental works [16] and [19 to 22] based on the observation of tracks, on the measurement of the mass losses of the electrodes, on the measurement of the energy dissipated in the electrodes have lead to values of the surface power density in the range $5 \cdot 10^9$ W/m² to $8 \cdot 10^{11}$ W/m².

As we can see there is a great scattering in the proposed values of these two parameters. The aim of this paper is then to try to explain this scattering. For

that, the root idea is that it may be due to the different space and time scales considered to describe the arc-electrode interactions. Indeed several spot structures have been observed and described in numerous works [1], [23 to 25]. In [1] Jüttner has proposed a classification of these structures through different parameters like the life duration, the size (diameter) and the intensity in the spot. It may be summed up as follows with the help of three levels of structures (according to Jüttner):

- Structures of level A: Cathode spots characterized by a current intensity around 50 - 100 A, diameters around 50 - 100 μ m and a life duration about some tens of μ s.
- Structures of level B: Fragments or microspots having diameters about 20 μ m, current about 20A and a life duration about 10 - 20 ns.
- Structures of level C: Subfragments or cells characterized by a current smaller than 5 A and diameters smaller than 5 μ m.

Figure 1 from Jüttner [1] shows an example of spot fragments (observed with the help of a high speed camera). According to Jüttner, the irregular structure indicates the presence of cells.

Other larger structures are also observed as soon as the arc current intensity or the arc duration increases. For instance figure 2a and 2b show macroscopic craters having an axi-symmetric geometry. They have been observed with the help of a 3D optical profiler. In the first case the copper cathode was submitted to an electric arc of 300 A with an arc duration of 300 μ s, in the second case the arc duration was equal to 5 ms and the mean current intensity to 100 A. In figure 2a, the crater diameter is about 1 mm and macroscopic waves of solidified liquid metal may be noticed at the crater edge. In these two examples, the crater shapes allow to think that they result from the action of a unique static heat flux having an axi-symmetric distribution on the cathode surface and the action of multiple fragments or small spots is not detectable on such tracks.

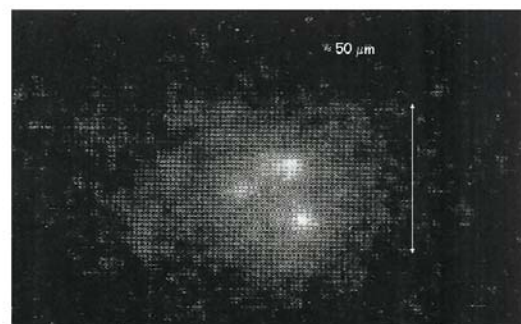
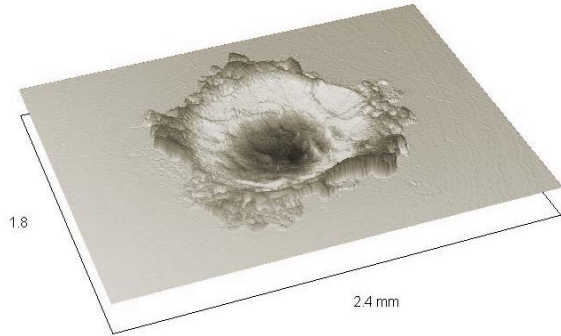


Figure 1: High speed photography of fragments (Jüttner [1])

For higher arc current intensities macroscopic liquid metal “bath” may be observed as well as macroscopic liquid metal droplets. Figure 3 from Devautour [13] shows macroscopic liquid copper droplets ejected from the cathode surface. In this case the arc intensity was equal to 1000 A the arc duration



to 5 ms.

Figure 2a: Macroscopic crater observed on a copper electrode. The arc duration is equal to 300 μ s and the current intensity is about 300 A.

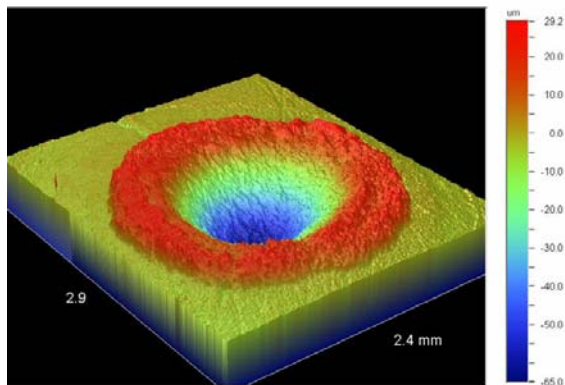


Figure 2b: Macroscopic crater observed on a copper electrode. The arc duration is equal to 5 ms and the current intensity is about 100 A.

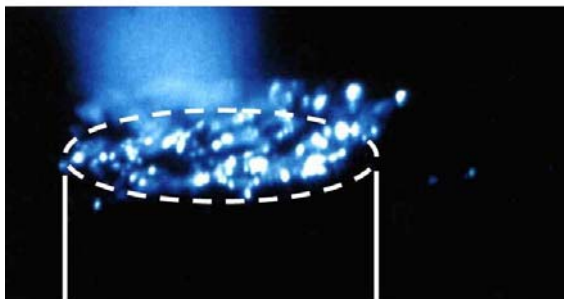


Figure 3: Copper electrode – Macroscopic droplet ejection under the arc action.

A question may be asked:

- How a set of microscopic structures like fragments may create tracks as the one observed in figure 2, that is to say a crater of 1 mm diameter having an axi-symmetric shape and showing a macroscopic molten zone and macroscopic molten waves? How may the connection between the various spot structures be done?

3. Proposition of a multi-scale approach

The aim of this paper is to find an equivalence between:

- the heating of an electrode under the action of multiple very intense mobile heat fluxes applied during a very short time

and

- the heating of an electrode by a static heat flux

The objective is also to find if it is possible to obtain crater shapes similar to the one presented in figure 2 under the action of numerous short duration mobile fragments and what is the relation between heat flux characteristics of each fragment and the characteristics of a static heat flux susceptible to cause crater of figure 2.

3.1 The transition from the fragment to the cathode spot (structure B to structure A)

The aim of the first step presented here is to find a relation between the heating of several fragments (structures of level B) and spot heating (structure of level A).

For that we have simulated the heating of five fragments of 10 A, with a life duration of about 20 ns for the whole life duration of a cathode spot of 50 A, that is to say 20 μ s. The electrode is a copper cylinder (8mm in diameter)

Fragments are unstable fluctuating structures [1]. According Jüttner [1], the spatial fluctuation of the fragments does not mean a real movement: one fragment dies and another is ignited at a different location. As a consequence the centre of gravity of the cathode spot constituted of the five fragments is displaced. Jüttner has described this displacement with the help of a random walk law. The probability $W(R)dR$ to have a displacement in the interval $(R, R+dR)$ irrespectively of the direction is given by :

$$W(R)dR = \frac{2R}{\langle R^2 \rangle} \exp\left(\frac{-R^2}{\langle R^2 \rangle}\right) dR \quad (1)$$

where $\langle R^2 \rangle = 4Dt$ is the mean value during a measuring interval t . D is the diffusion parameter.

Several authors have proposed values for D near $2 \cdot 10^{-3} \text{ m}^2/\text{s}$.

3.1.1 Modelling of the heating – Description of the numerical modelling of the electrode heating

In this part a brief description of the numerical model used to simulate the electrode heating under the set of fragments is given.

The main properties and boundary conditions of the model are the following:

- (i) The electrode is a copper cylinder of 8 mm diameter.
- (ii) At the beginning of the heating the fragments are disposed randomly around the spot gravity centre. An order of magnitude of the distance between the spot centre and each fragment centre has been given in [1] and is about $25 \mu\text{m}$. Each fragment has a life duration of 10 - 20 ns and the spot centre moves according to the law given by equation (1).
- (iii) The cathode material (copper) properties: specific heat and thermal conductivity are taken to be temperature dependent.
- (iv) The density has been taken constant. This approximation is not very restrictive because for metals like copper, the thermal dilatation coefficient is small.
- (v) Joule heating has been neglected. This approximation is valid as far as the current density values (denoted J) remain smaller than 10^{11} A/m^2 as it has been shown by He et al.[15] for a flat electrode
- (vi) The motions induced in the molten part of the electrode by Lorentz forces, Marangoni effects or plasma jets/electrode surface interactions, etc... are neglected.
- (vii) The heat flux on the lateral sides of the electrode has been neglected. This assumption is valid because we consider short duration electric arcs.
- (viii) The bottom temperature is fixed to $T = T_0 (=25^\circ\text{C})$ on the lower cross section of the electrode. This is justified if the electrode is tall enough (some millimetres) and if the arc duration is short enough to avoid the heat to diffuse to the electrode bottom during the arc.
- (ix) During its life duration each fragment brings an heat flux characterized by the power $P(t)$ and its surface power density $Q(r,t)$. The values taken for the power and the power density are discussed hereafter.
- (x) Mathematical formulation of the problem: If we neglect the liquid motion in

the molten zone, we have then to solve the following equations:

(1) The heat diffusion equation in the non-stationary regime in each phase (solid and liquid) which takes the following form :

$$\rho C_p(T) \frac{\partial T}{\partial t} = \text{div}(k(T) \vec{\nabla} T) + S \quad (2)$$

Where: ρ is the material volumetric mass, C_p the material specific heat, T the temperature, t the time, k the material thermal conductivity, S may represent some power density sources (Joule effect,...).

(2) The equation at the boundary between each phase which has the following form :

$$[k \nabla T]_n^2 = -\rho L_{1 \rightarrow 2} v_s \quad (3)$$

where v_s is the velocity of the boundary between two phases and $L_{1 \rightarrow 2}$ is the latent heat of the change of state (state 1 \rightarrow state 2). This second condition is called ‘‘Stefan condition’’. Several numerical methods exist in order to simulate the melting front’s evolution [26] which require to track the melting front at each time step to apply equation (2). For that several authors have proposed methods using variable time or space steps. In fact the difficulty of the ‘‘Stefan problem’’ lies in the discontinuity of the enthalpy function $H(T)$. The method we used overcomes this difficulty by making the enthalpy function continuous. This function is schematically described in figure 4.

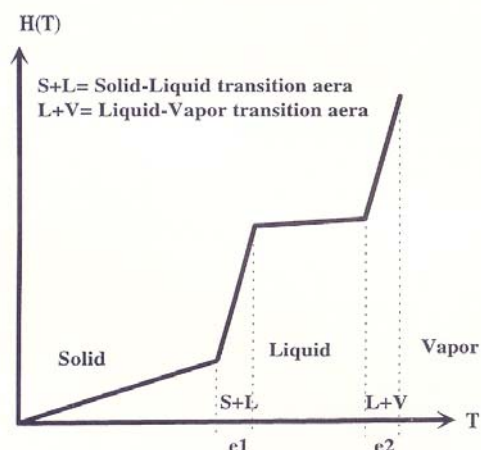


Figure 4: Schematic representation of the continuous enthalpy function used to treat the phase change problem.

The phase changes are continuously realized on a temperature interval $[T_c - \epsilon ; T_c + \epsilon]$,

where T_c may be the melting or the vaporization temperature. In fact, such a method consists of creating a fictitious specific heat equal to $L/2\varepsilon$. Then we have only to solve equation (1). The determination of the boundary between two phases is then realized *a posteriori* after the calculation of the temperature distribution. The use of a transition zone introduces an uncertainty in the determination of the liquid or vapour amount created during the heating. However, we have noted that as soon as ε is lower than 20°C the ε value has no real influence on these amounts. In our calculations we have taken $\varepsilon = 5^\circ\text{C}$.

Concerning the problem relative to the free moving vapour front, the method used has already been described in [27] and [28].

(xi) The discretization of the heat equation is based on a finite-difference numerical method with an implicit time scheme. The discretization time has been taken between 0.1 and 1 ns (according to Q value). The space discretization is not uniform: a high density mesh just under the electrode surface which evolves and becomes larger at the electrode bottom. The smallest values of the space discretization depend on Q and are included between 0.1 and $5\ \mu\text{m}$.

3.1.2 Example of results of multi fragment calculations.

The values chosen to characterize the power flux brought by a fragment are the following:

- the intensity in each fragment is taken equal to 10 A.
- The current density J in the fragment is equal to $7 \cdot 10^{10}\ \text{A/m}^2$ and the surface power density Q equal to $3 \cdot 10^{11}\ \text{W/m}^2$. These values correspond to results of different modelling works [17] or [18] concerning the fragment description.
- The arc duration is equal to $20\ \mu\text{s}$.
- The life duration of each fragment has been taken equal to 20 ns.

In figure 5 we have plotted the different positions of the various fragment centres and the shape of the total heated area.

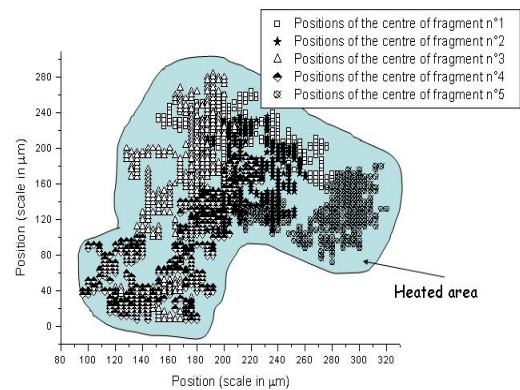


Figure 5: Example of the different positions of the various fragment centres and the shape of the total heated area.

Figure 6 is a photography of the track left by an arc of similar duration. We can note a qualitative correspondence between the two “tracks”

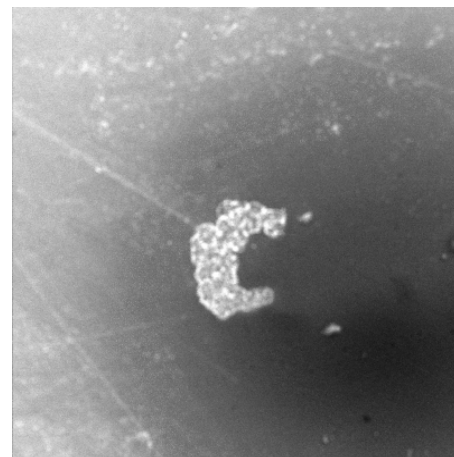


Figure 6: Photography of the track left by an electric arc (duration about $20\ \mu\text{s}$)

Numerous calculations are required in order to obtain significant information concerning the heating due to five fragments. We have realized 13 calculations (computation times are quite important). In figures 7 and 8 we present the different values obtained concerning:

- the maximal molten depth value
- the mean surface extension of the molten zone. The molten zone is not a symmetric crater however it is possible to reach an assessment of a characteristic spatial extension.

Concerning the maximal molten depth we have obtained a mean value of about $24.5\ \mu\text{m}$ and 127.5

μm for the mean value of the surface extension of the molten zone.

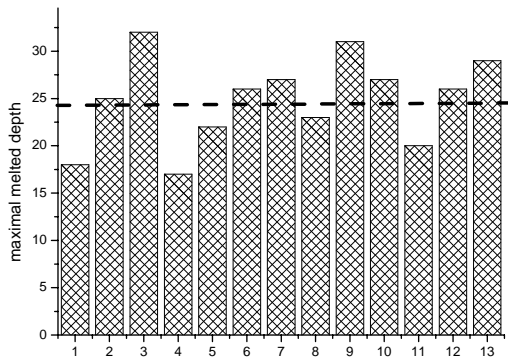


Figure 7: Maximal molten depth for 13 different calculations

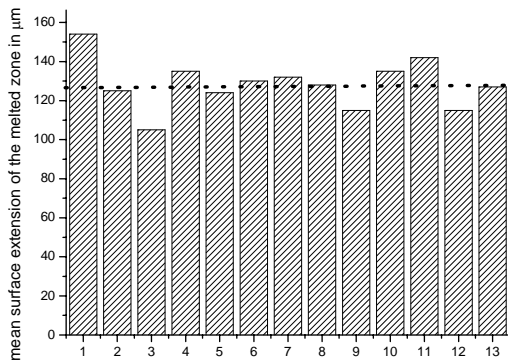


Figure 8: Mean surface extension of the molten zone for 13 different calculations

3.1.3 The research of an equivalent motionless unique heat flux.

The aim of this part is to answer to the following question: is it possible to find a heat flux able to create a “similar” heating to the one created by the previous five mobile fragments?

To define what we mean by “similar” heating we take comparison criterions which correspond to observable phenomena. In this case we have taken the molten depth and the surface extension of the molten zone.

We consider an unique motionless heat flux corresponding to an arc spot of 50 A. Its duration life is equal to 20 μs . The problem is then axi-symmetric.

We calculate the molten depth and the molten radius for various values of the surface power density and of the current density.

Presentation of the results:

J is the current density in the cathode spot and Q the surface power density brought to the electrode. In figures 9,10, 11 and 12 we have plotted the evolution of the molten depth and of the molten diameter versus the current density in the cathode spot for $Q = 10^{10}$, $3 \cdot 10^{10}$, $5 \cdot 10^{10}$ and 10^{11} W/m^2 respectively. We

have also recalled the value of 24.5 and 127.5 μm obtained with the multi-fragments calculation for the mean depth and surface extension respectively.

- For $Q \leq 5 \cdot 10^9 \text{ W}/\text{m}^2$ we do not observe melting for J in the range $10^8 - 10^{11} \text{ A}/\text{m}^2$
- For $Q = 10^{10} \text{ W}/\text{m}^2$ the molten depth value of 24.5 is never reached when J varies.
- For $Q = 3 \cdot 10^{10} \text{ W}/\text{m}^2$ the molten depth reaches the value of 24.5 μm when the molten diameter is practically two times greater than 127.5 μm .
- For $Q = 5 \cdot 10^{10} \text{ W}/\text{m}^2$ the two parameters (depth and diameter) are simultaneously near the two values (24.5 and 127.5 μm) obtained with the five fragments for $J \approx 5 \cdot 10^9 \text{ A}/\text{m}^2$
- For $Q = 10^{11} \text{ W}/\text{m}^2$ the molten depth is near 24.5 μm whereas the molten diameter is only equal to 65 μm .

The couple $Q = 5 \cdot 10^{10} \text{ W}/\text{m}^2$ and $J = 5 \cdot 10^9 \text{ A}/\text{m}^2$ then allows to obtain a heating very similar to the one obtained with the five mobile fragments (with $Q = 3 \cdot 10^{11} \text{ W}/\text{m}^2$ and $J = 7 \cdot 10^{10} \text{ A}/\text{m}^2$).

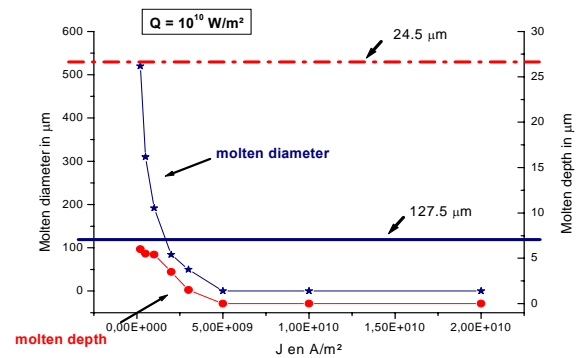


Figure 9: Evolution of the molten depth and of the molten diameter versus the current density in the cathode spot for $Q = 10^{10} \text{ W}/\text{m}^2$

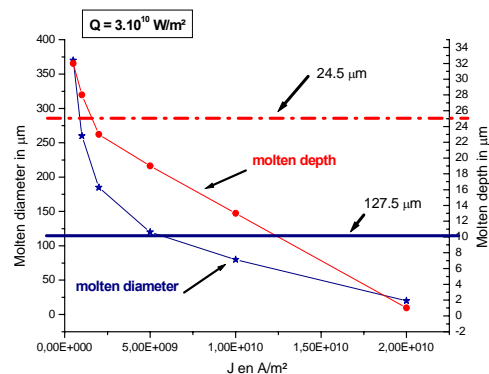


Figure 10: Evolution of the molten depth and of the molten diameter versus the current density in the cathode spot for $Q = 3 \cdot 10^{10} \text{ W}/\text{m}^2$

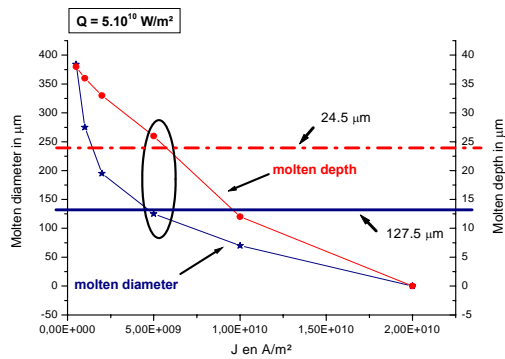


Figure 11 : Evolution of the molten depth and of the molten diameter versus the current density in the cathode spot for $Q = 5 \cdot 10^{10} \text{ W/m}^2$

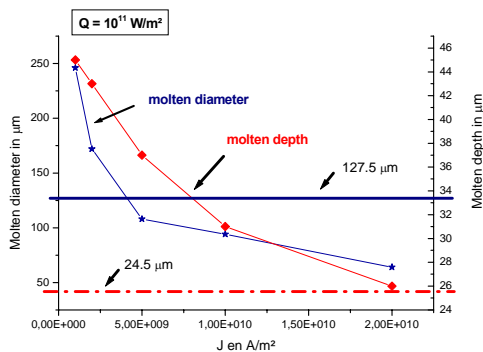


Figure 12 : Evolution of the molten depth and of the molten diameter versus the current density in the cathode spot for $Q = 10^{11} \text{ W/m}^2$

4 Conclusion, comments and questions

It is possible to consider that the action of several fragments (structure B according to Jüttner [1]) may be equivalent to the action of structures having the characteristics of a cathode spot (structure A [1]). The condition to achieve this equivalence is that the current density in the cathode spot is practically one order of magnitude smaller than the one in the fragment. That may contribute to explain a part of the scattering in the current density values proposed in literature.

However the “transition” to larger structures as the one presented in figure 2 (diameter $\approx 1 \text{ mm}$) has still to be done. Moreover, the existence of a macroscopic liquid metal “bath”, or of macroscopic liquid metal droplets, remains particularly difficult to explain with the sole consideration of fragments.

References

[1] B. Jüttner : “Cathode spots of an electric arc”, J. Phys. D: Appl. Phys. 34 (2001) R103-R123
 [2] E L Murphy and R H Good: “Thermionic emission, field emission and the transition region”, 1956, Phys. Rev. 102 1464
 [3] J Paulini, T Klein and G. Simon, “Thermo-field emission and the Nottingham effect”, J. Phys. D: Appl. Phys., 26, 1993, 1310-1315

[4] R. Gayet, R. Harel, C. Josso and H. Jouin, “A simple model for cathodic electronic emission enhanced by low-energy ions in high-pressure arcs”, J. Phys. D: Appl. Phys., 29, 1996, 3063

[5] Ph Teste and J.-P. Chabrierie: “Some improvements concerning the modelling of the cathodic zone of an electric arc”, J. Phys. D: Appl. Phys., 29, 1996, 697

[6] J. D. Cobine, James Dillon: “Gaseous Conductors: Theory and Engineering Applications” Dover Publications, New York, 1958

[7] C Sanger and P E Secker: “Arc cathode current density measurements”, J. Phys. D: Appl. Phys 1971, 4, p. 1941-45

[8] K P Nachtigall and J Mentel: “Optical investigation of arc spot formation on cold cathodes in air”, IEEE Trans. Plasma Sci. 1991, 19, 947

[9] A E Guile, “Oxide films on arc cathodes and their emission and erosion”, 1975 J. Phys. D: Appl. Phys. 8 663-669

[10] R N Szenté, M G Drouet, R J Munz: “Current distribution of an electric arc at the surface of plasma torch electrodes”, J. Appl. Phys., 69, 3 1991 p.1263-1268

[11] K C Hsu, K Etemadi, E Pfender: “Study of the free-burning high-intensity argon arc”, J. Appl. Phys., 54, 3 1983 p.1293-1301

[12] N Vogel and B. Jüttner: “Measurements of the current density in arc cathode spot from the Zeeman splitting of emission lines”, J. Phys. D: Appl. Phys. 24, 1991 p. 922-927

[13] J. Devautour, Thèse de doctorat 1992 : « Contribution à l'étude des interactions arc-électrodes. Influence de la structure métallurgique sur les mécanismes d'érosion des appareils de coupe », Université Paris 6

[14] A. Lefort, Thèse de doctorat 1982 : « Contribution à l'étude des arcs de coupe à fort courant en basse tension », Université Clermont II

[15] He Z.J., Haug R.: “Cathode spot initiation in different external conditions”, J. Phys. D: Appl. Phys., 1997, 26, pp. 603-613

[16] H. Salihou, M. Abbaoui, A. Lefort and R. Auby: “Determination of the power lost by conduction into the cathode at low current arc”, J. Phys. D: Appl. Phys., 28, 1995, p. 1883-1887

[17] S. Coulombe and J.L. Meunier, Plasma Sources Sci. Tech., 6, 1997, 508-517

[18] J. Rossignol, Thèse de doctorat 2001: « Théorie et simulation des phénomènes physiques du pied d'arc cathodique » Université B. Pascal, Clermont-Fd,

[19] B.J. Wang and N. Saka: “Thermal analysis of electrode heating and melting due to a spark”, IEEE Trans. On CHMT, 1993, May, 456-466

[20] J. Devautour, J.-P. Chabrierie and Ph. Testé : “The study of thermal processes in an electrode submitted to an arc root”, J. Phys. III, 3, 1993, p. 1157-1166

[21] A. Marotta, L.I. Sharakhovskiy and V. N. Borisjuk: “A theoretical and experimental investigation of copper electrode erosion in electric arc heaters: II. The experimental determination of arc spot parameters”, J. Phys. D: Appl. Phys., 30, 1997, pp.2018-2025

[22] Ph. Teste, T. Leblanc and R. Andlauer: “A method to assess the surface power density brought by an electric arc of short duration and short electrode gap to the electrodes – Example of copper electrodes”, Eur. Phys. J. AP 18, 181-188, 2002

[23] V I Rakhovskii: “Experimental study of the dynamics of cathode spot development”, IEEE Trans. Plasma Science 4, 81-102, 1976

[24] B E Djakov: “Cathode spot phenomena in low current vacuum arcs on arc cleaned electrode surfaces I. Spot size”, Cont. Plasma Sci. 33 201-207, 1993

[25] B E Djakov, : “ Cathode spot phenomena in low current vacuum arcs on arc cleaned electrode surfaces II Spot dynamics”, Cont. Plasma Sci. 33 307-316, 1993

[26] J. Poirier, J. Heat Transfer, 1988, 563

[27] J.-P. Chabrierie et al., Proc of 30th Eurotherm Conf., 1992, p.143

[28] P. Teste, Thèse Université P6, 1994

LOW VOLTAGE LITHOGRAPHIC FUSES: PRELIMINARY RESULTS OF BREAKING CAPACITY AND CYCLIC LOAD TESTS

D.H. Tourn⁽¹⁾ and J.C. Gomez⁽²⁾

^(1,2) Rio Cuarto National University, Ruta 36 km 601 (5800) Rio Cuarto ARGENTINE
dtourn@ing.unrc.edu.ar, jcgomez@ing.unrc.edu.ar

Abstract: High breaking capacity fuse of low rated current is one of the most difficult fuses to design and build. The fuse element is of such small dimensions that its mechanical fragility is too high. Besides the fuse filler, usually quartz sand could deteriorate the element after the assembling, mainly during the filling process. In order to solve this difficulty the fuse-on-substrate technique has been in use from the 1980 decade. Initially rigid substrate materials were used, such as alumina, silica, glass-polytetrafluoroethylene (PTFE), solidified quartz sand, etc. Also extra cooling was provided through a metallic plate applied to the other substrate face. Lately, lithographic techniques in use for printed circuit construction were extended for fuse manufacturing on flexible substrates. The offset printing technique on flexible substrate added to the use of new conductive inks, allows the manufacturing of good accuracy dimension fuses. The lithographic fuses could find an excellent application field on the protection of small size semiconductors. Several fuse samples on three dissimilar flexible substrate materials were manufactured, having rated current from 0.1 to 1 A. Rated current and temperature rise tests do not represent a problem due to the low current values. However the main manufacturers' concerns are related with cyclic long duration overload behavior and high current breaking performance. The paper presents the results of a limited number of cyclic loading, and high current breaking tests. The high current tests correspond to duties I_1 and I_2 specified by IEC 60127, carried out in a circuit with 230 V ac and currents of about 1,500 A. It is preliminarily concluded that fuses using one of the tested substrates present a reasonably good performance, no far away from the conventional HBC fuse. Further research is necessary especially on the fuse material dimensions accuracy and on substrate material behavior under arcing conditions.

Keywords: Fuse on substrate, lithographic circuits, cyclic load, breaking capacity.

1. Introduction

Introduction of fuse in substrate using lithographic technology

The lithographic fuse was born as a derivation of the concept of lithographic printed circuits. The traditional printed circuits (Printed circuit board, PCB), is conformed by thin layers of conductive material deposited on a base of laminate resin, by means of photographic procedure and of engraving (etching). During more than fifteen years, many research groups have been working on the substitution of such a methodology for the lithographic printing, on flexible substrate similar to normal paper, using inks with metallic load. This new methodology, denominated Conductive Lithographic Film (CLF) has been applied in circuits for telephones, temperature detectors, impact detectors, etc. [1].

The printing procedure is very fast (6,000 to 10,000 prints per hour), simple and very well-known, for what their low cost makes it very attractive. Another negative aspect of the traditional printed circuit boards is the ecological one, since the production effluents and the circuit de-activation require of the elimination of toxic materials. Also, 90% of the copper that is on the resin base is transformed into waste.

Among the printing processes, the most appropriate is the offset that is based on the indirect deposition of ink on the substrate. The first cylinder possesses the print plate, where the ink is deposited that is subsequently transferred to an intermediate cylinder (blanket). The cylinder (blanket) transfers the image to the substrate that is wound on the printing cylinder [2].

Once the printing process is selected, the ink characteristics should be defined. The ink must be conductive and lithographically printable, and besides, the substrate should be compatible with the adopted ink (appropriate ruggedness and having affinity with the ink).

In this printing process, the thickness of the deposited ink is of the order of the 3 μm , which should be compared with the 50 μm of the thick conductors obtained by serigraphy and the 100 μm of the traditional printed circuits. The thickness of the deposited ink can be increased by re-impression, with excellent discrimination, of the order of 25 μm and attainable white space of 35 to 75 μm . The appropriate conductance is reached by means of the use of inks with metallic particles, fundamentally silver suspended in an organic non conductive resin. The silver

particles, in form of flakes with an average size smaller than 1 μm , represent 80% of the weight of the compound. The layer resistivity is in the order of the 0.025 $\Omega\text{mm}^2/\text{m}$ that decreases between 40 and 50% for being heated by some minutes to 80 $^{\circ}\text{C}$, which after being in rest for 72 hours reaches its final value of 0.015 $\Omega\text{mm}^2/\text{m}$. This resistivity is of the order of the one reached with the PCB technology. The circuit once printed must remain invariable in its characteristics in front of the environmental conditions that in the event of not being possible, it requires impregnation, covering or imprint of intermediate layers.

With this methodology resolution limits between 1 and 10 μm are reached, according to the state of the printer. The several electric components, such as resistances, capacitors and inductances can be created easily with this technology. For instance, resistances can be achieved by printing long meandrous conductive paths, reaching values from 1 to 100 k Ω ; capacitors are achieved by inter-fingered forks or with metallic and dielectric successive layers getting capacities of some hundreds of pico-farads. This concept can easily be extended to simple T or π filters, to humidity detectors (the capacity is influenced by the substrate absorption), thermometers (variation of electric conductivity with the temperature), deformation meters, etc. [2].

This type of construction can be extend to the creation of conductive paths that behave like to low voltage fuses, with thickness of the order of 5 μm , resistivity of the order of 12 times that of the copper, that is to say 0.22 $\Omega\text{mm}^2/\text{m}$ and six times that of the PCB. This idea have been exploited for some years, in the self-regenerated capacitors whose structure is composed of several small plates interconnected by means of conductive bridges that act as fuses. Preliminary experiences of low voltage and low current fuse operations have been published, carried out by the group of the Brunel University (England), using ink with copper in the following substrates: high density expanded polyethylene paper, art enamelled paper and polyethylene, being detected certain negative presence of carbon and of its derivate compounds [3].

2. Experimental results

The application of fusible in substrate has been in use for several years. Here are presented preliminary results of the study related to the possibility of applying this methodology to "lithographic fuses". For the experimental determinations, two types of samples were used, both supplied by the Brunel University group:

- Samples *type A*: With copper fuse element on polyart, expanded polyethylene of high density, and

on teslin polyethylene substrate, both obtained by offset methodology whose general form and dimensions are shown in Fig. 1a.

- Samples *type B*: With silver fuse element on glossy paper, obtained by the offset methodology whose general form and dimensions are shown in Fig. 1b.

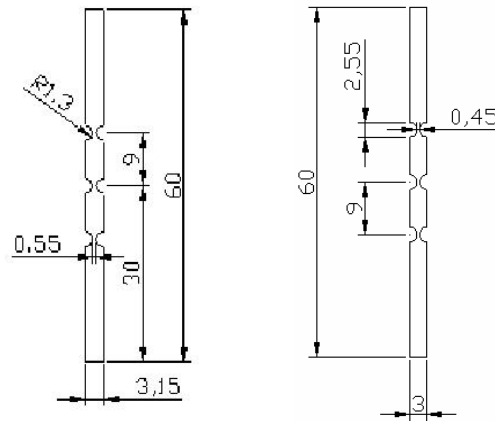


Figure 1a Type A,
thickness: 0.13mm

Figure 1b Type B,
thickness: 15 μm

Form and dimensions of lithographic fuse on flexible substrate

For constructive simplicity, the fuse elements were mounted in NH fuse, size 1 structures normalized by DIN 43620 standard, immersed in quartz sand. The assembly was carried out following the very well-known "rules of art".

2.1. Determination of rated current

Samples type A:

To determine the rated current value an iterative procedure was carried out. The heating test was carried out according to [4] with an assumed initial current value according to the dimensions of the conductive layer. Once the thermal balance is reached, dissipated power and temperatures on the body and fuse-base terminals were measured. By comparing the value of dissipated power with the maximum reference values given by the mentioned Standard, it is determined if the rated current is higher or lower of the test value. The value is adjusted and the test is repeated, until obtaining a value of dissipated power corresponding to certain rated current. Similarly, several samples were operated in order to draw the time current characteristic. With this methodology a rated current of 40 A was determined, based on IEC 60269 standard.

Samples type B:

The same procedure was carried out, but since the rated current is of a very inferior value, approaches shown in [5] were applied. A wider dispersion of the obtained results was observed, resulting an average rated current value of 100 mA. It should be clarified that the ruggedness of the paper used as substrate, makes that the ink spreads in the paper giving a very

variable thickness of deposited material with values between 5 and 14 μm that generate a high dispersion of the rated current values.

2.2. Behaviour interrupting short circuit currents

In order to determine their behaviour as an interrupting device, several samples underwent breaking tests, with short circuit currents.

Samples type A:

For this determination the test current was chosen in order to produce the maximum arc energy. This current is established in [4], as the test duty 2 and its value are determined in the following way:

It is the current value that produces an instantaneous value at the arc beginning, between 0.85 and 1.06 times the rms value of the prospective current.

To carry out the described tests, a circuit was mounted according to that indicated in [4], with the possibility of adjusting different values of prospective current. The test voltage was adopted as 230 V, considered as rated value due mainly to the fuse element possesses only three notches or cross-section reductions. The current was adjusted for maximum arc energy. For this calibration several preliminary tests were carried out, determining a prospective current of 960 A with pf of 0.23. The obtained values, all with switching angle of 0° are shown in Table I. Figure 2, shows the typical form of the voltage and current oscillograms.

Table I, Measured values corresponding to breaking capacity duty 2.

Sample N°	I_{max} [A]	V_{max} [V]	I^2t_{prearc} [A ² s]	I^2t_{arc} [A ² s]	Insulation resistance [k Ω]
1	927	481	817	1984	10
2	1002	461	897	2651	10
3	1032	502	1146	2624	10

11-Apr-06
12:00:16

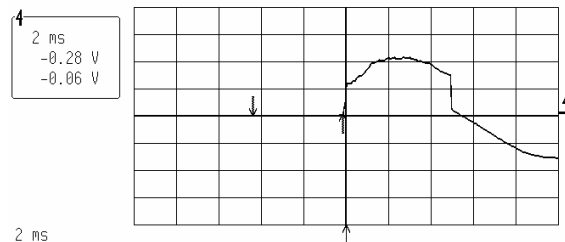
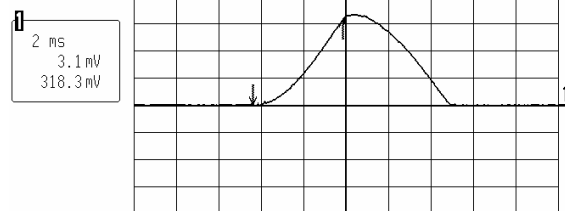


Figure 2, Typical oscillograms of current (above) and voltage (below), 2ms/div. for tests shows in Table I. $I_p=960\text{A}$, $V=230\text{V}$

Although the results are satisfactory, it is noticeable the low value of the insulation resistance after the fuse operation. According to [4], this value should be measured between 6 and 10 minutes after the fuse operation and must be higher than 50 k Ω . Evidently, the carbonaceous residuals of the substrate material are responsible for the low insulation resistance values.

Samples type B:

In this case the test prospective current values are lower than the previous ones, carrying out tests with currents of 1.7A pf of 0.7 and 2.6A pf of 0.2. The tests were carried out on samples assembled without extinguisher filling (quartz sand). The obtained values, all with switching angle of 0° , are shown in Table II. Figure 3, shows the typical form of voltage and current oscillograms.

Table II, Breaking capacity test measured values.

Sample N°	$I_{\text{prospective}}$ [A]	p.f.	I_{max} [A]	V_{max} [V]	I^2t_{prearc} x1000 [A ² s]	I^2t_{arc} x1000 [A ² s]	Insulation resistance [k Ω]
1	1.7	0.7	1.47	1090	3.6	2.1	>100
2	1.7	0.7	1.83	493	3.7	3.2	>100
3	1.7	0.7	1.7	820	3.0	2.6	>100
4	2.6	0.2	2.03	451	3.0	13.7	>100
5	2.6	0.2	1.87	919.5	4.3	2.6	>100
6	2.6	0.2	2.09	552	3.6	7.4	>100

24-Apr-07
19:00:37

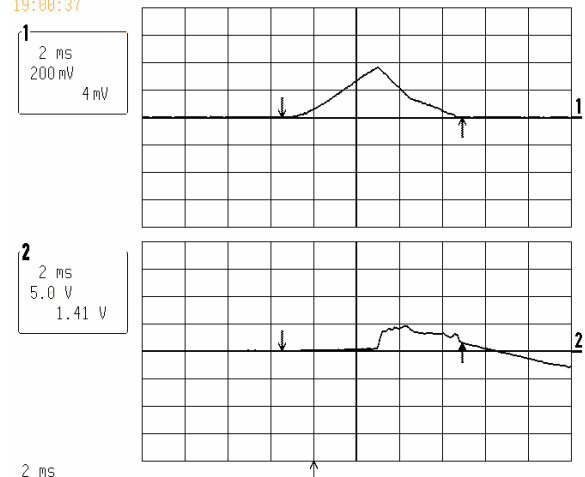


Figure 3, Typical oscillograms of current (above) and voltage (below), 2ms/div. for tests shows in Table II.

From the results, comes off that the current limitation with these fuses is obtained with very low values of prospective current and without high overvoltage surges. What indicates the advantage of being able to have an appropriate fuse element design for rated currents as low as 100 mA.

With the utilization of the paper as substrate, the problem of the low insulation resistance after the fuse

operation is eliminated, always obtaining values above the 100 k Ω .

The dispersion in the values of prearcing specific energy (I^2t_{pa}) is due to the already mentioned effect, of ink diffusion in the paper.

2.3. Behaviour with cyclic load

Sample type B:

These tests were carried out to assess the behavior of the lithographic technology in the face of the fuse element fatigue with cyclic loads. At the present time, only are available results of tests carried out on type B samples.

The tests were carried out with the rated current, 100 mA, circulating during 15 minutes, followed by a 45 minute period without load. Using for these tests a low voltage circuit (2.5V).

Two samples were tested, the first one operated after 320 cycles and the second one overcame 1500 cycles without deterioration neither appreciable change in the voltage drop.

In Fig. 4 is shown the voltage drop evolution of the operated sample and in Fig. 5 a picture of the operated sample is shown, where can be observed that the cause of the operation is a fissure (marked with a circle on the notch) probably due to a defect in the ink deposition in this area.

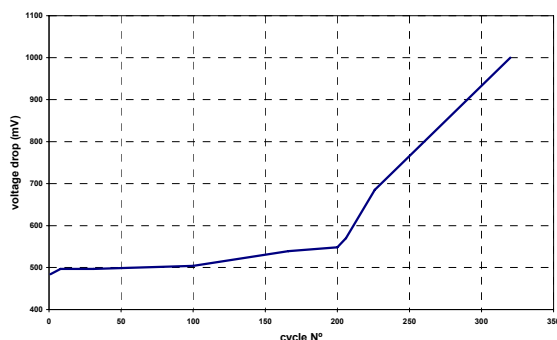


Figure 4, Voltage drop during the cyclic load test.

3. Conclusions

The preliminary experimental studies allow to conclude that the offset technology for fuses on flexible substrate, for the analyzed methods, is extremely promissory.

Keeping in mind the low rated currents that are achieved with this technology, fuses having characteristics of high breaking capacity can be obtained for applications on very low power.

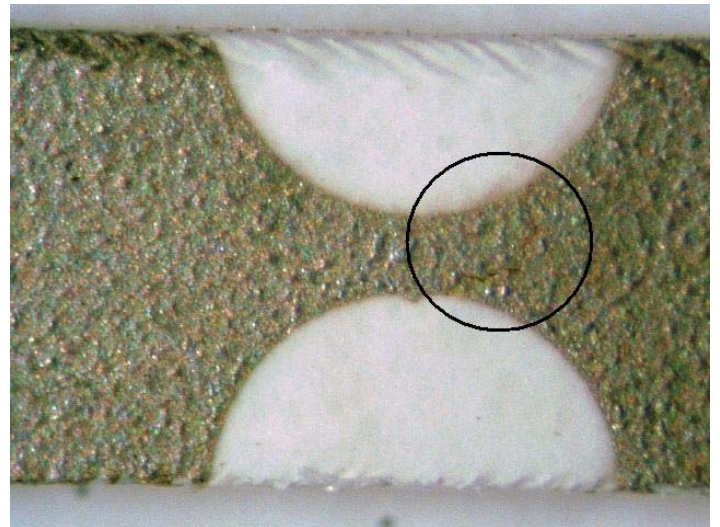


Figure 5, Picture of the fuse element notch that failed during the cyclic load test.

For the development of this technology it is necessary to deepen the studies in the following points, where higher difficulties have been detected:

- To determine the best material to be used as flexible substrate. Of the material used for the experimental determinations, it was found that the polyethylene film produces a low isolation resistance after the short circuit operation, while the glossy paper is very porous and the ink diffusion that takes place generate fuse thickness non-uniformities.
- To deepen the study with cyclic loads to determine the cause of the inopportune and unwanted operations.
- To develop a fuse element assembling structure that allows to obtain an appropriate contact among the fuse element (conductive layer) and the fuse terminals.

References

- [1] Ramsey, B.J., Evans, P.S., Harrison, D., A novel circuit fabrication technique using offset lithography, *Journal of Electronic Manufacturing*, Vol. 7, n° 1, pp. 63 – 67, March 1997.
- [2] Evans, P.S., Ramsey, B.J., Harrey, P.M., Harrison, D.J., Printed analogue filter structures, *IEE Electronic Letters*, Vol. 35, n° 4, pp. 306-308, February 1999.
- [3] Tourn, D., Gomez, J. C., Estado del arte y posibilidades de aplicación de Fusibles Sobre Substrato para media tensión, Congreso Internacional de Distribución Eléctrica CIDEL 2006, Buenos Aires, 28-30/11/2006, pp. 21.
- [4] Norma IEC 60269-1 fourth edition 2006-11.
- [5] Norma IEC 60127-1 second edition 2006-06.

RADIATION OF SYSTEM OF LINEAR WIRES IN MAGNETOPLASMA

N.M.Yatsenko⁽¹⁾, and E.A.Yatsenko⁽²⁾

IT Department, Kharkiv National University⁽¹⁾, 53 Pushkinska St., Kharkiv 61002, Ukraine,
jatsenkok@rambler.ru

Radiophysics Department, Karazine Kharkiv National University⁽²⁾, 4 Svoboda sq., Kharkiv 61077, Ukraine
jatsenkok@rambler.ru

Abstract. A problem of excitement of currents in the system consisting of two thin parallel wires, arbitrarily oriented in anisotropic plasma (magnetoplasma) was solved by method of partial averaging. Numerical analysis of obtained expressions was carried out and dependencies of current distribution and electromagnetic field from lengths of wires, distances between them and parameters of plasma were explored.

Keywords: magnetoplasma, linear wires, currents distributions, electromagnetic field, power in far zone.

1. Introduction

The studies of linear wires in anisotropic mediums are important in such applications as radio communication in space, heating of plasma by high-frequency electromagnetic fields, diagnostics of magnetoactive plasma, electromagnetic compatibility of electronic devices, etc. The purpose of the present work is the solution of the problem on excitation of a system of thin impedance wires arbitrary located in anisotropic plasma and to determine conditions of effective transfer of energy from the wires to plasma.

2. Statement of the problem

We consider a system of parallel linear impedance wires (Fig.1) located under an arbitrary angle γ to the direction of an external magnetic field (the axis of anisotropy) in magnetoactive plasma, permittivity of which is a diagonal tensor

$$\varepsilon = \begin{pmatrix} \varepsilon_1 & 0 & 0 \\ 0 & \varepsilon_1 & 0 \\ 0 & 0 & \varepsilon_3 \end{pmatrix}$$

with components

$\varepsilon_1 = 1 - \omega_N^2 / (\omega^2 - \omega_B^2)$, $\varepsilon_3 = 1 - \omega_N^2 / \omega^2$, ω_N^2 is the Lengmur's frequency; ω_B^2 is the Larmor's frequency; ω is the working frequency. The magnetic field is directed along axis OZ .

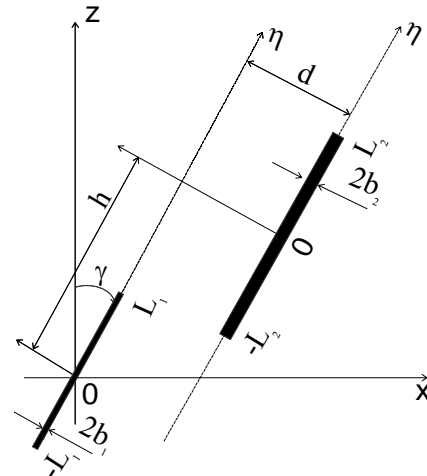


Fig. 1. Geometry of wires

Our goal is to study the dependence of the current in each wire, fields of radiation in far zone and radiation pattern of the antenna system on the sizes of wires, distance between wires (d and h), values of the complex surface impedance of wires, orientations of wires concerning the axis of anisotropy and values of components of permittivity tensor of plasma.

3. Method of the solution.

The solution of our problem is to be obtained on the basis of integral equations of electromagnetics derived from exact expressions of the Green's function for uniaxial anisotropic medium [1]. These equations are completely equivalent of the Maxwell equations and boundary conditions; they can be written as

$$\begin{aligned} i\omega\sqrt{\varepsilon_1} [\vec{E}(\vec{r}_n) - \vec{E}_0(\vec{r}_n)] = \\ = (\text{grad div} + k_0^2 \varepsilon_1 \varepsilon_3 \varepsilon^{-1}) [A_{n1}(\vec{r}_n) + A_{n2}(\vec{r}_n)] + \\ + ik_0 \text{rot} \vec{e}_z [B_{n1}(\vec{r}_n) + B_{n2}(\vec{r}_n)], \quad (1) \\ i\omega\sqrt{\varepsilon_1} [\vec{H}(\vec{r}_n) - \vec{H}_0(\vec{r}_n)] = \end{aligned}$$

$$= ik_0 \varepsilon_1 \varepsilon_3 \varepsilon^{-1} \text{rot} \left[\vec{A}_{n1}(\vec{r}_n) + \vec{A}_{n2}(\vec{r}_n) \right] - \left(\text{grad} \frac{\partial}{\partial z} - \vec{e}_z \Delta \right) [B_{n1}(\vec{r}_n) + B_{n2}(\vec{r}_n)], \quad (2)$$

where

$$\vec{A}_{nm}(\vec{r}_n) = \int_{V_m} \frac{\vec{j}_m(\vec{r}'_m) \exp \left(-ik_0 \sqrt{\varepsilon_3 |\vec{\rho}_n - \vec{\rho}'_m|^2 + \varepsilon_1 (z_n - z'_m)^2} \right)}{\sqrt{\varepsilon_3 |\vec{\rho}_n - \vec{\rho}'_m|^2 + \varepsilon_1 (z_n - z'_m)^2}} d\vec{r}'_m,$$

$$B_{nm}(\vec{r}_n) = \int_{V_m} \left(\vec{j}_m(\vec{r}'_m) \times \text{grad} \left| \vec{\rho}_n - \vec{\rho}'_m \right| \right)_z \times \left[\frac{\exp \left(-ik_0 \sqrt{\varepsilon_1 |\vec{r}_n - \vec{r}'_m|} \right)}{\left| \vec{\rho}_n - \vec{\rho}'_m \right|} - \frac{\exp \left(-ik_0 \sqrt{\varepsilon_3 |\vec{\rho}_n - \vec{\rho}'_m|^2 + \varepsilon_1 (z_n - z'_m)^2} \right)}{\left| \vec{\rho}_n - \vec{\rho}'_m \right|} \right] d\vec{r}'_m,$$

where \vec{E}_0, \vec{H}_0 are the electric and magnetic fields of the source; \vec{E}, \vec{H} are the scattered electric and magnetic fields; $k_0 = \omega/c$ is the wave number, ω is the frequency, c is the velocity of light; V_m is the volume of m -th wire; \vec{e}_z is the ort along the axis of anisotropy; $\vec{r}_n = \vec{r}_n(x_n, y_n, z_n)$ and $\vec{r}'_m = \vec{r}'_m(x'_m, y'_m, z'_m)$ are the radius-vectors of points of observation and integration respectively; the index z in the expressions for $B_{nm}(\vec{r}_n)$ points out to the projection of the vector product on the axis of anisotropy (axis OZ);

$|\vec{\rho}_n - \vec{\rho}'_m| = \sqrt{(x_n - x'_m)^2 + (y_n - y'_m)^2}$; $\vec{j}_m(\vec{r}_m)$ is the volume density of the current in the m -th wire; in all formulas $n, m = 1, 2$.

The advantage of the method of integral equations [2] is that it enables us, in an analytical form, to solve a large class of boundary problems of electromagnetism. The algorithm of solution by this method contains two stages. At the first stage we find the currents excited in each wire by the field of the source and the field produced by the other wire. In this case initial integral equations (1), (2) form a set Fredholm's integral equations of the first kind having a unique solution. At the second stage, based on already known currents we construction the total field. In this case equations (1), (2) are identifies

representing the total field as a sum of the field of the source and the scattered field.

A problem about excitement of electrical current in the system consisting of two parallel linear wires with lengths $2L_1, 2L_2$, radiuses b_1, b_2 , situated under any angle γ to axis of anisotropy will consider on the base of these integral equations. As far as wires are fine: $b_i/L_i \ll 1$; $b_i/\lambda \ll 1$, $i=1,2$, where λ - a wavelength of falling electromagnetic field, only that electrical currents will be essential which current along wire; it is possible to neglect of transverse currents.

Considering that tangential components of full electrical field on surfaces of perfectly conducting wire are a zero, equations for density of currents, induced in each wire by given falling field and field, which generate other wire, will be obtained having designed equations (1) on axis of wires. For this it's need move over in new coordinate system $\chi\eta\xi$, having directed one of its axis's ($\text{o}\eta$) parallel to axis of wires. Relationship between coordinates of new and old systems is installed by formulas

$$\chi = x, \quad \eta = y \sin \gamma + z \cos \gamma, \quad \xi = -y \cos \gamma + z \sin \gamma$$

Then equations for density of currents are obtained in the manner of

$$-i\omega \sqrt{\varepsilon_1} E_{0\eta_1}(\eta_1) = \left(\frac{\partial^2}{\partial \eta_1^2} + k_0^2 \delta^2 \right) \times \left\{ \int_{V_1} \frac{j_{1\eta}(\vec{r}'_1) \exp(-ik_0 R_{11})}{R_{11}} d\vec{r}'_1 + \int_{V_2} \frac{j_{2\eta}(\vec{r}'_2) \exp(-ik_0 R_{12})}{R_{12}} d\vec{r}'_2 \right\} + ik_0 \sin^2 \gamma \frac{\partial}{\partial \chi_1} \times \left\{ \int_{V_1} j_{1\eta}(\vec{r}'_1) (\chi_1 - \chi'_1) \frac{\exp(-ik_0 \sqrt{\varepsilon_1 |\vec{r}_1 - \vec{r}'_1|}) - \exp(-ik_0 R_{11})}{T_{11}} d\vec{r}'_1 + \int_{V_2} j_{2\eta}(\vec{r}'_2) (\chi_1 - \chi'_2) \frac{\exp(-ik_0 \sqrt{\varepsilon_1 |\vec{r}_1 - \vec{r}'_2|}) - \exp(-ik_0 R_{12})}{T_{12}} d\vec{r}'_2 \right\}, \quad (3)$$

where $\delta^2 = \varepsilon_3 \sin^2 \gamma + \varepsilon_1 \cos^2 \gamma$,

$$-i\omega \sqrt{\varepsilon_1} E_{0\eta_2}(\eta_2) = \left(\frac{\partial^2}{\partial \eta_2^2} + k_0^2 \delta^2 \right) \times$$

$$\begin{aligned}
& \times \left\{ \int_{V_2} \frac{j_{2\eta}(\vec{r}'_2) \exp(-ik_0 R_{22})}{R_{22}} d\vec{r}'_2 + \int_{V_1} \frac{j_{1\eta}(\vec{r}'_1) \exp(-ik_0 R_{21})}{R_{21}} d\vec{r}'_1 \right\} + \\
& + ik_0 \sin^2 \gamma \frac{\partial}{\partial \chi_2} \times \\
& \times \left\{ \int_{V_2} j_{2\eta}(\vec{r}_2) (\chi_2 - \chi'_2) \frac{\exp(-ik_0 \sqrt{\varepsilon_1} |\vec{r}_2 - \vec{r}'_2|) - \exp(-ik_0 R_{22})}{T_{22}} d\vec{r}_2 + \right. \\
& \left. + \int_{V_1} j_{1\eta}(\vec{r}_1) (\chi_2 - \chi'_1) \frac{\exp(-ik_0 \sqrt{\varepsilon_1} |\vec{r}_2 - \vec{r}'_1|) - \exp(-ik_0 R_{21})}{T_{21}} d\vec{r}_1 \right\}, \\
(4)
\end{aligned}$$

where

$$\begin{aligned}
R_{ij} &= \sqrt{\delta^2 (\eta_i - \eta'_j)^2 + \varepsilon_3 (\chi_i - \chi'_j)^2 + (\varepsilon_1 \varepsilon_3 / \delta^2) (\xi_i - \xi'_j)^2}, \\
T_{ij} &= [(\eta_i - \eta'_j) \sin \gamma - (\xi_i - \xi'_j) \cos \gamma]^2 + (\chi_i - \chi'_j)^2; \\
E_{0\eta_i}(\eta_i) & \text{-tangential to surface of } i\text{-th wire} \\
& \text{component of intensity of falling electrical field} \\
& \text{(field of the source), } i, j = 1, 2.
\end{aligned}$$

It's possible to consider equations (3), (4) as analogues of Poclington's equations well-known in theory of secluded linear wire situated in isotropic medium, spreading and generalising its to the linear wire system, situated in the anisotropic medium. In these equations integral addends in right parts, co-keeping $R_{11}, R_{22}, T_{11}, T_{22}$, have a singularity when coinciding the points of the source and observation ($\vec{r}_i = \vec{r}'_i$, $i = 1, 2$). As far as singularities in the dynamics and in the static have one and same nature, it's possible to select their, determining electrostatic parts corresponding integral addends. As a result we obtain equations with small parameters for currents $I_1(\eta_1)$ and $I_2(\eta_2)$, generated in each wire:

$$\begin{aligned}
& \frac{d^2 I_1(\eta_1)}{d\eta_1^2} + k_0^2 \varepsilon_{eq} I_1(\eta_1) = \\
& = \alpha_1 \delta \left\{ i\omega \sqrt{\varepsilon_1} E_{0\eta_1}(\eta_1) + F_{11}(\eta_1, I_1) + \right. \\
& \left. + F_{12}(\eta_1, I_2) + [K_{11}(\eta_1, I_1) + K_{12}(\eta_1, I_2)] \sin^2 \gamma \right\}, \quad (5)
\end{aligned}$$

$$\frac{d^2 I_2(\eta_2)}{d\eta_2^2} + k_0^2 \varepsilon_{eq} I_2(\eta_2) =$$

$$\begin{aligned}
& = \alpha_2 \delta \left\{ i\omega \sqrt{\varepsilon_1} E_{0\eta_2}(\eta_2) + F_{22}(\eta_2, I_2) + \right. \\
& \left. + F_{21}(\eta_2, I_1) + [K_{22}(\eta_2, I_2) + K_{21}(\eta_2, I_1)] \sin^2 \gamma \right\}, \quad (6)
\end{aligned}$$

where $\varepsilon_{eq} = \delta^2 \cos^2 \gamma + \delta \sqrt{\varepsilon_1} \sin^2 \gamma$ - equivalent permittivity;

$$\alpha_1 = -\frac{1}{2 \ln \left(\frac{2L_1}{b_1} \frac{2\delta^2 / \sqrt{\varepsilon_3}}{\sqrt{\varepsilon_1} + \delta} \right)},$$

$$\alpha_2 = -\frac{1}{2 \ln \left(\frac{2L_2}{b_2} \frac{2\delta^2 / \sqrt{\varepsilon_3}}{\sqrt{\varepsilon_1} + \delta} \right)} \text{ - small parameters.}$$

The addends F_{11}, K_{11} and F_{22}, K_{22} describe own fields of first and second wires accordingly, addends F_{12}, K_{12} describe an influence of fields, generated second wire, on the amperage, excited in the first wire. Similarly, F_{21} and K_{21} describe an influence of field's first wire on the current in the second wire.

$$F_{11}(\eta_1) = \left(\frac{\partial^2}{\partial \eta_1^2} + k_0^2 \delta^2 \right) \times$$

$$\times \int_{-L_1}^{L_1} \frac{I_1(\eta'_1) \exp(-ik_0 \sqrt{\delta^2 (\eta_1 - \eta'_1)^2 + r_{eq1}^2}) - I_1(\eta_1)}{\sqrt{\delta^2 (\eta_1 - \eta'_1)^2 + r_{eq1}^2}} d\eta'_1,$$

$$F_{12}(\eta_1) = -\frac{dI_2(\eta'_2)}{d\eta'_2} \times$$

$$\times \frac{\exp(-ik_0 \sqrt{\delta^2 (\eta_1 - \eta'_2)^2 + d_{eq}^2})}{\sqrt{\delta^2 (\eta_1 - \eta'_2)^2 + d_{eq}^2}} \Big|_{\eta'_2 = -L_2}^{\eta'_2 = L_2} +$$

$$+ \int_{-L_2}^{L_2} \left[\frac{d^2 I_2(\eta'_2)}{d\eta_2'^2} + k_0^2 \delta^2 I_2(\eta'_2) \right] \times$$

$$\times \frac{\exp(-ik_0 \sqrt{\delta^2 (\eta_1 - \eta'_2)^2 + d_{eq}^2})}{\sqrt{\delta^2 (\eta_1 - \eta'_2)^2 + d_{eq}^2}} d\eta'_2,$$

where $d_{eq}^2 = d^2 \varepsilon_3 \delta^2 (\delta^2 \sin^2 \tau + \varepsilon_1 \cos^2 \tau)$ - equivalent distance between wires, τ - angle between d (on planes $\chi O \xi$) and axis $O \xi$, where

$r_{eqi}^2 = (\varepsilon_3 \sqrt{\varepsilon_1} / \delta) b_i^2$ - equivalent radius i-th wire, $i = 1, 2$;

$$F_{22}(\eta_2) = \left(\frac{\partial^2}{\partial \eta^2} + k_0^2 \delta^2 \right) \times \left[\int_{-L_2}^{L_2} \frac{I_2(\eta'_2) \exp\left(-ik_0 \sqrt{\delta^2(\eta_2 - \eta'_2)^2 + r_{eq2}^2}\right)}{\sqrt{\delta^2(\eta_2 - \eta'_2)^2 + r_{eq2}^2}} d\eta'_2 - \int_{-L_2}^{L_2} \frac{I_2(\eta_2)}{\sqrt{\delta^2(\eta_2 - \eta_2)^2 + r_{eq2}^2}} d\eta'_2 \right],$$

$$F_{21}(\eta_2) = - \frac{dI_1(\eta'_1)}{d\eta'_1} \cdot \frac{\exp\left(-ik_0 \sqrt{\delta^2(\eta_2 - \eta'_1)^2 + d_{eq}^2}\right)}{\sqrt{\delta^2(\eta_2 - \eta'_1)^2 + d_{eq}^2}} \Big|_{\eta'_1=-L_1}^{\eta'_1=L_1} + \int_{-L_1}^{L_1} \left[\frac{d^2 I_1(\eta'_1)}{d\eta_1'^2} + k_0^2 \delta^2 I_1(\eta'_1) \right] \times \frac{\exp\left(-ik_0 \sqrt{\delta^2(\eta_2 - \eta'_1)^2 + d_{eq}^2}\right)}{\sqrt{\delta^2(\eta_2 - \eta'_1)^2 + d_{eq}^2}} d\eta'_1,$$

$$K_{11}(\eta_1) = ik_0 \times \left\{ \int_{-L_1}^{L_1} I_1(\eta'_1) \frac{\exp\left(-ik_0 \sqrt{\varepsilon_1} \sqrt{(\eta_1 - \eta'_1)^2 + b_1^2}\right)}{(\eta_1 - \eta'_1)^2 + b_1^2} d\eta'_1 - \int_{-L_1}^{L_1} I_1(\eta'_1) \frac{\exp\left(-ik_0 \sqrt{\delta^2(\eta_1 - \eta'_1)^2 + r_{eq1}^2}\right)}{(\eta_1 - \eta'_1)^2 + b_1^2} d\eta'_1 \right\} - k_0^2 \left[\int_{-L_1}^{L_1} I_1(\eta_1) \frac{\sqrt{\varepsilon_1} \sqrt{(\eta_1 - \eta'_1)^2 + b_1^2}}{(\eta_1 - \eta'_1)^2 + b_1^2} d\eta'_1 - \int_{-L_1}^{L_1} I_1(\eta_1) \frac{\sqrt{\delta^2(\eta_1 - \eta'_1)^2 + r_{eq1}^2}}{(\eta_1 - \eta'_1)^2 + b_1^2} d\eta'_1 \right],$$

$$K_{12}(\eta_1) = ik_0 \times \left\{ \int_{-L_2}^{L_2} I_2(\eta'_2) \frac{\exp\left(-ik_0 \sqrt{\varepsilon_1} \sqrt{(\eta_1 - \eta'_2)^2 + d^2}\right)}{(\eta_1 - \eta'_2)^2 + d^2} d\eta'_2 - \int_{-L_2}^{L_2} I_2(\eta'_2) \frac{\exp\left(-ik_0 \sqrt{\delta^2(\eta_1 - \eta'_2)^2 + d_{eq}^2}\right)}{(\eta_1 - \eta'_2)^2 + d^2} d\eta'_2 \right\};$$

$$K_{22}(\eta_2) = ik_0 \times \left\{ \int_{-L_2}^{L_2} I_2(\eta'_2) \frac{\exp\left(-ik_0 \sqrt{\varepsilon_1} \sqrt{(\eta_2 - \eta'_2)^2 + b_2^2}\right)}{(\eta_2 - \eta'_2)^2 + b_2^2} d\eta'_2 - \int_{-L_2}^{L_2} I_2(\eta'_2) \frac{\exp\left(-ik_0 \sqrt{\delta^2(\eta_2 - \eta'_2)^2 + r_{eq2}^2}\right)}{(\eta_2 - \eta'_2)^2 + b_2^2} d\eta'_2 \right\} - k_0^2 \left[\int_{-L_1}^{L_1} I_1(\eta_1) \frac{\sqrt{\varepsilon_1} \sqrt{(\eta_1 - \eta'_1)^2 + b_1^2}}{(\eta_1 - \eta'_1)^2 + b_1^2} d\eta'_1 - \int_{-L_1}^{L_1} I_1(\eta_1) \frac{\sqrt{\delta^2(\eta_1 - \eta'_1)^2 + r_{eq1}^2}}{(\eta_1 - \eta'_1)^2 + b_1^2} d\eta'_1 \right],$$

$$K_{21}(\eta_2) = ik_0 \times \left\{ \int_{-L_1}^{L_1} I_1(\eta'_1) \frac{\exp\left(-ik_0 \sqrt{\varepsilon_1} \sqrt{(\eta_2 - \eta'_1)^2 + d^2}\right)}{(\eta_2 - \eta'_1)^2 + d^2} d\eta'_1 - \int_{-L_1}^{L_1} I_1(\eta'_1) \frac{\exp\left(-ik_0 \sqrt{\delta^2(\eta_2 - \eta'_1)^2 + d_{eq}^2}\right)}{(\eta_2 - \eta'_1)^2 + d^2} d\eta'_1 \right\}.$$

Equations obtained in this way are solved by the method of averaging [3]. The advantage of the method of averaging is that it enables us to obtain uniform analytical expressions for the currents that are correct for wires of any length, including resonant

one. The obtained analytical expressions describe the currents in wires of any length with positive and negative values of $\varepsilon_1, \varepsilon_3$. So for two symmetric active wires excited by δ -generators, connected in the centres of wires $E_{0\eta_1}(\eta_1) = V_{01}\delta(\eta_1)$, $E_{0\eta_2}(\eta_2) = V_{02}\delta(\eta_2)$, the expressions for currents look like

$$I_1(\eta_1) = V_{01} \frac{\sin k_1(L_1 - |\eta_1|)}{Z_{11}} + V_{02} \frac{U_{12}(\eta_1) \sin 2k_1 L_1 - M_{12} \sin k_1(L_1 + \eta_1)}{Z_{12}}, \quad (7)$$

$$I_2(\eta_2) = V_{02} \frac{\sin k_2(L_2 - |\eta_2|)}{Z_{22}} + V_{01} \frac{U_{21}(\eta_2) \sin 2k_2 L_2 - M_{21} \sin k_2(L_2 + \eta_2)}{Z_{21}}, \quad (8)$$

where

$$U_{12}(\eta_1) = \int_{-L_1}^{\eta_1} (\eta'_1) \sin k_1(\eta_1 - \eta'_1) \int_{-L_2}^{L_2} S_{12}(\eta'_1, \eta'_2) \cos k_2(\eta'_2 - L_2) d\eta'_2 d\eta'_1,$$

$$U_{21}(\eta_2) = \int_{-L_2}^{\eta_2} \eta'_2 \sin k_2(\eta_2 - \eta'_2) \int_{-L_1}^{L_1} S_{21}(\eta'_2, \eta'_1) \cos k_1(\eta'_1 - L_1) d\eta'_1 d\eta'_2,$$

$$M_{12} = U_{12}(\eta_1) \Big|_{\eta_1=L_1}, \quad M_{21} = U_{21}(\eta_2) \Big|_{\eta_2=L_2}$$

- integral functions describing mutual influence of wires, Z_{11}, Z_{22} - own entrance resistance of wires, Z_{12}, Z_{21} - mutual resistance; $k_n = k'_n + ik''_n = k_0 \left[\sqrt{\varepsilon_{eq}} + i\alpha_n \left(\delta \sqrt{\varepsilon_1 / \varepsilon_{eq}} / k_0 b_n \right) Z_n \right]$, where $Z_n = R_n + iX_n$ - complex skin impedance n -th wires normalized on 120π ; $n = 1, 2$.

The influence of the surface impedance of wires on the currents is characterised by variations of complex wave numbers $k_n = k'_n + ik''_n$, that include dielectric characteristics of medium, geometry of wires and their orientation in magnetoactive plasma.

The characteristics (Fig2., Fig.3) were calculated for symmetrical wires (7), (8) situated in the laboratory plasma with parameters: electron

concentration 10^8 sm^{-3} , constant magnetic field 3500 e, Langmuir frequency $\omega_N = 5.6 \cdot 10^8 \text{ Hz}$, Larmor frequency $\omega_B = 6 \cdot 10^{10} \text{ Hz}$. Under changing work frequency ω in range, where $\omega_B \gg \omega \gg \omega_N^2 / \omega_B$ plasma is described by diagonal tensor ε . In this range the component ε_1 doesn't depend on frequency ($\varepsilon_1 \approx 1$), component ε_3 is function of frequency.

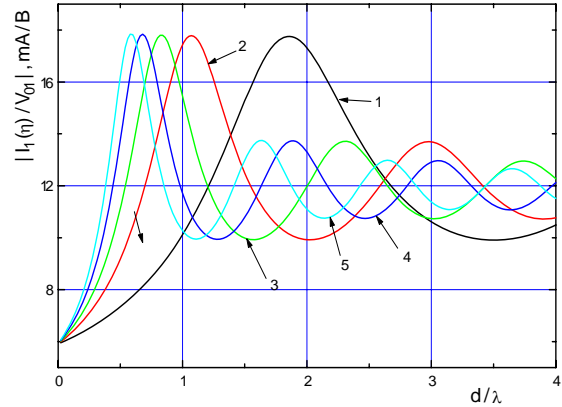


Fig.2. The dependence of input current ($\eta=0$) in first wire under $L_1/\lambda = 0,25, L_2/\lambda = 0,25$, from distance d/λ between wires under different ε_3 (1 -0,1; 2 - 0,3; 3 -0,5; 4 -0,75; 5 -1) and orientation $\gamma=0$ (parallel to anisotropy axis OZ).

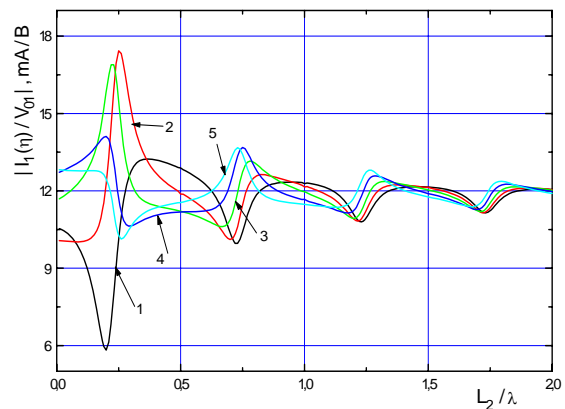


Fig.3. The dependence of input current ($\eta=0$) in first wire $L_1/\lambda = 0,25$, under, $d/\lambda = 1$ from different ε_3 (1 -0,1; 2 -0,3; 3 -0,5; 4 -0,75; 5 -1) under orientation $\gamma=0$ (parallel to axis of anisotropy OZ).

Based on the distributions of currents according to the formulas (1), (2), it is possible to find the fields of radiation at any distance from wires. In particular, the expressions for the fields in far zone in the spherical system of coordinates r, θ, φ are as follows:

$$E_r = H_r = 0,$$

$$E_{\theta} = \frac{k_0^2 \sqrt{\varepsilon_1 \varepsilon_3}}{i\omega N^3} \times (\sin\gamma \cos\varphi \cos\theta - \cos\gamma \sin\theta) \Pi_N \frac{\exp(-ik_0 Nr)}{r},$$

$$E_{\varphi} = \frac{k_0^2 \sin\gamma \sin\varphi}{i\omega} \Pi_O \frac{\exp(-ik_0 \sqrt{\varepsilon_1} r)}{r},$$

$$H_{\theta} = \frac{k_0^2 \sqrt{\varepsilon_1} \sin\gamma \sin\varphi}{i\omega} \Pi_O \frac{\exp(-ik_0 \sqrt{\varepsilon_1} r)}{r},$$

$$H_{\varphi} = \frac{k_0^2 \sqrt{\varepsilon_1 \varepsilon_3}}{i\omega N^2} \times (\sin\gamma \cos\varphi \cos\theta - \cos\gamma \sin\theta) \Pi_N \frac{\exp(-ik_0 Nr)}{r},$$

where

$$N = \sqrt{\varepsilon_3 \sin^2 \theta + \varepsilon_1 \cos^2 \theta},$$

$$\Pi_O = \Pi_{O1} + \Pi_{O2} \exp[-ik_0 \sqrt{\varepsilon_1} (h \cos\Gamma_1 + d \cos\Gamma_2)],$$

$$\Pi_N = \Pi_{N1} + \Pi_{N2} \exp[-ik_0 N (h \cos\Gamma_1 + d \cos\Gamma_2)],$$

$$\cos\Gamma_1 = \sin\gamma \cos\varphi \sin\theta + \cos\gamma \cos\theta,$$

$$\cos\Gamma_2 = \cos\gamma \cos\varphi \sin\theta - \sin\gamma \cos\theta,$$

$$\Pi_{Oj} = \int_{-L_j}^{L_j} I_j(\eta) \exp(ik_0 \sqrt{\varepsilon_1} \eta \cos\Gamma_1) d\eta;$$

$$\Pi_{Nj} = \int_{-L_j}^{L_j} I_j(\eta) \exp(ik_0 N \eta \cos\Gamma_1) d\eta;$$

$I_j(\eta)$ - current in j -th wire; Γ_j - angle between axis of j -wire and direction on observation point, $j=1,2$.

For the calculation of density of radiated power T we shall use the expression

$$T = (ck_0^4 / 8\pi r^2 \omega^2) (T_1 + T_2), \quad (3)$$

where

$$T_1 = \begin{cases} (\varepsilon_1 \varepsilon_3^2 / N^5) |\Pi_N|^2 (\sin\gamma \cos\varphi \cos\theta - \cos\gamma \sin\theta)^2, \\ \text{if } \operatorname{Re} N \neq 0 \\ 0, \text{ if } \operatorname{Re} N = 0 \end{cases}$$

$$T_2 = \begin{cases} \sqrt{\varepsilon_1} |\Pi_O|^2 \sin^2 \gamma \sin^2 \varphi, \text{ if } \varepsilon_1 > 0 \\ 0, \text{ if } \varepsilon_1 \leq 0 \end{cases}$$

4. Conclusion

Anisotropy of medium essentially changes all characteristics of wires. The functions of distribution of currents along wires is determined by equivalent permittivity ε_{eq} and equivalent distance between wires d_{eq} , which depend on the values of components $\varepsilon_1, \varepsilon_3$ of permittivity tensor and on the orientation of wire system in medium (angle γ). Hence, these factors determine the shape of patterns. It is possible to make a conclusion about two ways of the design of wires: electrical (changing the working frequency, that is $\varepsilon_1(\omega), \varepsilon_3(\omega)$) and mechanical (changing orientation in medium). It is known that if one of the components of permittivity tensor is negative, than with a certain orientation of wire system relatively to the axis of anisotropy, the current in the perfectly conducting wire not excited [4]. Excitation of significant currents in impedance wire in this case is possible, provided that surface impedance is selected so that it compensates the reaction of surrounding plasma. If in the expressions for the fields of radiation and currents one puts $\varepsilon_1 = \varepsilon_3$, we obtains the appropriate formulas for isotropic medium. By removing one of the wires to infinity, we obtain the formulas for the single wire.

Thus, in the present work a high efficiency of the method of integral equations is shown which has enabled us to solve the problem about excitation of two parallel wires arbitrary oriented in anisotropic medium. Without any special difficulties this method can be applied to studying the system consisting of large number of thin wires located in isotropic or anisotropic medium.

References

- [1] Khizhnyak N.A., Yatsenko E.A., Yatsenko N.M. "Green's function of Maxwell's equations for nonhomogeneous anisotropic medium", Vestnik Kharkovskogo universiteta. Radiofizika I Elektronika (Kharkiv), No 336, p.p. 19-23, 1989.
- [2] Khizhnyak N.A. "Integral equations of macroscopic electrodynamics", Kiev, Naukova dumka, 280 p., 1986.
- [3] Mitropolsky Yu.A. "Averaging in integro-differential and integral equations", Ukrainian Mathematical Journal, (Kiev), No 1, p.p. 30-48, 1972.
- [4] Felsen L., Marcuvitz N. "Radiation and Scattering of Waves", Prentice-Hall, Inc., Englewood Cliffs, New Jersey, 1973.